



**UNIVERSITÀ
DEGLI STUDI
DI TRIESTE**

UNIVERSITÀ DEGLI STUDI DI TRIESTE

XXXVI CICLO DEL DOTTORATO DI RICERCA IN
FISICA

GROWTH OF X-ENES AT SURFACES: GEOMETRIC, ELECTRONIC,
AND CHEMICAL PROPERTIES OF B AND P MONOLAYERS

Settore scientifico-disciplinare: FIS/03

DOTTORANDO
PIETRO BIASIN

COORDINATORE
PROF. FRANCESCO LONGO

SUPERVISORE DI TESI
PROF. ERIK VESSELLI

Abstract

Starting with the discovery of graphene in 2004, which provided the first experimental evidence of an atomically thin material, and advancing in the investigation of its peculiar and intriguing properties towards the successful synthesis of high-quality graphene films for industrial applications, the scientific interest into two-dimensional materials has grown exponentially. In the recent years, the desire to miniaturise devices capable of exploiting quantum phenomena has driven significant research interest in two-dimensional mono- elemental graphene-like materials called X-enes. Within this extended materials family, this thesis focuses on two selected members, namely borophene and phosphorene, consisting of elemental monolayers of boron and phosphorus atoms, respectively.

Boron is characterised by an intrinsic electron deficiency with respect to carbon, which induces, specifically in two dimensions, the tendency to multi-centric bonding and polymorphism. At surfaces, the electron deficiency could be compensated by electron doping provided by a supporting surface. In this thesis, I have characterised the growth of two-dimensional B structures at the Al(111) and Ni₃Al(111) terminations, with particular interest towards the investigation of the complex interplay between B and Al alloying and segregation, which again gives rise to the formation of a variety of B and B-Al polymorphs.

In the following, we investigated how the physical phenomena characterising the two-dimensional B structures at surfaces could be influenced by the presence of ubiquitous gases as oxygen and hydrogen. Upon gases exposure, the relative chemical affinity of B and of the supporting metals with respect to the adsorbates turned out to play a crucial role in determining the behaviour of the system: while atomic H exposure resulted in the direct reduction of the B layer, yielding the synthesis of a honeycomb borophane phase on Al(111), the interaction of the system with O₂ turned out to be far more complex, involving Al atoms segregation, the formation of Al and B oxide terminal structures, depending on the Al concentration in supporting surface.

Phosphorus shares with Boron the tendency to form different polymorphs, specifically at surfaces. Several stable two-dimensional phosphorus allotropes have been theoretically predicted, experimentally synthesised, and eventually exploited in technological devices, stimulating an increasing scientific interest.

Among the various phosphorene polymorphs, the single-layered blue phosphorus (BlueP) seemed to deliver promising premises for optical and electronic technologies, and it was experimentally synthesised in 2016, exploiting the Au(111) surface as a growth substrate. Interestingly, the effective structure model for the BlueP on this template turned out to be particularly debated, especially about the possible incorporation of Au adatoms from the underlying substrate. In the last part of this thesis, we provided solid experimental evidence in favour of the formation of a long-range ordered network of triangular BlueP islands linked together and stabilised by the incorporation of Au adatoms.

The experimental characterisation of growth and properties of X-enes at surfaces has been carried out in a multi-technique experimental approach, exploiting Infrared-Visible Sum Frequency Generation spectroscopy (IR-Vis SFG), Scanning Tunnelling Microscopy (STM), X-ray Photoelectron Spectroscopy (XPS), Surface X-Ray Diffraction (SXRD), Near Edge X-ray Absorption Fine Structure spectroscopy (NEXAFS), and Low-Energy Electron Diffraction (LEED). The experimental measurements were corroborated by theoretical calculations in collaboration with SISSA (group of Prof. Stefano Baroni) and the University of Trieste (group of Prof. Maria Peressi).

Contents

1	Introduction	1
1.1	2D Materials	1
1.2	Elemental Boron	1
1.2.1	Bulk phases and allotropes	1
1.2.2	Borophenes	3
1.2.3	B at surfaces	7
1.2.4	Chemically modified Borophene	18
1.3	Elemental Phosphorus	22
1.3.1	Bulk phases and allotropes	22
1.3.2	Phosphorene	25
1.3.3	BlueP/Au(111)	26
2	Methods	29
2.1	Spectroscopies	29
2.1.1	XPS	29
2.1.2	NEXAFS	35
2.1.3	IR-Vis SFG	39
2.2	Diffraction	48
2.2.1	SXRD	48
2.3	Microscopy	56
2.3.1	STM	56
2.4	Laboratories	60
2.4.1	The FlexPES beamline at MAX IV	60
2.4.2	The PEARL beamline at P.S.I.	61
2.4.3	The IR-Vis SFG laboratory	64
2.4.4	The SIXS beamline at SOLEIL	66
2.4.5	STRAS Laboratory	67

3	Borophene Growth	71
3.1	B/Al(111)	71
3.1.1	Sample Preparation	71
3.1.2	XPS and NEXAFS	72
3.1.3	STM	76
3.2	B/Ni ₃ Al(111)	82
3.2.1	Sample preparation	82
3.2.2	LEED	82
3.2.3	STM	84
3.2.4	XPS	92
3.2.5	Interpretative Model	98
4	Redox properties of borophene	105
4.1	Borophane on Al(111)	105
4.1.1	Sample Preparation	105
4.1.2	LEED	106
4.1.3	XPS and NEXAFS	106
4.1.4	SFG	110
4.1.5	Comparison with DFT	113
4.2	Oxidation of B/Al(111)	119
4.2.1	Sample Preparation	119
4.2.2	XPS and NEXAFS	119
4.2.3	SFG	122
4.2.4	STM	123
4.2.5	Comparison with DFT	125
4.3	Oxidation of B/Ni ₃ Al(111)	129
4.3.1	LEED and AES	129
4.3.2	XPS	130
5	P/Au(111)	139
5.1	Sample Preparation	139
5.2	Black and Red P yield the same Blue	141
5.3	Structure determination of BlueP/Au(111)	141
5.3.1	STM	142
5.3.2	ARPES	142
5.3.3	SXRD	147

6	Conclusions	159
A	XPS Parameters	163
A.1	B/Al(111) + H _{at}	164
A.2	B/Ni ₃ Al(111)	166
A.3	B/Ni ₃ Al(111) + O ₂	169
B	SFG Parameters	173
B.1	B/Al(111) + H _{at}	173
B.2	B/Al(111) + O ₂	174
C	SXRD Models and Parameters	175
	Bibliography	179
	Acronyms	189

Contents

Chapter 1

Introduction

1.1 2D Materials

In recent years, 2D materials have emerged as a major research topic in the field of materials science due to the various advantages they offer. These materials consist of single or few atomic layers, resulting in low-dimensional properties that differ from those of conventional bulk materials due to the introduction of an electron confinement direction. The mentioned properties are attributed indeed to effects arising from the latter reduction of dimensionality, which is closely linked to quantum size effects. The confinement of electrons in one direction, at the nanoscale and beyond, significantly impacts band structure and density of states, leading to unpredictable physical phenomena that are not observable in 3D. In recent years, the desire to miniaturise devices that can exploit quantum phenomena has elicited significant research interest in two-dimensional, mono-elemental materials resembling graphene, known as X-enes. This thesis focuses on two selected members of this extended family, namely borophene and phosphorene, which are mono-elemental layers composed of boron and phosphorus atoms, respectively.

1.2 Elemental Boron

1.2.1 Bulk phases and allotropes

The precise number of stable bulk boron allotropes is still debated despite much experimental and theoretical research aimed at uncovering their structure and

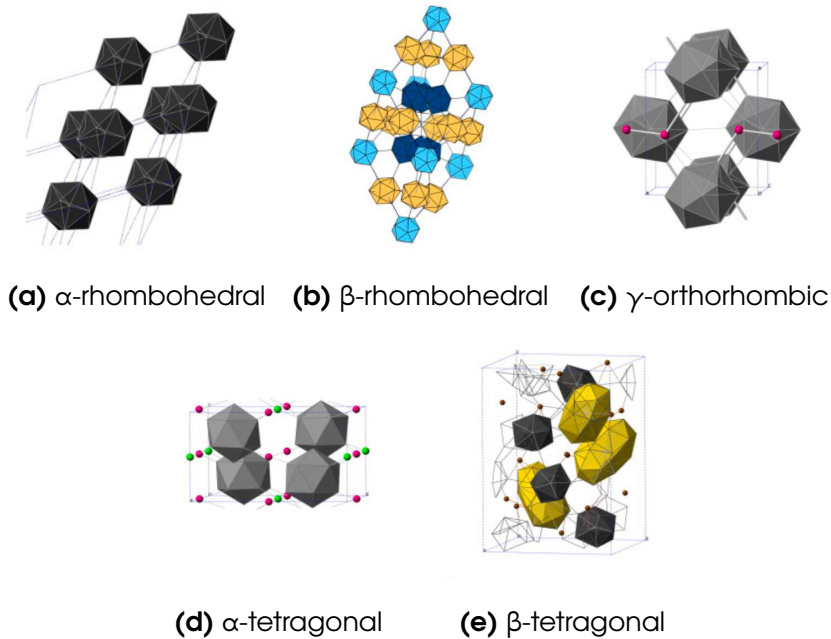


Figure 1.1: Structures of icosahedra-based boron allotropes. *Adapted from [2].*

properties. The reason for this has to be researched in the intricate and subtle structure of most of the boron allotropes. The initially supposed existence of more than 14 different boron allotropes [1], while presently the number may be reduced to just five [2], testifies the complex nature of the subject. In particular, three all-boron allotropes are widely known, namely the α - and β -rhombohedral and the γ -orthorhombic phases, while two others, namely the α - and β -tetragonal, are currently under debate. All boron allotropes described above share the same structural motif, i.e. the almost regular B_{12} icosahedron, as can be appreciated in Fig. 1.1, which depicts the structures of the main boron allotropes. It is important to note that an isolated regular boron icosahedron is electron-deficient, resulting in both energetic and structural instability. When boron icosahedra are arranged together to form a larger cluster or a bulk phase, the lack of available electrons leads to multicenter bonding and to the complex polymorphism observed in 3D boron structures. Because of the bonding geometry in the boron icosahedron cluster, each atom is encircled by five neighbouring atoms, resulting in a coordination number of five, or possibly six if bonded to another cluster.

Upon closer examination of real boron crystals, the situation turned out to

be even more complex. In fact, several boron polymorphs display intrinsic defects through partial occupancy or vacancies, as well as extrinsic defects through impurities. Nevertheless, these features are not to be regarded as defects of the crystal structure, but rather as requirements that nature dictates to stabilise the boron 3D structure. In fact, experimental findings indicate that the β -rhombohedral boron allotrope is the most thermodynamically stable and exhibits semiconducting properties. On the other hand, *ab initio* DFT studies revealed that the defectless β -rhombohedral boron crystal structure is less stable than that of the α -rhombohedral form. Furthermore, a lack of valence electrons was predicted, leading to a metallic nature of the defect-less β -rhombohedral boron allotrope [3]. This inconsistency between theory and experiments demonstrates that the real boron crystal structure has intrinsic defects, that increase the number of atoms in the unit cell, thereby enhancing its energetic and structural stability, while also defining its physical and electronic properties.

1.2.2 Borophenes

Atomically thick layers of boron are known to exist in nature in metal borides crystals, such as MgB_2 and ZrB_2 . These stacked boron sheets were originally called *boraphenes*. Then, as the subject drew researchers' attention towards this new atomic layer besides graphene, *borophene* was named as an extension of the B_{36} 2D cluster, in 2014 [4, 5]. After a first attempt to find the most stable free-standing boron layer in trigonal lattices, atomic defects and vacancies turned out to be crucial in order to stabilise the structures, in line with what happens in the 3D case.

The initially proposed structural patterns for free-standing 2D boron sheets were derived from the arrangement of boron atoms found in various metal diborides, as well as the element's natural tendency to hybridise sp^2 arising from its three valence electrons. In particular, the stacked boron layers in MgB_2 have a honeycomb structure, with Mg atoms above and below each hexagon centre. In fact, boron has one electron less than carbon, which naturally forms the honeycomb *free-standing* structure in graphene. Consequently, the hexagonal unit cell featuring two boron atoms has an intrinsic deficiency of two electrons that must be overcome. In MgB_2 , the Mg atoms provide the additional charge, becoming di-positively charged and resulting in a stoichiometric for-

mula of $\text{Mg}^{+2}(\text{B}^-)_2$. In an ideal all-boron sheet, the additional metal atoms would have to be replaced by boron atoms. However, this would result in several consistent differences. Specifically, the addition of one boron atom in each hexagon centre, i.e. in each unit cell, introduces three supplementary electrons into the skeletal bonding, exceeding the required two electrons per unit cell. The surplus charge would occupy the anti-bonding levels, thereby compromising the stability of the structure. At least two routes could be proposed in order to overcome this problem. In particular, the buckling of the triangular lattice was found to enhance the system stability by reducing the anti-bonding overlap of the frontier bands. On the other hand, the formation of Hexagonal Holes (HH) by removing one third of the boron atoms per unit cell would reduce the exceeding electrons, resulting in an electronic configuration similar to that of graphene or MgB_2 .

Therefore, when designing a flat boron layer, it is crucial to create a well-balanced mixture of triangular lattice, which tends to produce an excess of electrons in anti-bonding states, and honeycomb lattice, which is electron deficient. Basically, borophene structures could be described as a triangular B lattice with hexagonal hollow vacancies in order to compensate for the exceeding electronic charge. In particular, it is possible to catalogue borophene phases by means of the *hexagonal hole density*:

$$\eta = \frac{\text{number of hexagonal holes}}{\text{number of atoms in the original triangular sheet}} \quad (1.1)$$

In particular, η can range from $\eta=0$, which corresponds to the close packed triangular lattice, to $\eta=1/3$, which corresponds to the honeycomb lattice. The most stable free-standing borophene structures lie in the vicinity of $\eta \sim 0.1-0.15$, as attested by two independent approaches that yield qualitatively compatible results [6, 8], as can be appreciated in Fig. 1.2.

The most recent nomenclature for boron sheet structures was established by X. Wu *et al.* [9]. Specifically, the monolayer phases are denoted with Greek letters representing the different coordination numbers of the boron atoms, as described in table 1.1, followed by an Arabic digit as a subscript. Figure 1.3 depicts the stable borophene structures predicted by *ab initio* calculations.

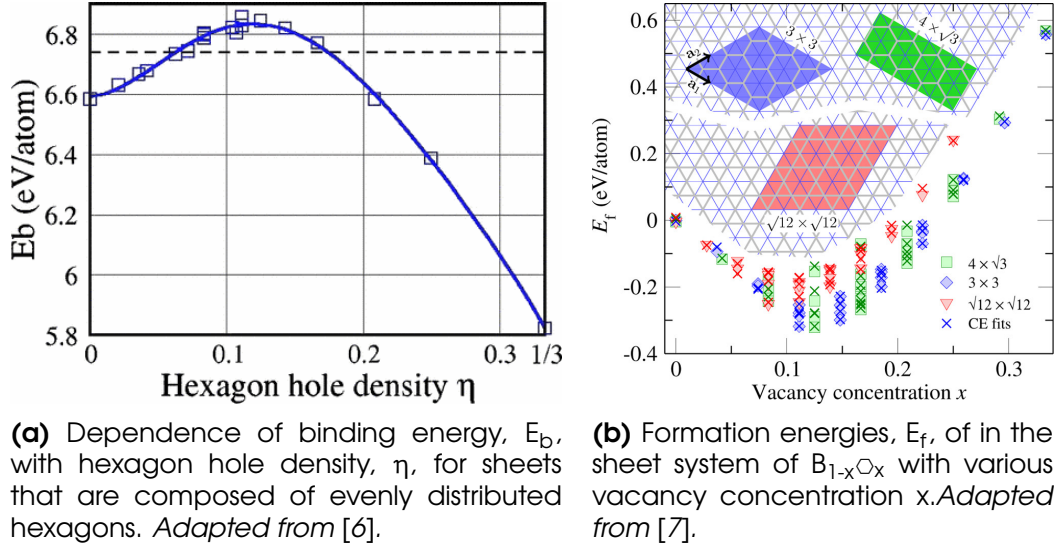


Figure 1.2: Stability of the various 2D boron structures as a function of the hexagonal vacancy concentration η .

	α	β	χ	φ	δ
Coordination Number	5, 6	4, 5, 6	4, 5	3, 4, 5	a single value

Table 1.1: Classification of Borophene geometries based on the Coordination Number (CN) of boron atoms in the structure model [9].

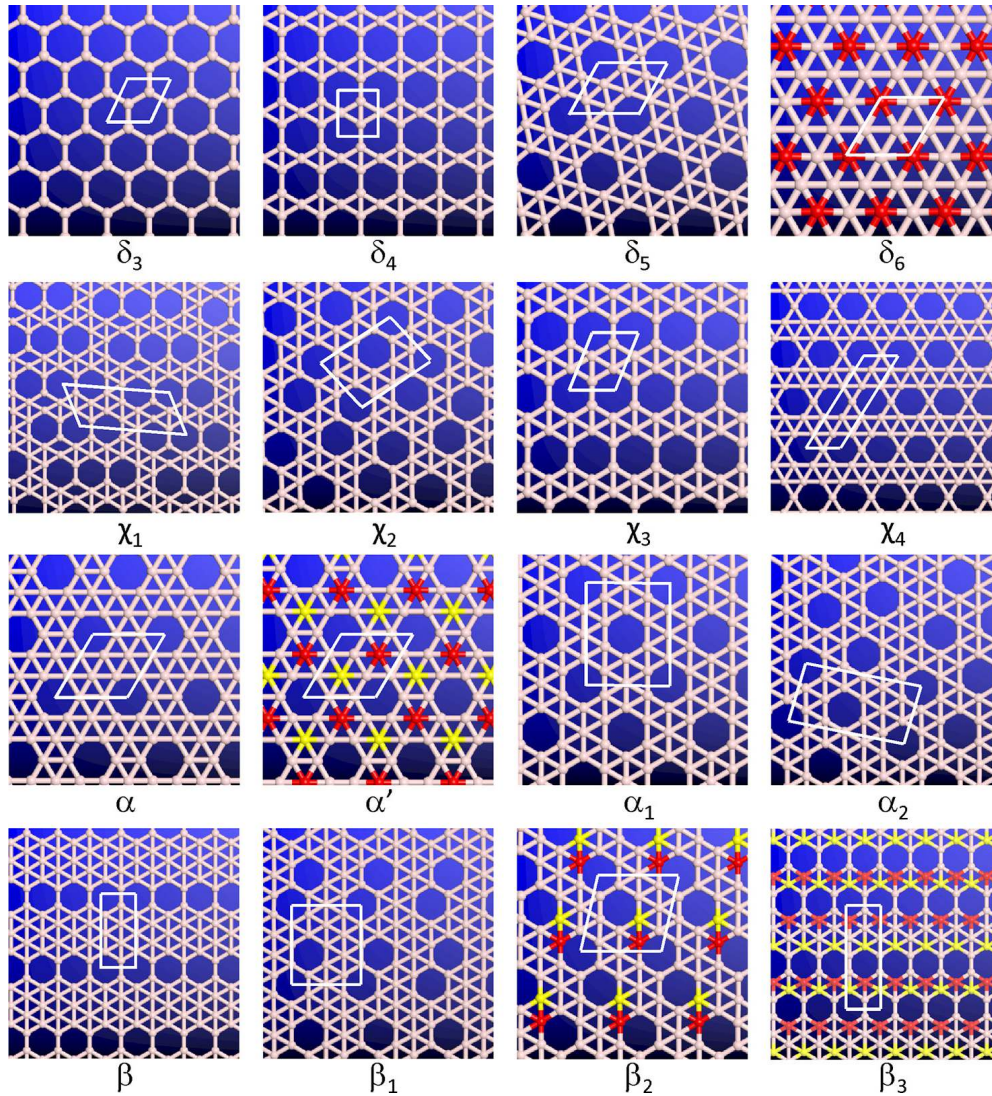


Figure 1.3: Classification of the boron monolayer sheets. Specifically, the monolayer phases are denoted with Greek letters representing the different coordination numbers of the boron atoms, as described in table 1.1, followed by an Arabic digit as a subscript. *Adapted from [9].*

1.2.3 B at surfaces

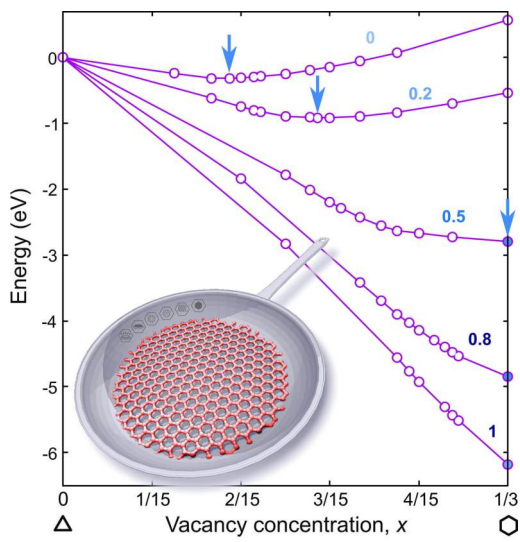
Although the aforementioned theoretical predictions pertain solely to free-standing borophene, it is important to note that the stability of the boron bidimensional structure experiences significant alterations when in contact with a supporting substrate. This consequently leads to the emergence of novel, fascinating geometric and electronic structures. Due to the overlap with the metal bands, electron transfer to the boron sheet occurs, resulting in the stabilisation of free-standing lattices with a higher electron deficiency. In particular, the electronic charging of the various boron layers has been theoretically examined, pointing out the increasing dependence on density and configuration of HH of the stability of the boron structures as the doping gradually increases. As shown in Fig. 1.4a, the stability of the honeycomb boron lattice progressively rises through electron doping, eventually becoming the most stable structure when the $0.5 e^-/\text{atom}$ value is exceeded [8]. This finding stands in sharp contrast to the fact that the free-standing honeycomb borophene (hB) is unstable, compared to other boron sheets.

Generally, as shown in Fig. 1.4b, calculations show that supported borophene layers are more stable than the corresponding free-standing planes in vacuo. Nevertheless, experimental synthesis of a single well-defined borophene phase has become a challenging task for researchers. The reason has to be searched in the fact that, theoretically, the energy per boron atom in borophene is much higher than that in bulk boron, which indicates that borophene is thermodynamically unstable. In other words, large numbers of boron atoms would preferentially form 3D bulk structures rather than the 2D borophene. Furthermore, different borophene polymorphs with similar degrees of stability tend to coexist because of the intrinsic polymorphism of borophene; this will also make it difficult to synthesise large-scale single-phase borophene.

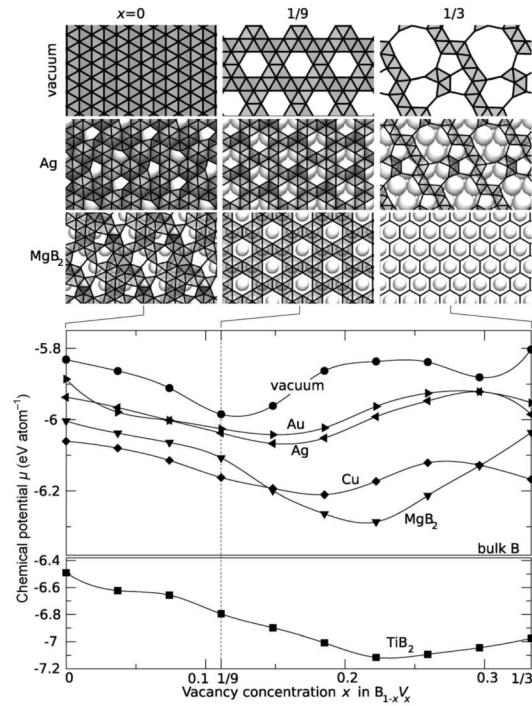
Nonetheless, experimental synthesis of borophene has been achieved on various substrates. This section provides a list of experimental achievements in boron layer realisations at surfaces, without any claim to be exhaustive and mainly focusing on results relevant to the present thesis.

B/Ag(111)

The first experimental synthesis of borophene was achieved on the Ag(111) termination, nearly simultaneously by two independent groups [11, 12]. Boron was



(a) Change of energy per boron atom of $B_{1-x}O_x$, where O is the vacancy in triangular (Δ) boron lattice ($x = 0$), at various doping in the range from 0 to $1 e^-$ /atom. The calculation was made to describe a honeycomb borophene lattice (\circ) on a surface of aluminum. Adapted from [8].



(b) Stabilities of 2D boron sheets with various vacancy concentrations on different substrates. Adapted from [10].

Figure 1.4

evaporated by MBE on the onto the Ag(111) sample, which was heated to a constant temperature in a range from 720 K to 970 K. STM revealed the presence of two main borophene phases at the surface. In particular, in Fig. 1.5 it is possible to appreciate a striped phase, called S1, showing a rectangular lattice with a $0.51 \times 0.29 \text{ nm}^2$ unit cell, and a homogeneous phase, called S2, consisting of periodic atomic chains (with 0.3 nm periodicity), with a short rhombohedral moiré pattern and a long-range 1D moiré pattern. It is possible to associate these two phases with triangular boron structures including HH discussed above (See Sec. 1.2.2 and Fig. 1.3 [9]). Specifically, S1 corresponds to the β_{12} sheet ($\eta = 1/6$) and S2 corresponds to the χ_3 sheet ($\eta = 1/5$). The structural models corresponding to β_{12} and χ_3 are superimposed to DFT simulated images in Fig. 1.5. It is noteworthy that both boron sheets remain planar without any obvious vertical corrugations, thus indicating a relatively weak interaction with the substrate. The relative coverage of the two phases turned out to be strongly dependent on the deposition rate and the substrate temperature. Higher growth temperatures, and low deposition rate prevalently lead to the formation of the stable β_{12} phase, while low temperature and high deposition rate favour the metastable χ_3 phase. Moreover, annealing at a higher temperature can convert the χ_3 phase to the β_{12} phase, indicating greater stability of the latter.

The XPS investigation of the B/Ag(111) system provided useful information about the chemical bonding environment of boron atoms in the borophene sheet. Figure 1.6 depicts the XPS spectra for borophene samples grown at about 570 and 670 K, which show three spectral components for the S1 phase and two for the S2 phase. The peaks intensity ratio shows that at low temperature roughly the 90% of the surface is covered by the χ_3 phase and just the 10% by the β_{12} , while at higher sample temperature the ratio is basically opposite, corroborating the findings achieved by STM. Moreover, the three spectral components related to the S1 phase show an intensity ratio of roughly 2:2:1, while the two S2 phase components show 1:1 ratio. These findings turned out to be consistent with the predicted ratios of fourfold, fivefold, and sixfold coordinated boron atoms contained in the β_{12} and χ_3 borophene crystal structures, respectively, as can be appreciated by looking at the unit cell models of the two phases in Fig. 1.6.

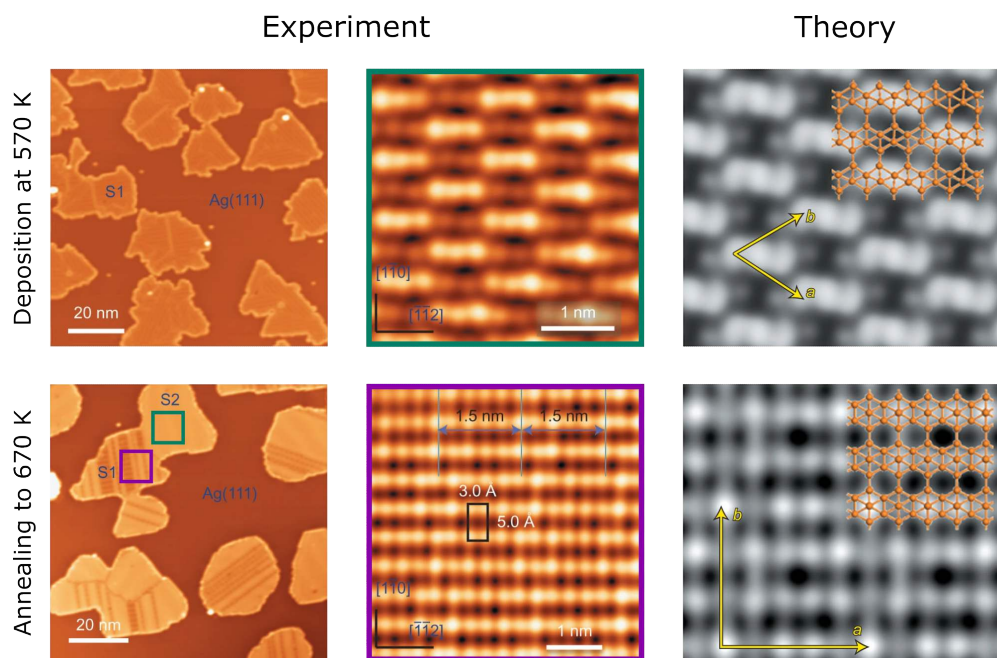


Figure 1.5: Experimental and DFT simulated STM images, together with the structure models for phases S1 and S2 (namely β_{12} and χ_3) Adapted from [12].

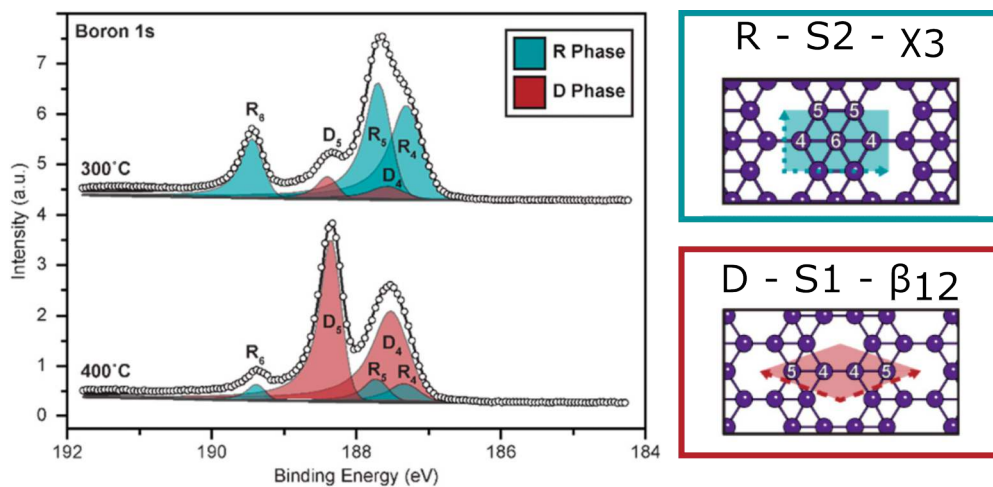


Figure 1.6: High-resolution XPS B 1s core level spectra for borophene samples grown at 570 and 670 K, together with unit cell models for the (R-S2- χ_3) and (D-S1- β_{12}) phases, with the boron atomic coordination numbers labeled. Adapted from [13].

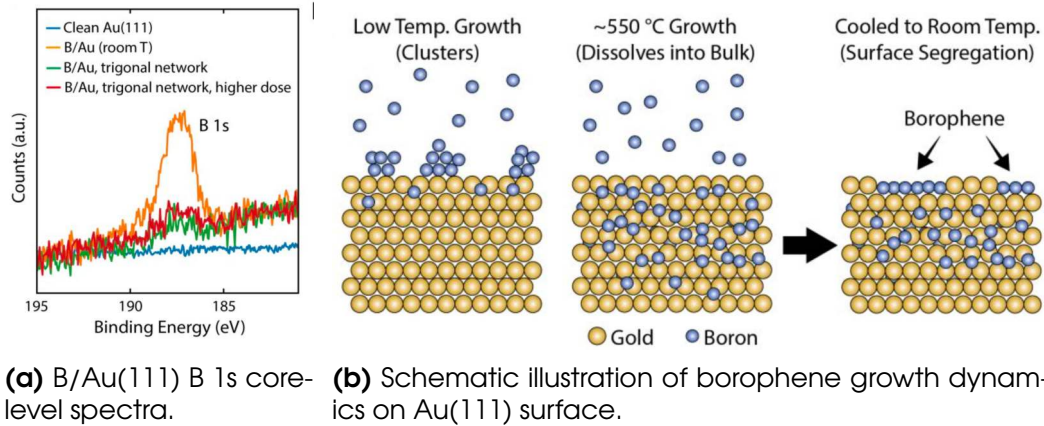


Figure 1.7: Adapted from [14]

B/Au(111)

Gold, in comparison to silver, is a noble metal which generally exhibits lower chemical reactivity. Furthermore, the Au (111) surface is one of the rare low-energy metal surfaces that undergoes reconstruction to minimise surface energy. In 2019, *Kiraly et al.* reported the experimental synthesis by MBE of borophene on this metal termination [14].

When boron is deposited at room temperature, it clusters on the Au(111) surface, contributing with a pronounced peak in the XPS spectra of the B 1s core level (see Fig. 1.7a) as a result of the limited solubility of boron in Au at room temperature. On the other hand, when the growth temperature is increased above 820 K, the integrated signal intensity in the B 1s spectrum considerably decreases, indicating a reduced boron surface coverage. Thus, the process of borophene growth involves the initial dissolution of boron into the bulk at high temperatures, followed by surface segregation upon temperature reduction, as schematically depicted in Fig. 1.7b.

Upon boron deposition, the herringbone reconstruction of the Au(111) transforms into a strain-relieving trigonal network, with a characteristic periodicity ranging from 5.5 to 8.0 nm, which acts as a growth template for small borophene islands nucleating at the nodes. The STM images in Fig. 1.8 depict the boron growth process, with the dashed hexagons illustrating the trigonal network. Increasing the boron dose eventually results in the breakdown of the trigonal network and in the formation of larger borophene islands that are embedded in the topmost layer of Au. As the boron dose further increases, the borophene sheets

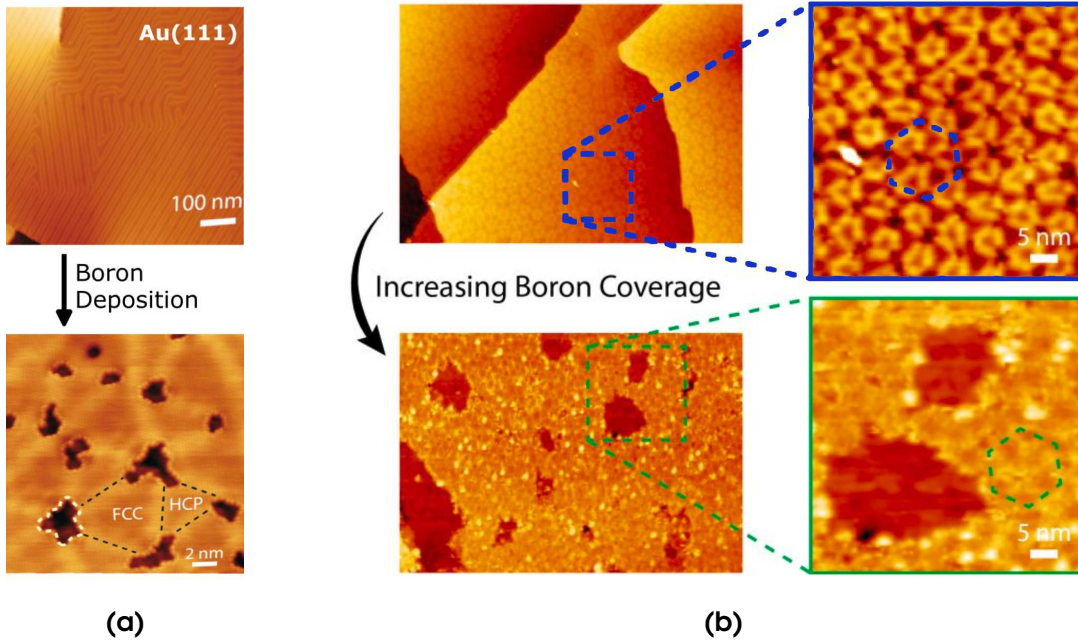


Figure 1.8: (a) STM images of the clean Au(111) surface, that shows the herringbone reconstruction and of the following boron deposition at ~ 820 K (b) Increasing boron dose results in the breakdown of the trigonal network and growth of larger borophene islands. Adapted from [14].

grow producing domains that extend for at least several tens of nanometers, as can be seen in Fig. 1.8b.

B/AI(111)

Honeycomb borophene (hB) stands out among the 2D boron polymorphs due to the highest HH density ($\eta = 1/3$) and its similarity to graphene, which hosts massless Dirac fermions and numerous other intriguing properties. The hB structure exists in nature as a part of the layered MgB_2 which is a well-known high T_c superconductor. Moreover, it is believed that the superconducting properties of this metal diboride stem from the honeycomb structure exhibited by the boron layers. Therefore, the mastery of the hB structure could pave the way to control superconductivity in two-dimensional systems.

Nevertheless, regarding free-standing borophene phases, the honeycomb lattice emerged as the least stable one, due to its high hole density and critical electron deficiency. However, the stability of the honeycomb phase dra-

matically increase with electron doping of the layer. When the doping value reaches approximately $0.8 e^-/\text{atom}$ (meaning each boron atom acquires one electron, making it electronically equivalent to carbon), the honeycomb structure becomes the ground state. Consequently, the substrate plays a pivotal role in stabilising the boron layer through net charge transfer.

Eventually, hB was experimentally synthesised in 2018 by *Li et al.* [15] by exploiting the Al(111) surface termination as a substrate. Boron was deposited by MBE and the substrate temperature was maintained at 500 K during the growth process. The Al(111) surface termination was chosen for two main reasons, the first one regards the low work function of aluminium, which facilitates the charge transfer towards the boron layer, achieving $0.7 e^-/\text{atom}$. The second one has to be searched in the symmetry and in lattice constant of the surface (0.286 nm), which is very close to the predicted freestanding hB one (0.3 nm). Using STM, they observed borophene islands with a height of 320 pm, which corresponds to the height of a single-layer borophene, as shown in the images and height profiles in Fig. 1.9. Atomically resolved STM images pointed out the honeycomb lattice structure and allowed to measure the borophene lattice constant, $a_{\text{AlB}_2} = 0.29 \text{ nm}$. In addition, larger scale STM images revealed the characteristic triangular corrugations of the borophene monolayer, with a period of roughly 7 nm and height difference in the range of 40–60 pm. The latter corrugation is associated with the moiré superstructure induced by the lattice mismatch between the hB layer and the Al(111) surface. The corresponding coincidence cell spans over $(24 \times 24)/(25 \times 25)$ unit cells of the hB/Al(111) lattices, respectively. In 2020, *Geng et al.* investigated the band structure of the B/Al(111) by means of ARPES, proposing the formation of a superficial AlB_2 layer. The analysis revealed multiple bands, namely α , β , and γ , that intersect with the Fermi level in the vicinity of the Γ point. Remarkably, these bands host two Dirac cones along the Γ -K and Γ -M directions, as indicated by the red arrows in Fig. 1.10. Another Dirac cone, arising from the p_z orbitals of boron, is located at the K point, as indicated by the red circle in Fig. 1.10a. Analysis of the ARPES measurements in Fig. 1.10b reveals the survival of the Dirac cones, without any distinct gap opening, thus indicating weak interaction between the AlB_2 layer and the substrate.

In 2021, *Preobrajenski et al.* [17] undertook one of the landmark studies regarding the understanding of the exact structure of hB on Al(111). Starting from the 24:25 coincidence supercell, two structural models were proposed:

- **Model 1:** (24×24) hB unit cells are matching (25×25) unit cells of Al(111)

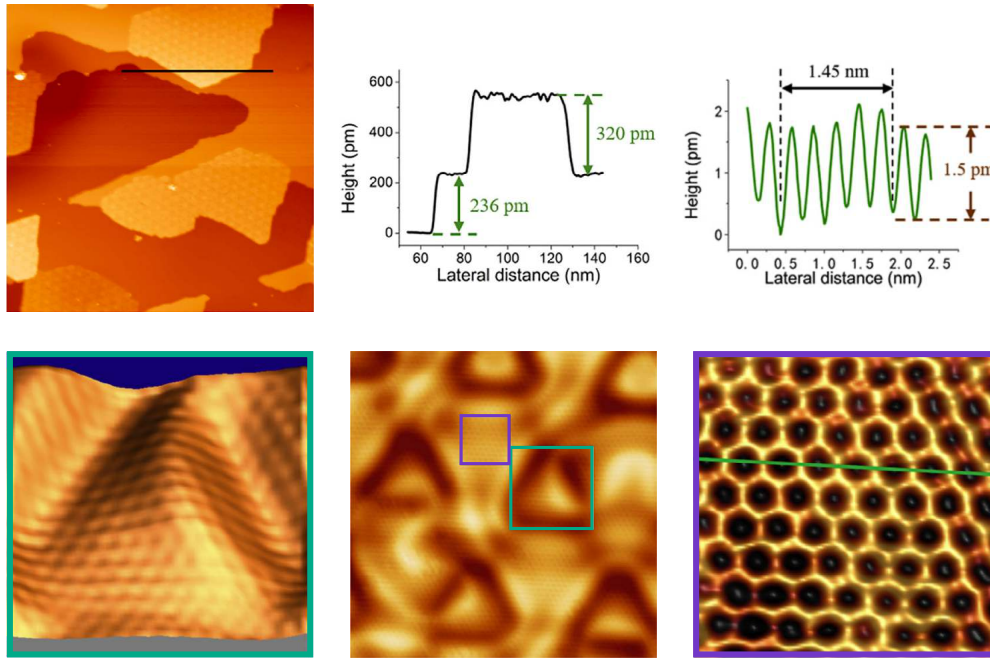
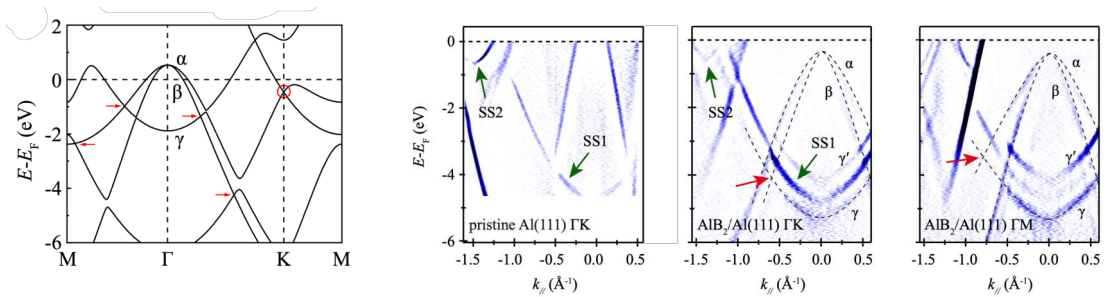


Figure 1.9: STM images of the B/Al(111) system, together with the corresponding height profiles Adapted from [15].



(a) Calculated band structure of the monolayer AlB_2 .

(b) ARPES second derivative image of pristine Al(111) and of $\text{AlB}_2/\text{Al}(111)$, along the directions indicated, measured with 25, 40 and 35 eV photons, respectively.

Figure 1.10: Calculated and experimental band structure for the $\text{AlB}_2/\text{Al}(111)$ system. The three characteristic bands are indicated by α , β , and γ . Red arrows indicate the Dirac cones protected by mirror symmetry along the high-symmetry lines, while the red circle indicates the Dirac cone derived from the p_z orbitals of boron. The Al(111) surface state is observed and emphasised by the green arrows, demonstrating the high order and cleanliness of the sample surface. Adapted from [16]

directly;

- **Model 2:** hB is lattice-matched to the topmost Al layer forming a one-layer AlB_2 and then (24×24) unit cells of this AlB_2 layer are matched to the (25×25) unit cells of $\text{Al}(111)$.

The main difference in the two model lies in the density of the topmost Al layer, which is the same of the other Al layers for *Model 2* while slightly less for *Model 1*. The result of geometry optimisation, performed by DFT calculations, on both models is shown in Fig. 1.11. The optimised structures turned out to be significantly different in the two cases.

Regarding *Model 1*, the hB and topmost Al layers become both strongly corrugated in-phase, with a corrugation as large as 2.4 \AA . The latter corrugation arises due to the tendency of Al atoms in the top Al layer to lattice-match the hB sheet, in the largest possible surface area. Specifically, the topmost Al layer is diluted to perfectly align with boron atoms at the corners of the supercell, pushing the exceeding atoms towards the second Al layer, which, in turn, undergoes considerable corrugation. Similar qualitatively results were obtained by allowing one more Al layer to relax during calculations. On the other hand, in *Model 2*, the topmost Al layer is already lattice-matched with the hB layer, without exceeding Al atoms, resulting in faster convergence and smaller corrugation of all layers with respect to *Model 1*. The hB layer and the top Al layer are again corrugated in-phase, but the corrugation amplitude does not exceed 0.35 \AA , being considerably closer to the experimentally measured values. To conclude, it appears that the creation of a lattice-matched AlB_2 layer on the surface cannot be avoided, occurring even starting from the *Model 1* configuration.

By comparing the system STM images with the geometrical optimisation results, it is possible to exclude the formation of a nearly free-standing hB sheet on the bare $\text{Al}(111)$, as the high corrugation amplitude characteristic of *Model 1* was never experimentally observed. Nevertheless, neither the milder corrugation topography of *Model 2* can completely reproduce the peculiar triangular feature exhibited by the experimental STM images of AlB_2 on $\text{Al}(111)$. In order to sort out the electronic features behind this specific appearance it is necessary to define the *differential electron density*

$$\Delta\rho = \Delta\rho_{\text{AlB}_2/\text{Al}(111)} - \rho_{\text{Al}} - \rho_{\text{B}} \quad (1.2)$$

where the latter two electron densities are calculated at the positions of Al and

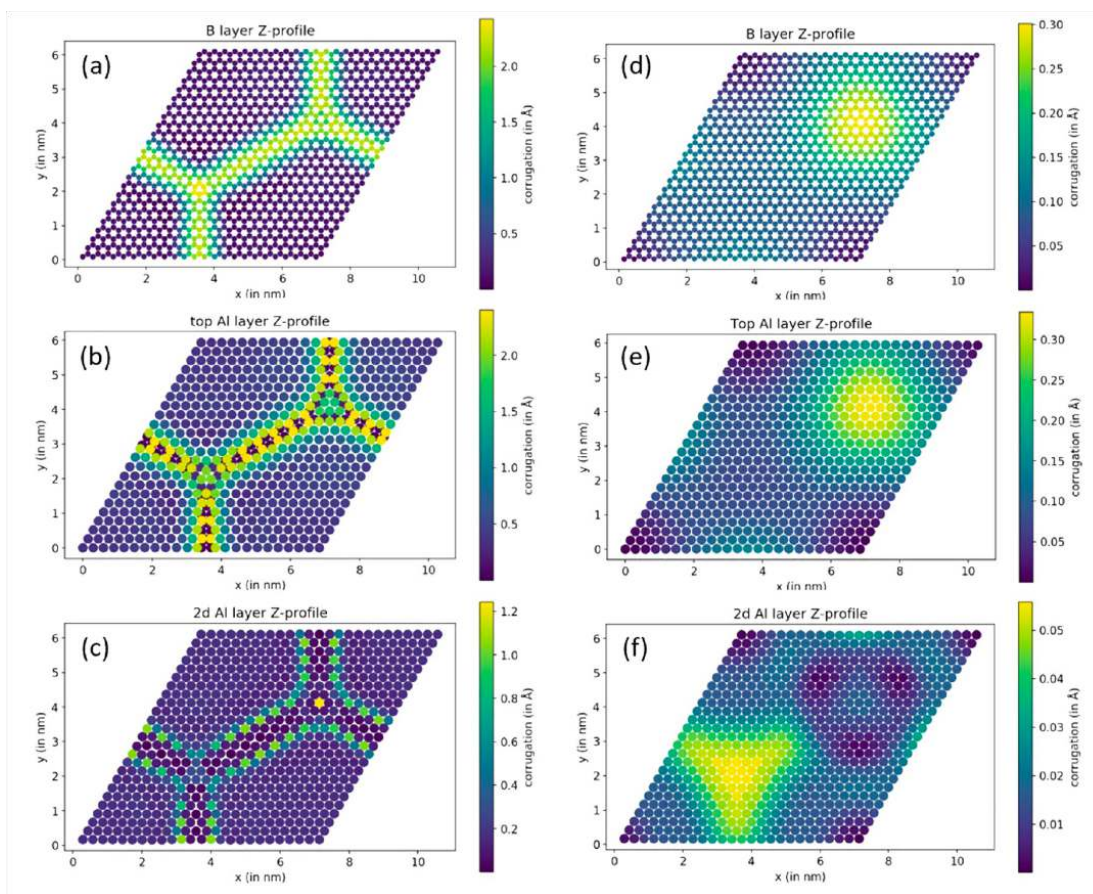


Figure 1.11: Layer-by-layer height profile maps for two models under study after DFT geometry optimisation. For each model the profile map is shown for the honeycomb B layer (*Model 1* in (a) and *Model 2* in (d)), the top Al layer (*Model 1* in (b) and *Model 2* in (e)), and the second Al layer (*Model 1* in (c) and *Model 2* in (f)). Notice the strong difference in corrugation figures between the two models. the. *Reported from [17].*

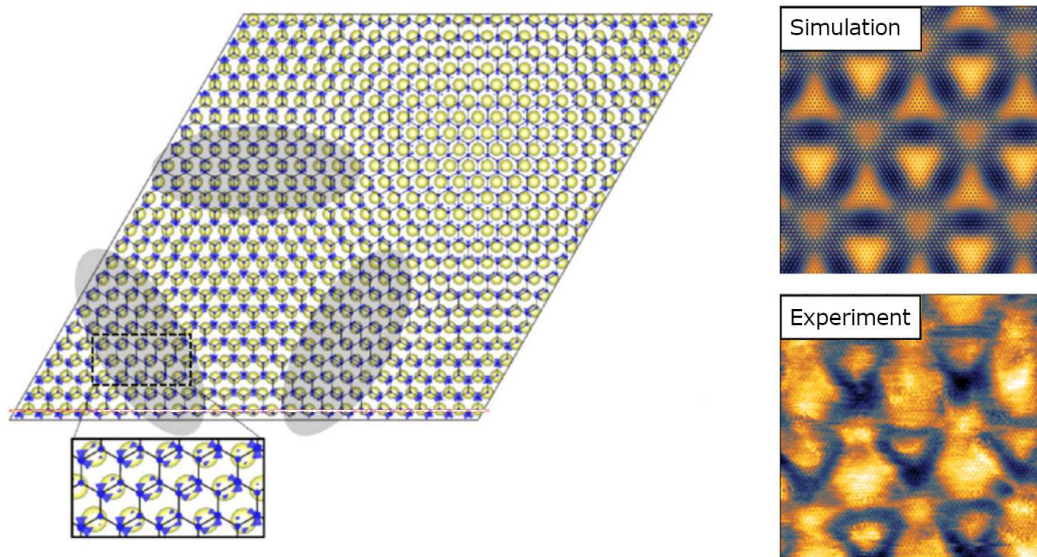


Figure 1.12: Origin of the supercell contrast in STM for the AlB_2 monolayer on $\text{Al}(111)$. On the left, isosurfaces of differential electron density (blue color, $\Delta\rho = -0.007 \text{ e}^-/\text{\AA}^3$) superimposed on the hB mesh (black lines) and second Al layer (light yellow balls). Top Al layer is lattice-matched to hB and is therefore omitted for clarity. Areas where hB is in bridge position relative to the second Al layer are shown in gray; On the right, a comparison between a simulated and corresponding experimental STM image in the constant current mode ($20 \times 20 \text{ nm}$, average tip height 4.7 \AA above the top B layer). Adapted from [17].

B atoms in the geometry-optimised *Model 2*. Figure 1.12 depicts an example of a $\Delta\rho$ isosurface superimposed on the hB mesh and the second Al layer. It can be noted that small variations in the electron density, across the supercell, originate from the mismatch with the underlying Al substrate and explain the observed STM contrast. Indeed, in the areas outlined by grey ovals in Fig. 1.12, the negative electron density is mainly concentrated along the B-B bonds rather than on the B atoms, as in the remaining part of the cell. By assuming darker appearance for these specific areas it is possible to simulate an STM image of the supercell. Given the good theory-experiment match, depicted in Fig. 1.12, it is reasonable to conclude that the STM contrast in this system originates essentially from the variations of electron density of the surface dipole across the supercell rather than by real topography.

1.2.4 Chemically modified Borophene

The desire to both decouple borophene from the underlying substrate and increase its energetic stability prompted us to attempt a chemical modification of the borophene layer by exposure to gas phases. Indeed, the complex interplay of multiple phenomena that affect the 2D boron allotropes (i.e. HH density and distribution, charge transfer, substrate bonding, segregation, diffusion, alloying, and others) can be influenced by the chemical potential associated with a gas phase, which may have an impact on the decoupling of borophene from the substrate. In particular, oxygen and hydrogen are ubiquitous gases, which, upon dissociative chemisorption, are expected to affect the geometric and electronic structures of the 2D boron sheets and their interaction with a specific metal substrate.

Borophene Oxide

Based on first-principles calculations, honeycomb borophene oxide (B_2O) was theoretically predicted to exhibit high stability, strong anisotropy [18] and superconductive properties [19]. Incorporation of oxygen atoms was proposed as a promising way to oxidise an already prepared borophene layer. In fact, it should be noted that the intrinsic electron deficiency of B atoms makes B-B bonds unstable, particularly under oxygen-rich conditions. Basically, borophene is indeed an electron-deficient monolayer, especially in case of a high HH density structure, thus possibly favouring the formation of B-O bonds.

Nevertheless, when investigating borophene reactivity to molecular oxygen at surfaces the role of the substrate cannot be neglected. In fact, oxygen interaction with the metal can be strong enough to induce relevant mechanisms of surface metal segregation, responsible for the formation of surface oxide films. This is e.g. the case of the self-limited growth at high temperature of the well-known ultra-thin alumina film on $Ni_3Al(111)$. Kinetic restrictions apply to the mechanism, which involves the ejection of Al atoms from the surface to form the oxide film and formation of a low-density Al interface layer [20, 21].

Borophane: Hydrogenated Borophene

Recently, a Hückeloid model has been developed for planar boranes, where, given a Kekulé structure (namely $\kappa(S)$) of a planar conjugated hydrocarbon, a

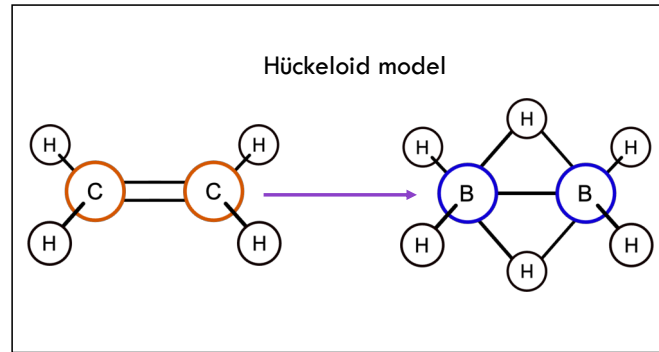
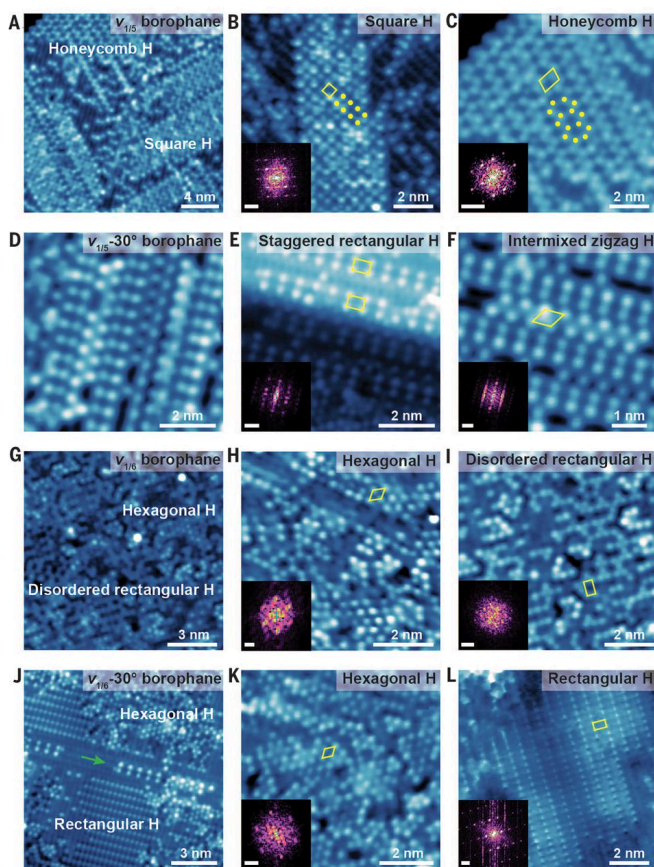


Figure 1.13: Hückeloid model for planar boranes: given a Kekulé structure (namely $\kappa(S)$) of a planar conjugated hydrocarbon, a corresponding borane can be obtained by replacing C with B atoms and by adding two H atoms in bridge position instead of each double bond [22].

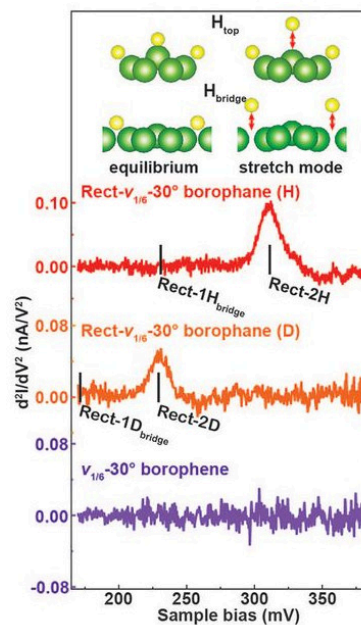
corresponding borane can be obtained by replacing C with B atoms and by adding two H atoms in bridge position instead of each double bond, yielding $B(\kappa(S))$ structures with added bridge hydrogen atoms [22]. Figure 1.13 depicts the simple case of the ethylene molecule *transforming* into the diborane one. Similarly, but starting from graphene, we clearly end up with hydrogenated hB, namely honeycomb *borophane*.

Borophene hydrogenation could pave the way to intriguing new properties of the 2D layer. Regarding hB, its hydrogenated counterpart is predicted as dynamically stable and is expected to maintain (anisotropic) Dirac cones between the Γ and X points in its electronic configuration, at least within the framework of a tight-binding model with terminal H atoms adsorbed on top of B atoms [23].

Moreover, the successful hydrogenation of a variety of supported borophene polymorphs on Ag(111) was recently reported. The hydrogenated phases included short-range ordered islands, as can be appreciated in Fig. 1.14a, stimulating the efforts towards the search for monophasic hydrogenated boron monolayers. Nevertheless, the chemical modification of borophene revealed indeed quite complex aspects, mainly associated with the typical B multicentred bonding configuration and the anisotropic features of borophene. In fact, hydrogenated borophene layers are characterised by the co-presence of several distinct polymorphs, with most of the lattice geometries remaining elusive due to the wide configurational space [25]. In fact, the co-existence of different hydrogenation patterns on the same borophene polymorph significantly increases the number of possible borophane configurations. As a



(a) Representative STM images of various hydrogenated borophene polymorphs



(b) IETS spectra taken with the stretch modes shown on top.

Figure 1.14: Reported from [24].

result, the majority of these polymorphs could be mainly characterised only by means of local surface science techniques like STM or STS (See Fig. 1.14) [24–26]. Moreover, the favoured hydrogen adsorption sites on different borophene allotropes (like β_{12} , χ_3 and α') depend on both the element ratios between B and H (i.e. also on the hydrogen pressure) and on the local overlap between B p_z and H s orbitals [25, 26]. Interestingly, reduction of borophene results in a certain, advantageous chemical passivation, in particular by lowering the oxidation rates [24].

In this thesis, we present the synthesis and thorough characterisation of a highly ordered hydrogenated honeycomb boron (H-hB) phase on Al(111) featuring a single H-bonding site, as a step towards the realisation of a single, stable honeycomb borophane phase. (see Sec. 4.1).

1.3 Elemental Phosphorus

1.3.1 Bulk phases and allotropes

Phosphorus, similar to Carbon and Boron, has several allotropic forms. Indeed, at least five crystalline polymorphs have been observed, in addition to various amorphous or vitreous forms [27]. Three of these polymorphs, namely white, red and black phosphorus, possess distinctive and contrasting physical and chemical properties [28].

Phosphorus chemistry can be understood by considering its most common allotrope: the waxy white phosphorus, which consists of P_4 molecular building blocks [29]. In fact, bulk crystals of this allotrope typically result from condensation from gaseous or liquid states, forming a complex structure in which P_4 units are held together by van der Waals interactions. The four atoms in the P_4 molecule form a tetrahedral structure by linking each atom to its three neighbours. This involves the formation of six single bonds, which result from the $3p$ atomic orbitals. However, in this tetrahedral configuration, the bonds cannot adopt a 90° angle like pure $3p$ orbitals would, thus resulting in the well-known instability of the P_4 molecule. Due to the weak P-P bonds in the P_4 unit, white phosphorus is the most reactive and volatile solid allotrope and, thermodynamically, the least stable. As a result, under certain experimental conditions, it can transform into either black or red phosphorus, which are thermodynamically more favourable.

Amorphous Red Phosphorus (RedP) was first obtained in 1848 by heating white P out of contact with air for several days. The structure of RedP is considered to be a polymeric network of different building units. The building blocks of RedP structures can be viewed as a derivative of the P_4 molecule wherein one P-P bond is broken, and one additional bond is formed with the neighbouring tetrahedron, resulting in a chain-like structure, as can be appreciated in Fig. 1.15. While these networks typically exhibit only short or intermediate range order, further heating or irradiation of RedP leads to its crystallisation, forming several different crystalline allotropes [30].

Black Phosphorus (BlackP), which is the thermodynamically most stable form of the element, exists in three crystalline and one amorphous forms. BlackP was first obtained in its orthorhombic form by exposing RedP to high pressure and high temperature [31]. Higher pressures convert it successively

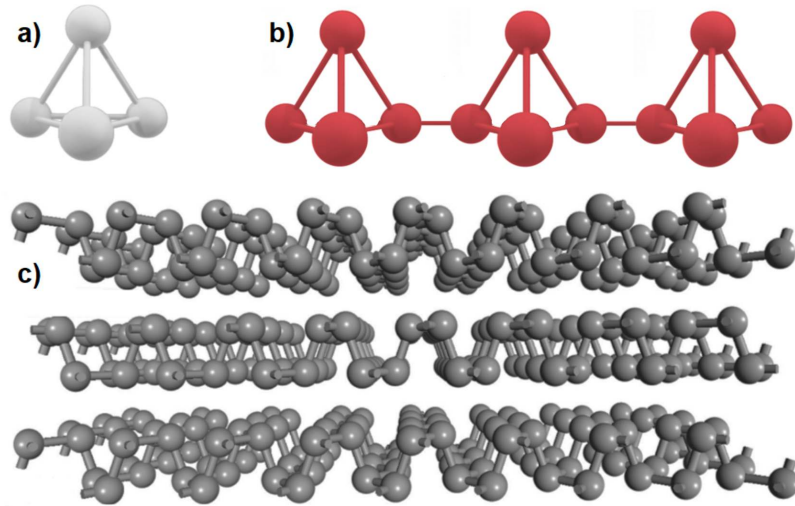


Figure 1.15: Atomic structures of most common phosphorus allotropes: white (a), red (b), and black (c) phosphorus.

to the rhombohedral and cubic forms. Nevertheless, among all the BlackP allotropes, the semiconducting puckered orthorhombic form received much more interest owing to its unique graphitic structure and intriguing properties. Specifically, unlike other allotropes, orthorhombic BlackP is characterised by a layered structure with strong covalent in-plane bonds with respect to the weak van der Waals interlayer interaction. Each phosphorene layer consists of a distorted honeycomb structure with six-atoms rings in chair conformation. Armchair and zigzag edges can be identified in the lattice, with the atoms in a single armchair chain located in two different atomic planes, resulting in a strongly puckered honeycomb layer. Notably, the stacking sequence of orthorhombic BlackP is different from the ones adopted by other layered materials like graphite and h-BN, with no atoms in a layer which are directly below an atom of the neighbouring layer [32].

Recent studies have shown that BlackP can be exfoliated, similarly to graphite, to fabricate few-layer thick sheets. Notably, *ab initio* calculations indicate a strongly thickness-dependent lattice constant, as illustrated in Fig.

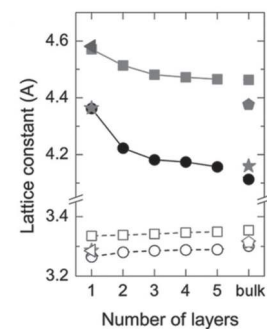


Figure 1.16: Evolution of lattice constants with thickness. Different symbols represent different computational methods. Adapted from [32].

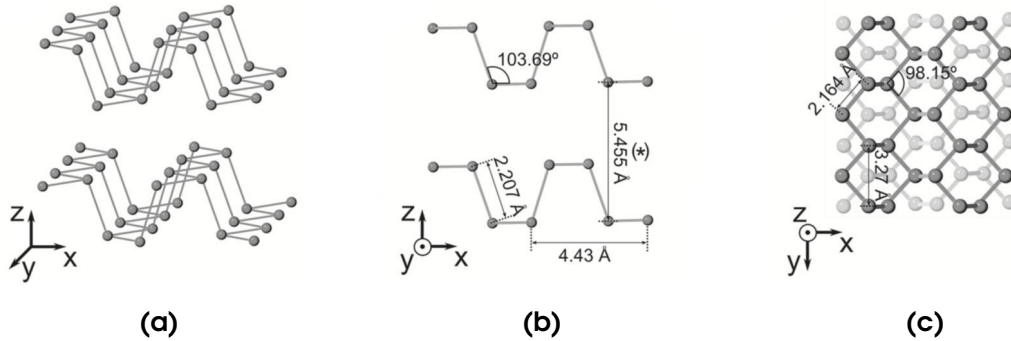


Figure 1.17: Schematic diagram of the BlackP crystalline structure of obtained from the relaxation of the structure using DFT calculations. The layered structure is composed of sheets with the phosphorus atoms arranged in a puckered honeycomb lattice. Adjacent layers interact by weak van der Waals forces and are stacked with no atoms in a layer which are directly below an atom of the neighbouring layer. **(a)** 3D representation. **(b)** Lateral view. **(c)** Top view. The distances and angles displayed have been obtained by relaxing the crystal structure of a single-layer black phosphorus sheet. The distance value marked with (*) has been obtained by relaxing the bulk structure. *Adapted from [33].*

1.16, denoting a robust interlayer coupling. In addition, photoluminescence measurements indicated a thickness dependence and called for a calculation of the band structure as a function of the number of layers [33]. Since all three valence electrons participate in bonds, black phosphorus would be semiconductor with a predicted direct bandgap of 2 eV at the Γ point of the first Brillouin zone [34]. Figure 1.18 shows the evolution of the calculated band structure with the number of layers. The calculated bandgap increases going towards the single-layer case, as a result of decreasing interlayer interactions, but, interestingly, the direct gap feature is always maintained, in contrast to the behaviour of many other atomically thin materials.

Despite the poor stability of bulk BlackP in ambient conditions, the potential to easily exfoliate the material and obtain thin sheets with selected electronic and geometric structure holds promise for technological applications requiring miniaturisation.

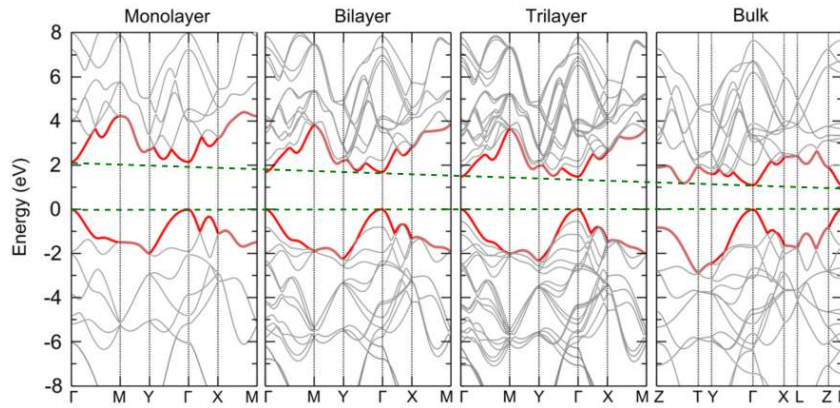


Figure 1.18: Calculated electronic band structure for monolayer, bilayer, trilayer and bulk BlackP sheets at all high-symmetry points in the Brillouin zone. The energy is scaled with respect to the Fermi energy E_F . *Adapted from [33].*

1.3.2 Phosphorene

Black Phosphorene

One monolayer, or few layers of BlackP are known as Black Phosphorene (BP). Structurally, monolayer BP consists of covalently bonded phosphorus atoms. In particular, each P atom is saturated by bonding with three neighbouring P atoms and has a lone pair of electrons. This bonding configuration results in a quadrangular pyramidal structure resembling a wrinkled honeycomb. In fact, while free-standing borophene is mainly characterised by its intrinsic electron deficiency, BP has exceeding valence electrons with respect to graphene. This results in the sp^3 hybridisation of P atoms, in contrast with the sp^2 state of carbon atoms in graphene, which stabilise the flat honeycomb lattice.

Blue Phosphorene

The intriguing features of BP and its successful implementation in prototypical technological devices have stimulated research on phosphorene, resulting in the theoretical prediction of several other stable 2D phosphorus allotropes [35]. Amid them, single-layer Blue Phosphorene (BlueP) has emerged as one of the most promising. It is nearly as stable as BP and has several intriguing characteristics in common with it, namely the buckled quasi-planar honeycomb atomic structure [36] (See Fig. 1.19), its conductivity properties [37] and the tuneable

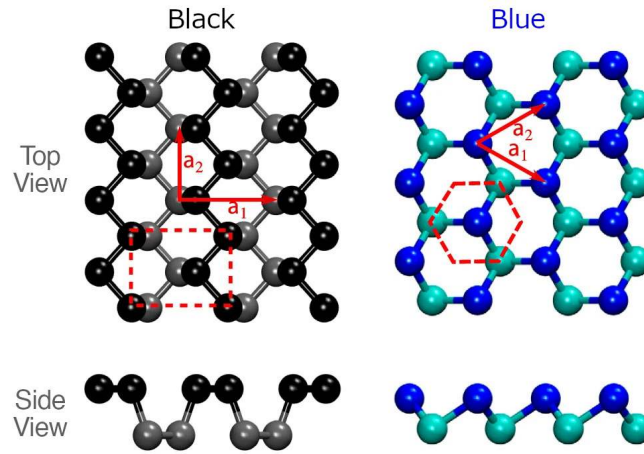


Figure 1.19: Crystal structure of BP and BlueP. Atoms in different planes are denoted by different colours and the unit cell and the in-plane lattice vectors are shown in the top views. The lattice constants are $|a_1| = 4.43 \text{ \AA}$ and $|a_2| = 3.28 \text{ \AA}$ for BP, and $|a_1| = |a_2| = 3.15 \text{ \AA}$ for BlueP. *Adapted from [39].*

semiconducting band gap, which is achieved via layers addition [36] or external field interaction [38].

1.3.3 BlueP/Au(111)

Due of the lack of a 3D counterpart, BlueP could be obtained only with a bottom-up approach, i.e. by controlled deposition of P atoms on a suitable substrate. The first experimental synthesis reported in literature regarded the formation of BlueP triangular patches on Au(111) [40–42], upon evaporation of BlackP, arranged in a periodic rhombic unit cell corresponding to a (5×5) supercell with respect to the substrate. The initial proposal for the surface structure consisted of a pair of mirrored triangular islands, each containing 16 phosphorus atoms, and was conceived by starting from standard STM topographic images [41]. Subsequently, exploiting complementary DFT simulations and new, atomically-resolved STM imaging, the model was repeatedly revised, with increasing accuracy and insight. In 2018, *W. Zhang et al.* proposed a more complex unit cell with 38 P atoms [43], while *Zhao et al.* [44] revisited the original model, suggesting the inclusion of single Au adatoms in the 2D unit cell. The latter model, consisting of 18 P and 9 Au atoms, was obtained through a stochastic surface walking algorithm, and offered the most accurate match with both STM images [45] and dynamic LEED-I(V) [46] measurements.

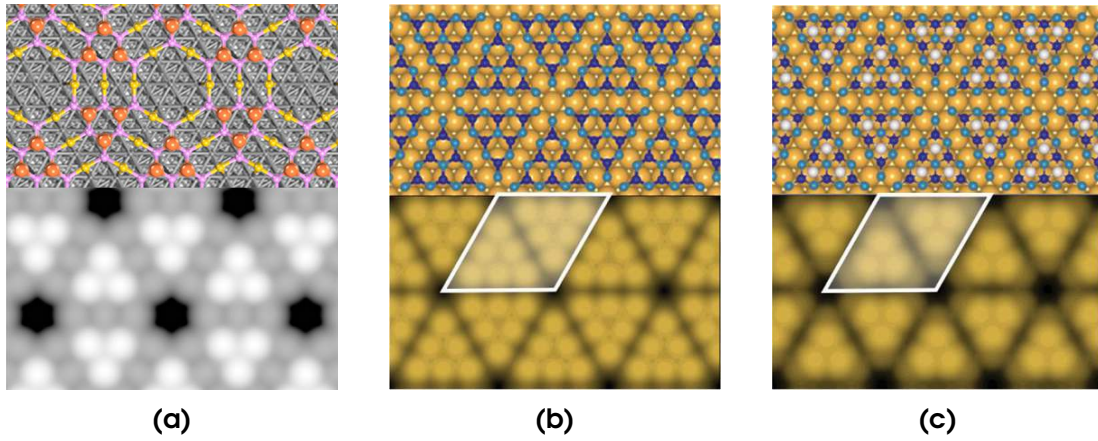


Figure 1.20: Top view and DFT simulated STM images of: **(a)** the first model proposed with 16+16 P atoms in the (5x5)-Au supercell [41]; another supposed model with 19+19 P atoms [43]; the last model proposed with only 9+9 P atoms and 9 additional Au adatoms [44].

Remarkably, the band structure of numerous proposed models exhibited common features in agreement with ARPES measurements, providing evidence for a dominant P-induced band dispersion between the Fermi level and the Au sp-band, situated approximately 2 eV below. In fact, *Zhuang et al.* claimed that the observed bandgap of the P states matched the calculated one, despite a very different band dispersion shape along k_{\parallel} [42]. For the same model, *Golias et al.* showed that the simulated P-related bands consistently fall between the Fermi level and the Au sp-band, although placed at a different BE with respect to the experimental results [40]. Also the 18P-9Au alloy model exhibits a dispersive band structure at low BE, partially resembling the experimental evidence of *Zhao et al.* [44].

To summarise, developing a reliable atomic structure model of BlueP on Au(111) has proved to be highly controversial and challenging, especially with respect to the potential inclusion of Au adatoms bridging the triangular P patches in the 2D sheet. In this thesis, we present the SXRD characterisation of the BlueP/Au(111) system, with complementary support from STM and ARPES experimental findings and from the comprehensive comparison with theoretical DFT results. The aim of this work was to demonstrate the soundness of the proposed atomic model, with particular attention on the potential inclusion of Au adatoms within the BlueP 2D mesh. Indeed, looking towards

future research, shedding light onto the driving force behind the incorporation of hetero-atoms could aid in selecting suitable substrates for the growth of complex 2D materials, such as BlueP, in the form of single, pure phases.

Chapter 2

Methods

The experimental results presented in this thesis were achieved exploiting several complementary techniques, namely Infrared-Visible Sum Frequency Generation spectroscopy (IR-Vis SFG), Scanning Tunnelling Microscopy (STM), X-ray Photoelectron Spectroscopy (XPS), Surface X-Ray Diffraction (SXR), Near Edge X-ray Absorption Fine Structure spectroscopy (NEXAFS), and Low-Energy Electron Diffraction (LEED). In this chapter, a brief description of some of the exploited techniques is provided, without any claim to be exhaustive.

2.1 Spectroscopies

2.1.1 XPS

X-ray Photoelectron Spectroscopy (XPS) is a photon-in-electron-out surface science technique. This spectroscopy is based on the investigation of the energy distribution of core-level photoelectrons, extracted from the sample exploiting the photoelectric effect stimulated by X-Rays. Specifically, one can determine the binding energy E_B of the electrons in the sample by using the measured kinetic energy E_{kin} of detected photoelectrons exploiting Einstein's relation

$$E_B = h\nu - E_{kin} - W \quad (2.1)$$

where $h\nu$ is the X-rays photon energy, and W is the work function of the electron analyser (see Fi. 2.3). The analysis of the photoemitted electrons allows to gain information about their chemical environment, the structural dishomogeneities in the system and the lifetime of the excited state induced by photoemission

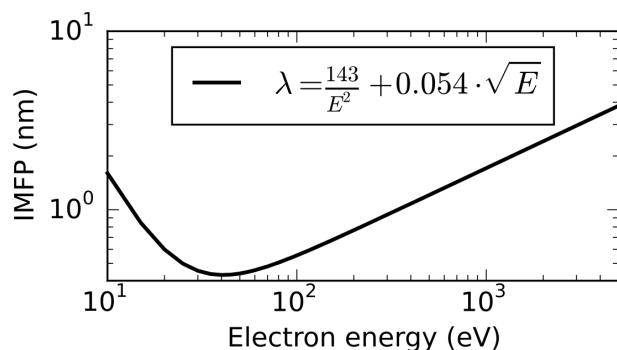


Figure 2.1: The universal curve of electron mean free path in solid matter based on the equation in [47].

process. The short mean free path of photoelectrons through gas phase require to work under UHV conditions (commonly up to $\sim 10^{-6}$ mbar), but the even shorter mean free paths in solids provides to this technique excellent surface sensitivity, as shown in the graph in Fig. 2.1, which reports the inelastic mean free path as a function of electrons energy. This curve is commonly referred to as the *universal curve* as it is largely unaffected by the chemical composition of the solid. Of note, photoelectrons with a kinetic energy ranging from 10 to 1000 eV are particularly well-suited for surface elemental analysis as their mean free path measures below ~ 10 Å.

Lineshape and data analysis

The basic lineshape of a photoemission process is given by a Lorentzian function [48]. The natural line width is determined by the lifetime of the core hole created by the missing photoelectron in the ionised atom, which is related, by the Heisenberg principle, to the probability of the core hole being filled by an electron in a lower binding energy level. The core hole's lifespan decreases as the number of decay channels for electrons to fill it increases. The schematic in Fig. 2.5 illustrates possible decay channels, such as Auger or radiative processes.

The uncertainty relation shows a link between the intrinsic peak width Γ and the core hole lifetime τ :

$$\Gamma = \frac{h}{\tau} \quad (2.2)$$

where h is the Planck constant. Using Fermi's golden rule for matter-radiation

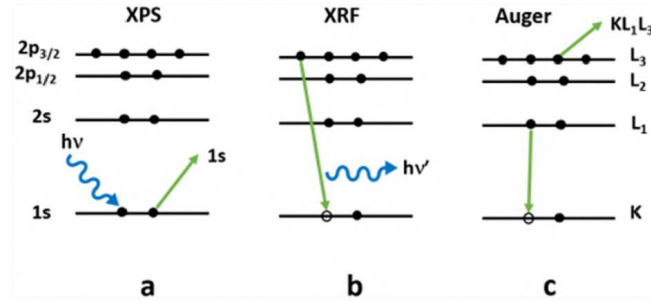


Figure 2.2: Energy level diagram showing the filling of a core hole, giving rise to (a) direct photoemission, (b) X-Ray Fluorescence, and (c) non-radiative Auger electron emission. *Reported from [52].*

interaction, the X-ray photoemission cross section can be evaluated considering the metal ground state and the Fermi sea + one hole + the photoelectron in the initial and final states, respectively [53]. The line shape of the photoemission peak is therefore generally expressed as:

$$I_{Lor}(E_{Kin}) = I_0 \frac{\Gamma/2\pi}{(E_{Kin} - E_0)^2 + \Gamma^2/4} \quad (2.3)$$

where the Full Width at Half Maximum (FWHM) is denoted by Γ , and E_0 is the position of the maximum intensity I_0 . The experimental energy resolution (related to both the photon source and the energy analyser), the excitation of phonons in the solid and the intrinsic sample inhomogeneity contribute to a Gaussian broadening of the photoemission peak. In addition, shake-up and shake-off events can affect the line shape with an asymmetry contribution: when a photoelectron is ejected, it can lose part of its energy to other electrons. In metals, for example, photoelectrons can create electron-hole pairs at the Fermi level or excite plasmons (shake-up event). In a generic system, other electrons may be emitted as a consequence of core ionisation (shake-off event). In both cases, the actual photoelectron kinetic energy is lowered, so that the XPS peak has an asymmetric tail at higher binding energies. The most common parameterisation for the core level line shape in photoemission spectra, including all the physical effects mentioned above, is a Doniach-Šunjić function convoluted with a Gaussian function [53]. The mathematical expression for a Doniach-Šunjić is basically

a Lorentzian function with an asymmetry parameter α :

$$I_{DS}(E_{Kin}) = I_0 \frac{\Gamma_E(1-\alpha)}{((E_{Kin} - E_0)^2 + \Gamma^2/4)^{(1-\alpha)/2}} \zeta(E_{Kin}) \quad (2.4)$$

where Γ_E is the Euler Gamma function, and $\zeta(E)$ is defined as:

$$\zeta(E) = \cos \left[\frac{\pi\alpha}{2} + (1-\alpha) \tan^{-1} \left(\frac{E_0 - E}{\Gamma/2} \right) \right] \quad (2.5)$$

The spectra were analysed with a fitting procedure based on χ^2 minimisation. As explained earlier, the fitting function is a Doniach-Šunjić profile convoluted with a Gaussian. Each peak is described by five parameters: the Lorentzian linewidth (Γ), the asymmetry parameter (α), the Gaussian linewidth (G), the intensity (I_0), and the binding energy position (E_0).

2.1.2 NEXAFS

Near-Edge X-ray Absorption Fine Structure spectroscopy (NEXAFS) is a spectroscopic technique, initially devised in the 1980s with the goal of investigating the structure of molecules bonded to surfaces, based on the investigation of X-ray absorption of condensed matter. The technique constantly developed during the following decades [54] and now is routinely exploited in surface science. Despite the technical requirements, first of all the need for a high performance synchrotron source, NEXAFS spectroscopy is a major method in order to achieve reliable information about the geometric and electronic structure at surfaces.

When an electron absorbs a photon it can be either photoemitted or excited to an unoccupied state, depending on the amount of acquired energy. In both cases a hole is created in the inner shell, with a finite lifetime. There are two major ways for the hole to be filled: X-ray fluorescence and Auger electron emission (See Fig. 2.6). In the first one, the recombination creates a photon with energy correspondent to the electron transition, while in the second one the exceeding energy is transferred to another electron that is emitted from the atom. The latter is called an Auger electron. These two different possibilities of recombination allow to investigate x-ray absorption by detecting either photons or electrons. Auger electrons detection is usually preferred because Auger emission has bigger probability with respect to fluorescence in low Z electrons,

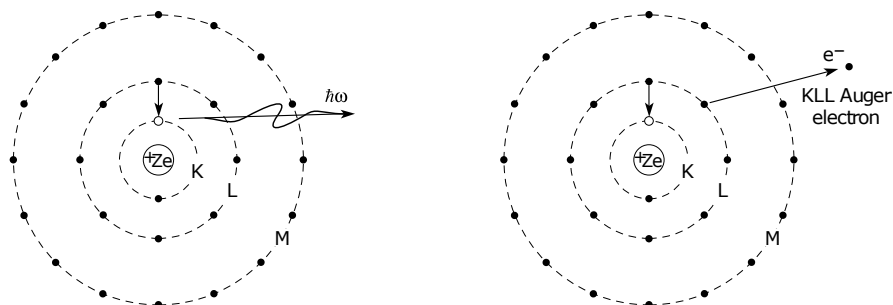


Figure 2.3: Schematic representation of the two major ways for the hole to be filled: X-ray fluorescence photon emission (left) and Auger electron emission (right). *Adapted from [55].*

mainly present in biological molecules. In addition, Auger signal detection offers a better surface sensitivity because electrons have a way smaller inelastic mean free path in solids with respect to fluorescence photons.

The NEXAFS experiments discussed in this work were performed in the so-called *partial electron yield* (PEY) mode, consisting in suppressing lower kinetic energy electrons, emerging from the sample, by applying a retarding voltage. In fact, this mode is frequently exploited for the investigation of adsorbates on surfaces because the surface sensitivity is considerably enhanced, allowing only those electrons that emerge from the outermost surface region to be detected. Further available options are the *total electron yield* (TEY) mode, where all electrons that emerge from the surface are detected and the *Auger electron yield* (AEY) mode, where electrons are selected in energy in order to collect only Auger electrons.

Dichroism

Through NEXAFS it is possible to obtain important information on the geometric structure of the molecules absorbed on a surface. In particular, investigation of transitions to MO is usually revealing. In fact, one important feature of molecular orbitals is that they have strong directional character and there is a one-to-one correlation between the spatial orientation of the orbitals and the molecular geometry. Thus for oriented molecules and polarized X-rays the intensities of resonances associated with, for example, σ^* and π^* final states should exhibit a dramatic and different angular dependence.

The angular dependence in the cross section is contained in the dipole matrix

element, that for linearly polarized X-rays in the direction of unit vector \mathbf{e} assumes a simpler form

$$\langle f | \mathbf{e} \cdot \mathbf{p} | i \rangle = \mathbf{e} \cdot \langle f | \mathbf{p} | i \rangle = \mathbf{e} \cdot \mathbf{O} \quad (2.6)$$

where $\langle f | \mathbf{p} | i \rangle$ is the Transition Dipole Moment (TDM) and for a 1s initial state points in the direction of the final state orbital \mathbf{O} . The cross section and therefore also the transition intensity become

$$I_{if} \propto |\langle f | \mathbf{e} \cdot \mathbf{p} | i \rangle|^2 = |\mathbf{e} \cdot \mathbf{O}|^2 \propto \cos^2 \delta \quad (2.7)$$

where δ is the angle between vector field \mathbf{E} and final state TDM \mathbf{O} .

2.1.3 IR-Vis SFG

Infrared-Visible Sum Frequency Generation spectroscopy (IR-Vis SFG) is a surface sensitive photon-in photon-out technique that provides both vibrational and electronic information. As a second order optical technique, the SF signal can only be generated from non-centrosymmetric materials and is therefore an intrinsically surface-sensitive technique. These second-order processes typically have a low cross-section, so pulsed laser radiation is required to provide the high peak power required to obtain a detectable output signal [56]. The surface sensitivity, combined with the long mean free path of photons in the gas phase, makes this technique suitable for the study of many interfaces (such as solid-vacuum, solid-liquid, solid-gas, liquid-gas) at both UHV and NAP conditions. For the system to be SF-active for a given normal mode on a metal surface, the corresponding dipole must have a net component normal to the surface and a net orientation in the range of a few hundred nanometres, which is the typical wavelength of a visible photon [57, 58].

Theory

The IR-Vis SFG signal is generated at an interface using two laser beams, one in the visible light region and the other in the IR region: in our setup the visible beam is green with 532 nm wavelength, and the one in the infrared region is tuneable between 2300 and 10000 nm. In order to generate SFG radiation IR and visible laser pulses need to overlap at the surface, both spatially and temporally. The visible beam induces an electronic transition to an excited virtual state, while the

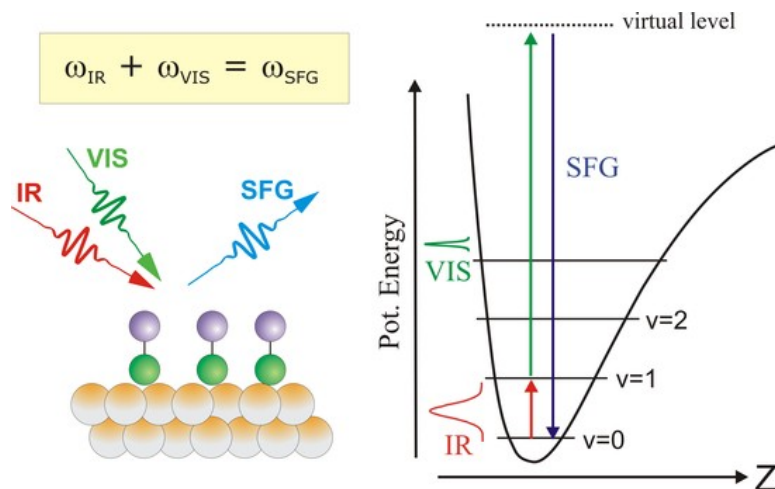


Figure 2.4: On the left an SFG signal is generated from two laser beams, IR and visible, impinging on a surface. On the right a schematic representation of SFG transitions.

tunable IR beam can excite a vibrational transition when the radiation energy matches the energy of a vibrational resonance of the system. Both the IR or the Vis photons can be first absorbed, but since the vibrational excited state has a longer life-time than the electronic one, the anti-stokes process is generally favoured (absorption of IR photon prior to Vis photon). The relaxation of this excited state generates the emission of radiation with energy given by the sum of the visible and infrared energies

$$\omega_{SFG} = \omega_{VIS} + \omega_{IR} \quad (2.8)$$

A schematic representation of the process is reported in Fig. 2.7. SFG radiation intensity is measured as a function of the IR energy to identify molecules and gas adsorbates through their specific vibrational energies.

SFG as a non-linear optical process

In the description of a material's response to an oscillating external electric field, it is easier to start from a scalar electric field $E(t)$ that generates a polarisation $P(t)$. In linear optics processes, the polarisation dependence on the electric field is usually expressed by

$$P(t) = \epsilon_0 \chi^{(1)} E(t) \quad (2.9)$$

where ϵ_0 is the vacuum dielectric constant and $\chi^{(1)}$ is the first order susceptibility of the material. This relation is valid for weak fields. In the presence of strong external fields ($E \sim 10^6$ V/m) this relation is no longer valid and it is necessary to expand the polarisation as a power series in $E(t)$: using the formalism of [59] the expression for the polarisation becomes

$$\begin{aligned} P(t) &= \epsilon_0[\chi^{(1)}E(t) + \chi^{(2)}E^2(t) + \chi^{(3)}E^3(t) + \dots] \\ &\equiv P^{(1)}(t) + P^{(2)}(t) + P^{(3)}(t) + \dots \end{aligned} \quad (2.10)$$

where the coefficients are now given by higher orders susceptibilities. It is possible to generalise this description to take into account the vectorial nature of $E(t)$ and $P(t)$ using tensorial notation for the susceptibilities: $\chi^{(1)}$ becomes a second-order tensor and $\chi^{(2)}$ a third order tensor.

If the external impinging electric field is given by the sum of two different components, oscillating at different frequencies, it can be written in the form

$$\mathbf{E}(\mathbf{r}, t) = \mathbf{E}_1(\omega_1)e^{-i(\omega_1 t - \phi_1)} + \mathbf{E}_2(\omega_2)e^{-i(\omega_2 t - \phi_2)} + c.c. \quad (2.11)$$

where $\mathbf{E}_n(\omega_n) \equiv \frac{1}{2}\mathbf{E}_n e^{i\mathbf{k}_n \cdot \mathbf{r}}$ and \mathbf{E}_n is the product of the amplitude and the polarization vector. Using the relation $\mathbf{E}_n(-\omega_n) = \mathbf{E}_n^*(\omega_n)$ a more compact form of (2.25) can be written:

$$\mathbf{E}(\mathbf{r}, t) = \sum_n \mathbf{E}_n(\omega_n) e^{-i(\omega_n t - \phi_n)}, \quad n = -2, -1, 1, 2 \quad (2.12)$$

where the sum extends over positive and negative frequencies, with $\omega_{-n} = -\omega_n$, taking into account the complex conjugate. It is now possible to write a cartesian component of the second order polarisation as

$$P_i^{(2)}(\mathbf{r}, t) = \epsilon_0 \sum_{jk} \sum_{nm} \chi_{ijk}^{(2)}(\omega_n + \omega_m; \omega_n, \omega_m) E_j(\omega_n) E_k(\omega_m) e^{-i[(\omega_n + \omega_m)t - (\phi_n + \phi_m)]} \quad (2.13)$$

where it is easy to see that the resulting components of the second order polarisation oscillate at different frequencies $\omega_n + \omega_m$ with respect to the oscillation frequencies of the field components. The sum over n and m produces different components: second harmonic generation (SHG) at $2\omega_1$ and $2\omega_2$, difference frequency generation (DFG) at $\omega_1 - \omega_2$, sum frequency generation (SFG) at $\omega_1 + \omega_2$ and optical rectification (OR) that is a non-oscillating term.

We can now focus on the SFG component, with $\omega_3 = \omega_1 + \omega_2$, that becomes

$$P_i^{(SFG)}(\mathbf{r}, t) = \epsilon_0 \sum_{jk} \left[\chi_{ijk}^{(2)}(\omega_3; \omega_1, \omega_2) E_j(\omega_1) E_k(\omega_2) + \chi_{ijk}^{(2)}(\omega_3; \omega_2, \omega_1) E_j(\omega_2) E_k(\omega_1) \right] e^{-i(\omega_3 t - \phi_3)} \quad (2.14)$$

using the relation $\chi_{ijk}^{(2)}(-\omega_3; -\omega_1, -\omega_2) = \chi_{ijk}^{(2)}(\omega_3; \omega_1, \omega_2)^*$. Assuming that the nonlinear susceptibility has intrinsic permutation symmetry $\chi_{ijk}^{(2)}(\omega_3; \omega_1, \omega_2) = \chi_{ikj}^{(2)}(\omega_3; \omega_1, \omega_2)$ [59], the dummy indexes j and k can be interchanged, thus SFG polarisation can be expressed by

$$\begin{aligned} P_i^{(SFG)}(\mathbf{r}, t) &= 2\epsilon_0 \sum_{jk} \chi_{ijk}^{(2)}(\omega_3; \omega_1, \omega_2) E_j(\omega_1) E_k(\omega_2) e^{-i(\omega_3 t - \phi_3)} + c.c. \\ &= \frac{1}{2} \epsilon_0 \sum_{jk} \chi_{ijk}^{(2)}(\omega_3; \omega_1, \omega_2) E_{1,j} E_{2,k} e^{i(\mathbf{k}_3 \cdot \mathbf{r} - \omega_3 t + \phi_3)} + c.c. \end{aligned} \quad (2.15)$$

and, neglecting the spatial and temporal dependence, a more compact form is obtained:

$$P_i^{(SFG)} = \epsilon_0 \sum_{jk} \chi_{ijk}^{(2)} E_{1,j} E_{2,k} \quad (2.16)$$

Equation (2.30) is useful to derive a fundamental property of the SFG signal that is the surface specificity, due to the fact that $\chi^{(2)}$ vanishes for centrosymmetric materials. When parity symmetry is applied to the polarisation and electric field vectors they change sign (because they are polar vectors), while $\chi^{(2)}$ does not change sign because a centrosymmetric material is identical under inversion, thus $\chi_{ijk}^{(2)} = \chi_{-i-j-k}^{(2)}$. It is possible to write

$$\begin{aligned} -P_i^{(SFG)}(\mathbf{r}, t) &= \epsilon_0 \sum_{jk} \chi_{ijk}^{(2)}(-E_{1,j})(-E_{2,k}) \\ &= \epsilon_0 \sum_{jk} \chi_{ijk}^{(2)} E_{1,j} E_{2,k} \end{aligned} \quad (2.17)$$

that for a centrosymmetric materials only holds when $\chi_{ijk}^{(2)}$ vanishes.

This property is largely exploited in SFG spectroscopy experiments: due to the fact that gas phases and many bulk materials are centrosymmetric, they are not SFG active and they don't contribute to the SFG signal. Therefore, SFG spectroscopy is the perfect technique to obtain vibronic information about sur-

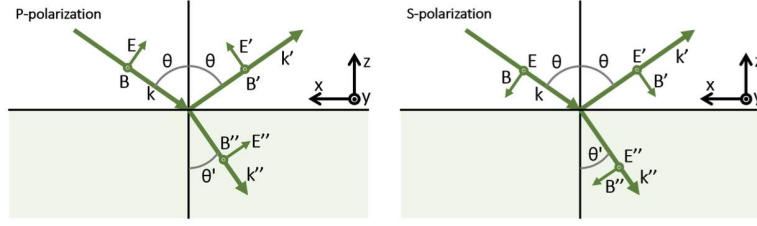


Figure 2.5: Reflection at an interface for p and s polarized radiation.

faces and interfaces that are intrinsically non-centrosymmetric media.

SFG in reflection geometry

In our case, the imping electric fields consist of a visible beam and a tunable infrared beam. In the description of reflection at a surface, it is useful to decompose an incident field \mathbf{E}_I into components polarized parallel (p) and perpendicular (s) to the incidence plane as follows:

$$\begin{aligned} E_{I,x} &= -E_p \cos \theta \\ E_{I,y} &= E_s \\ E_{I,z} &= E_p \sin \theta \end{aligned} \quad (2.18)$$

where θ and the coordinate convention refer to Fig. 2.8. The total electric field at the surface is given by the sum of the incident and reflected beams. If we define the Fresnel amplitude coefficients for reflection (r_p, r_s) as in [57], the components of the total electric field at the surface can be written as

$$\begin{aligned} E_x &= -(1 - r_p)E_p \cos \theta \equiv K_x E_p \\ E_y &= (1 + r_s)E_s \equiv K_y E_s \\ E_z &= (1 + r_p)E_p \sin \theta \equiv K_z E_p \end{aligned} \quad (2.19)$$

Exploiting equation (2.33), the SFG polarization in (2.30) can now be expressed in term of the amplitude of the incident fields $E_{I,1} = E_{IR}$ and $E_{I,2} = E_{VIS}$:

$$P_i^{(SFG)} = \epsilon_0 \sum_{jk} \chi_{ijk}^{(2)} K_{IR,j} E_{IR} K_{VIS,k} E_{VIS} \quad (2.20)$$

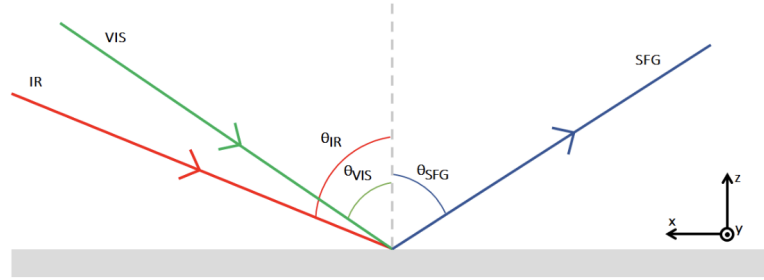


Figure 2.6: Generation of an SFG signal on a surface from IR and visible laser beams in reflection geometry.

The nonlinear polarization generates a surface bound SFG electric field. The emission angle of the SFG signal is determined by the phase-matching condition [57] that expresses the momentum conservation at the interface:

$$n_{SFG}k_{SFG} \sin \theta_{SFG} = n_{IR}k_{IR} \sin \theta_{IR} + n_{VIS}k_{VIS} \sin \theta_{VIS} \quad (2.21)$$

where n is the refractive index of the propagation medium, k the wavevector and θ the angle between the beam and the normal to the surface. In our case all the beams propagate in the same medium, thus refractive indexes can be neglected. Angle notation refers to Fig. 2.9. It is possible to express the SFG electric field in term of the induced polarization introducing the nonlinear SFG Fresnel factors (L factors) defined in [57] and not reported here

$$E_{i,SFG} = L_i P_i^{(SFG)} \quad (2.22)$$

The intensity of the SFG signal depends on the square modulus of the electric field, therefore the following relations hold:

$$\begin{aligned} I_{SFG} &\propto \left| \sum_i E_{i,SFG} \right|^2 \\ &\propto \left| \sum_i L_i P_i^{(SFG)} \right|^2 \\ &\propto \left| \epsilon_0 \sum_{ijk} L_i \chi_{ijk}^{(2)} K_{IR,j} E_{IR} K_{VIS,k} E_{VIS} \right|^2 \end{aligned} \quad (2.23)$$

Using the convention of Fig. 2.8, we note that p polarisation can have x and z components, while s polarisation only has y components. The polarisation of the incident beams determines the susceptibility tensor's components that can

be measured, thus it is important to have the control over polarisation in SFG experiments.

Microscopic approach

The relation between SFG signal intensity and $\chi^{(2)}$, that is the macroscopic average of molecular polarisabilities, has been found in the previous paragraph. Microscopic molecular polarisation $\boldsymbol{\mu}$ and imping electric field \mathbf{E} are linked by the relation

$$\boldsymbol{\mu} = \boldsymbol{\mu}_0 + \alpha\mathbf{E} + \beta\mathbf{E}^3 + \gamma\mathbf{E}^3 + \dots \quad (2.24)$$

which includes non-linear effects. β and γ are the first and second order hyperpolarisabilities of the molecules adsorbed on the surface [66]. The tensor β is a third-rank tensor, the same dimension of $\chi^{(2)}$, describing the nonlinear response of molecules on the surface to incident electric fields: different components refer to different vibrational modes. The second-order susceptibility tensor is the macroscopic average of β : hyperpolarisability β undergoes substantial changes when IR radiation is tuned through a resonance that is observed, through SFG measurements, as a change in $\chi^{(2)}$. We can use a molecular bound coordinate system identified with indexes (a, b, c) instead of the surface one (i, j, k) : an example is reported in Fig. 2.10 where a molecule adsorbed on the surface is tilted of a θ angle. The molecular coordinate system is simply related to the surface one by three rotational matrixes $R(\psi)R(\theta)R(\phi)$ that refer to the Euler angles (ψ, θ, ϕ) . The hyperpolarisability tensor becomes $R(\psi)R(\theta)R(\phi)\beta$ and its macroscopic averaging can be written as:

$$\chi_{ijk}^{(2)} = \frac{N}{\epsilon_0} \sum_{abc} \langle R(\psi)R(\theta)R(\phi)\beta_{abc} \rangle \quad (2.25)$$

where N is density of adsorbed molecules and the matrix element represents an orientational averaging. A quantum mechanical expression for β_{abc} can be derived using perturbation theory [60]. In the case of visible radiation ω_{VIS} far from electronic resonances and infrared radiation ω_{IR} close to a vibrational resonance ω_0 , the following simplified version can be used:

$$\beta_{abc} = \frac{1}{2\hbar} \frac{M_{ab}T_c}{\omega_0 - \omega_{IR} - i\Gamma} \quad (2.26)$$

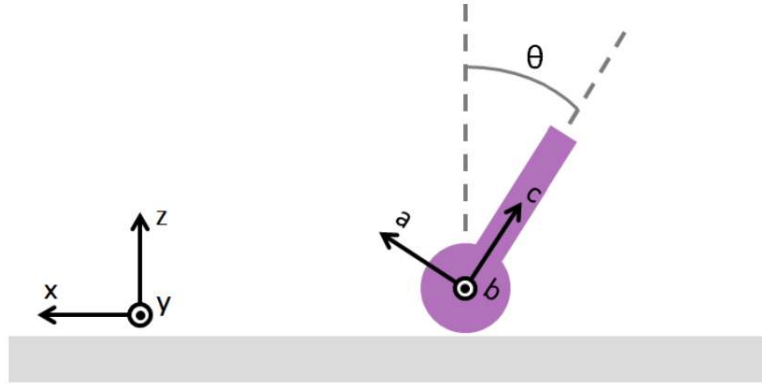


Figure 2.7: A molecule adsorbed on a surface, tilted of an angle θ . The two coordinate systems are related by a rotation matrix $R(\theta)$.

where Γ^{-1} is the relaxation time of the vibrational excited state, M_{ab} and T_c are the Raman and infrared transition moments respectively, defined in [61]. A selection rule is immediately derived from (2.40): a resonance must be both Raman and infrared active in order to be observed by means of an SFG transition [62]. Eq. (2.40) has the shape of a Lorentzian resonance and when inserted in (2.39) it reveals the origin of the SFG signal intensity increasing near a vibrational resonance.

Lineshape modeling

The description that led us to eq. (2.40) is based on an oversimplification of real systems: a generic system composed of molecules adsorbed on a surface produces an SFG signal that is the combination of both the molecular and substrate contribution. The molecular contribution to the susceptibility tensor $\chi_{RES}^{(2)}$ varies sensibly as the infrared radiation is tuned through the vibrational resonances. The substrate contribution doesn't change, in a first approximation, with the infrared tuning and, together with the constant part of the molecular susceptibility, it contributes to the non-resonant $\chi_{NR}^{(2)}$ susceptibility, usually approximated with a constant value. The total susceptibility is therefore

$$\chi^{(2)} = \chi_{RES}^{(2)} + \chi_{NR}^{(2)} \quad (2.27)$$

For dielectric materials $\chi_{NR}^{(2)}$ contribution is small compared to the resonant part. When the substrate is metallic $\chi_{NR}^{(2)}$ contribute is significant, due to the presence of surface plasmon resonances [57].

To a practical extent, it is common to replace the susceptibility tensor introducing an effective scalar susceptibility [56] shaped as

$$\begin{aligned}\chi^{(2)}(\omega_{IR}) &= A_{NR}e^{i\phi_{NR}} + \sum_n \frac{A_n e^{i\phi_n}}{\omega_{IR} - \omega_n + i\Gamma} \\ &= e^{i\phi_{NR}} \left[A_{NR} + \sum_n \frac{A_n e^{i\Delta\phi_n}}{\omega_{IR} - \omega_n + i\Gamma} \right]\end{aligned}\quad (2.28)$$

where the sum runs over the various resonances of the system. The parameters are real-valued amplitudes A_n , phases ϕ_n , resonance frequencies ω_n and resonance broadenings Γ_n related to their lifetimes. In the second line of eq. (2.42) the non-resonant phase has been factorised and the phase differences $\Delta\phi_n$ have been introduced: these represent the relative phase-shift of the n^{th} resonance to the non-resonant background. The amplitudes A_n depend on the density of molecules N and the electronic and vibrational transition moments, respectively M_n and T_n as

$$A_n \propto NM_n T_n \delta\rho_n \quad (2.29)$$

and the population difference between the ground and excited state $\delta\rho_n$ [63]. As said, SFG spectra can be modelled exploiting an effective scalar susceptibility, and combining equation (2.42) with (2.37) we obtain an expression for the SFG signal intensity as a function of the infrared frequency

$$I_{SFG}(\omega_{IR}) \propto \left[A_{NR} + \sum_n \frac{A_n e^{i\Delta\phi_n}}{\omega_{IR} - \omega_n + i\Gamma} \right]^2 I_{VIS} I_{IR}(\omega_{IR}) \quad (2.30)$$

Frequency dependence has been explicitated in the infrared intensity to emphasise that, while visible radiation intensity is constant (except for laser instabilities), I_{IR} varies with the IR tuning: it is thus important to normalize the measured SFG intensity taking into account for this effect.

SFG Setup

SFG measurements were performed exploiting a customised setup purchased from the Lithuanian laser manufacturing company EKSPLA. All the components

are controlled via LabVIEW software.

SFG measurements are performed using pulsed laser radiation: green light at 532 nm and infrared radiation in the range 2300-10000 nm are generated in the laser setup, overlap at the sample surface and then SFG output signal is measured. The principal components of the setup are:

- a fourth class PL2230 Series Laser, generating the fundamental infrared pulsed radiation at 1064 nm. The pulses are ~30 ps long with a repetition rate of 50 Hz and maximum pulse energy of 25 mJ. The peak power of the fundamental radiation, defined as $P = E/\Delta t$ (E being the maximum pulse energy and Δt the pulse duration) is ~1 GW; the mean power is therefore ~1.25 W. The beam diameter is ~6 mm;
- a Harmonic Unit H500 where second harmonics radiation at 532 nm (green) is generated. Three outputs are produced at this stage: a beam at the fundamental wavelength (1064 nm) with maximum pulse energy of 15 mJ and two visible beams. One of the visible beams, with 1 mJ maximum energy per pulse, is directly used to produce SFG radiation; the other, with 10 mJ maximum energy per pulse, is exploited to generate the tuneable infrared radiation. In this unit the temporal overlap of IR and visible pulses can be modified by means of a delay line;
- an Optical Parametric Generator PG501/DFG1P where the 2300-10000 nm tuneable mid-IR radiation is generated using the fundamental radiation and one of the visible beams. The measured pulse average energy is ~200 mJ;
- the SFG box: here the polarisations of the tuneable mid-IR and visible beams are selected and the beams are spatially overlapped on the sample, generating a SFG signal in the range 432-505 nm.

Fig. 2.11 is a schematic top view of the laser setup and SFG spectrometer where the different sections described above can be identified. Additional information and technical details are reported in appendix A; information about the laser setup and SFG spectrometer can be found in [64].

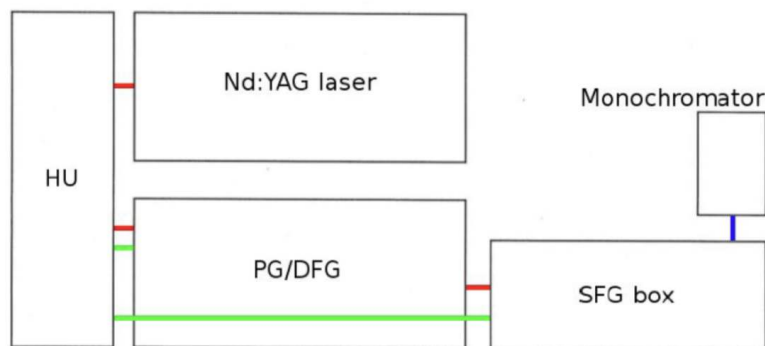


Figure 2.8: A molecule adsorbed on a surface, tilted of an angle θ . The two coordinate systems are related by a rotation matrix $R(\theta)$.

2.2 Diffraction

2.2.1 SXRD

Surface X-Ray Diffraction is a powerful technique that allows to determine with high accuracy the structure of crystalline surfaces. SXRD technique is based on the investigation of the so-called *Diffraction Rods*, generated by the X-ray scattering from surfaces or interfaces. Being a photon-in photon-out technique, SXRD has the great advantage that is possible to neglect the multiple scattering effects, with respect for instance to LEED. The high penetration length of X-rays also allows to usually lift the require to work in strict UHV conditions. On the other hand, to achieve sufficient surface sensitivity this technique requires a collimated X-ray beam with very high intensity, i.e. synchrotron radiation, and to work at grazing incidence.

Theory

Using X-Rays with an energy high enough it is possible to describe the diffraction process in the framework of the so-called, *kinematic approximation*, neglecting multiple scattering processes and the interaction between the incoming and scattered beams.

Considering X-rays as electromagnetic waves scattered by an electron-density distribution $\rho(\mathbf{r})$, the diffracted intensity $I(\mathbf{q})$ can be expressed in terms

of the Fourier transform of $\rho(\mathbf{r})$ as:

$$I(\mathbf{q}) \propto \left| \int \rho(\mathbf{r}) \exp(i\mathbf{q} \cdot \mathbf{r}) d^3r \right|^2 \quad (2.31)$$

Introducing a periodic crystal with $N_1 \times N_2 \times N_3$ cells and a periodicity $\mathbf{R}_n = n_1 \mathbf{a}_1 + n_2 \mathbf{a}_2 + n_3 \mathbf{a}_3$ (where $\mathbf{a}_1, \mathbf{a}_2, \mathbf{a}_3$ are primitive vectors and n_1, n_2, n_3 are integer numbers), the former expression can be factorised as:

$$I(\mathbf{q}) \propto |F(\mathbf{q})|^2 \left| \sum_{n_1, n_2, n_3}^{N_1, N_2, N_3} \rho(\mathbf{r}) \exp(i\mathbf{q} \cdot \mathbf{R}_n) d^3r \right|^2 \quad (2.32)$$

where the first term is the square of the *structure factor* $F(\mathbf{q}) = \int \rho(\mathbf{r}) d^3r$, which includes the contribution to the scattering from the individual atoms in the unit cell, while the second term contains the information about the periodicity and can be rewriting as:

$$I(\mathbf{q}) \propto |F(\mathbf{q})|^2 \left| \prod_{j=1,2,3} \frac{\sin^2 \frac{1}{2} N_j \mathbf{q} \cdot \mathbf{a}_j}{\sin^2 \frac{1}{2} \mathbf{q} \cdot \mathbf{a}_j} \right|^2 \quad (2.33)$$

In bulk crystals, the intensity $I(\mathbf{q})$ is maximised when the transferred moment \mathbf{q} matches points in the reciprocal lattice $\mathbf{q} = h\mathbf{a}_1^* + k\mathbf{a}_2^* + l\mathbf{a}_3^*$ with h, k, l integer numbers, and in these points the intensity is given by:

$$I_{hkl} \propto |F_{hkl}|^2 N_1^2 N_2^2 N_3^2 \quad (2.34)$$

which diverges in the ideal case of an infinite crystal. Thus, the crystalline periodicity results in a set of discrete spots, so-called *Bragg points*, in the diffraction pattern, illustrated in Fig. 2.12a). Each Bragg peak is broadened and presents weak lateral oscillations in intensity determined by the function in the second term of eq. (2.47)

$$s(h) = \frac{\sin^2 N\pi h}{\sin^2 \pi h} \quad (2.35)$$

providing information about the degree of order of the probed area. In addition, the intensity of the Bragg spots decays as a function of the distance from the origin of the reciprocal space due to the finite size of the electron density distribution within the atoms, whose contribution is included in the structure factor.

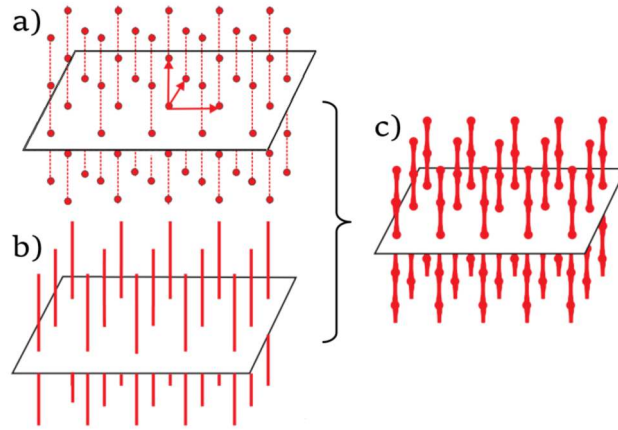


Figure 2.9: Diffraction in reciprocal space in the case of a 3D bulk crystal (a), a 2D thin film (b) and a truncated surface (c). Adapted from [65].

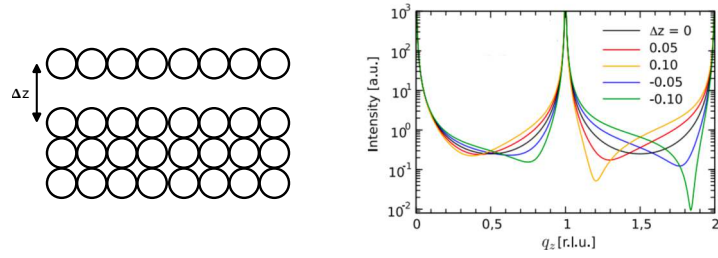
In the case of a thin film, with periodicity only in the in-plane directions, $\mathbf{R}_n = n_1\mathbf{a}_1 + n_2\mathbf{a}_2$, the component q_z of \mathbf{q} , lifted from periodic constraints, becomes a continuous variable. This gives rise to the *rods* in the diffraction pattern, as depicted in Fig. 2.12b). The associated intensity then becomes:

$$I_{hk} \propto |F_{hk}(q_z)|^2 N_1^2 N_2^2 \quad (2.36)$$

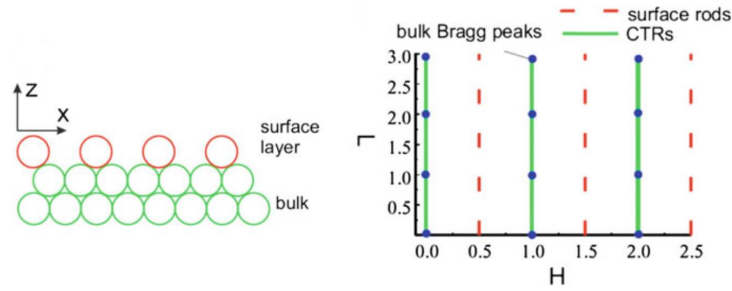
Notably the dependence of structure factor on the continuous out-of-plane component q_z account for the arrangement of the atoms in the direction normal to the surface, within the unit cell.

When a crystal is cut along a plane, creating a surface, the periodicity along the out-of-plane direction is broken and the diffraction pattern results in a superposition of 3D and 2D features, points and rods, as shown in Fig. 2.12c). The resulting objects in reciprocal space are the aforementioned Crystal Truncation Rods (CTR). By analysing the intensity modulations along the CTRs, it is possible to get insight into the symmetry and positions of the atoms within the unit cell.

However, we are not usually dealing with an ideal truncation of the crystal structure. Besides the cases molecular or atomic adsorption, phenomena such as relaxation or reconstruction often occur in most real bare surfaces in order to minimise the energy of the system. This usually lead to different periodicity with respect to the bulk unit cell. Different out-of-plane periodicity results in intensity modulations along the CTRs. On the other hand, the formation of a in-plane



(a) Adapted from [66].



(b) Adapted from [67].

Figure 2.10: Influence on the diffraction pattern generated by the relaxation of surface (a) or formation of a surface superlattice (b).

superlattice creates new features, the so-called *Surface structure Rods*, that are normally placed in different areas of the reciprocal space with respect to CTRs, i.e. they correspond to non-integer values of Miller indexes. Both cases are illustrated in Fig. 2.13.

Because of the intrinsically different signal originating from the surface and from the bulk, it is convenient to express the total structure factor as the sum of the two distinct contributions:

$$F_{hkl}^{tot} = F_{hkl}^{bulk} + F_{hkl}^{surf} \quad (2.37)$$

The surface contribution will modify the total structure factor amplitude if the surface structure differs from the bulk. Starting from the general definition of the surface structure as the Fourier transform of the electron density distribution within the unit cell, as in eq. (2.46), it can be simplified as:

$$F_{hkl}^u = \sum_j f_j e^{-M_j} e^{i\mathbf{q}\cdot\mathbf{r}} = \sum_j f_j e^{-M_j} e^{2\pi i(hx_j + ky_j + lz_j)} \quad (2.38)$$

where the j index runs over the atoms in the unit cell, defined by the positions $\mathbf{r}_j = x_j\mathbf{a}_1 + y_j\mathbf{a}_2 + z_j\mathbf{a}_3$, f_j is the atomic scattering factor, and e^{-M_j} is the Debye Waller term that contains the contribute of the thermal vibration in the lattice.

In the case of the surface, it can be included also an occupancy parameter θ_j , which accounts for the fact that, at the topmost layers, not all positions need to be fully occupied:

$$F_{hkl}^{sur} = \sum_j \theta_j f_j e^{-M_j} e^{i\mathbf{q}\cdot\mathbf{r}} = \sum_j f_j e^{-M_j} e^{2\pi i(hx_j + ky_j + lz_j)} \quad (2.39)$$

In the case of the bulk, the scattering from all layers below the surface has to be considered. Then, summing over all layers from $-\infty$ to 0, it can obtained:

$$F_{hkl}^{bulk} = \sum_n \theta_j F_{hkl}^u e^{2\pi i n \alpha} e^{n\alpha} = F_{hkl}^u \frac{1}{1 - e^{2\pi i n \alpha} e^{-\alpha}} \quad (2.40)$$

where α is the attenuation factor, accounting for different contribution of unit cells deep inside the substrate. If we consider a small attenuation, i.e. $\alpha \ll 0$, the bulk contribution can be approximated by:

$$F_{hkl}^{bulk} \approx \frac{F_{hkl}^u}{1 - e^{-\alpha}} \approx \frac{F_{hkl}^u}{\alpha} \approx \frac{F_{hkl}^u}{2 \sin \pi l} \quad (2.41)$$

which, for integer values of l , diverges, as already qualitatively observed in the previous paragraph.

Finally, surface roughness usually affect the intensity of the CTRs. This contribution can be formally expressed by a prefactor multiplying the total structure factor

$$F_{hkl}^{rough} = \frac{1 - \beta}{\sqrt{1 + \beta^2 - 2\beta \cos 2\pi l}} F_{hkl}^{tot} \quad (2.42)$$

calculated using an exponential roughness model, the so-called β -model, in which the occupancy of the first layer equals $(1 - \beta)$, the second layer $(1 - \beta)^2$, and so on, as illustrated in Fig. 2.14.

Data analysis and Simulations

The raw SXRD data collected at the SixS beamline consists of a series of 2D intensity maps relative to the diffraction angles ω and δ . In addition to the desired diffraction rod intensities, these data contain background scattering, tails of substrate Bragg peaks and other unwanted signals. Careful data reduction is

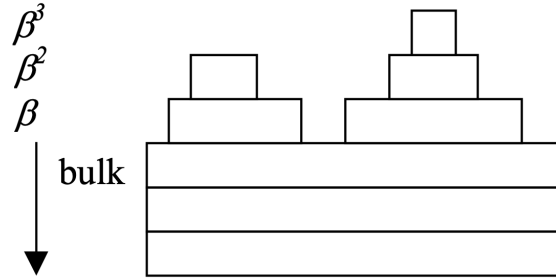


Figure 2.11: Surface roughness according to the so-called β -model.

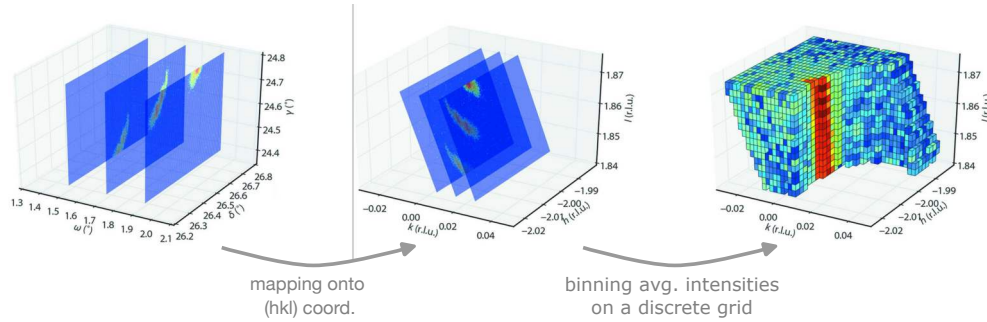


Figure 2.12: Graphical overview of the process performed by BINoculars. Adapted from [68].

therefore required prior to analysis in order to extract the significant signal from raw diffraction data. In general, data processing consists of background subtraction and integration of the intensities, which are finally adjusted with some experimental correction factors.

The data collected in this experiment have been processed by the BINoculars [68] software, which takes a series of images from a 2D detector, calculates the corresponding reciprocal lattice coordinates (hkl) for each pixel, and reduces the image collection to a single data set by averaging the intensities of pixels taken at identical (hkl) positions within a user-specified resolution. The intensity of each pixel is projected onto a three-dimensional grid in reciprocal lattice coordinates using a binning algorithm. This transformation and the pixels averaging are illustrated in Fig. 2.15. The integrated intensities are finally converted into structure factors by simply applying the square root and introducing some correction factors according to Eq. (2.50).

In order to analyse the collected rods, we exploited ANA-ROD, a specifically developed software for surface X-ray crystallography [69]. Given the initial atomic position in real space, the program computes the structure factors separating surface Eq. (2.53) and bulk Eq. (2.54) contributions. The structural model of the system can be parametrised exploiting several different variables (atomic position, roughness factor, etc.), which are then left free to vary in order to minimise the discrepancies, measured in terms of the χ^2 , between the experimental data and the simulated intensities. ANA-ROD is designed to work with three types of input files: the *data file*, containing the measured structure factors as a function of the (h, k, l) coordinates for each diffraction rods, the *surface file*, containing the positions of the atoms on the surface of the sample and a *bulk file*, consisting of the theoretical positions of the atoms in the bulk substrate. The surface file can contain more than a single layer, including the topmost layers of the substrate which can be relaxed or reconstructed. An additional fitting file can be created to introduce the specific displacements from the initial positions to optimise the model.

The program allows for the displacement in three spatial directions, and each atom can be moved singularly or collectively with other equivalent atoms, according to the choice of the user, on the basis of symmetry arguments. This can be obtained by labelling equivalent atoms with the same index, thus imposing constraints in calculating the fit coefficients. Then, the x position of a generic atom is calculated as:

$$x = x_{start} + C_x^1 V(N_{\delta 1}) + C_x^2 V(N_{\delta 2}) \quad (2.43)$$

where x_{start} is the initial position, C_x^1 and C_x^2 are coefficients, while $V(N_{\delta 1})$ and $V(N_{\delta 2})$ are the values of the displacement parameters labeled $N_{\delta 1}$, $N_{\delta 2}$. In addition to atomic displacements, ANA-ROD allows the introduction of several supplementary degrees of freedom to refine the model. The most commonly used are:

- β : the roughness parameter, as defined in Eq. (2.56);
- f_S : the surface fraction parameter that indicates the percentage of crystal that is covered by surface layer.
- θ : the occupancy parameter indicating the probability of a certain posi-

tion at the surface to be occupied.

- B : the Debye-Waller parameter, that accounts for the thermal contribution.

To find the best fitting coefficients, the algorithm in ANA-ROD minimises the χ^2 , but also calculates the R-factor, which is defined as:

$$R = \frac{\sum_j |F_j^{theo} - F_j^{exp}|}{|\sum_j |F_j^{exp}|} \quad (2.44)$$

This is another figure of merit function, as well as the χ^2 , that measures the data-model discrepancies and can be used to check the reliability of the test structure, especially when dealing with several degrees of freedom.

2.3 Microscopy

2.3.1 STM

Scanning Tunnelling Microscopy (STM) represented a significant step forward in surface science, allowing for the imaging of surfaces at the atomic scale. It was first employed by Binnig and Rohrer in 1982 [70]. The measuring process involves scanning a surface while locally probing it with an extremely sharp conducting tip to examine its topological and electronic structure. By utilising this approach, samples can be examined with atomic resolution in the real space, leading to the observation of crucial information, such as the shape of the unitary cell, adsorbates distribution and deformation within the cell, and long-range structures, including moiré pattern.

The physical principle underlying STM is the quantum mechanical phenomenon of the tunnelling effect, in which a particle can surpass a potential barrier that cannot be overcome classically. In quantum mechanics, an electron is characterised by a wave-function $\psi(z)$ that satisfies Schrödinger's equation:

$$-\frac{\hbar^2}{2m} \frac{d^2}{dz^2} \psi(z) + U(z)\psi(z) = E\psi(z) \quad (2.45)$$

where m is the electron mass. Let's now consider the case of a piecewise-constant potential barrier, as sketched in Fig. 2.16. In the classically allowed

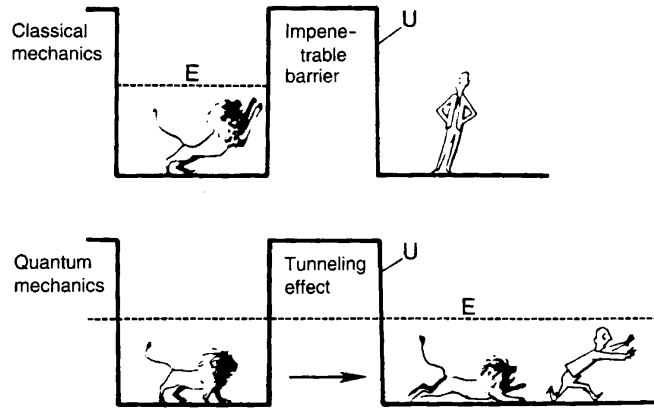


Figure 2.13: Difference between classical and quantum theory. In quantum mechanics, an electron has a non-zero probability of tunneling through a potential barrier. *Adapted from [71].*

region, where $E > U$, the solutions of the Schrödinger's equation are:

$$\psi(z) = \psi(0)e^{\pm ikz} \quad \text{where } k = \frac{\sqrt{2m(E - U)}}{\hbar} \text{ is the wave vector.} \quad (2.46)$$

While in the classical forbidden region, where $E < U$ the solution becomes:

$$\psi(z) = \psi(0)e^{\kappa z} \quad \text{where } \kappa = \frac{\sqrt{2m(U - E)}}{\hbar} \text{ is the decay constant.} \quad (2.47)$$

In this case, the probability density for an electron to be located in z is proportional to $|\psi(0)|^2 e^{-2\kappa z}$, which represents a non-zero probability for the electron to penetrate the barrier. Using this elementary model, we can explain the metal-vacuum-metal tunnelling, as shown in Fig. 2.17. STM measurements involve the application of voltage between a sharp metallic tip and the sample surface, while scanning the x and y coordinates. If a sample is biased positively with respect to the tip, electrons tunnel from the tip into the sample's empty states. For a negative bias, they tunnel from the sample's occupied states to the tip. The potential barrier can be approximated as the sample surface's work function (ϕ). This is the energy needed to remove an electron from the Fermi level (E_F) to the vacuum level. Therefore, for electron levels near E_F , neglecting the thermal energy contribution, we obtain the following current:

$$I \propto |\psi(0)|^2 e^{-2\kappa d} \quad \text{where } \kappa = \frac{\sqrt{2m\phi}}{\hbar} \text{ and } d \text{ is tip-sample distance.} \quad (2.48)$$

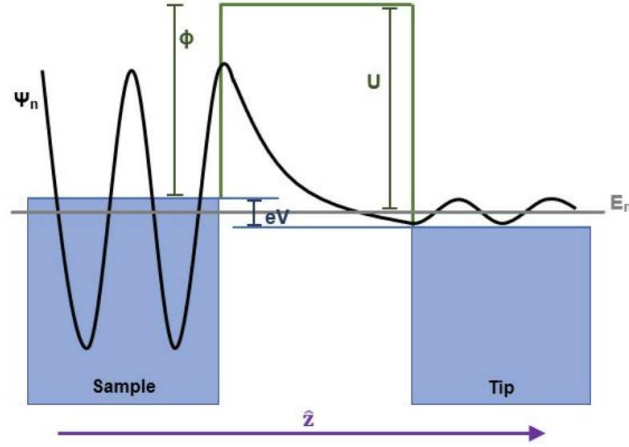


Figure 2.14: One-dimensional tunnelling model.

Considering a typical metal work function of $\phi \approx 4\text{eV}$, a reasonable value of the decay constant is about 1 \AA^{-1} . This gives an estimation of the current decay with distance of about one order of magnitude with a distance increase of 1 \AA .

To extend the tunnelling problem from one to three dimensions, we will adopt Bardeen's formalism [72]. The tunneling probability from a state ψ , on one side of the barrier, to a state χ , on the other side, can be expressed by the matrix element as:

$$M = \frac{\hbar}{2m} \int_{z=z_0} \left(\chi^* \frac{\partial \psi}{\partial z} - \psi \frac{\partial \chi}{\partial z} \right) dS \quad (2.49)$$

where $z = z_0$ is any separation surface lying entirely in the vacuum region between the sample surface and the tip. Then, the tunnelling current can be expressed through the Fermi golden rule as:

$$I = \frac{4\pi e}{\hbar} \int_{-\infty}^{-\infty} [f(E_F - eV + \varepsilon) - f(E_F + \varepsilon)] \rho_S(E_F - eV + \varepsilon) \rho_T(E_F + \varepsilon) |M|^2 d\varepsilon \quad (2.50)$$

Assuming that $k_B T$ is small enough to approximate the Fermi distribution $f(E)$ with a step function, and the matrix element M almost constant within the energy range of interest, the last equation is simplified as:

$$I \propto \int_0^{eV} \rho_S(E_F - eV + \varepsilon) \rho_T(E_F + \varepsilon) |M|^2 d\varepsilon \quad (2.51)$$

Within the Bardeen's formalism, the tunnelling current is then expressed as a convolution of the density of states of the sample and the tip. Considering now

the Tersoff-Hamann approximation, in which the tip has only one s-like orbital in the apex atom [73], the tunnelling current can be expressed as:

$$I \propto \int_0^{eV} \rho_S(\mathbf{r}_T, \varepsilon) d\varepsilon \quad (2.52)$$

where $\rho_S(\mathbf{r}_T, \varepsilon)$ is the local density of states of the sample at energy ε and at the position of the tip apex \mathbf{r}_T .

During STM measurements, the sample can be mapped by either measuring the resulting tunnelling current I or the sample-tip distance d . In the former method, the vertical coordinate z is fixed while the tunnelling current, which is dependent on d , is measured. In the second case, I is maintained at a constant value while z is constantly adjusted by a feedback loop to keep the current constant. The measured values of either I or z are used to generate a 2D graphical representation of the surface structure [74]. The tunnelling current depends not only on the sample-tip distance but also on the chemical species that the tip is probing, through the density of states.

Valuable information about the electronic Density of States (DOS) can also be obtained from Scanning Tunnelling Spectroscopy (STS). According to the Bardeen's formalism and assuming a constant DOS for the tip, from Eq. (2.66) its first derivative can be written as:

$$\frac{dI}{dV} \propto \rho_S(E_F - eV) \quad (2.53)$$

Thus, DOS near the Fermi level can be determined directly by analysing the first derivative of the tunnelling current. To obtain dI/dV spectra experimentally, the lock-in technique is utilised to extrapolate the signal of interest, which is the first derivative of the tunnelling current. STS measurements are generally carried out by placing the tip over a surface site of interest before switching off the feedback loop and ramping the voltage while recording the signal from the lock-in amplifier.

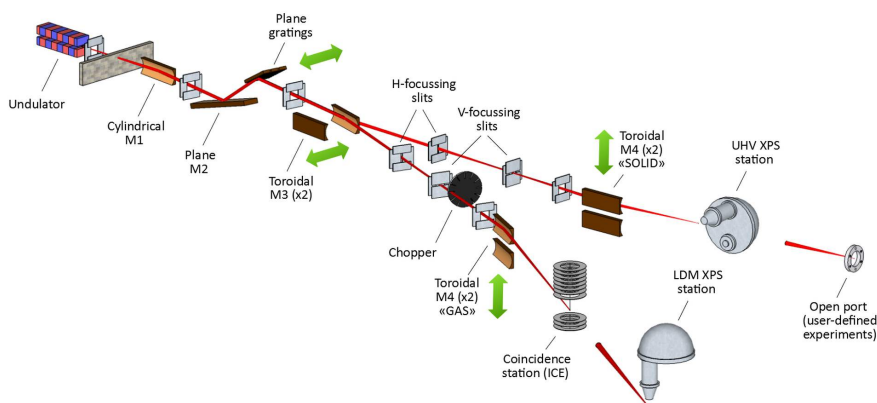


Figure 2.15: Schematic layout of the beamline optics.

2.4 Laboratories

2.4.1 The FlexPES beamline at MAX IV

The XPS and NEXAFS data relative to the B/Al(111) system presented in this thesis were collected at FlexPES (Flexible PhotoElectron Spectroscopy) beamline of the MAX IV Synchrotron located in Sweden.

The FlexPES beamline offers the possibility to perform a variety of photoemission and soft X-ray absorption experiments in the photon energy range 40-1500 eV. The photon source is a linearly-polarising undulator with 48 full periods and a maximum effective field of 0.8 T. The optical scheme, depicted in Fig. 2.18, is based on the collimated plane-grating monochromator (cPGM), astigmatic intermediate focus and switchable refocusing mirrors. The maximum beamline acceptance is 0.62 mrad x 1.36 mrad (h x v) and corresponds to full illumination of M1. Acceptance can be reduced using movable masks in the front end and/or baffles in front of the monochromator.

FlexPES beamline consists of two experimental stations, the Surface & Material Science (SMS) branch and Low Density Matter (LDM) Branch. We used the SMS branch, where there are two focal points; the first one is inside the permanent UHV end station (called EA01), which is used for studying various on-surface processes. The second focal point (2.5 m downstream) is on an open port (called EA02), which is reserved for user-provided end stations. The permanent UHV end station EA01 on the SMS branch is dedicated to photoelectron and x-ray absorption spectroscopy studies on surfaces and thin films.

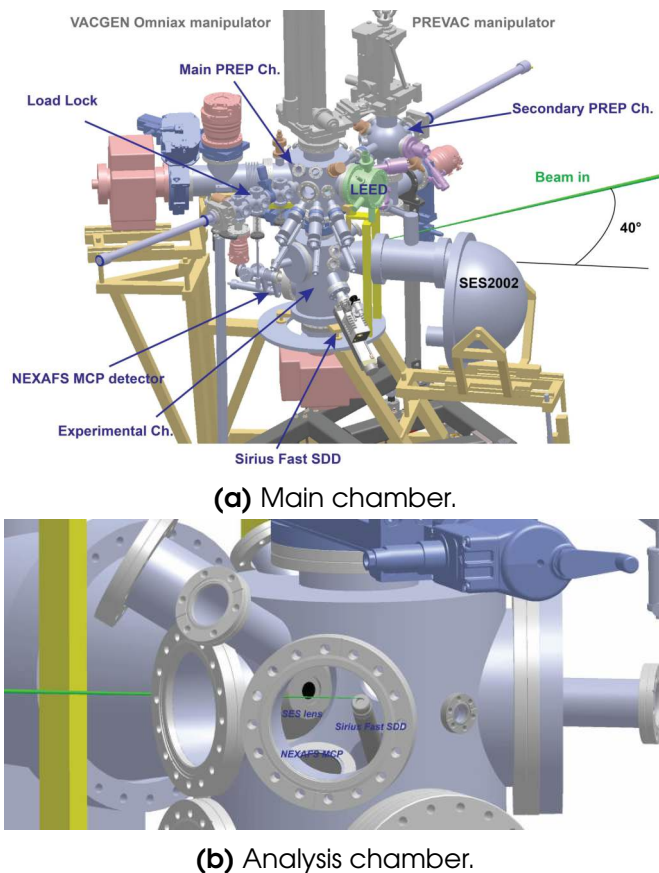


Figure 2.16

It comprises four chambers: an analysis chamber with detectors, two preparation chambers with sample transfer and treatment facilities, and a fast entry chamber with a sample garage.

2.4.2 The PEARL beamline at P.S.I.

The XPS and STM data relative to the B/Ni₃Al(111) system presented in this thesis were collected at PEARL (Photoemission and Atomic Resolution Laboratory) beamline of the SLS (Swiss Light Source) Synchrotron located at the Paul Scherrer Institute (PSI) in Switzerland.

The PEARL beamline is installed at a 1.4 T bending magnet X03DA which delivers a smooth photon spectrum with a critical energy of 5 keV. The main polarisation mode of the bending magnet is linear horizontal. By tilting the trajectory of the stored electron beam, the polarisation can be switched to elliptical. The

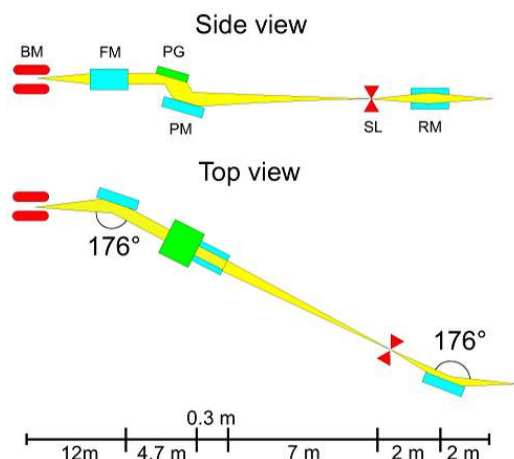
PEARL optics, which is schematically depicted and 3D rendered in Fig. 2.20, is designed for the 100-2000 eV photon energy range, covering the core-level XPS lines of most chemical elements. The beamline should deliver high photon flux at photon energies between 500 and 1000 eV. For measurements with chemical state specificity, the energy resolution should be tuneable to at least 0.1 eV in this energy range.

The experimental station, depicted in Fig. 2.20 is divided into three sub-systems: one (attached to the beamline) for the photoemission measurements, one for scanning tunnelling microscopy and one for surface preparation. All processes and measurements take place in UHV at a base pressure below 2×10^{-10} mbar. The sub-systems are connected by a reliable in situ sample transfer system. The sample preparation system provides standard surface science techniques for preparation (ion bombardment, annealing by radiative heating) and characterisation (LEED, AES, RGA). The low-temperature STM provides real-space sample characterisation down to atomic resolution. The photoemission station is designed as a state-of-the-art ARPES facility with a *Carving 2.0* six-axis manipulator designed by PSI and Amsterdam University, and a Scienta EW4000 hemispherical electron analyser with 2D detection.

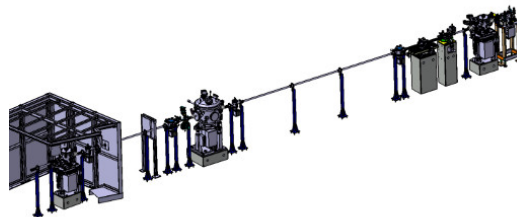
2.4.3 The IR-Vis SFG laboratory

The SFG, LEED and AES measurements presented in this thesis were performed at the Visible and Infrared Spectroscopy Laboratory (VISpLab, University of Trieste). Samples are prepared in a UHV chamber and SFG spectra are taken in a high-pressure cell. In order to obtain a reliable surface characterisation, it is important to prepare the samples in a controlled environment to prevent contamination both during the preparation and the measurements.

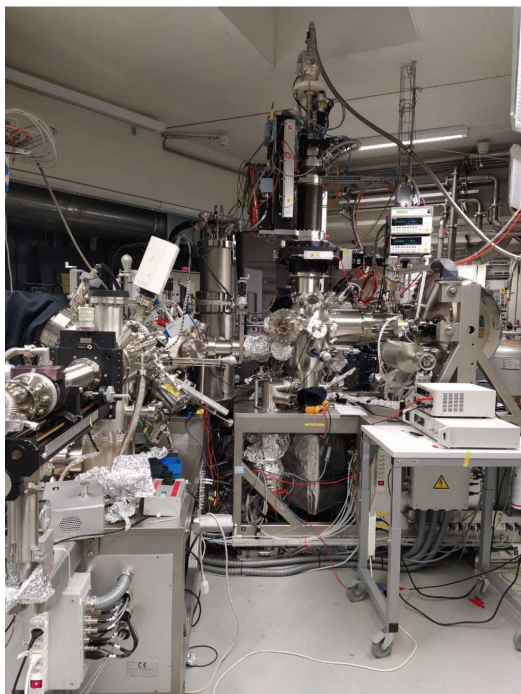
The experimental chamber, depicted in Fig. 2.21, consists of a cylindrical amagnetic stainless steel UHV chamber with 30 cm diameter, a pumping section and a high-pressure cell (HP cell) designed for the SFG experiments. The three sections are made independent through gate valves. The pumping section is located below the preparation chamber and hosts a cryogenic pump (10) coupled with a titanium sublimation pump, and an ion pump (12). The preparation chamber is also pumped by a turbo molecular pump (4), prepumped by a diaphragm pump. When the gate valve between the preparation chamber and the pumping section is opened, a background pressure of 5×10^{-11} mbar can



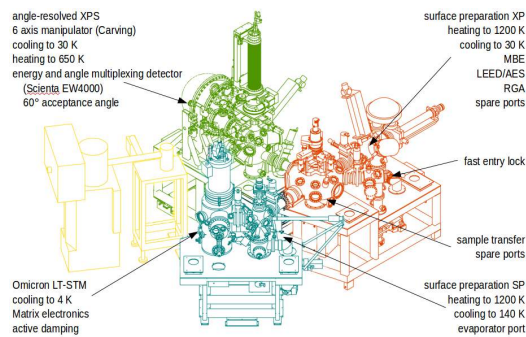
(a) Schematic layout of the beamline, showing the optical path of the X-rays from the bending magnet to the end-station. The principal optical elements are: bending magnet (BM), focusing mirror (FM), plane grating (PG), plane mirror (PM), exit slit (SL), refocusing mirror (RM).



(b) 3D rendering of the optics segment of the beamline. The X-rays from the synchrotron enter the beamline from the left hand side. The major components (on concrete supports) are, from left to right: Focusing mirror, monochromator, exit slit, gas cell (diagnostics), refocusing mirror. The beam exits on the right side to the experimental station (not shown).



(c) The experimental station at PEARL.



(d) Conceptual rendering of the end-station. The three substations for angle-resolved photoelectron spectroscopy and diffraction (XPS/XPD, green), scanning tunneling microscopy (LT-STM, blue) and surface preparation (red) are connected to a central, rotary sample transfer under UHV. The synchrotron radiation (SR) enters the XPS/XPD station along the path marked by an arrow.

Figure 2.17

be achieved. The presence of a fast entry lock loading system (5) allows the sample loading into the UHV system without breaking the vacuum. It is independently pumped by a turbomolecular pump coupled with a backing pump (11) for the pre-pumping (we will refer to this pumping group as turbo pumping station), that grants a background pressure lower than 10^{-8} mbar.

A magnetic transfer arm (7) is employed to load (or unload) the sample-holder from the fast entry lock and the two manipulators (the preparation chamber's one and the one present in the HP cell). The sample-holder allows to heat the sample up to 1300 K in UHV and 700 K at 1 bar by means of resistive heating. The sample is caged by a tantalum wire (0.2 mm diameter) fitting in a slot on the sample's side. Such configuration minimises the mechanical stress due to the wire thermal expansion and contraction, thus reducing the probability of sample damage during heating and cooling. The sample's temperature is measured via a K-type chromel-alumel thermocouple spot-welded at the back of the sample.

The HP cell is located behind the preparation chamber and coupled with the SFG box. It consists of a steel cylinder (6 cm diameter) and two barium fluoride (BaF_2) windows that allow the transmission of the visible, IR and SFG radiation with nearly 100% efficiency. They can sustain a pressure difference up to 1 bar. IR and visible beams are not at normal incidence with respect to the window, in order to avoid back reflection into the SFG setup (that may damage the optics). The cell is equipped with its own manipulator that provides (x,y,z) translations, polar rotation and the possibility to tilt the sample. Pressure is measured through a full range gauge (FRG) working in the 5×10^{-9} - 10^3 mbar range, that is made of a cold cathode gauge and a pirani gauge connected in series. A gas line, which can handle up to three different gases, is present. The SFG cell can be independently pumped by the scroll pump (9) and by the turbo pumping station (11).

As said before, the preparation chamber is dedicated to the preparation and characterisation of samples. It is equipped with a LEED (low energy electron diffraction) setup (6) and an AUGER electron spectroscopy setup. A mass spectrometer (2), an ion gun (used to sputter the sample) and a gas line (8) are also present. The pressure is measured using an ion gauge working in the range 3×10^{-11} - 10^{-3} mbar. The top part of the preparation chamber ends with the manipulator (1) that provides four degrees of freedom: the three translations (x,y,z) and the polar rotation.

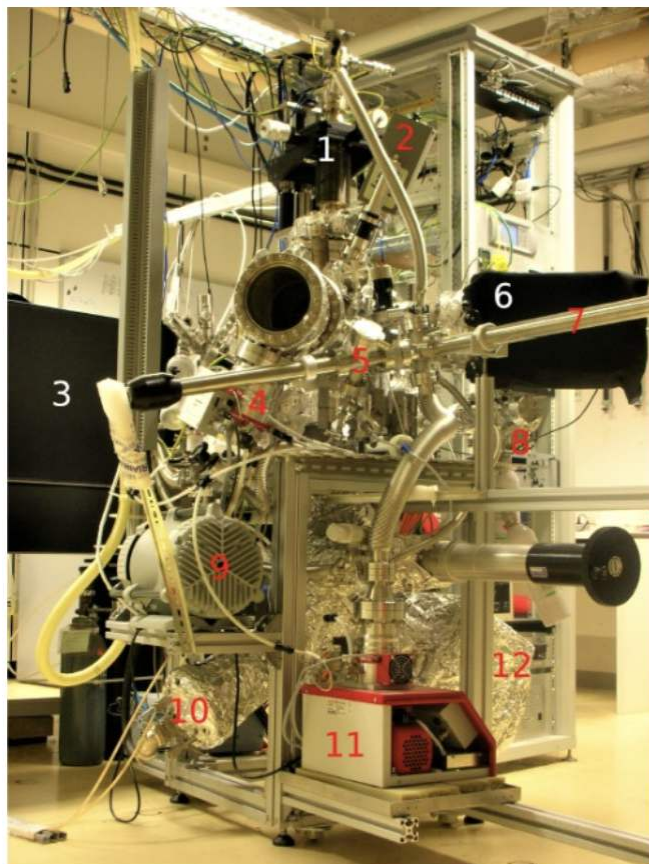


Figure 2.18: Overview of the preparation chamber, equipped with: (1) a manipulator, (2) a mass spectrometer, (4) a turbo molecular pump, (5) a fast entry lock loading system, (6) a LEED setup, (7) a transfer arm, (8) a gas line, (9) a scroll pump, (10) a cryogenic pump, (11) a turbo pumping station and (12) a ionic pump. The SFG box (3) can also be seen.

2.4.4 The SIXS beamline at SOLEIL

The SXRD data presented in this thesis were collected at SixS (Surfaces interfaces x-ray Scattering) beamline of the SOLEIL Synchrotron radiation facility, Gif-Sur-Yvette, France.

SixS is a wide-energy range (5 -20 keV) beamline dedicated to structural characterisation of surfaces, interfaces (solid-solid or solid-liquid), as well as nano-objects in controlled environments by means of many surface-sensitive x-ray scattering techniques. The SixS optics layout is schematically depicted in Fig. 2.22. SixS beamline consists of two experimental stations: the multi-environment diffractometer (MED) can accommodate various sample environments, such as high-pressure reactivity chambers, electrochemical cells, Langmuir troughs. It allows for vertical and horizontal diffraction geometry for surface-interface diffraction. The UHV endstation, exploited in this thesis work, is equipped with a z-axis diffractometer, depicted in Fig. 2.23, and a two-dimensional hybrid pixel detector (XPAD S140) to collect the scattered radiation intensities. This endstation has a unique design, consisting of an assembly of three chambers equipped with the standard UHV tools (evaporators, ion-guns, etc.) and specific instruments (STM, LEED, AES).

2.4.5 STRAS Laboratory

The STM measurements presented in this thesis have been performed at the STRAS laboratory at CNR-IOM laboratories in Trieste, in the groups of prof. G. Comelli. In particular, the STM instrument used was a commercial Omicron scanning tunnelling microscope operating at low temperature (LT-STM).

The LT-STM is basically an STM designed for working at very low temperatures, allowing to carry out stable imaging and spectroscopy of the sample surface. The system is formed by a preparation chamber separated from the STM chamber by a gate valve. The preparation chamber is pumped by a turbo pump together with an ion pump equipped with a titanium sublimation cartridge and a liquid nitrogen cooled cryopanel, keeping the vacuum in the low 10^{-10} mbar range. The vacuum in the STM chamber is maintained in the range of 10^{-11} mbar through an ion pump.

The experimental setup, depicted in Fig. 2.24 consists of a commercial Omicron LT-STM with a dedicated UHV chamber equipped with a carousel where tips and samples can be stored, retrieved and inserted into the LT-STM

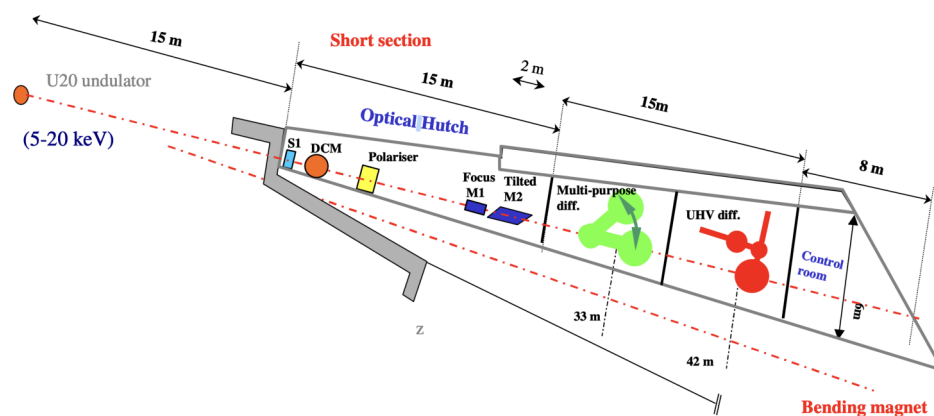


Figure 2.19: Scheme of SixS beamline at SOLEIL Synchrotron.

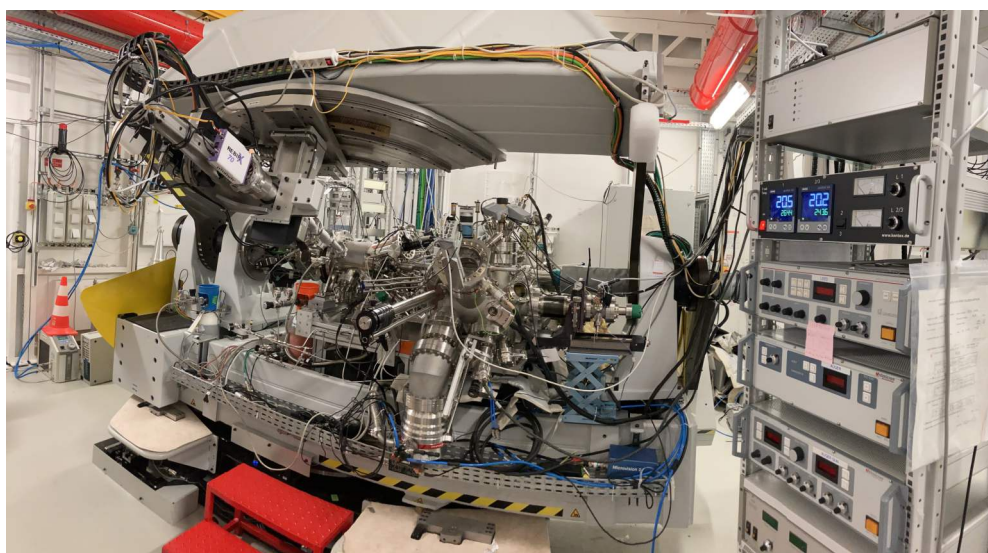


Figure 2.20: SixS beamline at SOLEIL Synchrotron facility.

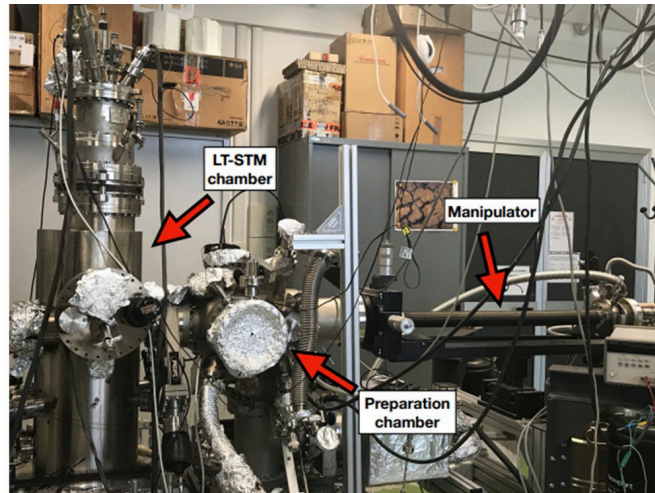


Figure 2.21: The STRAS Laboratory experimental setup: commercial Omicron LT-STM and preparation chamber.

using a wobble stick. To prevent any stray radiation from causing a rise in the temperature of the sample, the optical access windows of the chamber have been equipped with infrared filters. The Omicron LT-STM head accommodates a piezoelectric hollow cylinder made of a single tube, with the tip fixed at the top. The cylinder is divided into four quadrants by four electrodes, and by administering an appropriate voltage difference between the quadrants and the inner electrode, the piezoelectric cylinder can be bent to scan the tip across the sample (x-y plane) with sub-angstrom resolution. Furthermore, the scanning tunnelling microscope (STM) tip can be moved orthogonally to the surface of the sample in the z-direction by applying a voltage difference between the inner and outer surfaces of the cylinder. To ensure mechanical isolation, the STM head can be suspended using three springs. Additionally, an eddy current damping system is employed to effectively and smoothly dampen any possible low frequencies.

Chapter 3

Borophene Growth

In this chapter, a detailed description of the growth process of B-based bidimensional nanostructures on two selected metal surface terminations, specifically Al(111) and Ni₃Al(111), is provided. The as-grown materials were thoroughly characterised both structurally and electronically in a multi-technique experimental approach by means of XPS, NEXAFS, STM/STS, with a particular interest in investigating the intricate interplay between B and Al alloying and segregation, which subsequently leads to the formation of a range of B and B-Al polymorphs.

3.1 B/Al(111)

3.1.1 Sample Preparation

The clean Al(111) substrate was prepared by repeated cycles of Ar⁺ sputtering ($I_{\text{sputt}} = 10 \mu\text{A}$, $t = 10'$, $E_{\text{sputt}} = 1 \text{ keV}$) followed by annealing at about 600 K. Elemental Boron was evaporated from a pure boron rod of 5 mm diameter (Goodfellow) heated by electron bombardment, exploiting a homemade evaporator, (depicted in Fig. 3.1) in a residual background pressure in the range of 10^{-10} mbar. The B deposition rate was kept in a range between 0.05 and 0.20 ML/min by monitoring B coverage via a combination of LEED, XPS, and AES measurements. During B evaporation the sample was held at 500 K. The crystalline quality of both the Al surface and the B layer was checked by monitoring the LEED diffraction pattern. As shown in Fig. 3.2, the clean aluminium surface produced a clear (1 x 1) diffraction pattern with minimal background signal.

Upon boron evaporation, it was shown by *Preobrajenski et al.* [17] that the B layer is so strongly coupled to the substrate that the terminal Al layer is substantially involved in the formation of the hB phase, yielding a coupled AlB_2 superlattice with triangular symmetry and a coincidence supercell spanning over $(24 \times 24)/(25 \times 25)$ unit cells of the $\text{AlB}_2/\text{Al}(111)$ lattices, respectively. The LEED diffraction pattern undergoes significant changes following B evaporation, revealing additional spots indicating the formation of the AlB_2 lattice, encircled by further spots related to the moiré coincidence superstructure produced by the lattice mismatch between the overlayer and the underlying Al surface. The lattice parameters of the AlB_2 layer and the generated moiré superstructure were determined by accurately analysing the LEED diffraction pattern, with $a_{\text{AlB}_2} = 2.975 \pm 0.010 \text{ \AA}$ and $a_s = 7.5 \pm 0.6 \text{ nm}$, respectively. Our results are consistent with those reported in the literature [15–17], thus confirming the formation of the AlB_2 moiré superstructure.

When the evaporation rate is increased, additional spots are observed in the LEED pattern (red arrows in Fig. 3.2c). In particular, the supplementary configuration exhibits a 30° rotation, yet displays a reciprocal lattice vector in accordance with that of the $\text{Al}(111)$ surface termination.

3.1.2 XPS and NEXAFS

The investigations of electronic core levels and of X-Rays absorption edges, by means of XPS and NEXAFS techniques, are essential to reveal the chemical bonding environment of selected atomic species in the system. In this section, the analysis of the B 1s and Al 2p core levels and of the B 1s absorption edge are reported for the $\text{AlB}_2/\text{Al}(111)$ system. The dissection of the system electronic structure was crucial in order to provide experimental evidence of the theoretically predicted large charge transfer from the Al substrate to the hB system [8, 15, 17, 75] and to characterise the B atoms chemical environment in the B-based



Figure 3.1: Homemade evaporator, exploiting electron bombardment of a solid B rod from a tungsten filament, limited by a Wehnelt and isolated by a Tantalum screen.

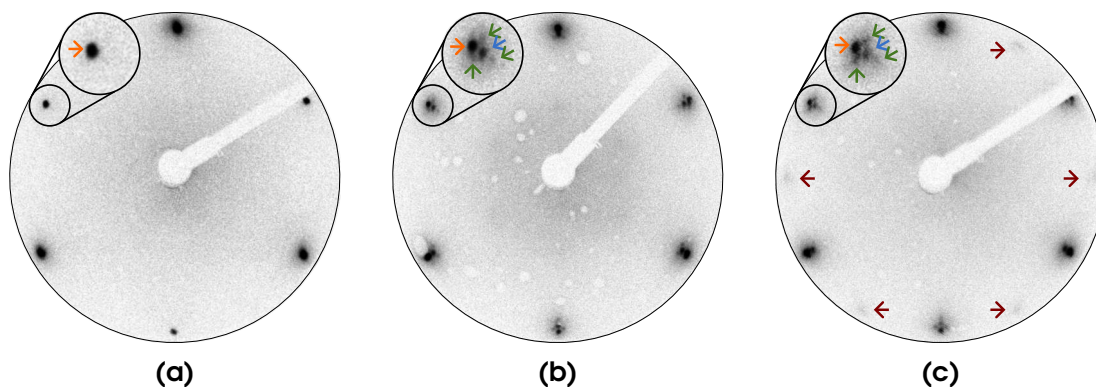


Figure 3.2: LEED diffraction patterns, corresponding to an electron energy of 47.5 eV, of the clean Al(111) surface (a) and of the AlB₂/Al(111) system obtained tuning the boron deposition rate to 0.05 (b) and 0.15 (c) ML/min. The arrows indicate the diffraction spots of the Al(111) surface (yellow), the AlB₂ layer (blue) and the moiré superstructure (green).

structures. In addition, these results will be used as a starting stage in order to understand the behaviour and the reactivity of the AlB₂/Al(111) system when it's exposed to ubiquitous gases as molecular oxygen and atomic hydrogen (See Sec. 4.1 and 4.2). The data presented in this section have been acquired at the FlexPES beamline at the MAX IV Synchrotron facility in Lund (Sweden).

B 1s

Figure 3.3a shows the B 1s core level photoemission spectrum collected at room temperature for the AlB₂/Al(111) system together with its best fit curve and the corresponding deconvolution profiles for each spectral components. The best fitting parameters are reported in Appendix A.1.

As already reported by *Preobrajenski et al.* [17], the formation of a second layer of AlB₂ starts before the first layer is complete. Due to this, the B 1s core level spectrum is characterised by three spectral components, at 187.76 (B₁), 187.47 (B₂) (-0.29), and 187.10 (B₃) (-0.66) eV, originating from the B atoms involved in the AlB₂ multilayered structure. In particular, the B atoms forming a single AlB₂ layer contribute to the B₁ component, which is the predominant one as expected for B coverages lower than 2 ML. By contrast, the B₂ and B₃ components originate with the formation of a second AlB₂ layer and are associated with B atoms in the topmost layer, which is elevated due to the presence of a B underlayer, and with the latter B underlayer itself, respectively. The balls model in Fig. 3.3a

depicts the system atomic structure, with each ball color reflecting the color of the corresponding component in the spectra. At higher binding energies the spectrum reveals a minor contribution at 188.46 (+0.70) eV, which is ascribed to residual oxygen contamination (of the order of 1% ML) interacting with B atoms. In the end, the core level deconvolution presents an additional component, namely BH, at 187.27 (-0.43) eV, associated with reduced B atoms, which intensity is compatible with zero, as indicated by the displayed error bar.

Al 2p

Figure 3.3b shows the Al 2p core level photoemission spectrum collected at room temperature for the $\text{AlB}_2/\text{Al}(111)$ system, together with its best fit curve and the corresponding deconvolution profiles for each spectral component. In the figure is presented also the XPS spectrum for the clean Al(111) system. The best fitting parameters are reported in Appendix A.1.

While the spectrum from clean Al(111) shows just a single spin-orbit doublet, namely Al_1 , with the $2p_{3/2}$ component at 72.70 eV, upon B evaporation the spectrum revealed two additional doublets, Al_2 and Al_3 , with the $2p_{3/2}$ components at 73.30 and 73.92 eV, respectively. The spin-orbit splitting was left free to vary, but constrained to the same value among all the doublets, and turned out to be equal to 0.41 eV. The Al_1 doublet, present in both the $\text{AlB}_2/\text{Al}(111)$ and pristine spectra, is associated with the contribution from bulk Al atoms, while the Al_2 and Al_3 doublets, which grow upon B evaporation, are associated with Al atoms consisting the topmost and buried AlB_2 layers, respectively. The balls model in Fig. 3.3b depicts the system atomic structure, with each ball color reflecting the corresponding component in the spectra.

B K-edge

Figure 3.4 shows the B K-edge NEXAFS spectra collected at room temperature for the $\text{AlB}_2/\text{Al}(111)$ system. The data, collected in the partial electron yield mode, are depicted as a function of the angle between the electric field of the impinging, linearly polarised X-ray radiation and the normal to the surface. The dichroic behaviour of the system can be further appreciated by examining the difference spectrum obtained from the 70° and 20° spectra. All NEXAFS spectra are normalised to the incident photon intensity and to the integral intensity under the curves.

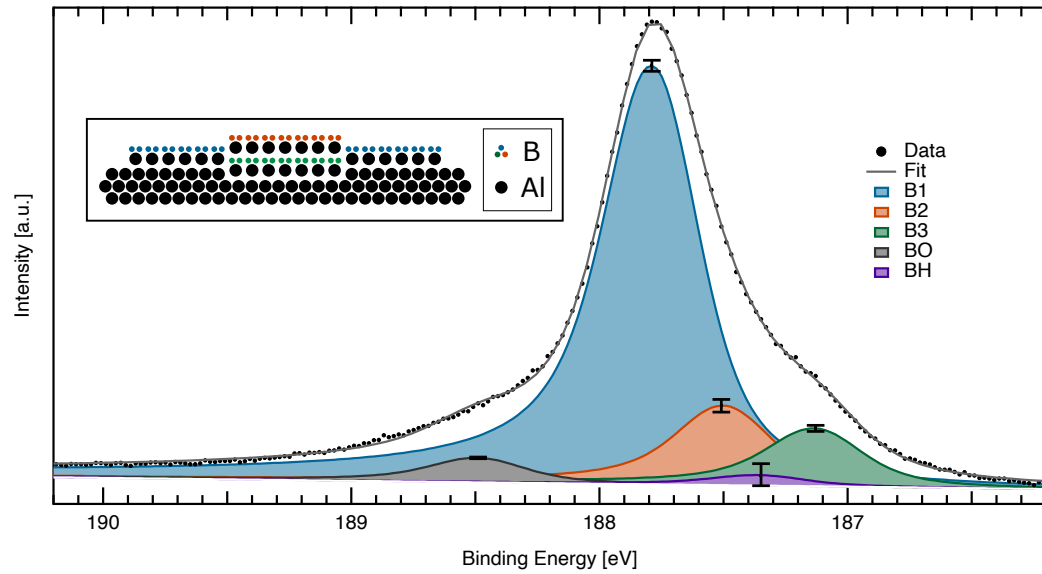
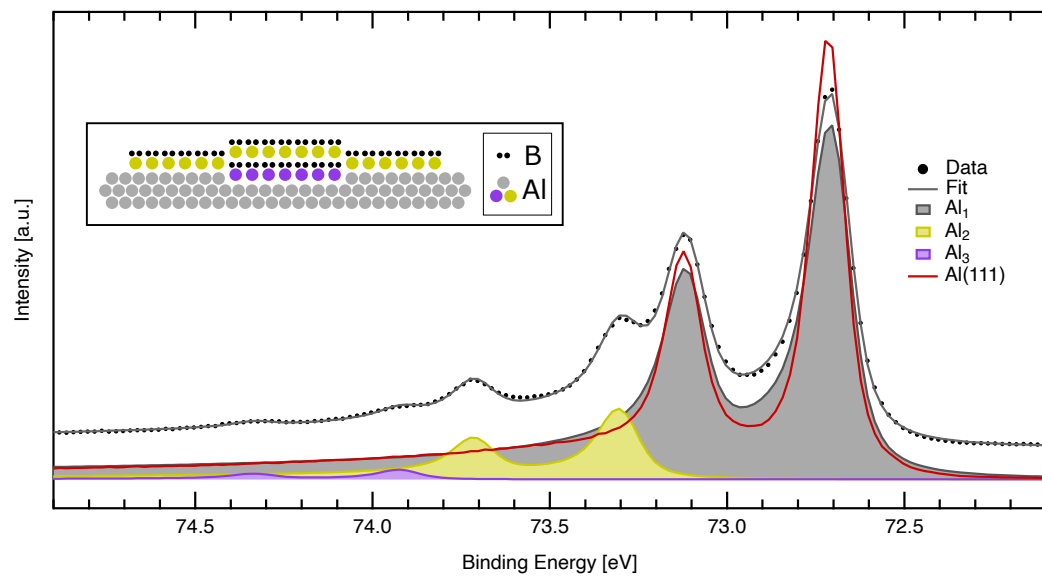
(a) B 1s XPS spectrum, $h\nu = 270$ eV.(b) Al 2p XPS spectrum, $h\nu = 150$ eV.

Figure 3.3: XPS spectra for the $\text{AlB}_2/\text{Al}(111)$ system together with their best fit curves and the corresponding deconvolution profiles for each spectral components. The accompanying structural models elucidate the colour code and component assignments with respect to the corresponding atomic species. In red the XPS spectrum for the clean $\text{Al}(111)$ system

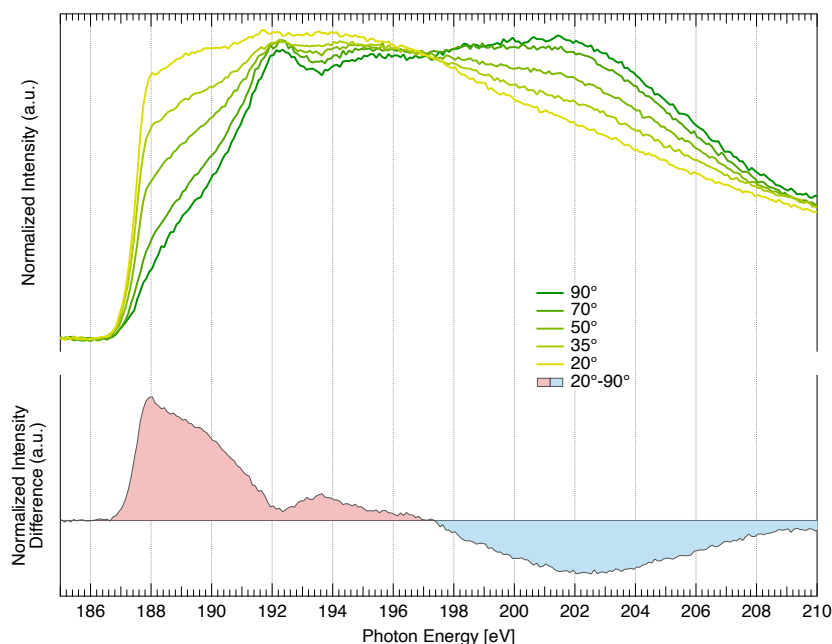


Figure 3.4: Angle-dependent NEXAFS B K-edge spectra for the $\text{AlB}_2/\text{Al}(111)$ collected in partial electron yield mode. The directions refer to the angle between the electric field of the impinging, linearly polarised X-ray radiation and the normal to the surface. The dichroic behaviour of the system can be further appreciated by examining the difference spectrum obtained from the 70° and 20° spectra.

Closer examination of the absorption spectra reveals that the intensity below 192 eV is associated with transitions from the B $1s$ level to unoccupied states with predominantly π (out-of-plane) character, and in particular a distinct feature is observed at 188.0 eV due to the $1s \rightarrow 2p(\pi^*)$ resonance. Above 197 eV, the spectra are dominated by transitions to σ -like (in-plane) states, but a sharp $1s \rightarrow 2p(\sigma^*)$ feature is yet visible at 192.4 eV, yielding an overall π^* - σ^* energy separation of 4.4 eV.

3.1.3 STM

The microscopic investigation of the system upon boron evaporation by means of STM allowed to further characterise the growth process. In particular, even with boron coverage close to 2 ML, which corresponds to a complete single layer of AlB_2 on $\text{Al}(111)$, small patches of clean Al can still be found on the sur-

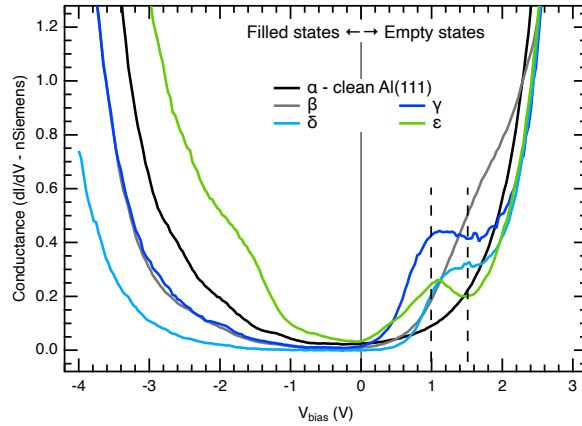
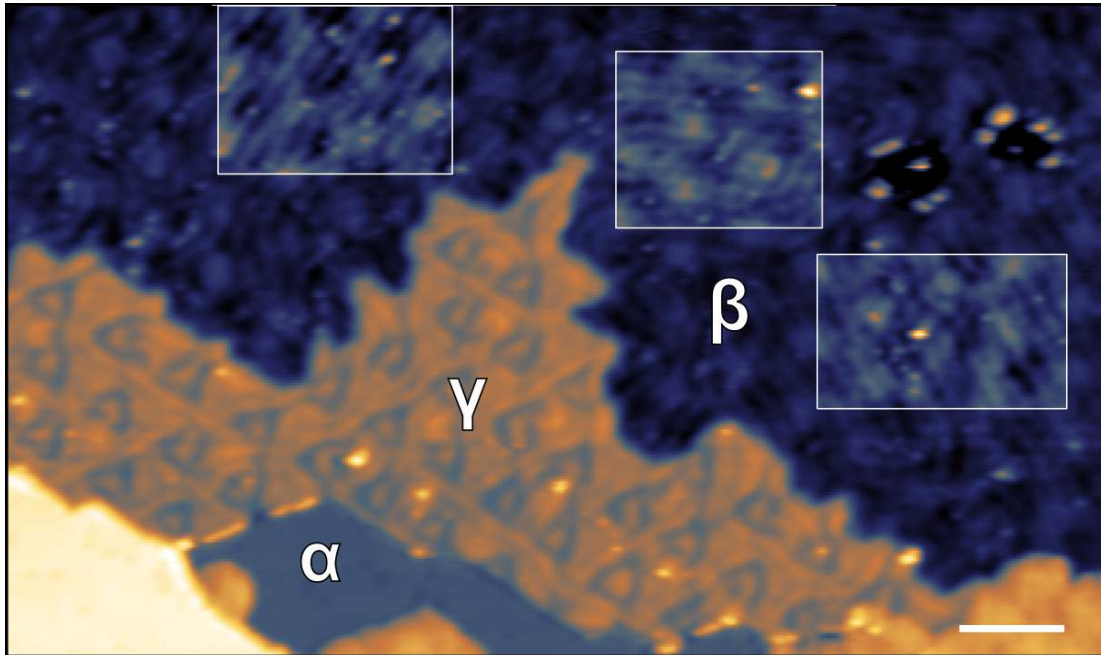


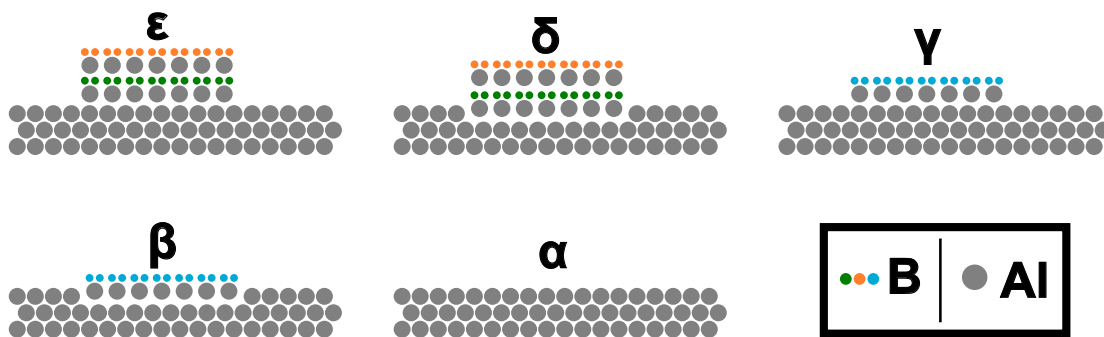
Figure 3.5: Current first derivative (dI/dV) STS data for each detected phases.

face. This is due to the previously discussed formation of a second AlB_2 layer before the first one is complete. However, in addition to clean Al patches and the AlB_2 multi-layered structure, careful inspection of the surface revealed the presence of additional, previously undiscovered, ordered phases, as shown in a selection of STM images in Figs. 3.6 and 3.7. Through adjustment of either the deposition rate or the substrate temperature during growth, it is possible to partially tune the relative abundance of the identified B-induced phases. Nevertheless, the small energy separation of the different phases and kinetic hindrance effects prevent to isolate one single phase. Consequently, we used the growth parameters that provided the best AlB_2 quality, rather than focusing on further mapping of the parameter space. Figure 3.5 presents the first derivative (dI/dV) STS data collected at each of the identified phases. Sampling different regions of the moiré pattern resulted in comparable dI/dV profiles. Thus, the depicted curves are obtained upon averaging over several sampling positions with no loss of information. Apart from the curve related to the α regions, which corresponds to clean Al terraces and correctly exhibits typical metallic behaviour, the remaining B-induced phases, indicated in the following with the letters β , γ , δ , and ϵ , can be divided in two groups by examining the electronic structure of empty states. Specifically, while the γ and ϵ structures show a distinct component at about 1 eV, in both the β and δ structures the latter state is detected at higher energy, about 1.5 eV above the Fermi Level, in the π region.

Getting into closer details of the system morphology, it can be noticed that the clean Al terraces appear as flat patches with atomic step boundaries preferentially oriented along the principal crystallographic directions. In addition,



(a) The insets highlight the alignment directions of the striped structures of the β phase; Measuring parameters: $V_{\text{bias}} = -2.0 \text{ V}$, $I = 300 \text{ pA}$, scalebar = 10 nm.



(b) Sketchy models of the various borophene phases, with B atoms colours matching the B 1s deconvolution in Fig. 3.3b.

Figure 3.6: STM imaging of the boron growth on Al(111).

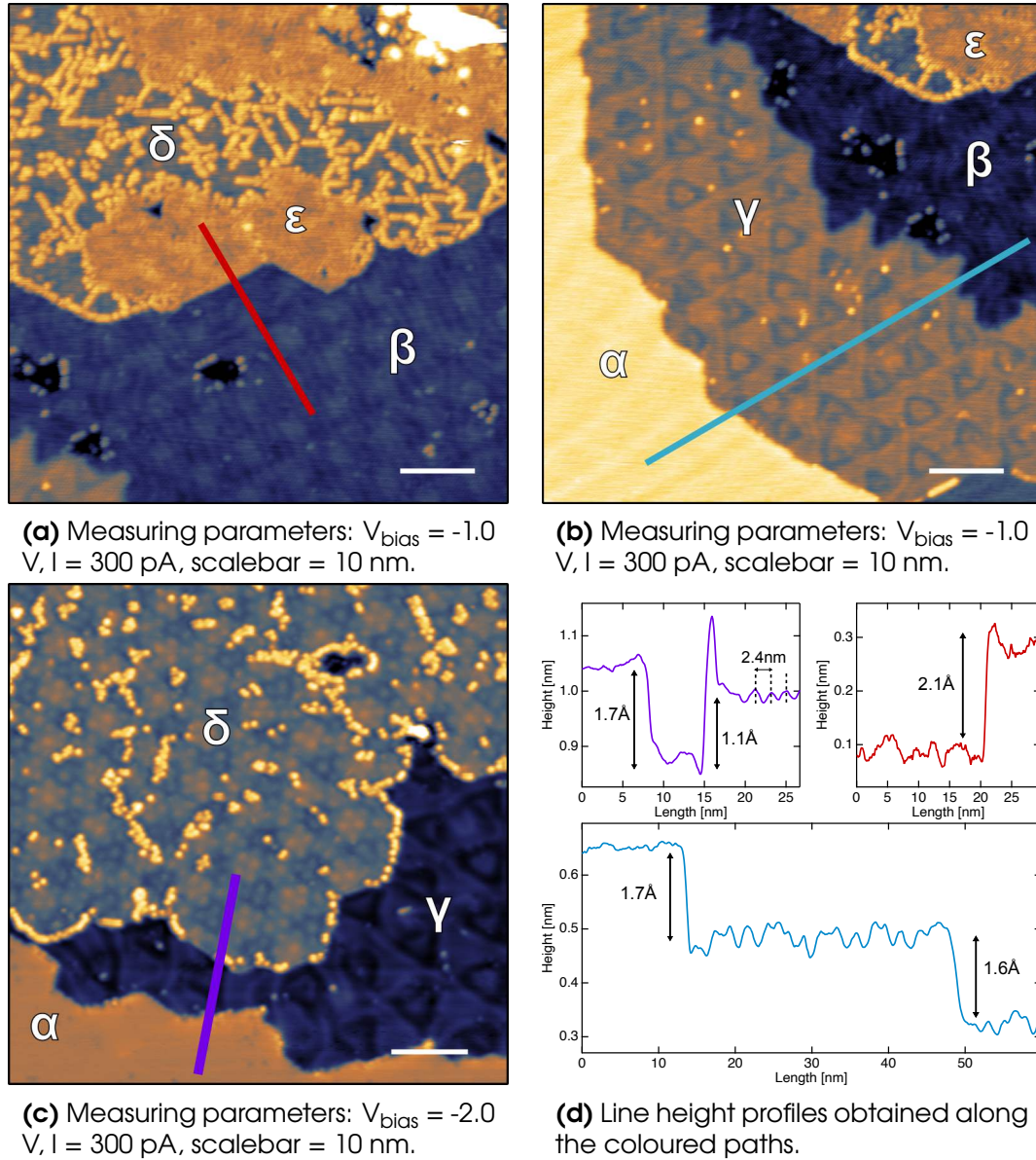


Figure 3.7: STM imaging of the boron growth on Al(111).

the characteristic and widely reported [15–17] moiré corrugation stands out in most of collected images.

Furthermore, it's worth noting that also the β phase exhibits a triangular superstructure, which, despite showing a different appearance, is related to that observed in the γ phase, as the two share the same lattice parameter and are in-phase. Moreover, the β regions include other structural features. Specifically, as highlighted by the high-contrast insets in Fig. 3.6a, this phase is characterised by the presence of 1D stripes rotated by 30° with respect to the moiré superstructure lattice. The β regions can be divided into separate domains in which all stripes are well-ordered and oriented in the same direction, with transverse periodicity of 2.0 ± 0.3 nm. The 30° angle between the stripes orientations and the main crystallographic directions suggests the association of these ordered structures with the formation of the supplementary spots detected in the LEED pattern in Fig. 3.2c although we don't have enough information to support or dismiss this hypothesis. Moreover, The physical reason behind the formation of these mono-dimensional structures is not completely clear, as they may be either related to the morphology of the system or to its local density of states. However, due to the lack of atomic resolution on this region, discrimination between the two possible explanations is not feasible.

Although the lack of atomic resolution precludes a deeper understanding of the geometric atomic structure of the B-induced phases in the system, it is still possible to propose a tentative model to explain the system's morphology and gain a better understanding of the growth process. The sketchy models in Fig. 3.6b depict the stacking arrangement of the B and Al layers in the different domains. In the framework of this interpretative picture, the γ and the ε phases are associated with the first and the second AlB_2 layers, respectively, which are widely documented in the literature. By contrast, the β and the δ phases represent previously undiscovered structures. In particular, the latter are associated with intermediate phases in the formation process of a complete and lifted AlB_2 layer. Specifically, when B is deposited on the Al surface, it readily forms the AlB_2 structure, coupling with the topmost Al layer. Nevertheless, the newly formed AlB_2 layer remains embedded in the surface, prevented from releasing the strain generated by the increasing lattice constant of the topmost Al layer [17]. This frustrated phase is associated with the previously described β domain, which suggests to interpreting the above-mentioned stripes as strain-releasing structures.




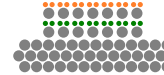
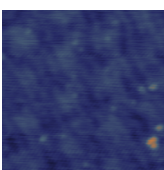
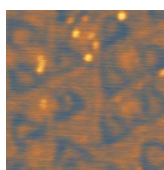
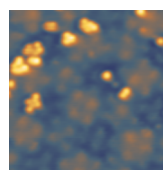
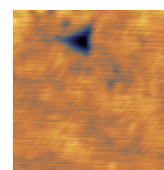
	β	γ	δ	ϵ
Heights	$1.6 \pm 0.1 \text{ \AA}$	$3.2 \pm 0.1 \text{ \AA}$	$4.3 \pm 0.1 \text{ \AA}$	$6.4 \pm 0.1 \text{ \AA}$
Ball Model				
Appearance				

Table 3.1: Heights of the different phases with respect to the underlying Al(111) termination together with the corresponding ball models and phase appearances.

Consistently, the δ phase is associated with the formation of a second (intercalated) B layer, namely AlB_2/B . In fact, this region displays both the $(24 \times 24)/(25 \times 25)$ moiré pattern, which coincides with the one of the AlB_2 , and a finer, well-evident corrugation with a periodicity of 2.4 nm. Again, we think that, in analogy to structure β , in the case of γ the strain at the $\text{AlB}_2/\text{AlB}_2/\text{Al}(111)$ interface is not yet released while, finally, a complete $\text{AlB}_2/\text{AlB}_2$ double-stack appears (ϵ) upon the complete lifting of γ .

The investigation of the relative heights among the different regions provides further evidences in support of this interpretative model. Figure 3.7d depicts the step profiles collected along the coloured paths in Figs. 3.7a–3.7c. By carefully examining the step profiles, we estimated the heights of the different phases with respect to the underlying Al(111) termination. The results are presented in Table 3.1, along with the corresponding ball models and appearances, to provide a comprehensive overview. It's worth notice that the measured height values for the γ and ϵ phases are compatible with the formation of one and two honeycomb AlB_2 layers, respectively. By contrast, the measured height values for the β and δ phases turned out to be roughly half of the latters (1.6 vs 3.2 \AA and 4.3 vs 6.4 \AA), supporting the interpretative model presented above.

3.2 B/Ni₃Al(111)

As discussed in the previous section, using the Al(111) surface termination as substrate, B evaporation resulted in the formation of an AlB₂ layer, a quite far situation with respect to the growth of an appealing quasi-freestanding borophene monolayer. By exploiting Ni₃Al(111) termination as substrate, instead of the pure aluminium, we would impact the charge transfer process between the substrate and the boron overlayer, due to the reduced fraction of Al atoms involved in electron doping compared to pure aluminium and to the considerably different electronic and geometric structure of this surface termination. As will be presented in the following section, this results in the formation of novel intriguing B-based 2D structures.

3.2.1 Sample preparation

The clean Ni₃Al(111) substrate was prepared by repeated cycles of Ar⁺ sputtering ($I_{\text{sputt}} = 10 \mu\text{A}$, $t = 10\text{-}15'$, $E_{\text{sputt}} = 2.5 \text{ keV}$) followed by annealing at about 1100 K. Exposure cycles to O₂ have been added in between the cleaning cycles in order to reduce sample contaminants such as carbon and its compounds. Elemental Boron was evaporated by PVD following the recipe described above for the Al(111) termination (see Sec. 3.1.1). The B deposition rate and the B coverage were monitored by means of AES or XPS.

3.2.2 LEED

A preliminary structural characterisation of the B/Ni₃Al(111) system was achieved by using LEED. In particular, Figure 3.8 displays two LEED diffraction patterns, corresponding to an electron energy of 60 eV, acquired before and after boron evaporation. The two LEED images exhibit well-defined diffraction spots with distinct intensity contrast against the background, providing evidence for the long-range chemical and structural order of the clean Ni₃Al(111) surface. Upon B evaporation, the LEED diffraction pattern does not undergo any macroscopic substantial modification. In particular, the persistence of sharp diffraction spots demonstrates the formation of well-ordered B structures on the surface. Otherwise, if the boron overlayer lacked any well-defined order, deposition of almost 2 ML of B on the surface would significantly deteriorate the LEED diffraction pattern. Furthermore, no new diffraction features can be

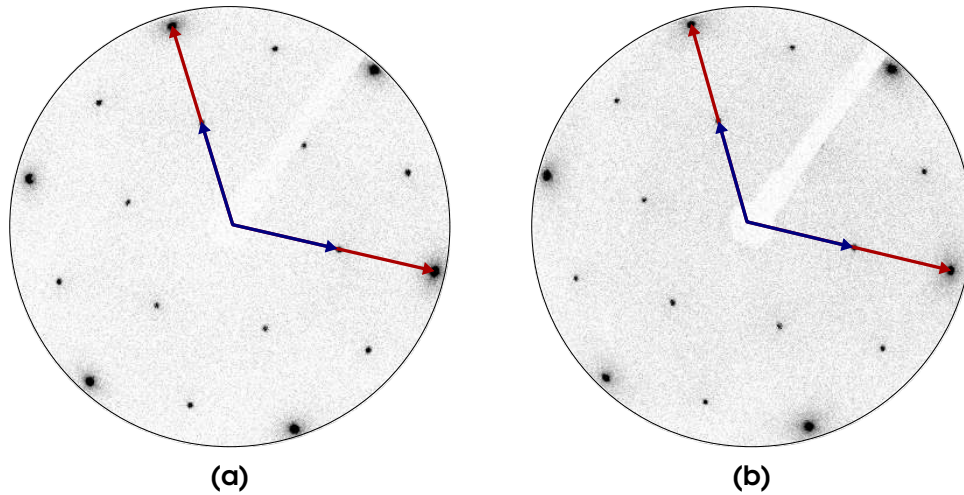


Figure 3.8: LEED diffraction patterns, corresponding to an electron energy of 60 eV, of the clean $Ni_3Al(111)$ surface before (a) and after (b) evaporation of an estimated boron coverage of 2 ML. The red and blue arrows indicate the reciprocal lattice vectors of the (1×1) and (2×2) structures, respectively.

detected upon evaporation, indicating that the boron layer is completely commensurate with the substrate. This implies that the symmetry and periodicity of the boron superstructure are analogous to that of the $Ni_3Al(111)$ substrate. In particular, after boron evaporation, the (2×2) LEED pattern persists, remaining almost completely intact, suggesting that the lattice formed by the boron atoms follows the (2×2) symmetry. Nevertheless, at this preliminary stage, we cannot exclude the formation of a boron superstructure commensurate to the (1×1) substrate structure with the (2×2) diffraction signal due to the underlying substrate structure or to patches of clean $Ni_3Al(111)$.

While the aforementioned observations stand true for LEED images gathered over an extensive energy range ranging from 40 to 200 eV, at some specific electron energies we have detected some slightly variations in the relative intensity of non-equivalent spots upon B evaporation. Indeed, Figure 3.9 depicts two LEED diffraction pattern, corresponding to an electron energy of 47 eV, acquired before and after boron deposition. The difference in the relative intensity of the (2×2) diffraction spots can be noticed upon direct inspection of the diffraction pattern but it's confirmed by examining the intensity profiles along the marked directions presented in the bottom insets of fig.3.9. Nevertheless, the implication of this detail is not immediately clear, and a qualitative analysis of LEED images does not provide conclusive evidence. Additionally, this qualitative analysis is

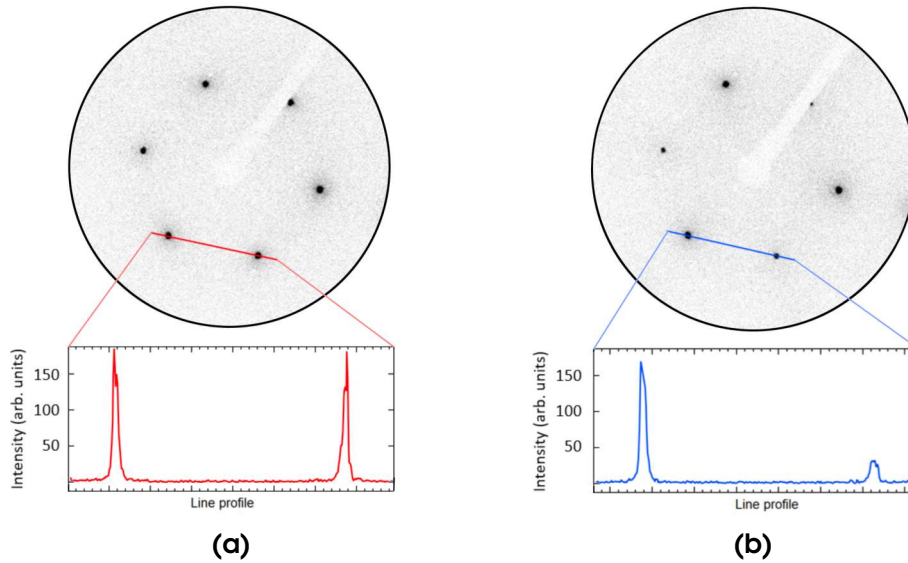


Figure 3.9: LEED diffraction patterns, corresponding to an electron energy of 47 eV, of the clean $\text{Ni}_3\text{Al}(111)$ surface before (a) and after (b) evaporation of an estimated boron coverage of 2 ML. In the insets at the bottom the intensity profiles along the marked paths, which intersect the (2×2) structure diffraction spots.

unable to provide exact details regarding the atomic structure of the surface system, including the adsorption sites and the chemical environment of boron atoms. In order to obtain a precise determination of the actual structure of $\text{B}/\text{Ni}_3\text{Al}(111)$ we performed additional measurements with a local surface science technique such as STM.

3.2.3 STM

Microscopic examination of the $\text{B}/\text{Ni}_3\text{Al}(111)$ system, exploiting STM, allowed further insight into the atomic structure of the B layer and its growth process. The data presented in this section have been acquired at liquid Helium temperature exploiting a LT-STM available at the PEARL beamline at the SLS (P.S.I.) in Villigen (Switzerland). Boron was evaporated on the $\text{Ni}_3\text{Al}(111)$ substrate, cleaned as described in Sec. 3.2.1, in UHV conditions at a deposition rate of 0.07 ML/min, for a deposition time $t = 10'$ and the substrate held at 495 K, for an overall boron coverage of 0.7 ML.

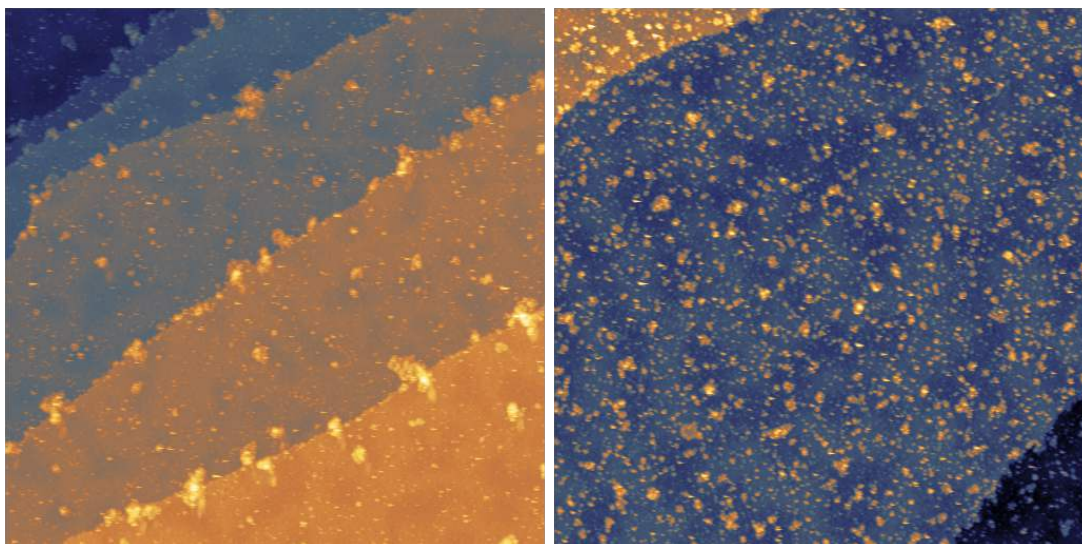
Figures 3.10a and 3.10b present large-scale STM images of the $\text{B}/\text{Ni}_3\text{Al}(111)$

surface. As can be noticed, the sample exhibits large and flat atomic terraces, as suggested by the quality of the LEED diffraction pattern analysed in Sec. 3.2.2. Nevertheless, it is important to note that the B coverage in this case is nearly a quarter of that in the LEED experiment. In fact, the morphological characteristics of the system do not seem to be homogeneous on a large scale. In particular, some wide darker islands with a size of around 10-20 nm are visible, as well as smaller bright protrusions ranging in size from less than one to five nanometers, associated with boron clusters.

Nevertheless, upon scrutinising the system on a smaller scale it becomes evident that the surface exhibits local ordering, as depicted in Fig. 3.10c. The dark islands that characterise the system at large scale are highlighted by green lines. The darker appearance of these regions is due to a fractional adsorbed carbon monoxide contamination. This assumption is supported by the XPS investigation of the system which compatibly revealed minor oxygen and carbon contaminations.

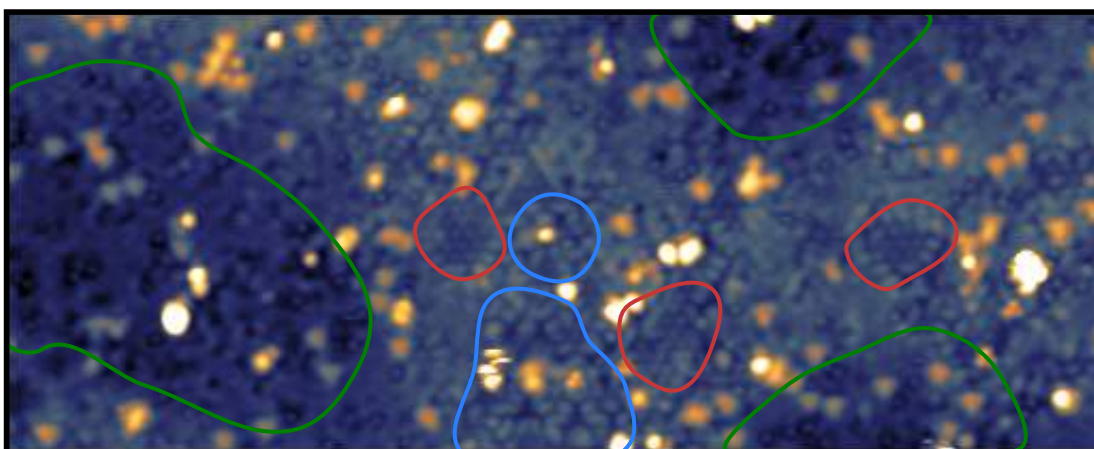
Bartels et al. [76] presented a reliable method for CO-functionalising a scanning tunnelling microscope tip by transferring a single molecule from the Cu(111) surface, and vice versa. CO molecules adsorbed on a metal surface appear as depressions with a protruding point in the centre (and a surrounding halo depending on the measuring bias) when examined with a functionalised tip. The comparison depicted in Fig. 3.11 clearly supports our identification of the darker regions of the surface as Ni₃Al(111) with fractional CO contamination. However, the adsorbed CO molecules seem to be essentially confined to these regions, hence having no impact on the growth of B-based structures in the rest of the surface, which we shall explore in the following sections.

Other distinctive features detected on the surface are some dark triangular depressions surrounded by two elongated protrusions on each side, highlighted by blue lines in Fig. 3.10c. We can ascribe these arrangements to a structure that is locally similar to the ultrathin alumina film on Ni₃Al(111), and thus to a local oxidation of the surface. The latter identification was based on the work by *Schmid et al.* [77] which determined the structure of the ultrathin ($\sqrt{67} \times \sqrt{67}$)R12.2° aluminium oxide on Ni₃Al(111) by a combination of STM and DFT. The comparison depicted in Fig. 3.12 between the Al₂O₃ film on Ni₃Al(111) and the above mentioned triangular features confirms our identification of the latter as a localised surface oxidation.



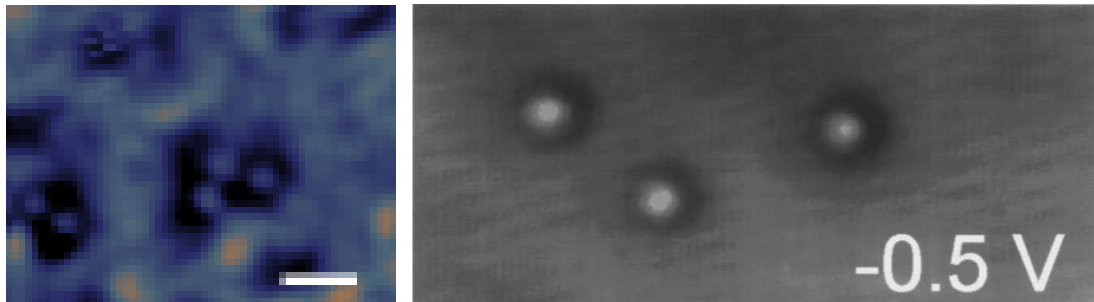
(a) Large scale STM image showing large and flat atomic terraces; measuring parameters: $V_{\text{bias}} = -2 \text{ V}$; $I = 100 \text{ pA}$; Size = $300 \times 300 \text{ nm}$.

(b) Large scale STM image showing some wide darker islands as well as smaller bright protrusions; measuring parameters: $V_{\text{bias}} = -0.8 \text{ V}$, $I = 100 \text{ pA}$, Size = $200 \times 200 \text{ nm}$.



(c) Measuring parameters: $V_{\text{bias}} = -0.5 \text{ V}$, $I = 300 \text{ pA}$, Size = $40 \times 16 \text{ nm}$.

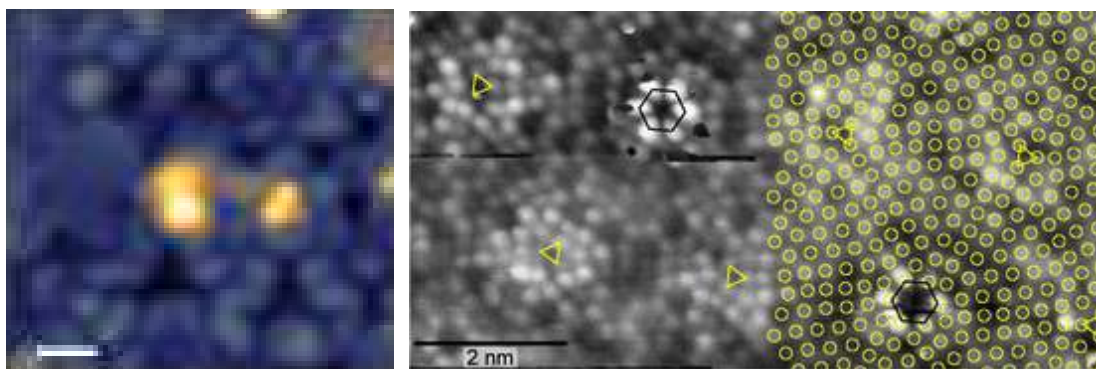
Figure 3.10: STM imaging of the boron growth on $\text{Ni}_3\text{Al}(111)$ at different examining scale.



(a) Measuring parameters: same as Fig. 3.10c; scalebar = 1 nm.

(b) Measuring parameters: $I = 1$ nA. Adapted from [76].

Figure 3.11: Comparison of STM images depicting **(a)** an enlargement of a CO domain from Fig. 3.10c measured on the $Ni_3Al(111)$ surface and **(b)** CO molecules adsorbed on $Cu(111)$ measured with a CO-functionalised tip.



(a) Measuring parameters: same as Fig. 3.10c; scalebar = 1 nm.

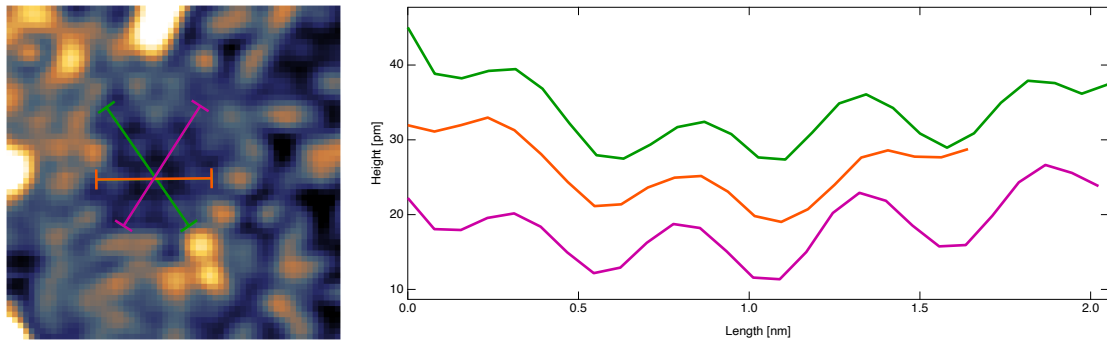
(b) Measuring parameters: $V_{\text{bias}} = 58$ mV; $I = 35$ nA; size = 10 nm wide. Adapted from [77].

Figure 3.12: Comparison of STM images depicting **(a)** an enlargement of a local oxidated region from Fig. 3.10c measured on the $Ni_3Al(111)$ surface and **(b)** surface oxide, with threefold and sixfold rotation axes of the oxide are marked by triangles and hexagons, respectively.

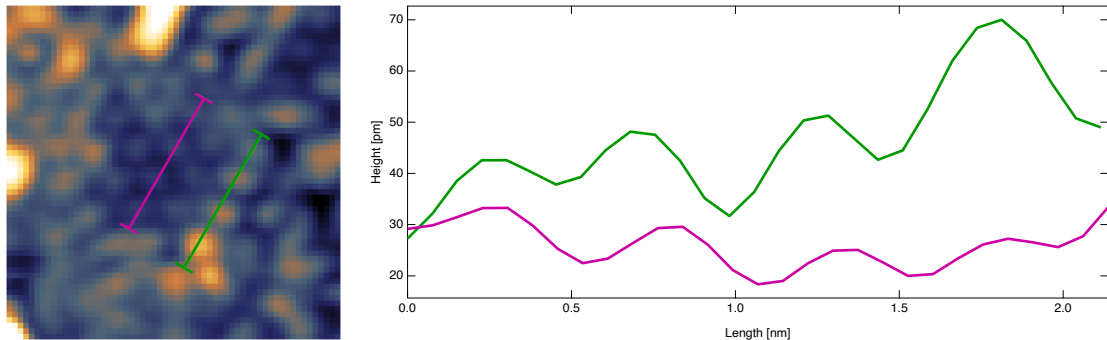
The red lines in Fig. 3.10c identify the clean $\text{Ni}_3\text{Al}(111)$ surface regions, which show the stoichiometric (2×2) surface arrangement of aluminium atoms. In particular, from the analysis of the height profiles along the main crystallographic directions depicted in Fig. 3.13a, we obtained a (2×2) lattice constant of $5.2 \pm 0.3 \text{ \AA}$, which is consistent with the value reported in the literature ($a_{(2 \times 2)} = 5.03 \text{ \AA}$). The apparent lack of regions displaying a discernible long range (2×2) lattice is attributed to the challenging imaging of the $\text{Ni}_3\text{Al}(111)$ surface termination via STM. In fact, this substrate is characterised by localised chemical disorder, largely resulting from regions with an incorrect stoichiometric ratio, and the presence of distorting charge density waves [78], which hinder collection of well-ordered images over a long range.

Closer examination of Fig. 3.13a reveals, besides the conventional bulklike (2×2) arrangement of aluminium atoms on the bare $\text{Ni}_3\text{Al}(111)$ termination, a distinct additional atomic arrangement displaying brighter spots. Notably, this supplementary structure appears to follow the (2×2) symmetry of the underlying substrate, as proved by the height profiles depicted in Fig. 3.13b that shows perfectly aligned maxima. Domains of this new structure are present in several regions around the surface, as can be appreciated by the series of STM images in Fig. 3.14. Based on the analysis of height profiles along the traces indicated in the latter figure, it was found that the height difference between the clean surface lattice and the newly observed bright protrusions lies within a range of $(0.10 - 0.25) \text{ \AA}$. As a result, we suppose that this distinctive configuration could be ascribed to the incorporation of boron atoms into the substrate lattice, thus substituting the topmost aluminium atoms.

In other regions of the surface, several distinct triangular-shaped protrusions can be detected, as can be appreciated by looking at Fig. 3.10c. The height difference between the clean $\text{Ni}_3\text{Al}(111)$ surface and these triangular protrusions has been measured by analysing the height profiles depicted in Fig. 3.15 and resulted in values ranging from 0.80 up to 1.00 \AA . The latter findings suggest that B atoms tend to aggregate, forming clusters with a triangular shape. Some of these clusters reveal an inner structure consisting of three bright spots while others are characterised by a blurred appearance. Moreover, we deduced that the triangular boron clusters form on the substrate by utilising substitutional boron atoms as nucleation sites, as can be inferred from Fig. 3.16, noticing how these structures grow directly along a main crystallographic direction of the B-embedded substrate.



(a) STM image showing a region of the clean $Ni_3Al(111)$ surface and respective height profiles along the main crystallographic directions. The analysis of the height profiles along the (2×2) lattice resulted in a distance between two aluminium nearest neighbour of $5.2 \pm 0.3 \text{ \AA}$, consistent with the tabulated value reported in the literature. The reported profiles have been vertically shifted for better clarity



(b) STM image showing a region of the clean $Ni_3Al(111)$ surface and the boron atoms embedded substrate, with their respective height profiles along a main crystallographic direction. The perfectly aligned maxima of the two profiles support the substitution of superficial aluminium atoms with embedded boron atoms.

Figure 3.13: STM images with the corresponding height profiles. The length of the markers at the ends of the line profiles in the STM images indicates the averaged thickness.

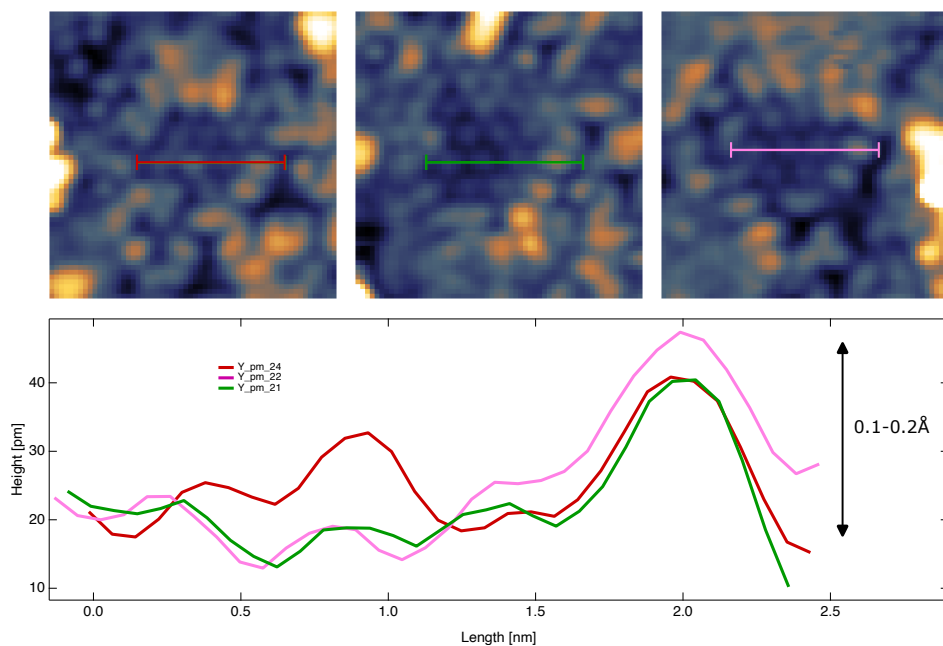


Figure 3.14: STM images the embedded boron atoms arrangement with the corresponding height profiles. The length of the markers at the ends of the line profiles in the STM images indicates the averaged thickness.

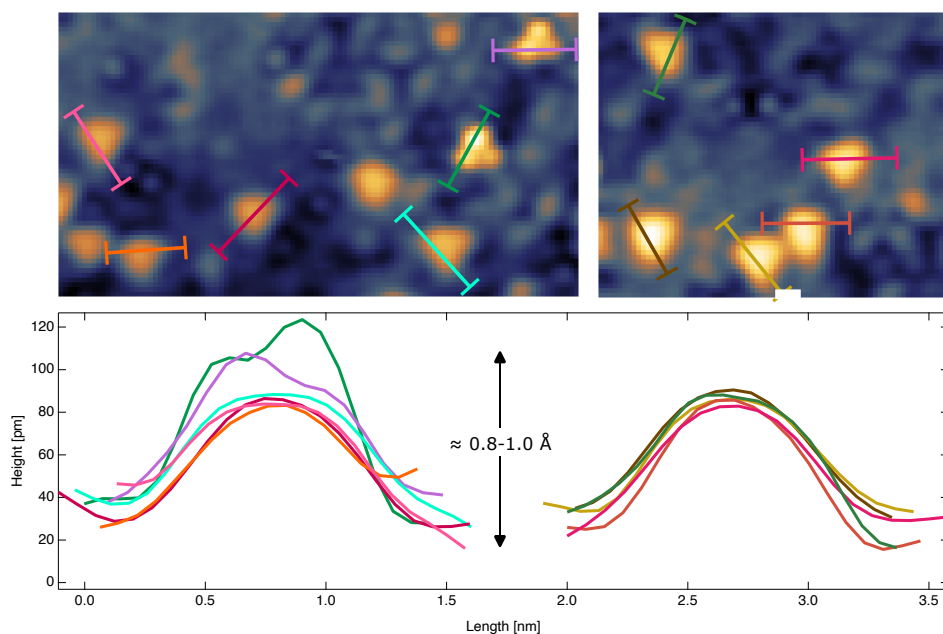


Figure 3.15: STM images depicting the triangular shaped B clusters with the corresponding height profiles. The length of the markers at the ends of the line profiles in the STM images indicates the averaged thickness.

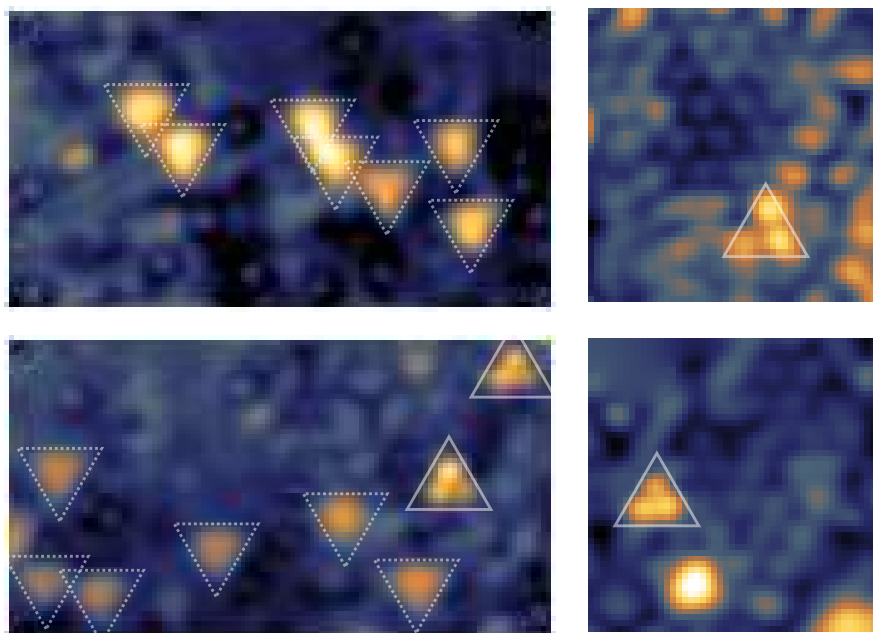


Figure 3.16: STM images depicting the triangular-shaped protrusions. Some of these B clusters reveal an inner structure consisting of three bright spots (solid line triangles) while the others are characterised by blurred appearance (dashed line triangles).

3.2.4 XPS

The investigation of electronic core level structure via XPS is crucial in disclosing the chemical bonding environment of selected atomic elements in the system.

In this section, the Ni 2p_{3/2}, Al 2p and B 1s core levels are reported. The analysis of the system electronic structure was crucial in order to shed light onto the internal structure of the B-based structures detected by STM and described in the previous section. In addition, these results will be used as a starting stage in order to understand the behaviour and the reactivity of the B/Ni₃Al(111) system to molecular oxygen (see Sec. 4.3). The data presented here have been acquired at the PEARL beamline at the SLS (P.S.I.) in Villigen (Switzerland).

To investigate the borophene growth process and to explore its complex parameters space, different sample temperatures and deposition times were employed to understand the role of each parameter in the system dynamics and kinetics, including surface and bulk atoms diffusion and segregation. Specifically, after the Ni₃Al(111) substrate was cleaned as described in Sec. 3.2.1, B was evaporated following three selected recipes, which are carefully described in table 3.2. The effective B coverage was experimentally evaluated exploiting

	Sample Temperature	Deposition Time	Deposition Rate	Measured B Coverage
A	495 K	10'	0.07 ML/min	0.7 ML
B	415 K	10'	0.07 ML/min	0.7 ML
C	490 K	30'	0.07 ML/min	1.6 ML

Table 3.2: Deposition parameters employed in the three sample preparation recipes.

XPS survey spectra taken at 750 eV photon energy, comparing the Al 2s and B 1s peak intensities, which were normalised in accordance with their respective photoionisation cross sections (B 1s: 0.047 Mbarn and Al 2p: 0.063 Mbarn). Considering the electron mean free path in the Ni₃Al alloy ($\lambda_{\text{Ni}_3\text{Al}} = 16.6 \text{ \AA}$) and the interlayer distance ($d_{\text{Ni}_3\text{Al}} = 2.00 \text{ \AA}$) we can thus estimate the number of layers contributing to the Al 2s signal intensity. Then, by comparing the intensities of B 1s and Al 2s core levels, we can determine the number of evaporated boron monolayers with respect to the Ni₃Al(111) substrate.

Upon analysis of the resulting B coverage from the various recipes, we observe that adjusting the sample temperature (415 K compared to 495 K) while

keeping the deposition time constant ($t = 10'$) led to the really same B coverage (Θ_B) of 0.7 ML. On the contrary, triplicating the deposition time ($t = 30'$), but keeping the sample at high temperature (490 K), resulted in a boron coverage just about doubled with respect to the previous cases. This clearly suggest the dissolution of boron atoms into the bulk with increasing coverage.

Ni 2p_{3/2}

Figure 3.17 shows the Ni 2p_{3/2} core level photoemission spectra collected at room temperature and at $h\nu = 1000$ eV for the B/Ni₃Al(111) and pristine Ni₃Al(111) systems, together with their best fit curves and the corresponding deconvolution profiles for each spectral components. The best fitting parameters are reported in Appendix A.2.

In the photoemission spectrum corresponding to the clean surface, two spectroscopic features can be distinguished at 852.24 eV (Ni₁) and at +6.143 eV (higher) binding energies, corresponding to the adiabatic Ni 2p_{3/2} core level signal and to a secondary peak due to a surface plasmon loss, respectively.

Upon boron evaporation, a new component grows at +0.446 eV (Ni₂), attributed to Ni atoms in direct contact with boron atoms. Furthermore, a modulation of the relative peak intensities is evident through a comparison of spectra corresponding to the various growth recipes. Specifically, we noted an increase in the Ni₂ component intensity at the expense of the Ni₁ one, by both lowering the sample temperature or increasing the boron coverage. The latter trends imply that, when the substrate temperature or B coverage are higher (495 K or 1.6 ML), boron atoms diffuse into the subsurface region, while at low substrate temperature (415 K), they mainly remain on the surface, in a manner similar to that reported in the case of borophene growth on the Au(111) substrate [14].

Al 2p

Figure 3.18 shows the Al 2p core level photoemission spectra collected at room temperature and at $h\nu = 150$ eV for the B/Ni₃Al(111) and pristine Ni₃Al(111) systems together with their best fit curves and the corresponding deconvolution profiles for each spectral components. The best fitting parameters are reported in Appendix A.2.

The photoemission spectrum relative to the clean surface displays the spin-orbit doublet associated with the bulk Al atoms, with the 2p_{3/2} peak at a binding

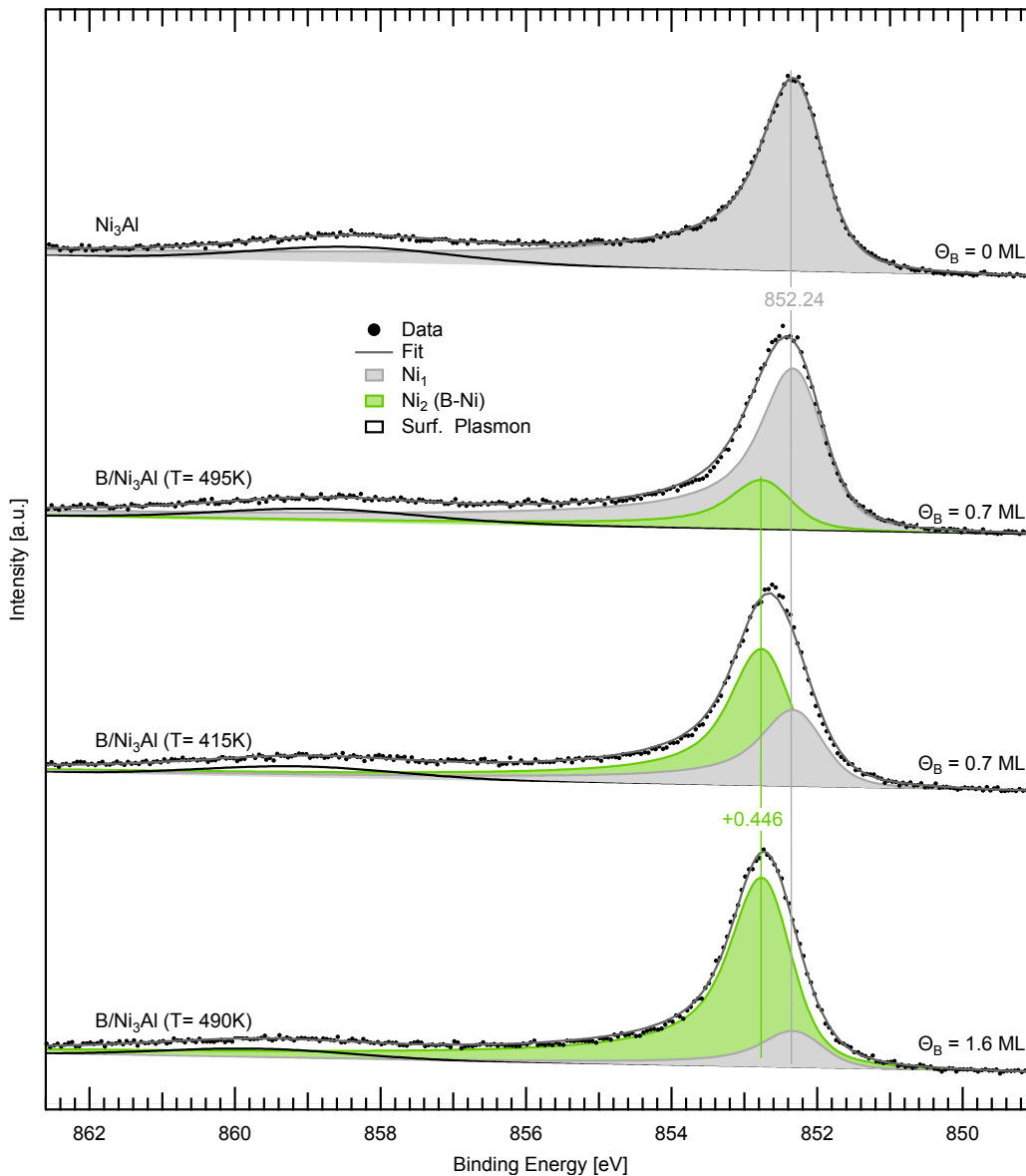


Figure 3.17: Ni $2p_{3/2}$ XPS spectra for the B/Ni₃Al(111) and pristine Ni₃Al(111) systems (acquired at $h\nu = 1000$ eV) together with their best fit curves and the corresponding deconvolution profiles for each spectral components. The spectra can be fitted with three individual components, attributed to: the bulk Ni atoms (Ni₁, grey) at 852.24 eV, Ni atoms bonded to B atoms (Ni₂, green) at +0.446 eV and the surface plasmon component (white).

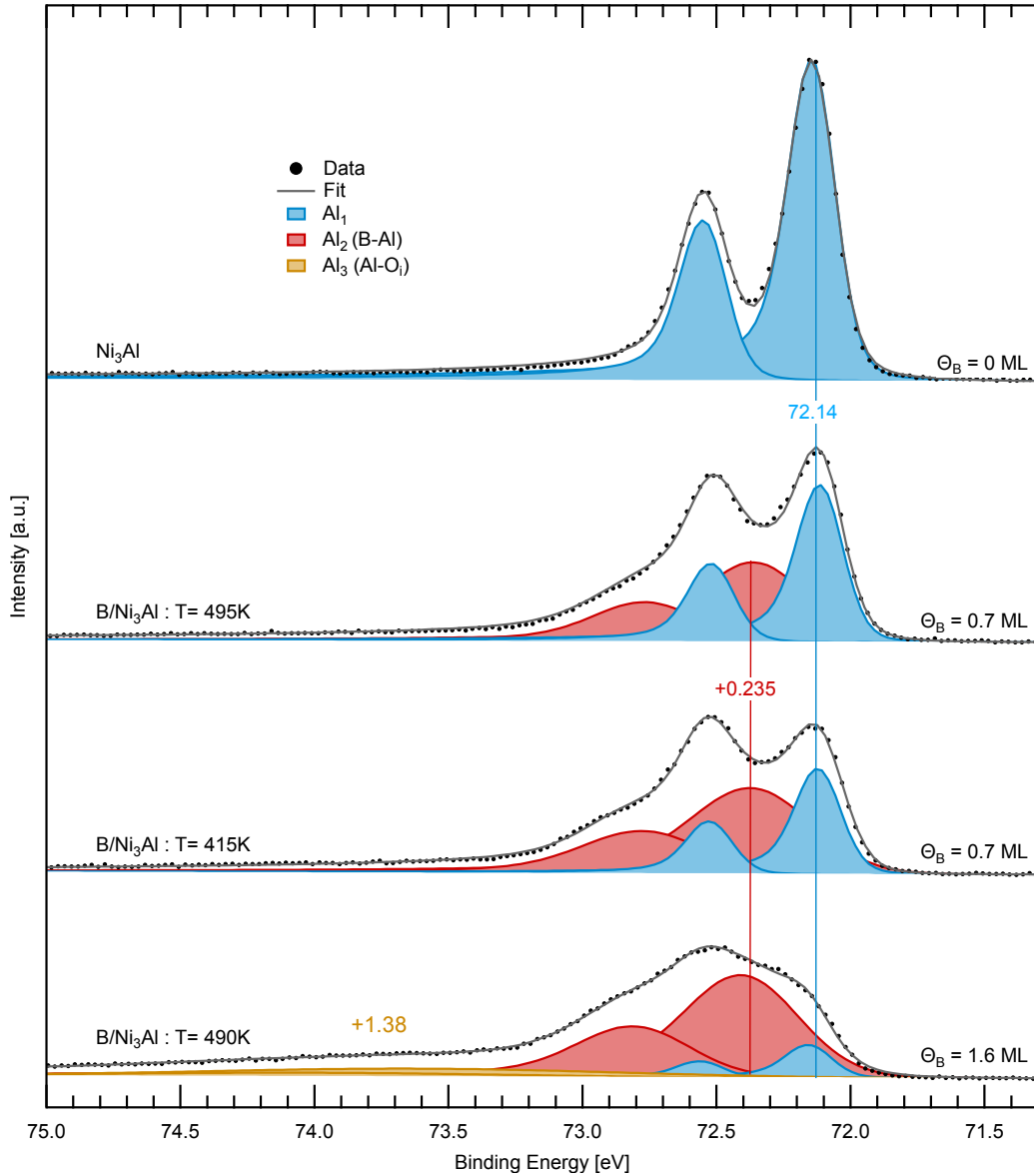


Figure 3.18: Al 2p XPS spectra for the B/Ni₃Al(111) and pristine Ni₃Al(111) systems (acquired at $h\nu = 150$ eV) together with their best fit curves and the corresponding deconvolution profiles for each spectral components. The spectra can be fitted with three spin-orbit components, attributed to: the bulk Al atoms (Al₁, blue) at 72.14 eV, Al atoms bonded to B atoms (Al₂, red) at +0.235 eV and a minor oxide contamination component (Al₃, yellow) at +1.38 eV.

energy of 72.14 eV (Al_1). The two components composing the doublet are constrained to have the same lineshape and 1:2 intensity ratio, as expected from the degeneracy of the two levels. The value of 0.405 eV for spin-orbit splitting was determined from the fit and subsequently held constant during the fitting process for the B-related spectra.

Upon boron deposition, a second spin-orbit doublet, with the 3/2 component at +0.235 eV (Al_2) higher binding energy, ascribed to B-interacting Al atoms, emerges at expenses of the Al_1 component. Notably, the Gaussian broadening of the B-induced features is more than doubled with respect to that of bare substrate contribution (0.43 vs 0.18 eV), suggesting a significant disorder component in the atomic structure of the B/ $Ni_3Al(111)$ system. The trend in relative intensity observed for the B-induced and pristine Al 2p components is in line with the one exhibited by the Ni $2p_{3/2}$ core level discussed above.

In addition, when the boron deposition time is substantially increased, we detected the growth of a minor contribution to the Al 2p envelope at higher binding energy (Al_3) associated with Al oxide formation, due to a minor oxygen contamination during the deposition process [21]. The presence of minority impurities is generally difficult to avoid when depositing boron on surfaces, as confirmed by the Al(111) case (See Sec.3.1.2).

B 1s

Figure 3.19 shows the high-resolution B 1s core level photoemission spectra collected at room temperature and at $h\nu = 270$ eV for the B/ $Ni_3Al(111)$ system together with their best fit curves and the corresponding deconvolution profiles for each spectral components. The best fitting parameters are reported in Appendix A.2.

The B 1s spectra can be resolved into five distinct components, namely B_1 , B_2 , B_3 , B_4 and B_5 . The higher binding energy peak (B_5) relates with the minor oxygen contamination and is attributed to boron atoms in chemical contact with aluminium oxide, while the remaining components can be ascribed to the formation of B-based structures. Upon comparing the deconvolution of B 1s spectra to the previously discussed findings on Ni $2p_{3/2}$ and Al 2p core levels, we observed comparable trends in intensity, which assisted in identifying the various boron species. In particular, focusing on the evolution of the B_2 and B_3 components with respect to the tuning of the deposition parameters,

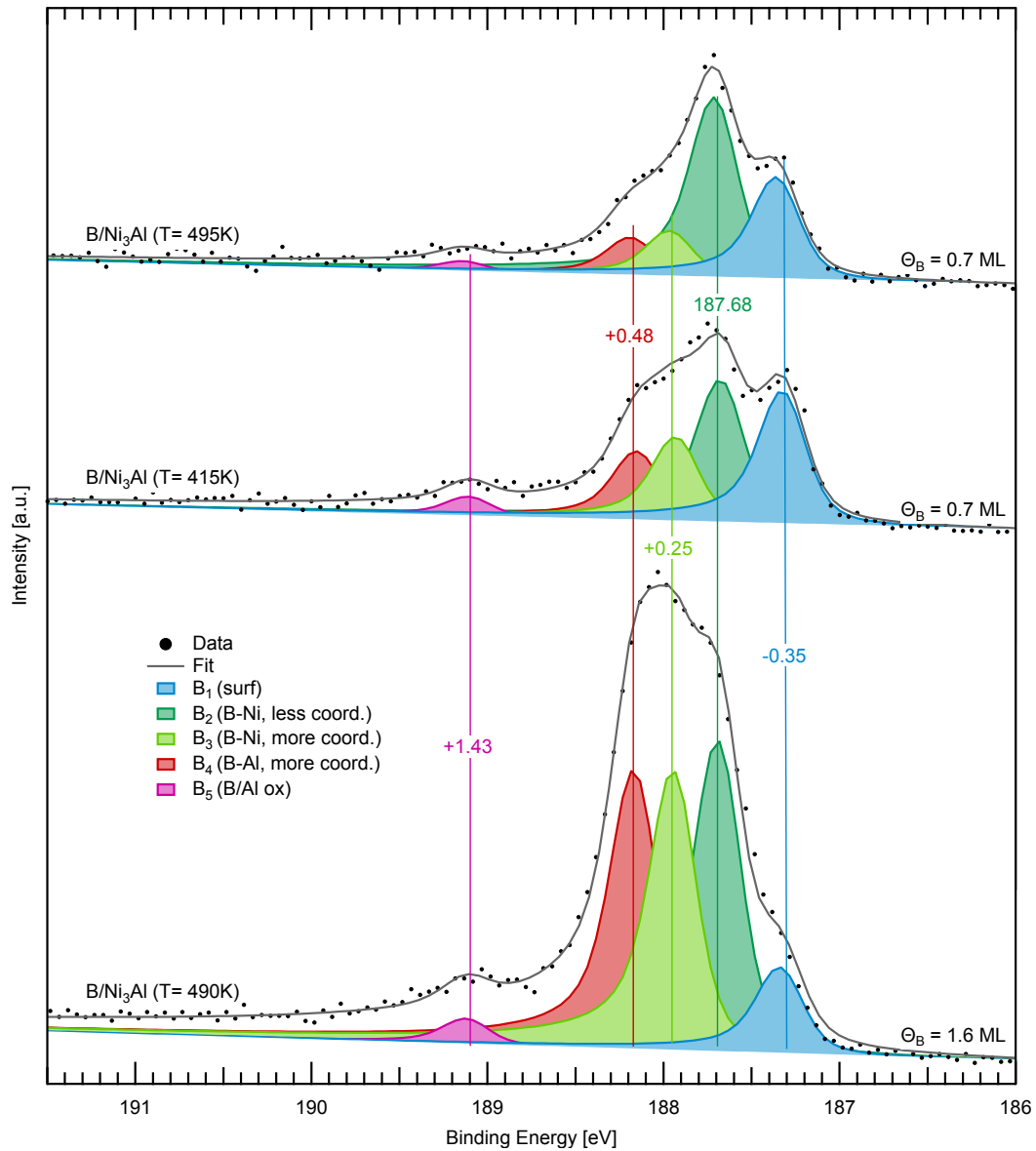


Figure 3.19: B 1s XPS spectra for the B/Ni₃Al(111) system (acquired at $h\nu = 270$ eV) together with their best fit curves and the corresponding deconvolution profiles for each spectral components. The spectra can be fitted with five individual components, attributed to: surface B atoms (B₁, blue) at -0.35 eV, less coordinated B atoms bonded to Ni atoms (B₂, dark green) at 187.68 eV, more coordinated B atoms bonded to Ni atoms (B₃, light green) at +0.25 eV, more coordinated B atoms bonded with Al atoms (B₄, red) at +0.48 eV and B atoms on Al oxide due to a minor oxygen contamination (B₅, pink) at +1.43 eV.

we detected increasing intensities both lowering the sample temperature and increasing the boron coverage. The same behaviour was observed for the Ni₂ component in the Ni 2p_{3/2} photoemission spectra, suggesting to ascribe the B₂ and B₃ components to the formation of B-Ni bonds upon evaporation. Previous studies on the B/Ag(111) system [13] suggest that higher binding energy in the B 1s core level corresponds to higher B coordination numbers, in line with the trend observed for graphene [79]. Therefore, based on the proved relation between BE ordering and chemical coordination, it is straightforward to attribute the B₃ spectral feature to more coordinated B atoms and B₂ to less coordinated B atoms at Ni sites. In the same way as for the Ni 2p_{3/2} core level, by comparing the Al 2p with the B 1s photoemission spectra, it is possible to attribute the B₄ component to the formation of B-Al bonds upon evaporation. Specifically, the intensity trend for the B₄ peak in the B 1s spectra mirrors that of the Al₂ peak in the Al 2p spectra. In fact, changing the sample temperature did not result in a significant adjustment of the B₄ peak intensity, whereas increasing the boron coverage led to a considerable boost. This trend is in line with the findings from the Al 2p spectra, indicating a prevalence of the Al₂ component over the Al₁ one at high coverage. Eventually, concerning B₁, low coordinated surface boron atoms can be attributed to this component, as its intensity decreases with increasing boron coverage.

3.2.5 Interpretative Model

The combined results obtained from STM and XPS investigations of the B/Ni₃Al(111) system shed light on the growth process of B-nanostructures on this specific substrate, enabling us to propose an interpretative model for the atomic arrangements of boron atoms that reconciles the findings of both techniques.

Before delving into the model description, it is worth noting that *Kiraly et al.* [14] carried out a study on borophene synthesis on Au(111), exploiting *ab initio* DFT calculations to quantify the adsorption energetics of boron atoms on this surface. In particular, the most stable configurations were found to consist of boron atoms in subsurface sites within the topmost layer, actually expelling a surface Au atom to accommodate a boron trimer cluster.

By combining our findings with relevant information from previous research,

our aim is to offer a thorough comprehension of the B/Ni₃Al(111) system and its intriguing features.

The STM image in Fig. 3.20 depicts the clean Ni₃Al(111) surface along with boron atoms embedded in the topmost layer and the triangular-shaped protrusion. On its side, the corresponding balls model of the surface morphology is presented: Al and Ni surface atoms are depicted in light blue and dark grey balls, respectively, while embedded boron atoms are depicted in dark green. The sketchy model reveals the inner structure of the triangular-shaped bright protrusion: each spot is a single trimer of boron atoms, similar to what has been observed in the B/Au(111) case. Notably, the arrangement of the trimers on the substrate lattice follows the main crystallographic direction of the B-embedded substrate. Thus, the boron atoms forming the trimers sit in the 3-fold adsorption sites offered by the substitutional boron atoms (depicted in light green). Furthermore, at the centre of this configuration of trimers, there is an Al adatom that links individual boron trimers to establish the triangular-shaped cluster. This creates a distinct chemical coordination for the boron atoms that face the triangle's centre and are connected to the Al adatom (higher coordination, illustrated in red) compared to the others (lower coordination, represented in cyan). The XPS measurements of the Al 2p core-level (refer to Fig. 3.18) confirm the presence of the Al adatom at the centre of the triangular boron cluster as they revealed a doublet (Al₂) associated with Al atoms which are bonded to B atoms. In addition, both from our result on the B/Al(111) system (See Sec. 3.1) and previously reported works in the literature [8, 15, 17, 75], it is evident how Al can stabilise and steer the geometry of B-based nanostructures by providing an intense charge transfer.

In Figure 3.21, we investigate the triangular bright protrusions highlighted in section 3.2.3. These features demonstrate a clear distinction in shape and image resolution between upward-oriented triangles (higher resolution, solid lines in Fig. 3.21) and in downward-oriented triangles (lower resolution, dashed lines in Fig. 3.21), which cannot be explained with just a rotation of 60°. In fact, by examining the proposed model in Figure 3.21 it becomes evident that the two crystallographic orientations of the triangles are characterised by different adsorption sites for the boron atoms, which are either FCC or HCP. Accordingly, this inconsistency in atomic arrangement results in the different appearances observed in

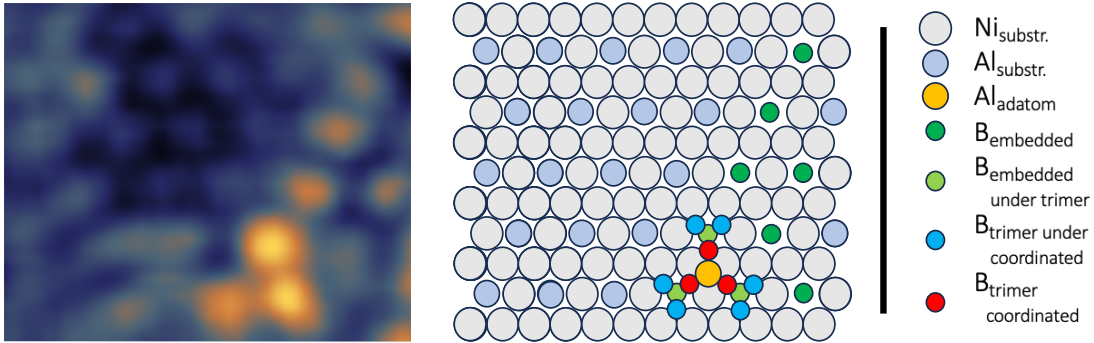


Figure 3.20: STM image (on the left) depicting the clean $\text{Ni}_3\text{Al}(111)$ surface along with embedded boron atoms and the triangular-shaped protrusion, together with the explaining balls model and the relative legend.

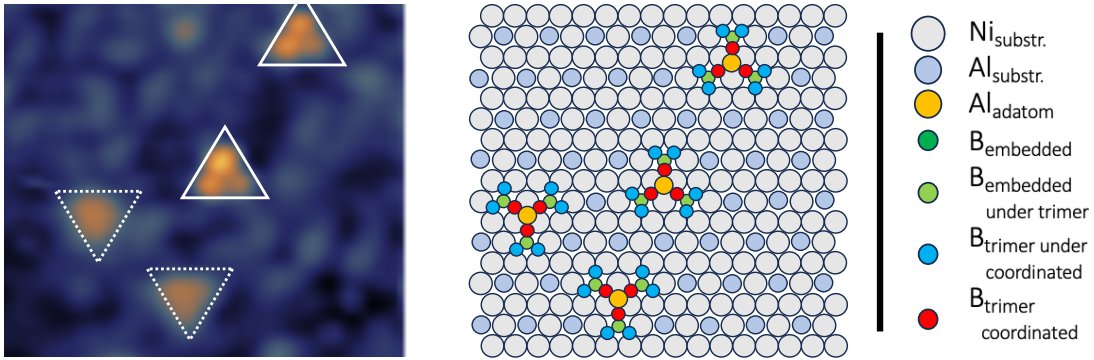


Figure 3.21: STM image (on the left) depicting the high resolution triangular clusters (solid lines) along with the high resolution triangular clusters (dashed lines), together with the explaining balls model and the relative legend.

the STM images. This finding consistently aligns with the behaviour detected in the B/Au(111) system [14]: the bias-dependent conductance maps, depicted in Fig. 3.22, demonstrate the electronic difference between the borophene and Au, as well as the difference between the FCC (red dashed triangle) and HCP (yellow dashed triangle) regions, where the contrast reverses between -0.2 and -0.4 V.

Based on the results obtained from XPS measurements, Fig. 3.23 depicts a comparison between the proposed model and the B 1s core-level spectra. In particular, boron atoms arranged in trimers can sit either in FCC or HCP adsorption sites, resulting in two distinct local atomic configurations (identified as Configuration 1 and 2 in Fig. 3.23) which differ in the numbers of boron

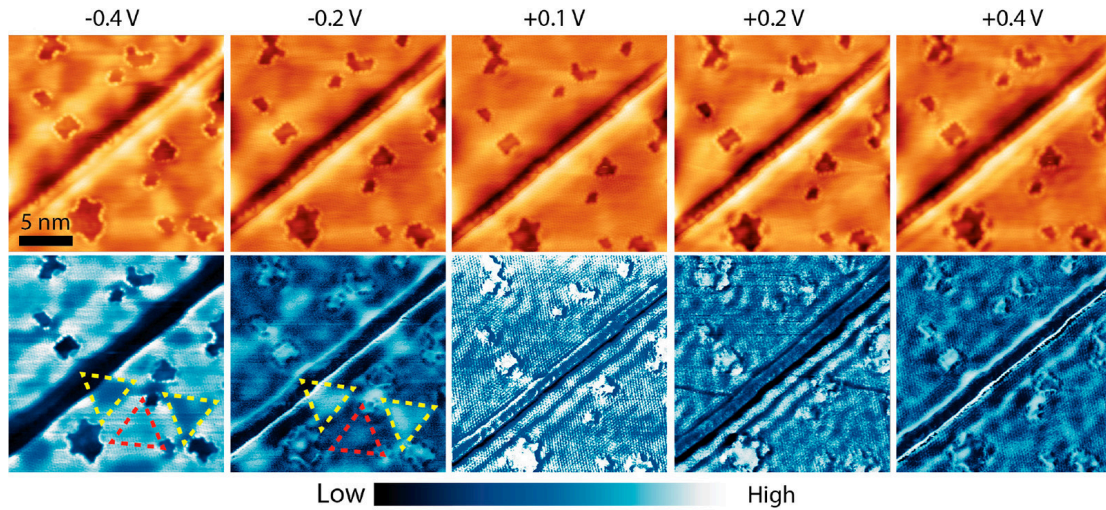


Figure 3.22: Series of bias-dependent STM images showing topography (top panels) and dI/dV maps (bottom panels) of the same region at the biases indicated above each panel. Red and yellow triangles represent FCC and HCP regions of the Au(111) surface. The borophene islands appear as depressions in topography at all biases ($I = 200$ pA). From [14].

atoms in the two distinct coordination environments. Specifically, the second configuration is characterised by a higher number of under-coordinated trimer boron atoms (depicted in cyan) with respect to the first one.

The proposed model enables a more specific assignments for the B 1s components revealed by XPS analysis (see Fig. 3.19). Specifically:

- **B₁** component is associated with under coordinated trimer boron atoms (depicted in cyan);
- **B₄** component is associated with more coordinated trimer boron atoms, i.e. bonded to the connecting Al adatom in the centre (depicted in red)
- **B₂** component is associated with less coordinated, i.e. isolated substitutional boron atoms bonded to Ni atoms (depicted in light green)
- **B₃** component is associated with more coordinated substitutional boron atoms, bonded to Ni atoms, which act as nucleation centres for the boron trimers (depicted in dark green)

The complete picture regarding the binding energy values and the assignments related to the spectral components of all the core levels discussed in this section

	BE [eV]	Attribution
Ni₁	852.24	Ni bulk atoms
Ni₂	+0.446	B-bonded Ni atoms
Al₁	72.14	Al bulk atoms
Al₂	+0.235	B-bonded Al atoms (Al adatoms)
B₁	-0.35	less coord. trimer B atoms
B₂	187.68	less coord. substitutional B atoms
B₃	+0.25	more coord. substitutional B atoms
B₄	+0.48	more coord. trimer B atoms (Al-bonded)
B₅	+1.43	B atoms on Al oxide

Table 3.3: Deconvolution components of Ni 2p_{3/2} Al 2p and B 1s core-level photoemission spectra and their respective binding energies and attributions.

3.2.4 can be appreciated in Table 4.1.

Figure 3.23 depicts the two proposed configurations alongside the B 1s photoemission spectra, for both low ($\Theta_B = 0.7$ ML) and high ($\Theta_B = 1.6$ ML) boron coverage. By comparing the results in the two cases it is possible to propose a tentative discrimination between the two local atomic configurations. Specifically, at low boron coverage the B₁ peak intensity prevails over that of the B₂ peak, but at higher coverage the intensity ratio turned out to be reversed. Consequently, by comparing the ratio of under- and more-coordinated boron trimer atoms at different coverages, Configuration 2 appears to be in better agreement with the photoemission data. Nonetheless, Configuration 1 cannot be conclusively rejected due to likely insufficient data to confirm the interpretative model with certainty. Further investigation and additional data may be necessary to obtain a conclusive result.

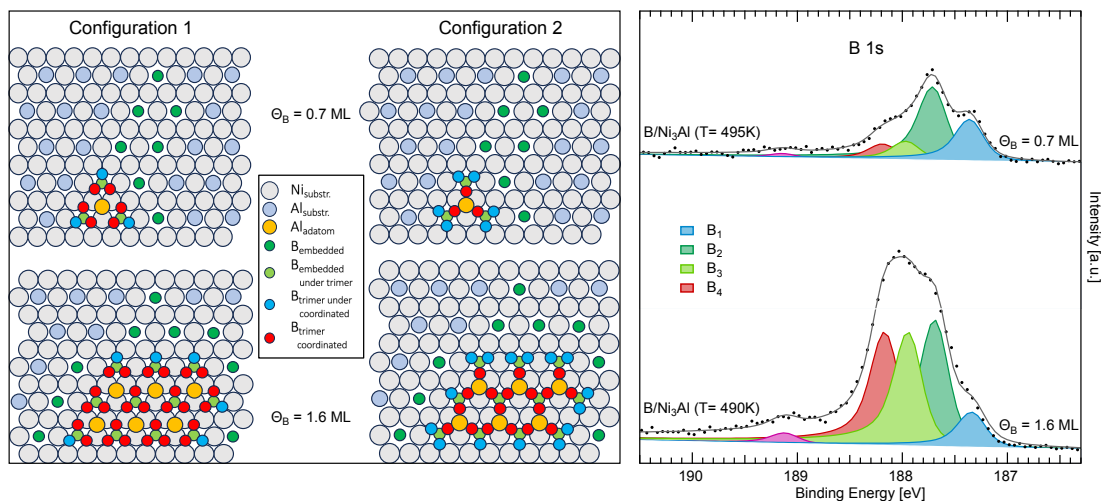


Figure 3.23: a) Interpretative model of the Configuration 1 and the Configuration 2, both at low coverage ($\Theta_B = 0.7$ ML) and high coverage ($\Theta_B = 1.6$ ML). The substrate is composed by Ni and Al atoms (grey and light blue, respectively). B atoms replace Al atoms to form the B-embedded substrate (dark green). The triangular protrusions are characterised by three trimers of boron atoms (cyan and red) arranged on a substitutional B atom (light green) and connected by an Al adatom (yellow). b) XPS measurements of B 1s core-level spectra at low coverage ($\Theta_B = 0.7$ ML) and high coverage ($\Theta_B = 1.6$ ML).

Chapter 4

Redox properties of borophene

In this section, we will investigate the borophene reactivity to ubiquitous gases as hydrogen and oxygen. By means of a combined experimental and theoretical approach, we will show that Al, B, O and H relative chemical affinities determine the redox behaviour of the B-induced structures. Specifically, atomic hydrogen exposure caused direct reduction of the B layer, resulting in the synthesis of a honeycomb borophane phase on Al(111). However, the interaction with molecular oxygen was more intricate, possibly leading to segregation of Al atoms and to the formation of Al and B oxide terminal structures on both Al(111) and Ni₃Al(111) substrates.

4.1 Borophane on Al(111)

4.1.1 Sample Preparation

Cleaning of the metal substrate and B evaporation were performed following the recipes described in Section 3.1.1. Hydrogenation of the AlB₂/Al(111) layer was achieved by exposing it to atomic hydrogen at room temperature. This was generated either on a resistively heated tungsten filament located in front of the sample in molecular hydrogen background ($p_{\text{H}_2} = 1 \times 10^{-8}$ mbar), or through the use of a *Bischler and Bertel* type thermal cracker [80]. The same outcome was achieved in both cases, with surface saturation at room temperature occurring after a 10 minutes exposure. As a result of the protracted and time-consuming recipe, required for an accurate sample preparation and involving 30-40 minutes for B deposition and 10 minutes for reduction, minimal residual oxygen sur-

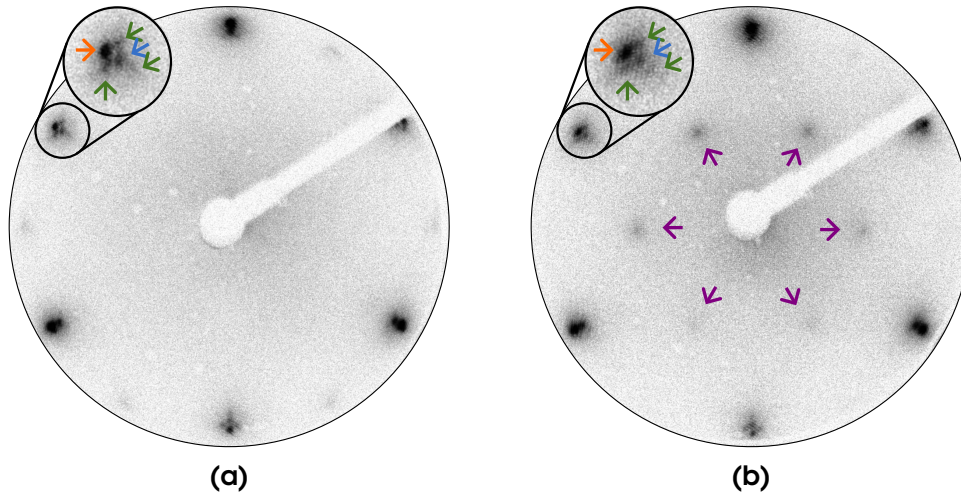


Figure 4.1: LEED diffraction patterns, corresponding to an electron energy of 47.5 eV, of the pristine **(a)** and reduced **(b)** $\text{AlB}_2/\text{Al}(111)$ system. The arrows indicate the diffraction spots related to the $\text{Al}(111)$ surface (orange), the AlB_2 layer (blue), the moiré superstructure (green), and the H-induced superstructure (purple).

face contamination (of the order of 1% of ML), albeit negligible, was detected by means of XPS or AES.

4.1.2 LEED

Upon hydrogenation of the $\text{AlB}_2/\text{Al}(111)$ system, additional diffraction spots appear in the LEED pattern, as can be appreciated in Fig. 4.1. These new spots indicate the formation of a well-ordered, long range $(\sqrt{3} \times \sqrt{3})\text{R}30^\circ$ superstructure, with lattice parameter $a_{\text{H}} = 5.10 \pm 0.02 \text{ \AA}$, induced by hydrogen atoms adsorption. Carefully examining the LEED pattern, we found that the H-induced superstructure is commensurate to the AlB_2 lattice. In fact, as proven by Fig. 4.2, just the ratio of the reciprocal lattice vectors $\frac{a_{\text{AlB}_2}^*}{a_{\text{H}}^*}$ is compatible with the $\sqrt{3}$ value, imposed by the $(\sqrt{3} \times \sqrt{3})\text{R}30^\circ$ symmetry.

4.1.3 XPS and NEXAFS

B 1s

Figure 4.4 shows the B 1s core level photoemission spectra collected at room temperature for the $\text{AlB}_2/\text{Al}(111)$ system, before and after exposure to atomic

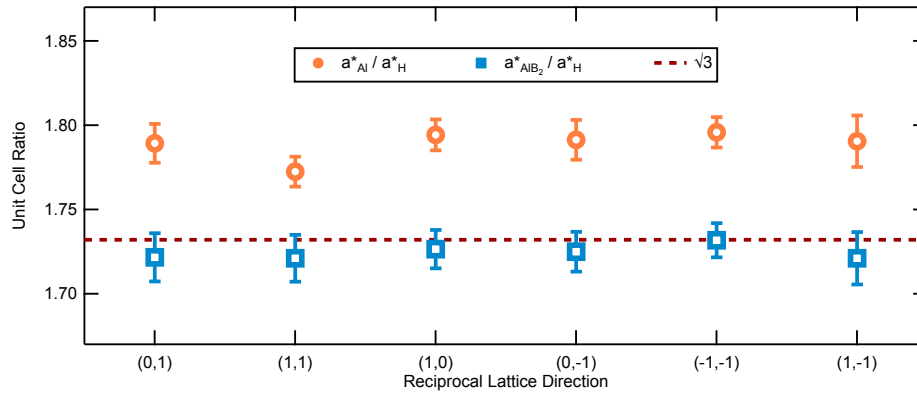


Figure 4.2: Compatibility of the H-induced unit cell size with the proposed $(\sqrt{3} \times \sqrt{3})R30^\circ$ superstructure referred to the AlB_2 phase obtained from LEED.

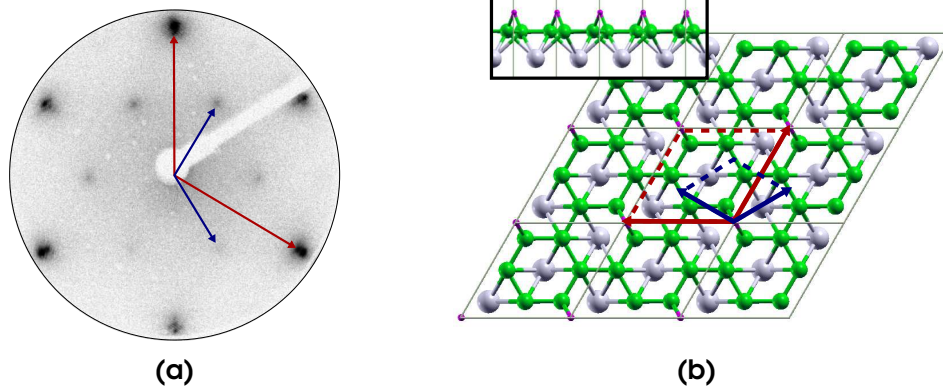


Figure 4.3: LEED diffraction pattern (a) and the best structural model (b) for the hydrogenated $(\sqrt{3} \times \sqrt{3})R30^\circ$ $AlB_2/Al(111)$ phase as obtained by means of *ab initio* DFT calculations (unit cells vectors are depicted with colours consistent with the reciprocal space vectors superimposed on the LEED image; spheres colour code: Al-grey, B-green, and H-violet; only the terminal Al layer yielding the AlB_2 phase is shown for best clarity).

hydrogen, together with their best fit curves and the corresponding deconvolution profiles for each spectral component. The best fitting parameters are reported in Appendix A.1.

Concerning the pristine $\text{AlB}_2/\text{Al}(111)$ system, its B 1s core level spectrum is characterised by three spectral components, originating from the B atoms forming a single AlB_2 layer (B_1), a second AlB_2 layer (B_2), and the B layer below the latter (B_3). Upon hydrogenation, a new component (B_H) grows at 187.27 (-0.43) eV, between B_2 and B_3 , at the expense of the former. As B_2 is associated with the B atoms of AlB_2 above a buried B layer, it can be inferred that H atoms bind to this elevated fraction of the AlB_2 multi-layered structure. Regarding spectral intensities, while B_1 remains substantially unaffected, we can observe that B_H is more intense compared to B_2 . Preferential hydrogenation of B_2 in relation to B_1 can be associated to a weaker AlB_2 - AlB_2 interaction compared to the AlB_2 - $\text{Al}(111)$ one. Further, the enhanced intensity of B_H compared to B_2 may suggest some boron interconversion process. Moreover, based on the symmetry of the hydrogenated honeycomb boron superstructure observed through LEED analysis, not all B atoms participate in bonding with hydrogen. Nevertheless, complementary theoretical results from DFT calculations, which will be carefully presented in Sec. 4.1.5, suggest the slight n-doping of all B atoms in the hydrogenated AlB_2 layer.

The employed fitting procedure included the simultaneous optimisation of fitting parameters across different photoemission spectra, which were collected upon several sample preparations, before and after hydrogenation, making the analysis faster and more reliable despite the presence of several overlapping components.

Al 2p

Figure 4.5 shows the Al 2p core level photoemission spectrum collected at room temperature for the $\text{AlB}_2/\text{Al}(111)$ system, before and after exposure to atomic hydrogen, together with their best fit curves and the corresponding deconvolution profiles for each spectral component. The best fitting parameters are reported in Appendix A.1.

Upon hydrogenation, the Al 2p core level spectrum undergoes only minor changes, which can hardly be quantitatively distinguished within the experimental error bar. In particular, hydrogenation of the $\text{AlB}_2/\text{Al}(111)$ layer yields a

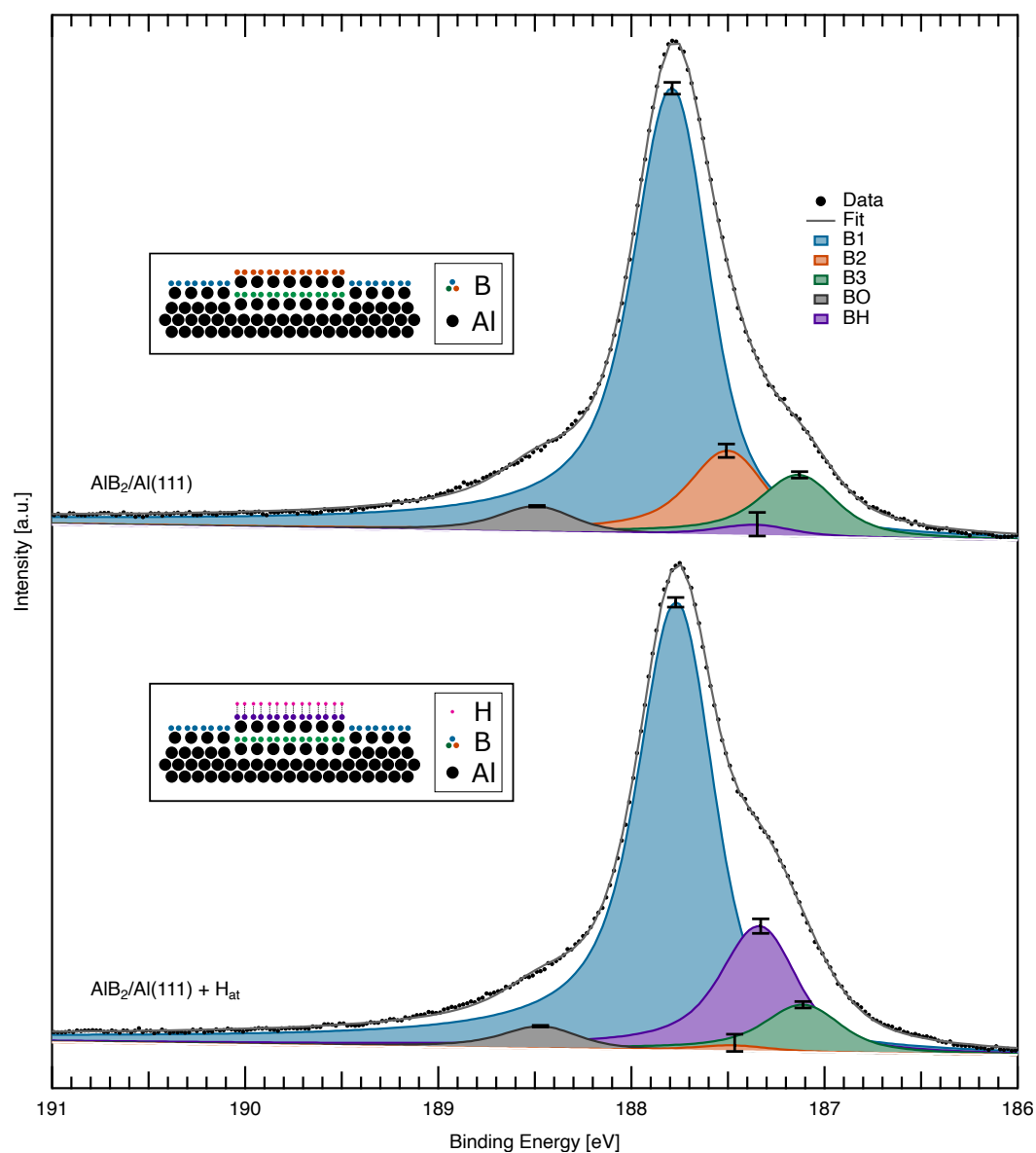


Figure 4.4: B 1s XPS spectra for the reduced and pristine $\text{AlB}_2/\text{Al}(111)$ system (acquired at $h\nu = 270$ eV) together with their best fit curves and the corresponding deconvolution profiles for each spectral components. The accompanying structural models elucidate the colour code and component assignments with respect to the corresponding atomic species.

general gaussian broadening of the B-related Al 2p components, together with an increased asymmetry, as a result of the geometric inhomogeneity induced by H adsorption. As verified by associated theoretical DFT findings (See 4.1.5), the analysis of the Al 2p core level indicates a negligible charge transfer to Al upon hydrogenation, at variance with B.

B K-edge

Figure 4.6 shows the B K-edge NEXAFS spectra collected at room temperature for the $\text{AlB}_2/\text{Al}(111)$ system, before and after exposure to atomic hydrogen. The data, collected in the partial electron yield mode, are depicted as a function of the angle between the electric field of the impinging, linearly polarised X-ray radiation and the normal to the surface. All NEXAFS spectra are normalised to the incident photon intensity and to the integral intensity under the curves.

Upon hydrogenation, the B 1s absorption edge is modified in both its π^* and σ^* regions, as can be specifically appreciated by examining the difference spectra between the hydrogenated and the bare $\text{AlB}_2/\text{Al}(111)$ layers. In particular, the π^* region close to the edge reveals significant modifications: a distinct resonance displaying strong dichroic behaviour grows at 187.3 eV, at the expenses of a non-modulating resonance previously evident at 189.3 eV for the bare AlB_2 layer. Concerning the σ^* region, a broad resonance is detected at about 201 eV. The dichroic behaviour of the latter feature is opposite with respect to that of the π resonance at 187.3 eV, suggesting the slight modification of the bonds orientation within the AlB_2 layer upon hydrogenation.

4.1.4 SFG

Figure 4.7a shows the IR-Vis SFG spectra collected at room temperature for the $\text{AlB}_2/\text{Al}(111)$ system, before and after exposure to atomic hydrogen, together with their best fit curves, which parameters are reported in Appendix B.1.

When probed by means of IR-Vis SFG vibronic spectroscopy, the bare $\text{AlB}_2/\text{Al}(111)$ does not contribute with any resonant signal in the investigated $1100\text{-}4000\text{ cm}^{-1}$ range, either in ppp or ssp polarisation configurations. Before disregarding any internal vibrational modes that can be attributed to the AlB_2 layer, it should be acknowledged that this particular technique, when applied to a metal, is only sensitive to the dipole components perpendicular to the surface. We found that, upon exposure to atomic hydrogen, a dispersive

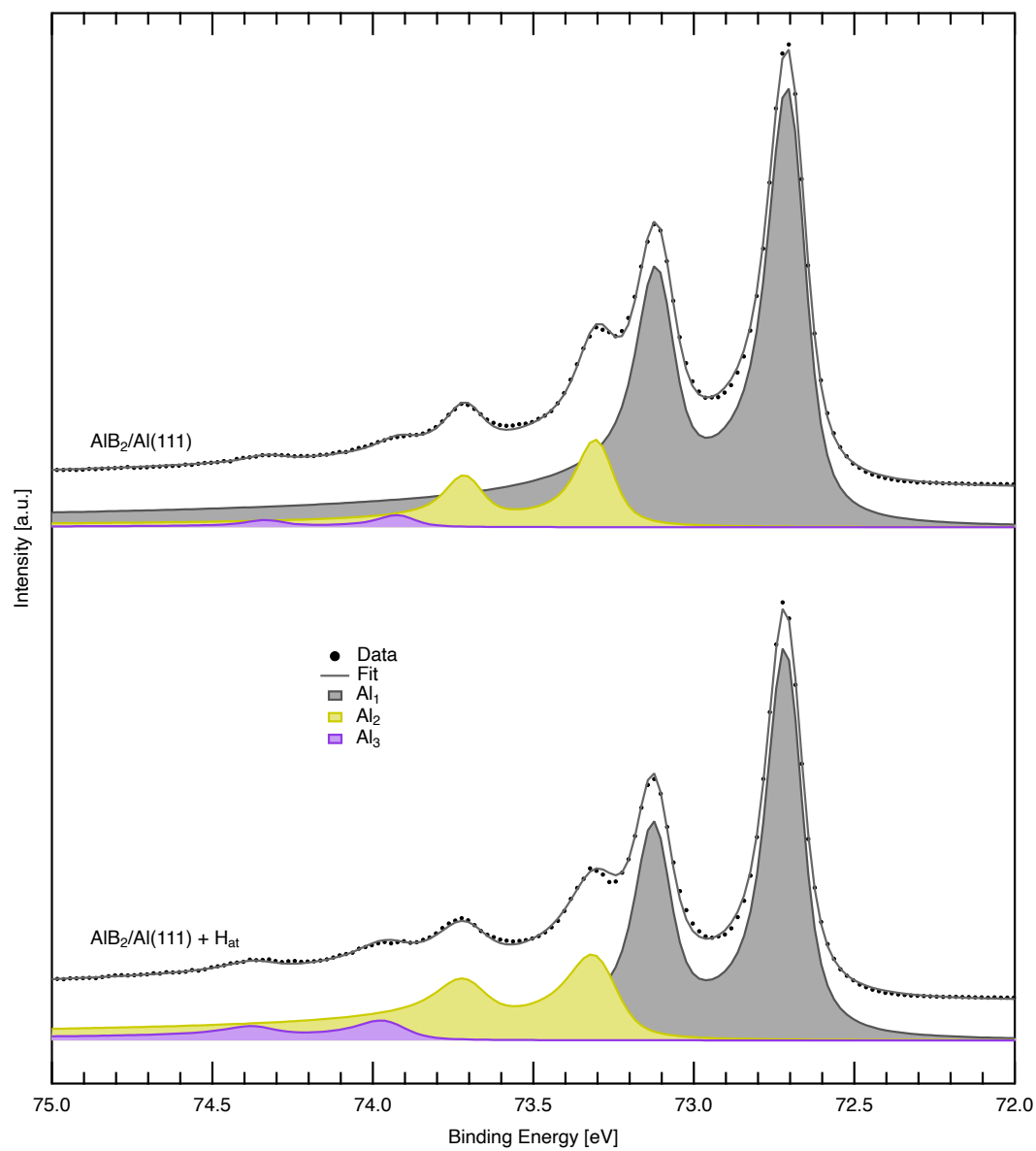


Figure 4.5: Al 2p XPS spectra for the reduced and pristine $\text{AlB}_2/\text{Al}(111)$ system (acquired at $h\nu = 150$ eV) together with their best fit curves and the corresponding deconvolution profiles for each spectral components.

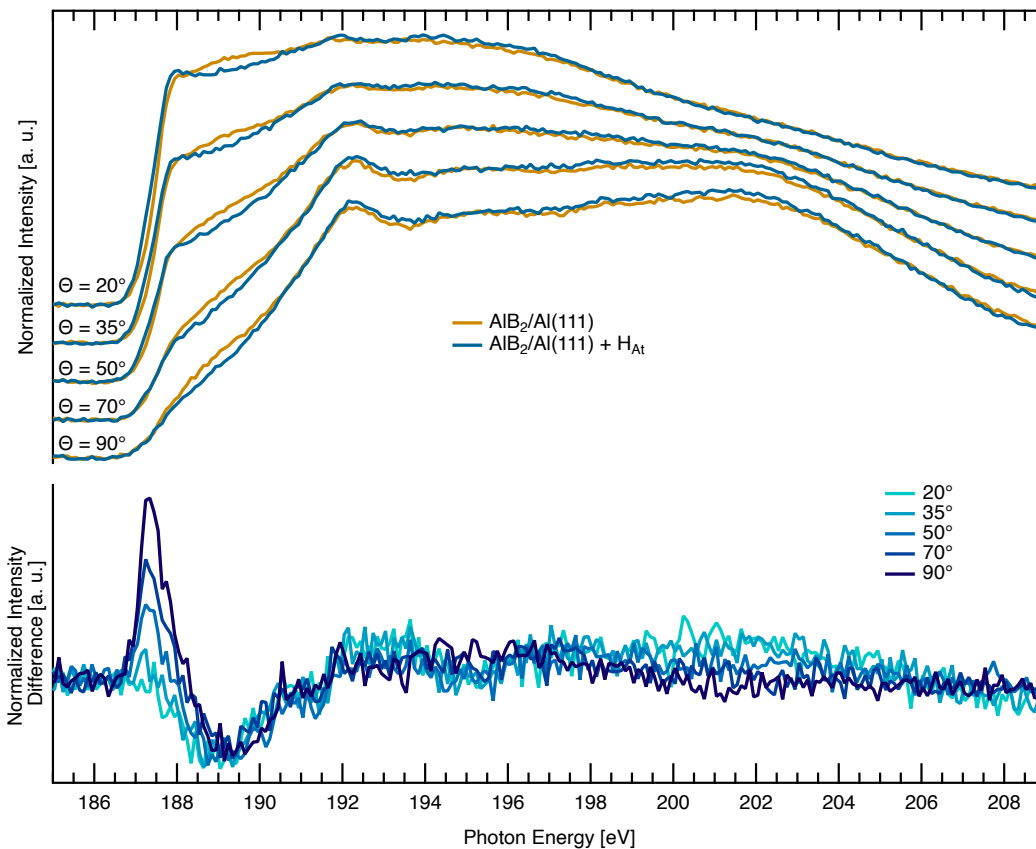


Figure 4.6: Angle-dependent NEXAFS B K-edge spectra for the $\text{AlB}_2/\text{Al}(111)$ system, before and after exposure to atomic hydrogen, collected in partial electron yield mode. The directions refer to the angle between the electric field of the impinging, linearly polarised X-ray radiation and the normal to the surface. The modifications in the B absorption K-edge can be further appreciated by examining the difference spectra between the hydrogenated and the bare $\text{AlB}_2/\text{Al}(111)$.

vibronic resonance appears at 1934 cm^{-1} , with a phase of 25° relative to the non-resonant background. We associate this feature with the B-H stretching mode, concluding that H atoms bind at the bridge sites of the honeycomb B network on the basis of specific *ab initio* calculations, which yield an expected B-H stretch value of 1973 cm^{-1} (see sec. 4.1.5), and by comparison with previous results from the literature, both theoretical (about 2040 cm^{-1} [81]) and experimental (about 1920 cm^{-1} [24]), on similar systems.

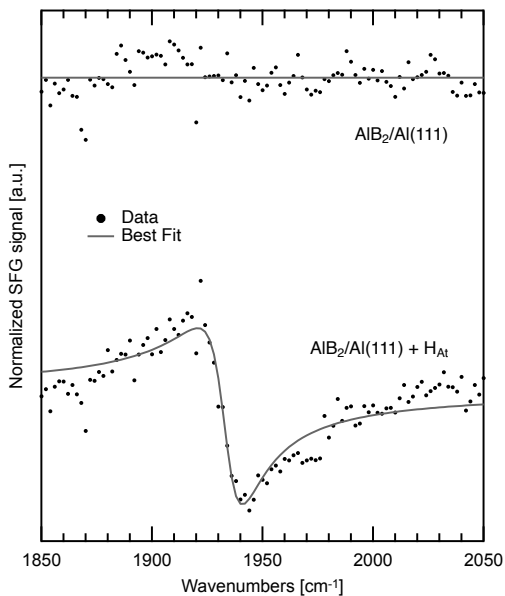
The thermal stability of the H-induced borophane superstructure was investigated by means of IR-Vis SFG spectroscopy by step-wise annealing the hydrogenated AlB_2 layer up to 473 K. The spectra collected at increasing annealing temperatures, along with best fit curves, are displayed in Figure 4.7b. By examining the results from the fit process we found out that the hydrogenated superstructure is stable up to approximately 400 K, at which point dehydrogenation occurs. This recovers the pristine AlB_2 phase, indicating that the reduction is reversible. These findings become clearer when studying the evolution of the SFG fitting parameters of spectra in Fig. 4.7b, with respect to the annealing temperatures. In particular, Figure 4.7c depicts the measured amplitude and gaussian width of the B-H resonance, with evolving trends highlighted by *guide for the eyes* lines. The sudden decrease in resonance amplitude at around 390 K suggests that most of the hydrogen atoms desorb at this temperature, while the gradual widening of the Gaussian width curve implies a simultaneous increase in thermal-induced disorder in the H superstructure as temperature rises.

The reversibility of the hydrogenation process was confirmed also on the basis of B 1s and Al 2p core level spectra.

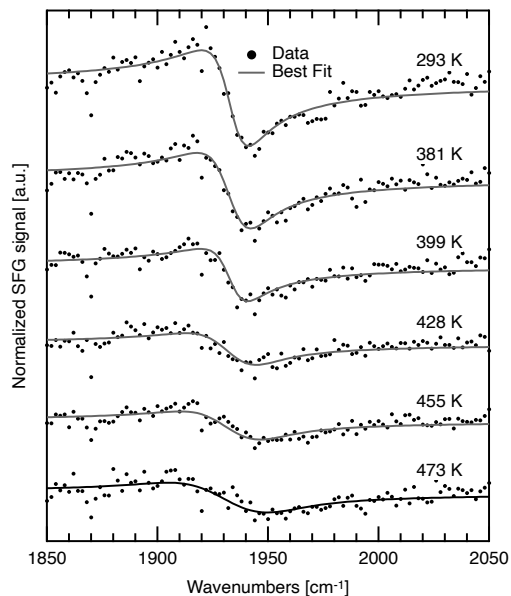
4.1.5 Comparison with DFT

The whole experimental picture presented above is corroborated by *ab initio* DFT approaches within the framework of an external collaboration.

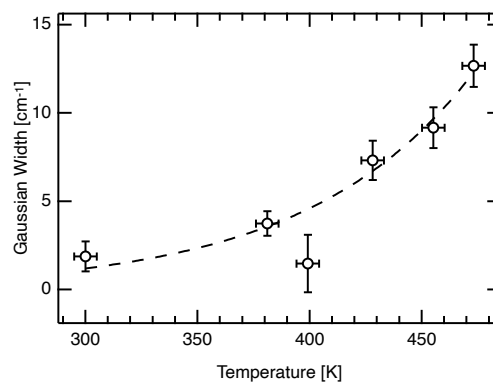
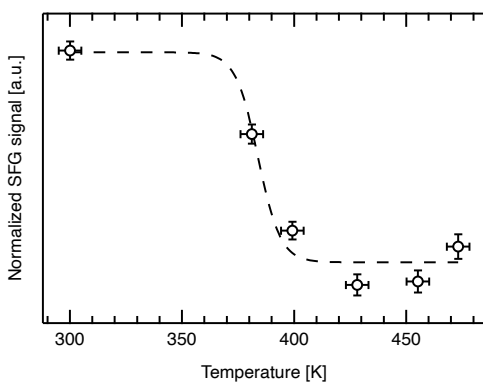
Global research for the best atomic structure for the hydrogenated $\text{AlB}_2/\text{Al}(111)$ system was performed by means of a genetic optimisation algorithm, based on several variation operators, including heredity, mutation, and permutation. Specifically, a precise set of structures, with varying B:H ratios, were generated based on the symmetry considerations of crystallography principles and thus energetically ranked in order to use the most energetically favourable configurations accessible as parents for the next generation. This



(a) IR-Vis SFG spectra of the pristine (top) and reduced (bottom) AlB_2 layer.



(b) IR-Vis SFG spectra of the reduced AlB_2 layer, annealed at increasing temperatures.



(c) Best Fit parameters of the IR-Vis SFG spectra in Fig. 4.7b with respect to the annealing temperature.

Figure 4.7

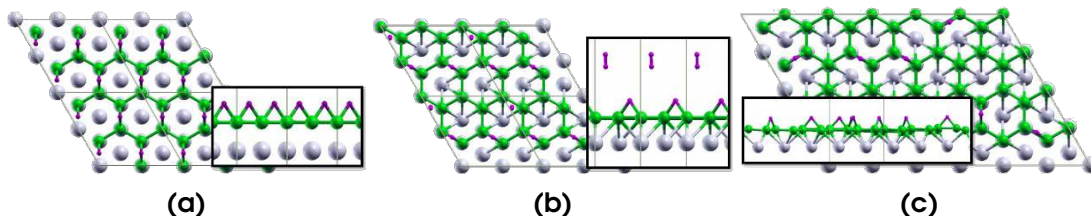


Figure 4.8: We report here the most significant H-hB/Al structures that we obtained by genetic algorithm methods. The saturated (1:2 H:B ratio) structure in **(a)** is energetically slightly less stable than the layer in **(b)**, where part of the H atoms was desorbed into the gas phase as H_2 molecules, leaving an average surface coverage of the order of 1:6 H:B ratio. The direct lateral interactions, however, are not sufficient to drive the ordering of the H network, neither if we enlarge the calculation cell **(c)**, meaning that a substrate-drive mechanism is expected.

iterative process allowed a comprehensive search of the interlayer/surface phase space, considering all possible combinations of structures, to identify the most stable and promising ones, which are depicted in Fig. 4.8. Notably, the best H structures on $AlB_2/Al(111)$ always yield bridge coordination sites for the H ad-atoms, thus confirming our experimental findings by means of IR-Vis SFG spectroscopy (See Sec. 4.1.4). Furthermore, we theoretically confirm that the 1:6 H:B ratio, previously suggested through LEED observations, represents saturation, since denser H loadings turned out to be energetically unstable, resulting in partial desorption of H atoms into the gas phase as H_2 molecules. Although the theoretical simulations correctly achieve the average saturation coverage, it is important to note that the weak H-H lateral interactions prevent to accurately account for layer ordering. Thus, symmetry and periodicity constraints observed experimentally were superimposed to the calculations, in order to obtain the final structure, which can be appreciated in Fig. 4.3.

In order to investigate the charge transfer induced by hydrogen adsorption on the AlB_2 layer, we compared the electronic accumulation and depletion induced by borophene or borophane bonding to the aluminium termination. The results are presented in Fig. 4.9, together with a plot of the averaged orthogonally charge transfer. Direct comparison of charge density difference between the bare and hydrogenated cases was prevented due to the impossibility to correctly simulate a single H atom in the used computational framework. The charge redistribution analysis, based on the DFT results, confirms that aluminium is hardly affected by hydrogenation, while mild n-doping of all boron atoms is

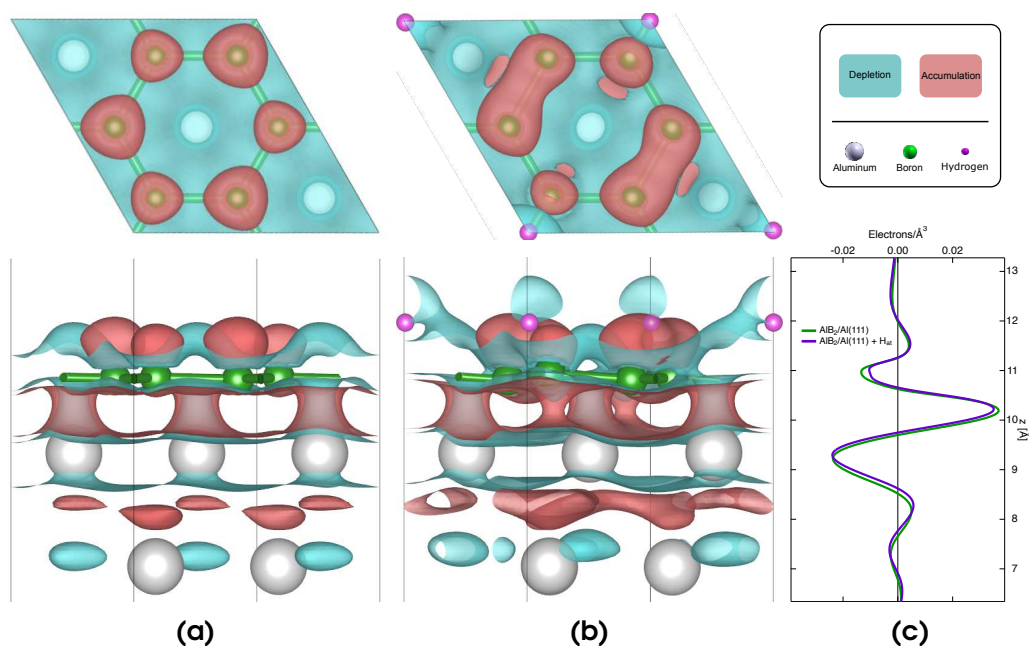


Figure 4.9: Electronic charge accumulation and doping. Electron depletion (cyan) and accumulation (red) induced by B bonding to the Al termination without **(a)** and with H **(b)** on the AlB_2 layer with respect to the separated phases evidenced by $0.002 \text{ e}^-/\text{\AA}^3$ isosurfaces (coloured envelopes) superimposed onto the relaxed structural models as obtained by *ab initio* calculations; **(c)** averaged charge accumulation/depletion in the direction orthogonal to the surface, aligned with the side views in **(a)** and H **(b)**.

observed, including those not directly bonded with H, with a stronger electron accumulation in the B-H bonding regions of the order of $10^{-3} \text{ e}^-/\text{\AA}^3$.

The impact of the atomic hydrogen exposure on the electronic configuration of the layer is most effectively evidenced by comparing the experimental spectroscopic data with theoretical calculations. Figure 4.10 depicts the comparison between the computed Density of States (DOS) and the collected valence band and B K-edge spectra. The DOS was calculated using the Quantum ESPRESSO code [82] and the occupation of tetrahedra method. This calculation is accompanied by a partial Density of States (pDOS), providing details on the various atomic orbitals' contributions to the AlB_2 DOS.

Examining the electronic structure of the system in detail reveals that the energy region just below the Fermi edge is mainly dominated by the boron σ contribution, which remains mainly unaffected by reduction. By contrast, above the Fermi level we witness several changes associated with the formation of the B-H bonds. As observed above, a distinct dichroic feature grows at 187.3 eV in the B edge π^* region, 0.3 eV above the energy zero (See Fig. 4.10). This is best observed in the difference spectrum reported below. Accordingly, our *ab initio* calculations put in evidence a 170 meV shift towards lower energies of both p_z and σ (p_x and p_y) DOS upon hydrogenation, accompanied by a narrowing of the σ gap from 4.65 to 4.50 eV.

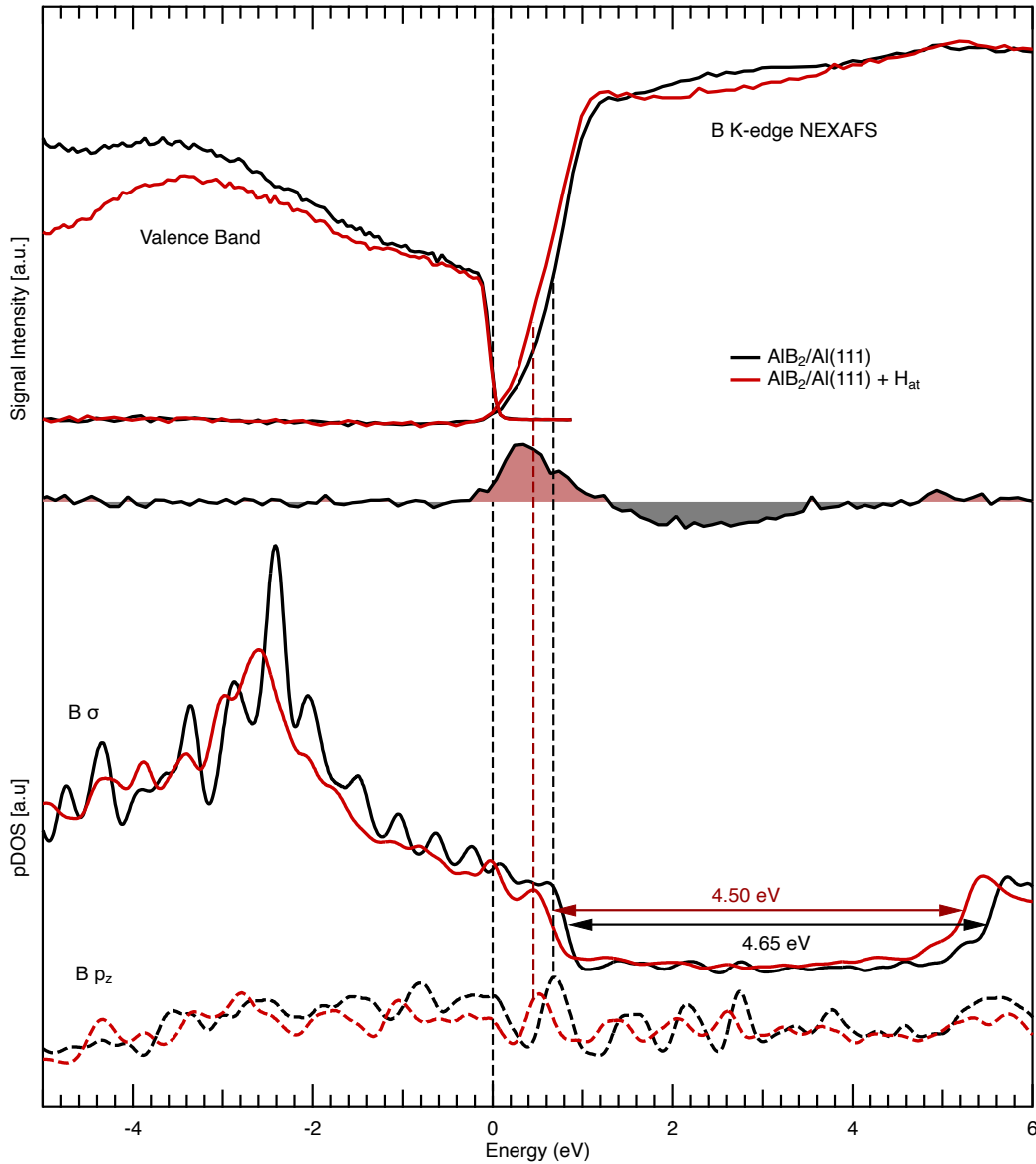


Figure 4.10: Experimental and theoretical characterisation of the electronic configuration of the layer. At the top, the experimental valence band (left, $h\nu = 80$ eV) and B K-edge NEXAFS spectra (right, \bar{E} vs z 20°) of the pristine (black) and hydrogenated (red) layers; just below the difference NEXAFS spectrum obtained from the spectra above; At the bottom, the calculated pDOS on the σ and p_z orbitals of the B layer. The alignment of the Fermi levels of the valence band spectra and calculated pDOS with the NEXAFS spectra was obtained according to recent work on the B mono- and multi-layers on Al(111) [17].

4.2 Oxidation of B/Al(111)

4.2.1 Sample Preparation

Cleaning of the metal substrate and B evaporation were performed following the recipes described in Section 3.1.1. Oxidation of the AlB_2 layer was obtained by post-exposure to molecular oxygen ($p_{\text{O}_2} = 10^{-8}$ - 10^{-7} mbar) in UHV background, in the range of 10^1 - 10^3 L.

4.2.2 XPS and NEXAFS

B 1s

Figure 4.11 shows the B 1s core level photoemission spectra collected at room temperature for the $\text{AlB}_2/\text{Al}(111)$ system, before and after exposure to molecular oxygen, together with their best fit curves and the corresponding deconvolution profiles for each spectral components.

Recalling the B 1s core level of the pristine layer, it features three spectral components that come from the B atoms forming a single B layer (B_1), a second B layer (B_2), and the B layer beneath the latter (B_3). Upon exposure up to 10^3 L of molecular oxygen at room temperature, two new boron components grow up. The small spectroscopic shoulder growing at 188.46 eV (B_5 , BE = +0.70 eV) is associated with interface boron species directly interacting with oxygen, contributing in the order of 1% to the overall intensity. Actually, this small sign of B oxidation occasionally appeared already at the stage of growing pristine AlB_2 due to a small oxygen contamination (See Fig. 3.3a) and is not exclusively related to the post-evaporation oxidation. Instead, a new distinct component develops at 187.0 eV (B_4 , BE = -0.72), at the expenses of the B_1 and B_3 components. The intensity of this new component grows gradually with increasing O_2 exposure, saturating at high doses (around 1000 L), and can be slightly increased further by post-annealing. The latter evolution can be appreciated in Fig. 4.11 together with the corresponding LEED images demonstrating that even prolonged oxidation cannot destroy the characteristic diffraction pattern of the pristine AlB_2 phase, proving the intrinsic high chemical stability of AlB_2 .

We assign the B_4 component to patches where AlB_2 has lost direct contact with the metallic substrate and is lying on the buried Al_xO_y termination. This is supported by the fact that the two components that left place for B_4 originate

from the AlB_2 layers in direct contact with the $\text{Al}(111)$ surface, namely the B_1 and B_3 components. In principle, it is not excluded that a hB monolayer and not the AlB_2 monolayer is on top of the Al_xO_y surface after this partial oxidation. However, the latter situation is deemed less favourable in terms of chemical stability. Notably, neither bulk oxide, nor B_xO_y phases, expected to contribute at much higher binding energies [83, 84], are observed, confirming the marginal influence of oxygen exposure upon the chemical state of B atoms.

Al 2p

Figure 4.12 shows the Al 2p core level photoemission spectra collected at room temperature for the $\text{AlB}_2/\text{Al}(111)$ system, before and after exposure to molecular oxygen.

Upon oxygen exposure, two not fully resolved spin-orbit doublets (indicated by up-pointing arrows in Fig. 4.12) can be detected at higher binding energies, as typical signs of aluminium oxidation at surfaces [85]. In addition, a small shoulder appears at lower binding energy ($2p_{3/2}$ at 72.4 eV, down-pointing arrows in Fig. 4.12) with respect to the main Al bulk peak ($2p_{3/2}$ at 72.6 eV), possibly due to low coordinated Al atoms associated with the roughening of the surface induced by oxygen adsorption, as can be appreciated examining the STM images in Fig. 4.15.

B K-edge

Figure 4.14 shows the B K-edge NEXAFS spectra collected at room temperature for the $\text{AlB}_2/\text{Al}(111)$ system, before and after exposure to molecular oxygen. The data, collected in the partial electron yield mode, are depicted as a function of the angle between the electric field of the impinging, linearly polarised X-ray radiation and the normal to the surface. All NEXAFS spectra are normalised to the incident photon intensity and to the integral intensity under the curves.

Upon oxygen exposure, NEXAFS B K-edge spectra do not undergo significant qualitative modifications, with the main resonances at 187, 189 (π^*), and 193, 202 eV (σ^*) remaining dominant also after oxidation. The resonances at 187 and 189 eV undergo a distinct change in their dichroic behaviour, suggesting a significant change in B atoms bonding orientation, but no significant energetic shift has been detected. This supports the conclusion that the topmost AlB_2 layer largely retains its electronic structure. The most significant change in the spectra

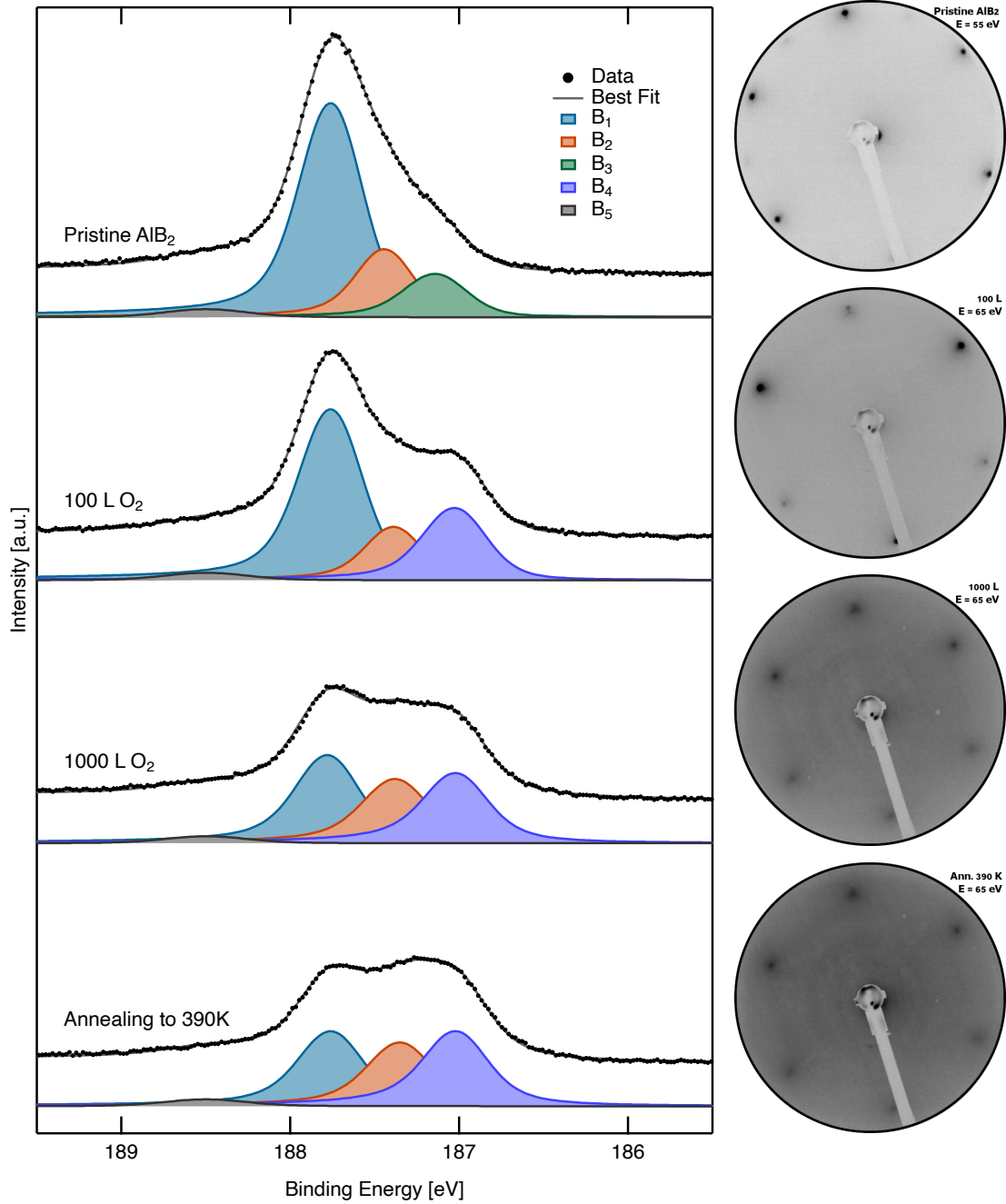


Figure 4.11: Dependence from oxygen exposure and post-annealing temperature of the AIB₂/Al(111) B 1s core level spectra (left, $h\nu=270$ eV) and LEED pattern (right).

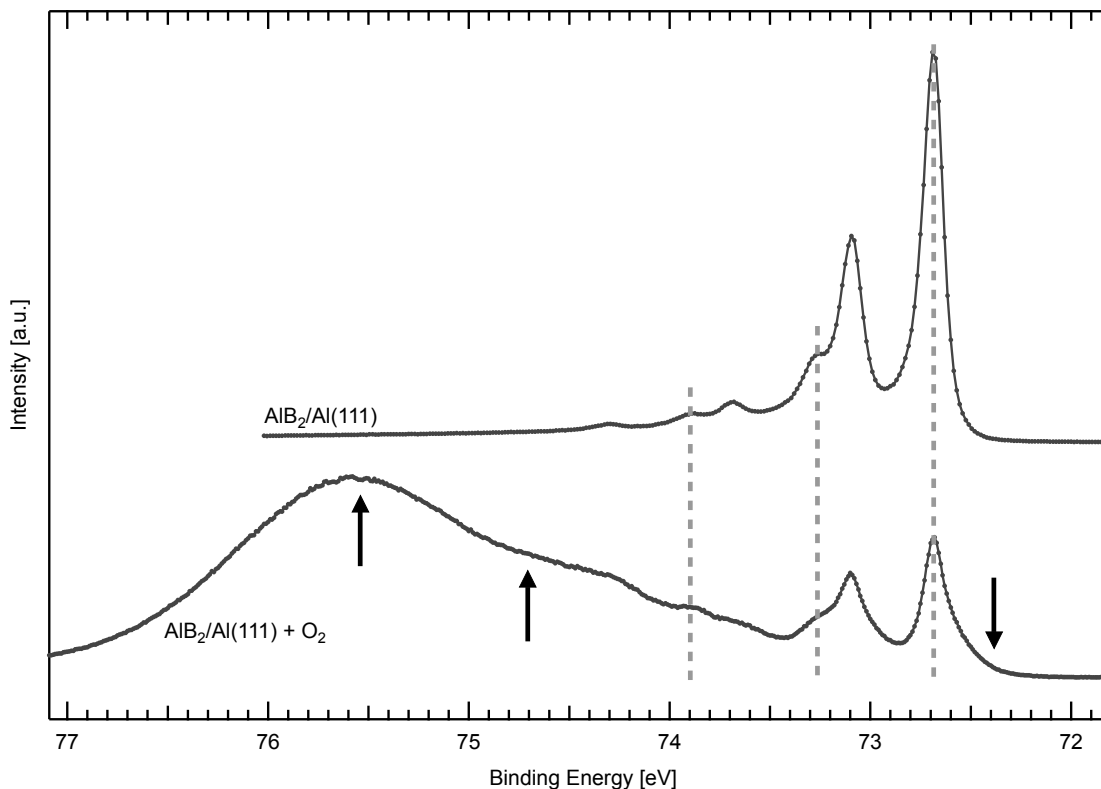


Figure 4.12: Al 2p XPS spectra for the oxidised and pristine $\text{AlB}_2/\text{Al}(111)$ system (acquired at $h\nu = 150$ eV).

occurs at 194.0 eV, where a small, yet distinct feature with π character can be detected. Specifically this resonance is a fingerprint of boron oxidation involving only a minor fraction of the layer, indeed associated with BO_3 planar groups on the basis of literature data [86–88]. This is fully consistent with our findings concerning the core levels analysis and the vibrational spectrum of the oxidised system.

4.2.3 SFG

Figure 4.14 shows the IR-Vis SFG spectra collected at room temperature for the $\text{AlB}_2/\text{Al}(111)$ system, before and after exposure to molecular oxygen together with their best fit curve and the corresponding deconvolution profile. The best fitting parameters are reported in Appendix B.2. As already mentioned in Sec. 4.1.4, the bare $\text{AlB}_2/\text{Al}(111)$ does not contribute with any resonant signal when probed by means of IR-Vis SFG vibronic spectroscopy. On the contrary, upon

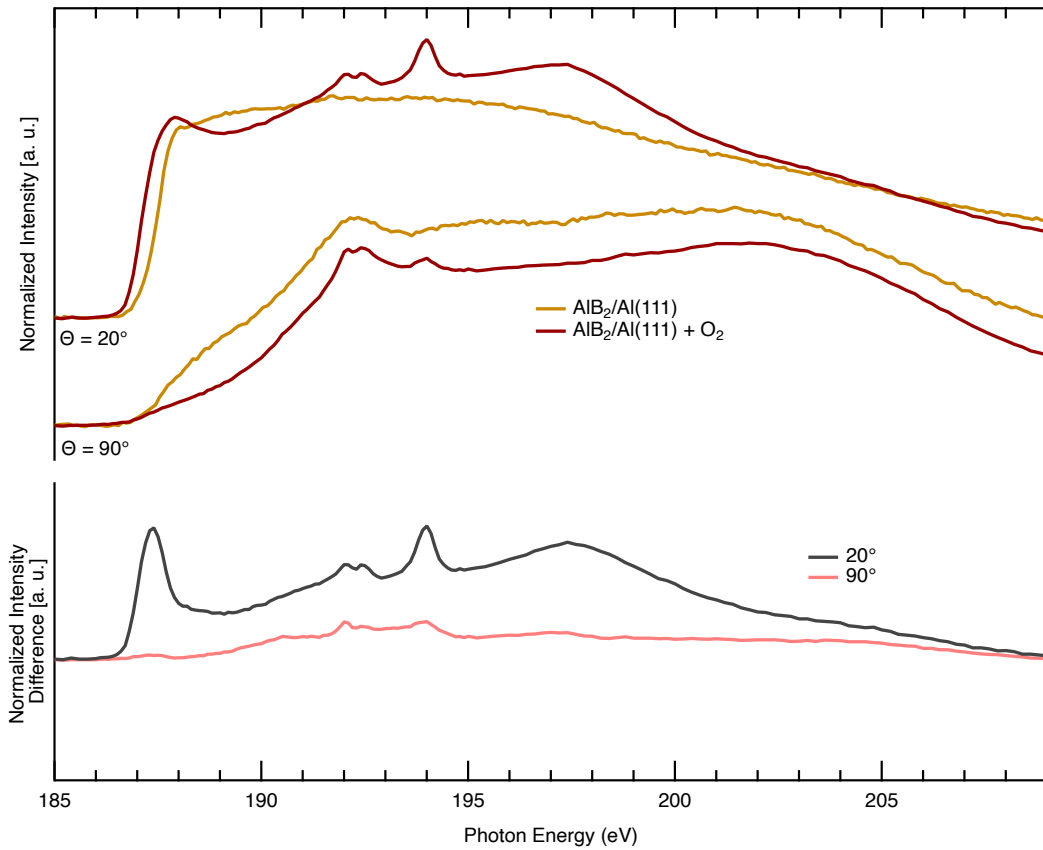


Figure 4.13: Angle-dependent NEXAFS B K-edge spectra for the $\text{AlB}_2/\text{Al}(111)$ system, before and after exposure to molecular oxygen, collected in partial electron yield mode. The directions refer to the angle between the electric field of the impinging, linearly polarised X-ray radiation and the normal to the surface. The modifications in the B absorption K-edge can be further appreciated by examining the difference spectra between the oxidized and the bare $\text{AlB}_2/\text{Al}(111)$.

oxidation, three low-amplitude resonances grow at 1200 , 1213 , and 1231 cm^{-1} , sharing a common decoherence-related linewidth but showing different phases with respect to the non-resonant background. This is compatible with the presence of different B-O bonds in minor interfacial boron species directly interacting with oxygen atoms. [89].

4.2.4 STM

The microscopic investigation of the system upon oxygen exposure by means of STM allowed to further characterise the oxidation process and to corroborate

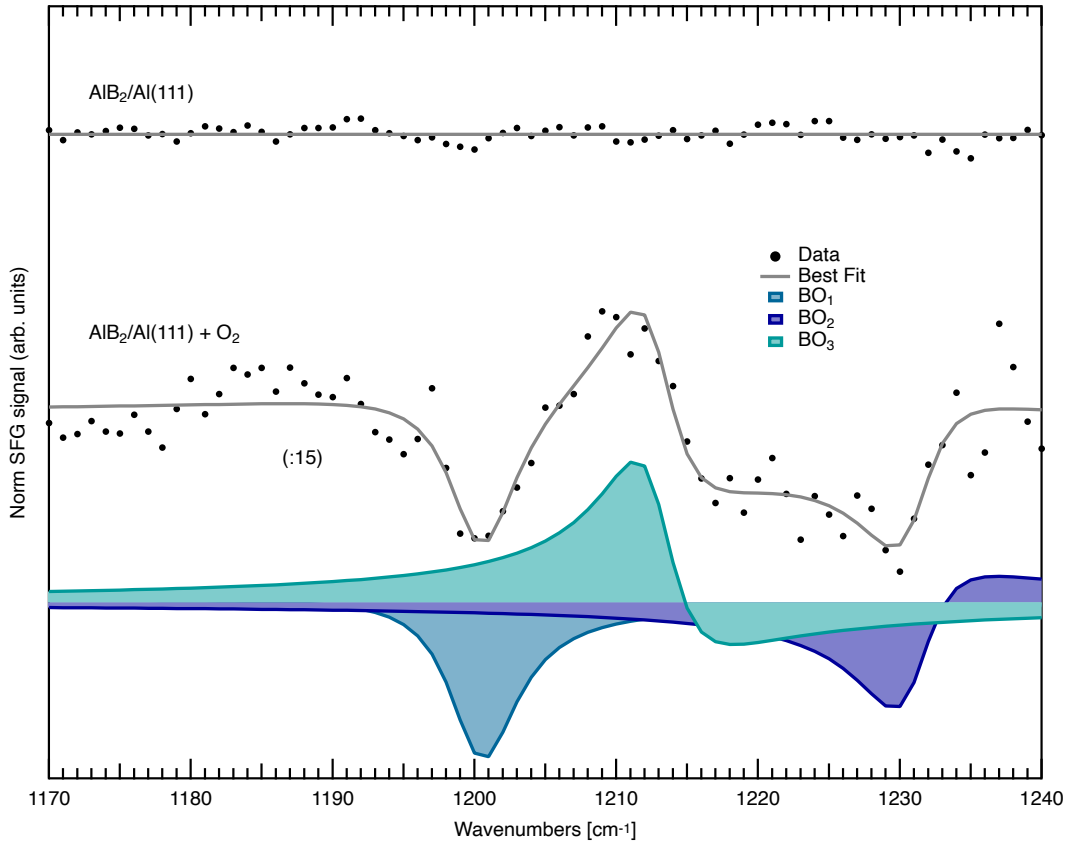


Figure 4.14: IR-Vis SFG spectra of the pristine and oxidised AlB_2 boron layer. The normalised data were best fitted and deconvoluted according to the line profile and non-linear susceptibility model described in the text and previously discussed.

rate the results from the spectroscopic analysis. In particular, in this section we will describe how the oxygen presence affects the Al-B phases (α , β , γ , δ , ϵ) detected on the bare $\text{AlB}_2/\text{Al}(111)$ system and described in Sec. 3.1.3. Specifically, the remaining clean Al islands (α) oxidise, developing amorphous Al_xO_y phases, characterised by their typical appearance [90], which can be appreciated in Figs. 4.15a and 4.15b. Regarding B-based phases, while apparently most of the order is lost on the $\text{AlB}_2/\text{AlB}_2$ (ϵ) phase, we observe instead 1D stripes growing on top of the β , γ , and δ phases, mainly oriented along the main crystallographic directions (See. Fig. 4.15). These stripes appear to be on top of pristine AlB_2 , showing a height corrugation of the order of $1\text{-}2 \text{ \AA}$, and a periodicity of 6.7 \AA , as can be appreciated examining the height profiles in Fig. 4.15. They could be ascribed to Al_xO_y clusters chains, accounting for both STM and Al 2p core level

evidences, at variance with borophene on Ag(111), where single O adatoms could be resolved and identified [91]. It's worth noting that these ordered 1D structures seem to appear only on AlB_2 phases characterised by the presence of the moiré superstructure, as can be appreciated in Table 3.1. This suggests that the moiré-induced corrugation of the AlB_2 layer steers the arrangement of the 1D cluster chains.

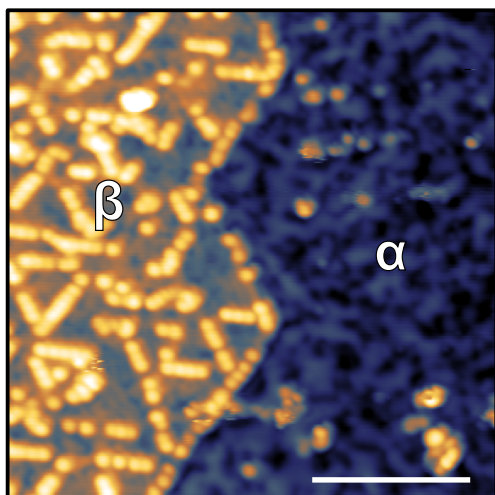
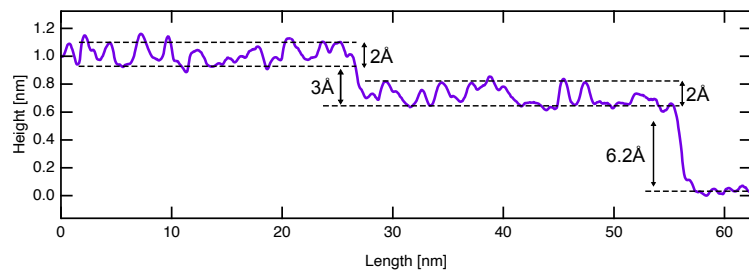
4.2.5 Comparison with DFT

The experimental picture presented above, in particular the oxygen tendency to intercalate the boron layers to strongly bond to Al, is corroborated by *ab initio* DFT approaches within the framework of an external collaboration.

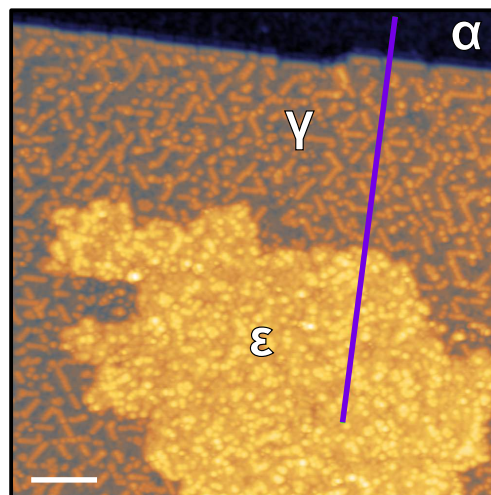
Specifically, the computational simulations did not focus on the entire AlB_2 supercell, which was already carefully characterised [17] and described in Sec. 1.2.3. Instead, we opted for a genetic algorithm approach with a smaller simulation cell. This method aimed to explore a broad range of relative B vs O coverage configurations, while simultaneously optimising various local structures and bonding geometries. By exploring the phase diagram along the oxygen and boron chemical potentials (See. Fig. 4.16), we can avoid the need to consider the entire AlB_2 supercell, which would be computationally too demanding. However, the drawback is the restricted simulation of the actual AlB_2 layer features that result from the strain caused by the $\text{AlB}_2/\text{Al}(111)$ lattice mismatch. Nevertheless, the charge redistribution upon formation of the AlB_2 layer is correctly reproduced as can be appreciated in Fig. 4.9a. We have thus tested several different starting parent structures, with oxygen atoms positioned both at the B layer or at the B-Al interface, spanning through the configurational space to identify the most energetically favoured candidates that were then relaxed so to reach the local metastable configurations.

Specifically, in the case of an oxygen-saturated surface and high B loadings (close to 2 ML of B, i.e. the nominal coverage of AlB_2 , corresponding to the γ structure as depicted in the STM images in Figs. 3.6 and 3.7), the lowest energy structures show oxygen intercalation at the interface, yielding Al oxidation.

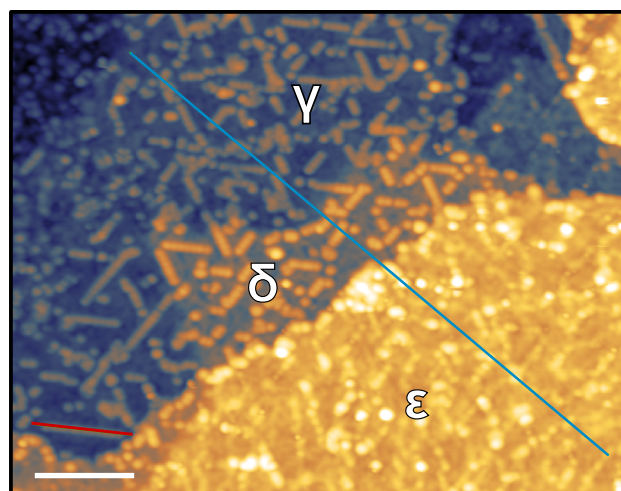
For lower local B loadings, or for low $\Delta\mu_{\text{O}}$, detachment of Al atoms from the substrate is energetically preferred, forming Al-O structures, or minor Al-B-O bonds at the boron layer, compatibly with the 1D stripes that we observe on top of the AlB_2 layers (See STM images in 4.15) and, thus, confirming our model



(a) Measuring parameters: $V_{\text{bias}} = +1.5 \text{ V}$, $I = 300 \text{ pA}$, scalebar = 10 nm.



(b) Measuring parameters: $V_{\text{bias}} = +1.0 \text{ V}$, $I = 300 \text{ pA}$, scalebar = 10 nm.



(c) Measuring parameters: $V_{\text{bias}} = +1.0 \text{ V}$, $I = 300 \text{ pA}$, scalebar = 10 nm.

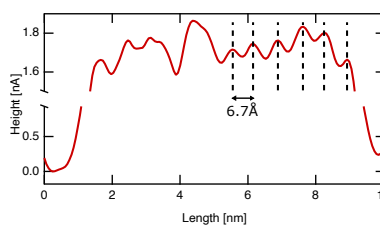
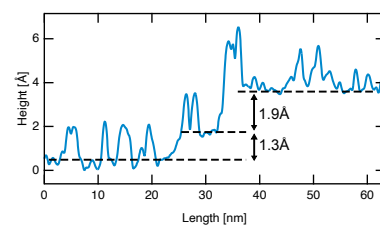


Figure 4.15: STM imaging of $\text{AlB}_2/\text{Al}(111)$ upon exposure to molecular oxygen with corresponding height profiles.

mechanism based on the experimental observations.

By spanning across the ($\mu_B - \mu_O$) chemical potential and ($\Theta_B - \Theta_O$) coverage spaces, several intermediate, metastable bonding geometries are achieved, but in all cases, preferential bonding of oxygen to Al rather than to B is observed. This results in the oxidation of the substrate termination, in single oxidised Al atoms segregated across the B layer, and in the formation of only minor ternary Al-B-O phases.

Regarding the induced charge transfer (boxes in Fig. 4.16), we obtain that in the pristine case electronic charge is accumulated at the B-Al interface up to $+0.035 e^-/\text{\AA}^3$, mainly originating from the Al atoms from the terminal Al(111) surface layer, well comparing with previous calculations on the complete supercell [17]. We then find that the oxidation process redistributes the charge, resulting in a charge density modulation of the order of $+0.015 e^-/\text{\AA}^3$. As a general trend, and as expected given its electronegativity, oxygen adsorption drains electrons from both the B termination of the film and from the interface (cyan shaded profiles in the boxes), accumulating electronic charge within the boron layer (red shaded profiles in the boxes).

In conclusion, boron oxide formation, on the Al(111) substrate, was neither theoretically predicted [92] nor observed experimentally. Instead, the oxidation of the Al termination induces the formation of 1D cluster arrays, favoured by the relative O-Al and O-B affinities, with the Al segregation and O diffusion processes across the B layers playing a critical role.

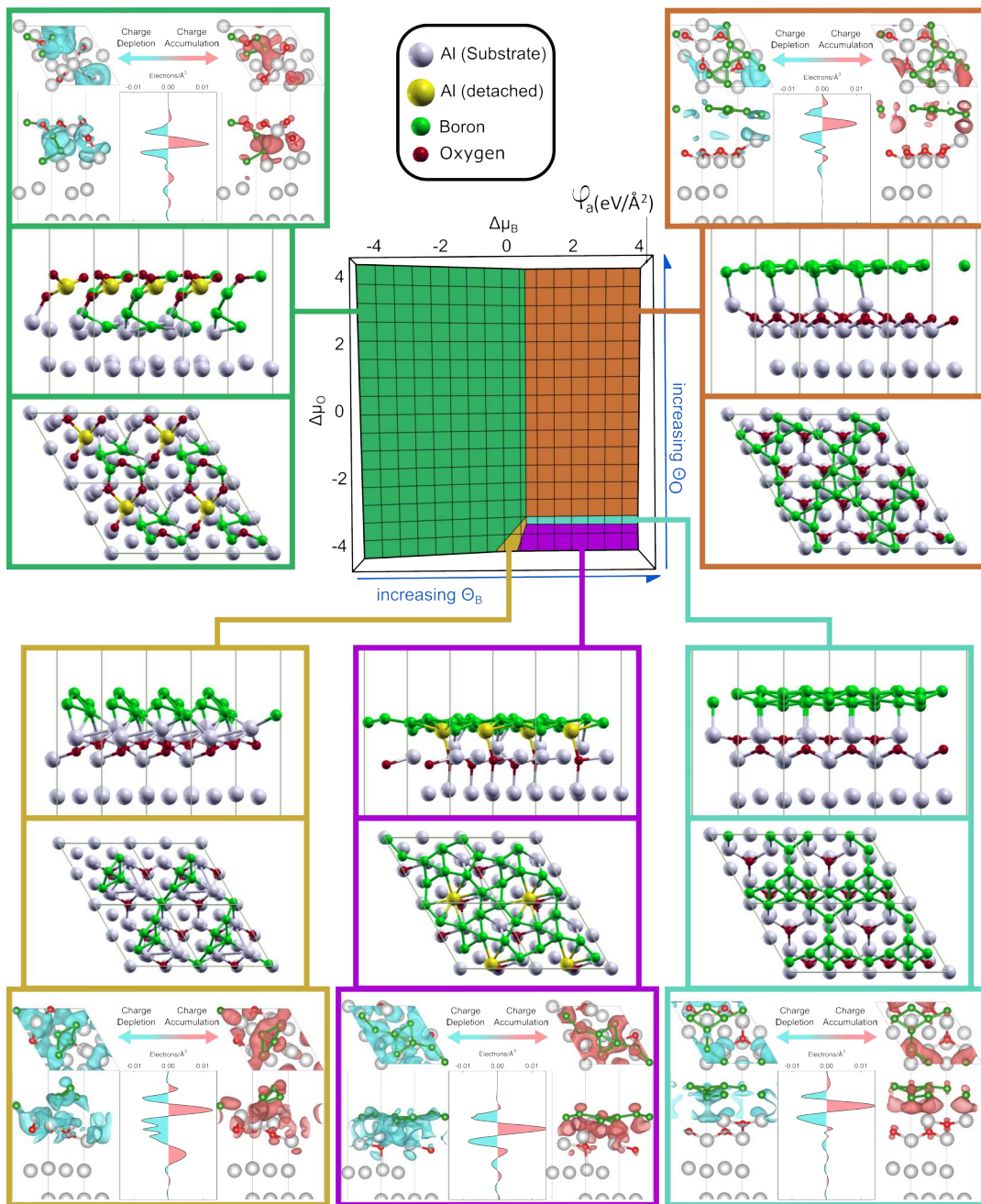


Figure 4.16: Best structures predicted by ab initio DFT combined with genetic algorithm search methods for the oxygen + boron system on Al(111). A phase diagram search was performed as a function of B and O coverage in relation with their chemical potential, confirming the tendency of oxygen to bind with aluminium and, under selected conditions, to promote its segregation to the top-most layer. For the most stable structures (boxes) geometry and charge transfer plots with corresponding $0.003 \text{ e}^-/\text{a.u.}^3$ charge density isosurfaces are shown.

4.3 Oxidation of B/Ni₃Al(111)

In this section we will investigate the B/Ni₃Al(111) system reactivity, which has been probed by controlled exposure of the sample to molecular oxygen. We are particularly interested in boron oxidation both for the possibility of decoupling and stabilising the B-layer through oxygen reactions but also for the likely significant practical implications for borophene-based applications as most devices require operation under ambient pressure conditions.

Although borophene is known to degrade quickly upon exposure to air [11], recent publications [93] report that it undergoes significantly more controlled oxidation when exposed to O₂ in UHV background. Thus, in this section we will explore this second route, investigating the possibility to oxidise the B/Ni₃Al(111) system by dosing O₂ both during and after boron evaporation.

4.3.1 LEED and AES

In this section, we will outline initial findings acquired through AES and LEED techniques, regarding the oxidation of the B/Ni₃Al(111) system during boron evaporation. Boron has been evaporated on the clean substrate (see Sec. 3.2.1) in molecular oxygen background at a controlled constant pressure in the UHV chamber. The exposure to O₂ has been varied between 9 and 36 L by tuning accordingly the oxygen pressure during each evaporation process, keeping the deposition time constant and consequently the amount of deposited boron fixed to the value of 2 ML.

Figure 4.17 displays the oxygen uptake through AES measurements, acquired in the energy ranges of the electronic transitions associated with the examined atomic species: boron, nickel, aluminium and oxygen. The growing amount of oxygen at the surface is confirmed by progressive increase in intensity of the O KLL transition (509 eV), which is below the detection limit for the bare Ni₃Al(111) and B/Ni₃Al(111) systems and becomes gradually more pronounced with the exposure. On the contrary, upon increasing the oxygen dose, the intensity of the metallic boron peak at 178 eV decreases in favour of two new features, left-shifted of about 10 eV and 25 eV, testifying the formation of B-O bonds. Regarding the Ni and Al LMM transitions region, the oxygen presence results in the dumping of both the Ni and Al peaks, with slight variations emerging in the relative intensities at the expense of the latter. At the oxygen exposure of 36 L,

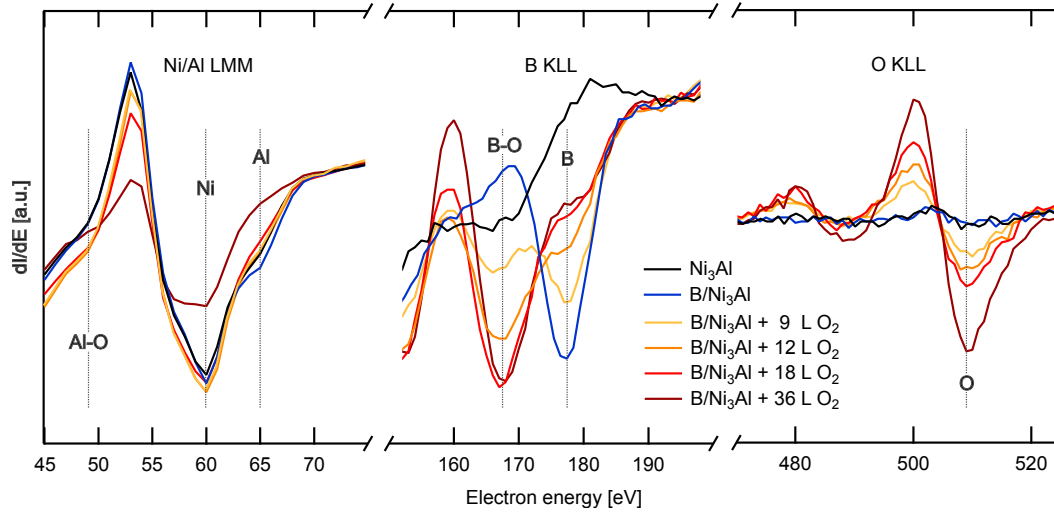


Figure 4.17: O_2 uptake illustrated by the AES spectra collected in three different energy ranges corresponding to boron, nickel-aluminium and oxygen transitions.

the aluminium peak intensity considerably decreases in favour of an amplitude modulation at 50 eV, which is attributed to the formation of aluminium oxide.

The oxygen uptake was monitored also by means of LEED (see Fig. 4.18), finding that the diffraction pattern progressively fades as a consequence of order loss at the surface as a consequence of oxygen adsorption. Nevertheless, upon oxygen exposure, some distinct changes in the relative intensity between different diffraction orders have been detected, suggesting the formation of ordered B-based oxidised structures.

4.3.2 XPS

In this section we report the spectroscopic investigation of the Ni $2p_{3/2}$, Al $2p$, B $1s$ and O $1s$ core levels in order to shed light onto the B/Ni₃Al(111) system electronic structure upon oxidation, by dosing molecular oxygen during and after boron evaporation. Specifically, here we report the results for three selected recipes:

- a) **B evaporation**, at sample temperature $T = 490$ K, with a deposition rate of 0.07 ML/min, for a deposition time $t = 30'$ and a measured B actual coverage $\Theta_B = 1.6$ ML;
- b) **Post-oxidation** of the B layer in a) to 18 L of O_2 , at $p_{O_2} = 4 \times 10^{-8}$ mbar, for $t = 10'$ and at sample temperature $T = 400$ K;

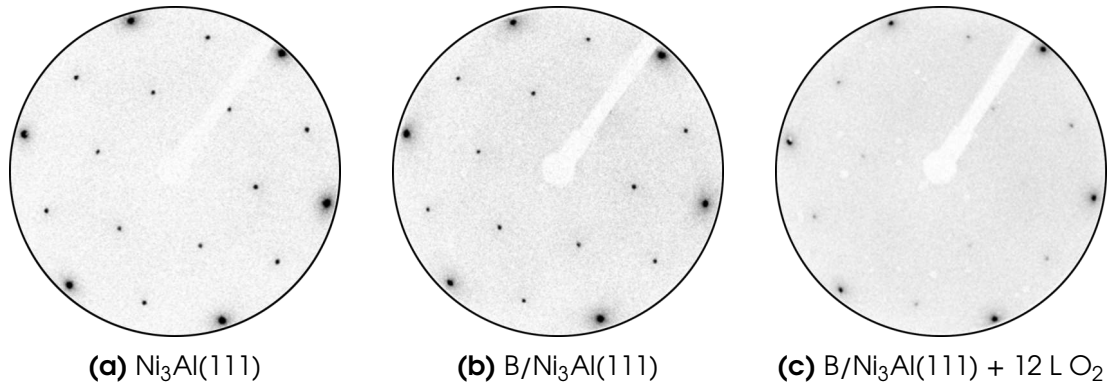


Figure 4.18: LEED diffraction pattern evolution upon boron evaporation and oxygen exposure (energy = 60 eV).

- c) **Peri-oxidation** during B evaporation, exposing the sample to 18 L of O₂, in a background pressure of $p_{\text{O}_2} = 1.3 \times 10^{-8}$ mbar for $t = 30'$ and at sample temperature $T = 490$ K, with B deposition rate of 0.07 ML/min.

Ni 2p_{3/2}

Figure 4.19 shows the Ni 2p_{3/2} core level photoemission spectra collected at room temperature and at $h\nu = 1000$ eV for the pristine, post-oxidised and peri-oxidised B/Ni₃Al(111) systems, together with their best fit curves and the corresponding deconvolution profiles for each spectral component. The best fitting parameters are reported in Appendix A.3.

Recalling the pristine B/Ni₃Al(111) system, its Ni 2p_{3/2} core level spectrum is characterised by two main deconvolution components, namely Ni₁ and Ni₂, ascribed to bulk and B-linked Ni atoms, respectively. Post-oxidising the system, the intensity of the Ni₂ component increases at the expense of that of Ni₁. Conversely, following the peri-oxidation, the observed trend is the opposite. Notably, oxidation during B evaporation results in the same Ni₂/Ni₁ area ratio as the pristine case. These relative intensity variations are likely the result of boron atom segregation to the surface due to oxygen adsorption, which consequently affects the fraction of Ni atoms bonded to B atoms and the concentration of Ni atoms on the surface.

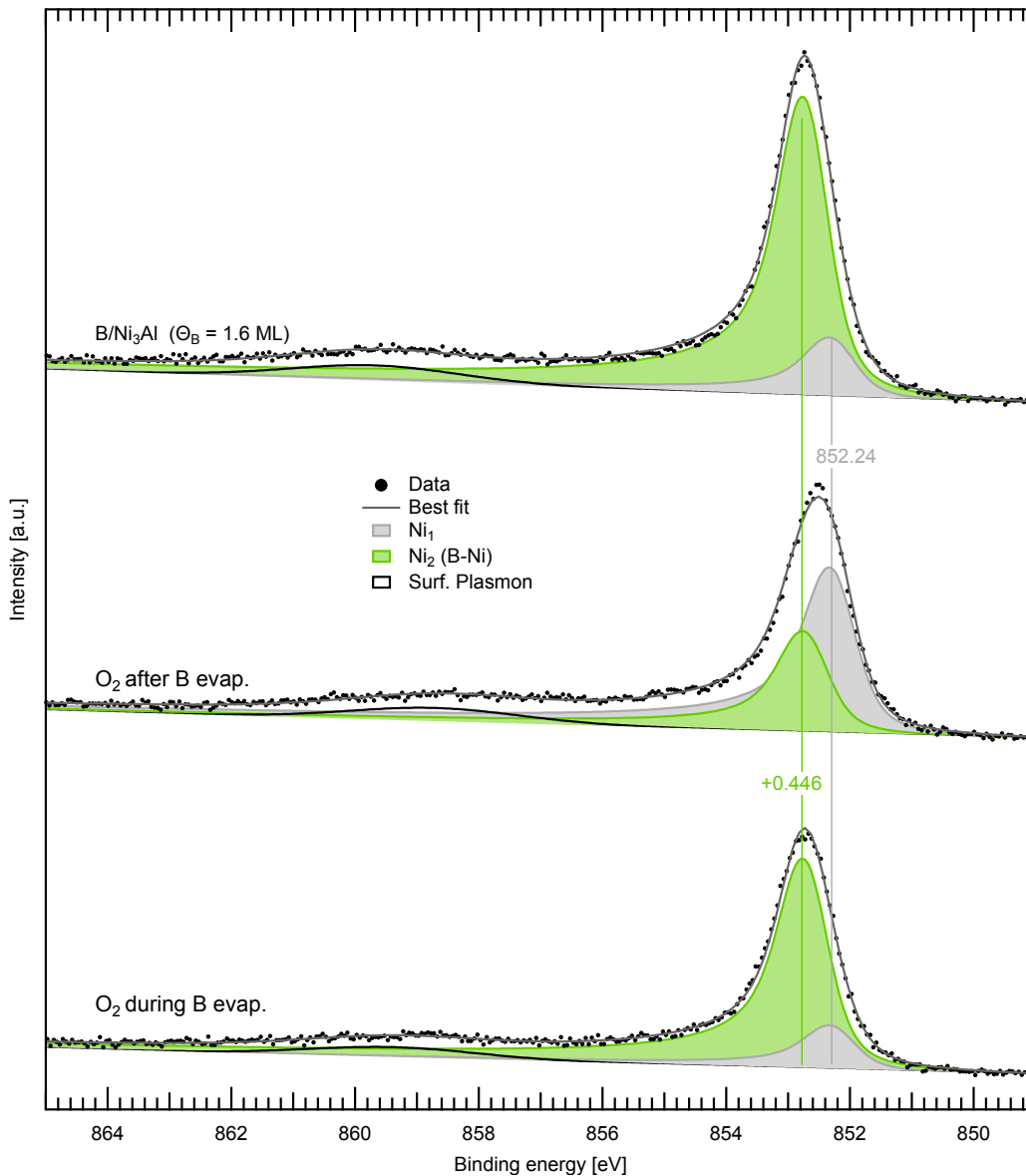


Figure 4.19: Ni $2p_{3/2}$ XPS spectra for the pristine and oxidised B/Ni₃Al(111) system (acquired at $h\nu = 1000$ eV) together with their best fit curves and the corresponding deconvolution profiles for each spectral components. The spectra can be fitted with three individual components, attributed to: the bulk Ni atoms (Ni₁, grey) at 852.24 eV, Ni atoms bonded to B atoms (Ni₂, green) at +0.446 eV and the surface plasmon component (white).

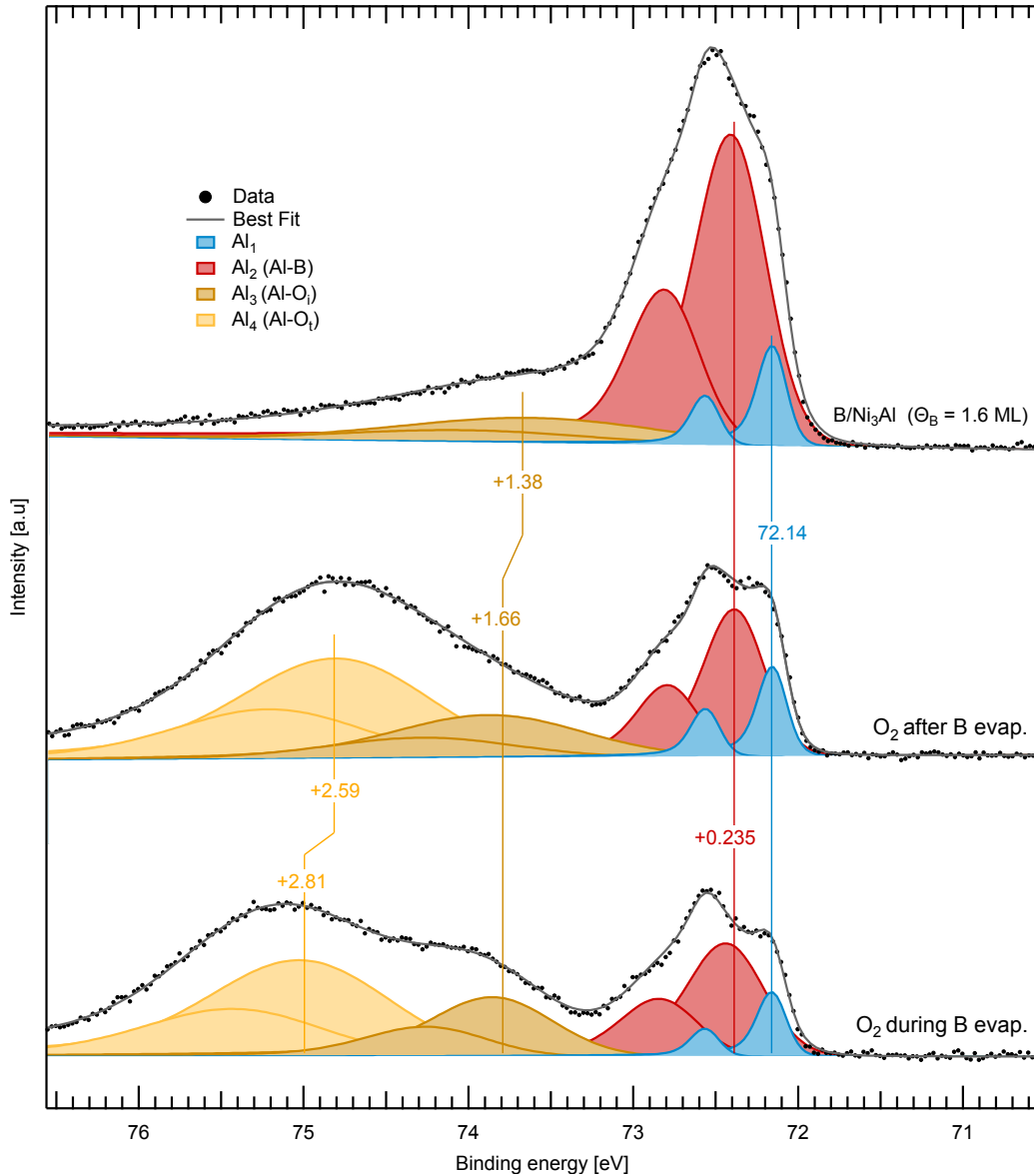


Figure 4.20: Al 2p XPS spectra for the pristine and oxidised B/Ni₃Al(111) system (acquired at $h\nu = 150$ eV) together with their best fit curves and the corresponding deconvolution profiles for each spectral components. The spectra collected upon oxygen exposure can be fitted with four spin-orbit components, attributed to: the bulk Al atoms (Al₁, blue) at 72.14 eV, Al atoms bonded to B atoms (Al₂, red) at +0.235 eV, the Al oxide interface (Al₃, brown) at +1.38/+1.66 eV, and the Al oxide termination (Al₄, yellow) at +2.59/+2.81 eV.

Al 2p

Figure 4.20 shows the Al 2p core level photoemission spectra collected at room temperature and at $h\nu = 150$ eV for the pristine, post-oxidised and peri-oxidised B/Ni₃Al(111) systems, together with their best fit curves and the corresponding deconvolution profiles for each spectral components. The best fitting parameters are reported in Appendix A.3.

Differently from the case of the Ni 2p_{3/2} core level, analysing the Al 2p spectra relative to oxidised systems, we detected similar evolution trends whether exposing B/Ni₃Al(111) to oxygen during or after B deposition. In particular, the intensities of both the Al₁ and Al₂ doublets decrease, with the latter showing a more pronounced reduction. Additionally, two larger features (Al₃ and Al₄), associated to aluminium oxide phases, emerge at higher binding energies. These new doublets are characterised by a significantly larger Gaussian broadening compared to that of the bare substrate contribution (0.81 and 1.20 vs 0.18 eV for Al₃ and Al₄, respectively). In addition, the Al₄ component undergoes a positive shift of 0.22 eV in the case of peri-oxidation with respect to the post-oxidation process. On the basis of previous studies from the literature, about the growth of aluminium oxide films on the NiAl(110) [94, 95] and Ni₃Al(111) [21] surfaces, the Al₃ and Al₄ doublets can be attributed to the oxide interface layer in contact with the substrate (+1.66 eV, Al-O_i) and to the oxide termination (+2.59 or +2.81 eV, Al-O_t), respectively, of an Al oxide bilayer film.

B 1s

Figure 4.21 shows the B 1s core level photoemission spectra collected at room temperature and at $h\nu = 270$ eV for the pristine, post-oxidised and peri-oxidised B/Ni₃Al(111) systems, together with their best fit curves and the corresponding deconvolution profiles for each spectral components. The best fitting parameters are reported in Appendix A.3.

The oxidation of the system, whether after or during B evaporation, results in significant intensity modulations in the B 1s core level spectrum. First of all, upon calculating the spectral integral, it is evident that the area of the spectra relative to the oxidised cases is approximately double that of the pristine B/Ni₃Al(111) spectrum. These findings provide further support for the interpretation that oxygen plays a crucial role in the segregation of boron atoms from the bulk to the surface. Getting into closer details, the intensities of the B₂ and B₃ components

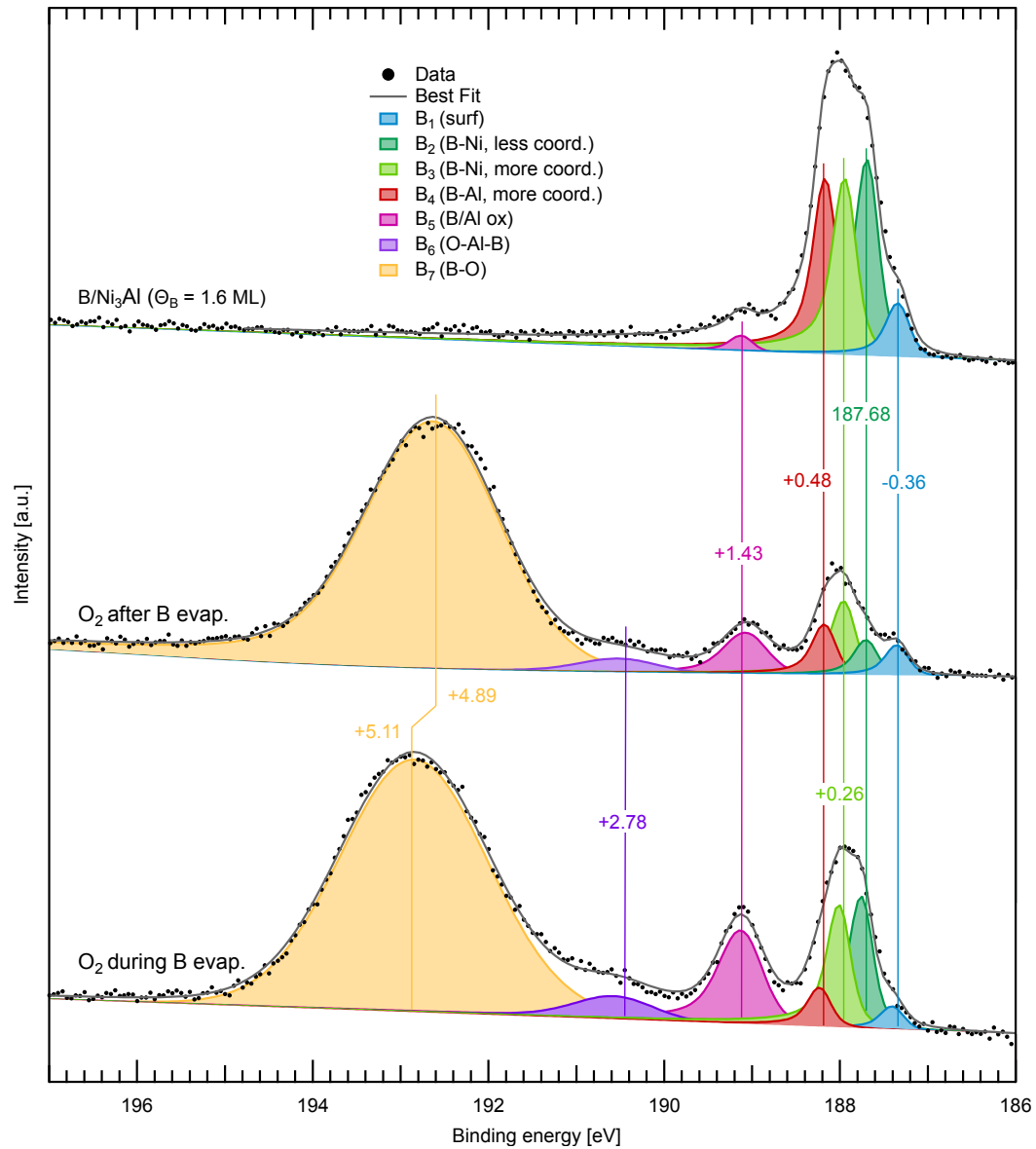


Figure 4.21: B 1s XPS spectra for the pristine and oxidised B/Ni₃Al(111) system (acquired at $h\nu = 270$ eV) together with their best fit curves and the corresponding deconvolution profiles for each spectral components. The spectra collected upon oxygen exposure with seven individual components, attributed to: surface B atoms (B_1 , blue) at -0.36 eV, less coordinated B atoms bonded to Ni atoms (B_2 , dark green) at 187.68 eV, more coordinated B atoms bonded to Ni atoms (B_3 , light green) at $+0.26$ eV, more coordinated B atoms bonded with Al atoms (B_4 , red) at $+0.48$ eV, B atoms on Al oxide (B_5 , pink) at $+1.43$ eV, B atoms involved in a ternary phase (B_6 , purple) at $+2.78$ eV, and B oxide atoms (B_7 , yellow) at $+4.89/+5.11$ eV.

and of B_4 follow the evolution trend of the Ni_3 and Al_2 components, respectively, reflecting their behaviour in the case of the pristine $B/Ni_3Al(111)$ system. Specifically, upon post-oxidation, all metallic B components (B_1 , B_2 , B_3 and B_4) decrease in intensity in favour of three distinct additional features (B_5 , B_6 and B_7) developing at higher binding energies. Upon peri-oxidation, the same trend is observed but with a weaker suppression of the B_2 and B_3 components, which are ascribed to Ni-bonded B species. Regarding the newly grown components, B_5 is ascribed to boron atoms on Al oxide, B_6 to boron atoms involved in a Al-B-O ternary phase, while B_7 , which is characterised by a Gaussian broadening six times larger than that of B_2 (1.68 vs 0.22 eV), is ascribed to boron oxide atoms. Moreover, the latter component exhibits a similar trend with respect to Al_4 undergoing a positive shift of 0.22 eV in the peri-oxidation case compared to the post-oxidation one.

O 1s

Figure 4.22 shows the O 1s core level photoemission spectra collected at room temperature and at $h\nu = 650$ eV for the pristine, post-oxidised and peri-oxidised $B/Ni_3Al(111)$ systems, together with their best fit curves and the corresponding deconvolution profiles for each spectral components. The best fitting parameters are reported in Appendix A.3.

The O 1s spectra relative to the oxidised cases are best fitted using two main deconvolution components, namely O_1 and O_2 . Based on the literature regarding $Ni_3Al(111)$ oxidation [21], the aluminium oxide formation leads to the growth of two distinct components in the O 1s core level spectrum, namely O_i and O_t , due to oxygen atoms at the metal-oxide interface and at the oxide terminal layer, respectively.

In the case of $B/Ni_3Al(111)$ oxidation, the peak at lower binding energy (O_1), at 531.0 eV, which positively shifts by 0.11 eV in both cases, can be attributed to both interface aluminium oxide atoms (O_i-Al) and atoms involved in the formation of a ternary phase (O-Al-B). However, it is not possible to resolve the two contributions due to the intrinsic linewidth of the O 1s spectral line, the further broadening due to local charging effects in the case of dielectric materials, and the variability of the nearest neighbour bond lengths resulting in a broad bond length distribution function [21, 77]. Regarding the ternary O-Al-B phase, we suppose that it relates the O_1 , Al_3 , B_5 and B_6 components, while previous

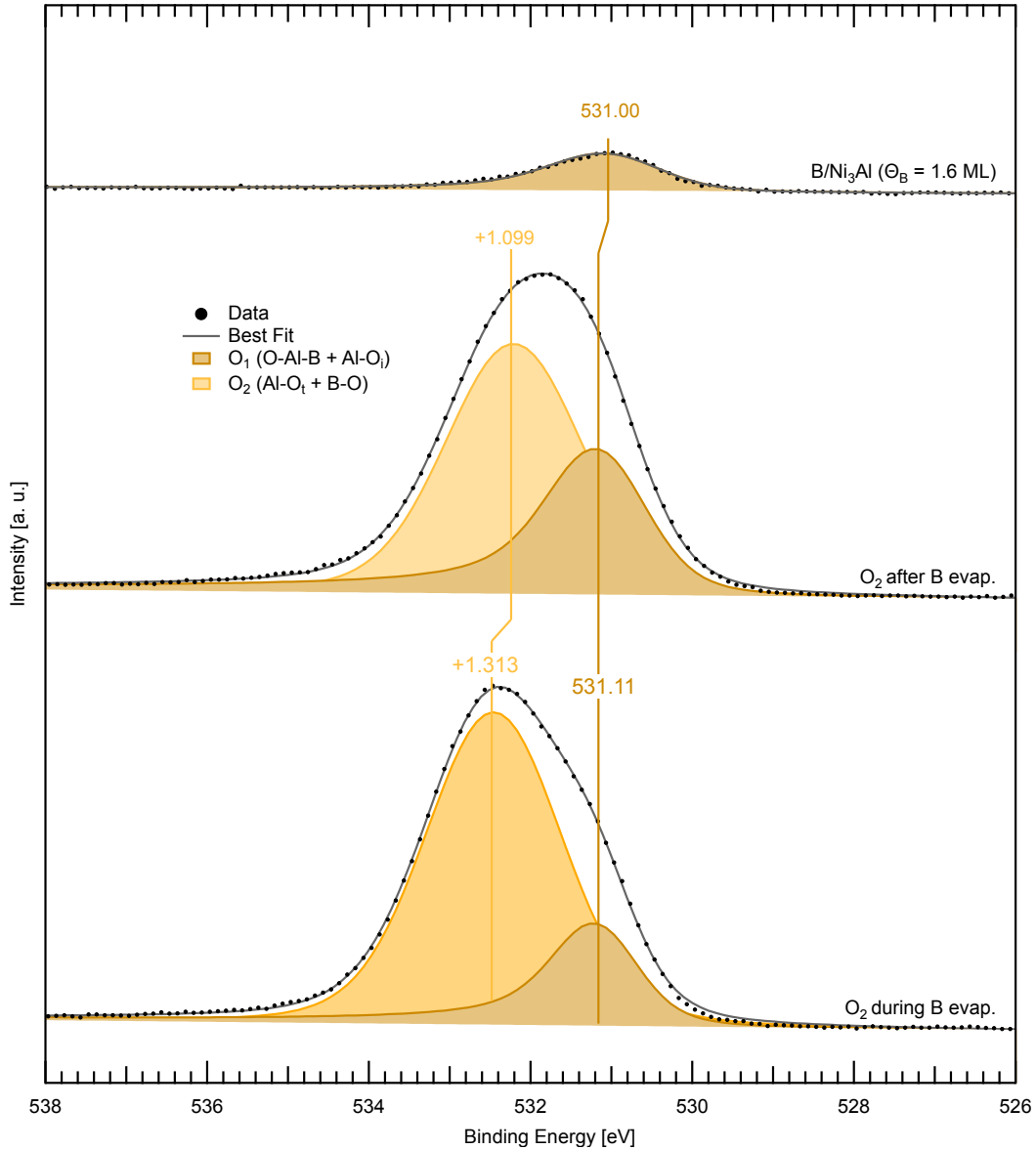


Figure 4.22: B 1s XPS spectra for the pristine and oxidised B/Ni₃Al(111) system (acquired at $h\nu = 650$ eV) together with their best fit curves and the corresponding deconvolution profiles for each spectral components. The spectra collected upon oxygen exposure with two individual components, attributed to: the Al oxide interface and a ternary phase (O_1 , brown) at 531.0/531.11 eV and the the Al oxide termination and the B oxide (O_2 , yellow) at +1.099/+1.313 eV.

	BE [eV]	Attribution
Ni₁	852.24	Ni bulk atoms
Ni₂	+0.446	B-bonded Ni atoms
Al₁	72.14	Al bulk atoms
Al₂	+0.235	B-bonded Al atoms (Al adatoms)
Al₃	+1.38 → +1.66	Aluminum Oxide interface phase
Al₄	+2.59 → +2.81	Aluminum Oxide terminal phase
B₁	-0.35	less coord. trimer B atoms
B₂	187.68	less coord. substitutional B atoms
B₃	+0.25	more coord. substitutional B atoms
B₄	+0.48	more coord. trimer B atoms (Al-bonded)
B₅	+1.43	B atoms on Al oxide
B₆	+2.78	Al-B-O ternary phase
B₇	+4.89 → +5.11	Boron Oxide
O₁	531.00 → 531.11	Al-B-O & Al-O _{interface}
O₂	+2.78	Al-O _{interface} & Boron Oxide

Table 4.1: Deconvolution components of Ni 2p_{3/2} Al 2p and B 1s core-level photoemission spectra and their respective binding energies and attributions.

works suggest that the metal-oxide interface might contribute to the O₁ and Al₃ peaks.

Concerning the higher binding energy peak (O₂), appearing at +1.099 eV or +1.313 eV in the two oxidation cases, it can be related to both terminal aluminium and boron oxides, but it is difficult to distinguish between these two contributions as they both belong to the same energy range. Specifically, the former species (O_†-Al) is related with O₂ and Al₄ components [21], while the latter (B-O) is attributed to O₂ and B₇ peaks [83, 96]. The assignment of O 1s spectral features are in line with the observations discussed previously and are summarized in Table 4.1.

Chapter 5

P/Au(111)

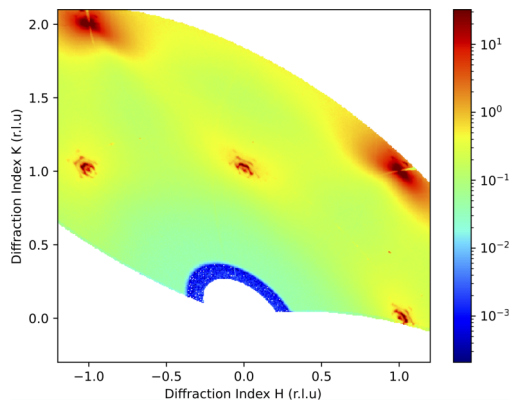
5.1 Sample Preparation

The Au(111) surface was cleaned by repeated cycles of Ar⁺ sputtering ($I_{\text{sputt}} = 10 \mu\text{A}$, $t = 15'$, $E_{\text{sputt}} = 1.5 \text{ keV}$) and annealing at about 870 K. The Blue Phosphorene (BlueP) film was grown on the Au surface by PVD: RedP (commercially available with 99.999% purity from Sigma Aldrich) and BlackP (prepared according to a known recipe [43] starting from commercial RedP as the source of P, and Sn and SnI₄ as mineralization additives) were sublimated from a Knudsen cell heated at about 600 K in UHV and directed towards the Au sample kept at 520 K.

The crystalline quality of both Au(111) and BlueP film were checked by monitoring the LEED and SXRD diffraction patterns before and after P deposition. The spots associated with the well-known herringbone reconstruction of the Au(111) surface are clearly visible both in the LEED and SXRD diffraction patterns of the pristine surface (see Figures 5.1a and 5.1b) but gradually disappear with the increasing P coverage, giving way to the spots associated with the formation of the (5 x 5) structure, characteristic of BlueP on this substrate, once the nominal coverage of 1 ML has been reached (see Figures 5.1e and 5.1f). At lower coverages, from the diffraction patterns in Figures 5.1c and 5.1d it is possible to appreciate the formation of a (6 x 6) structure of BlueP characterised by a lower surface density of P atoms.



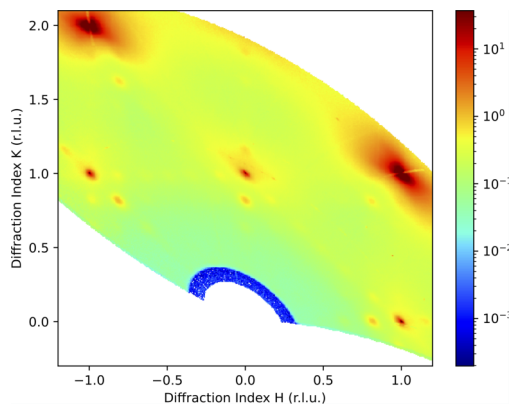
(a) LEED diffraction pattern of clean Au(111) surface at $E=60.6$ eV



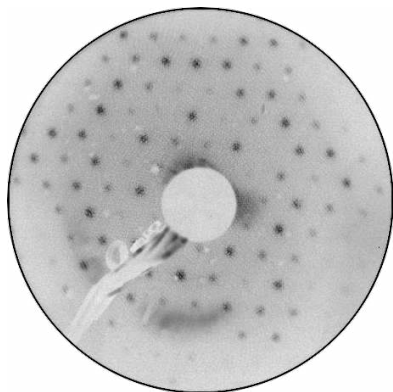
(b) SXR D in-plane reciprocal space map of clean Au(111) surface for $L=0.1$



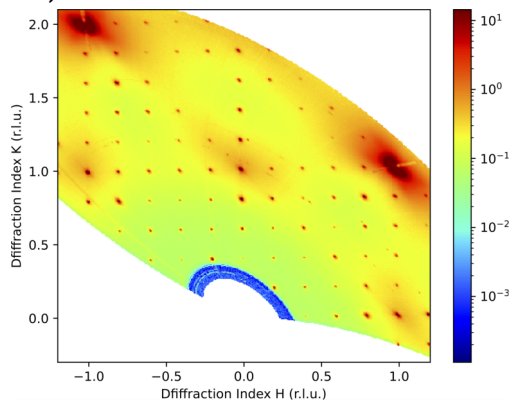
(c) LEED diffraction pattern of BlueP/Au(111) at $E=60.6$ eV ($\theta \sim 0.8$ ML)



(d) SXR D in-plane reciprocal space map of BlueP/Au(111) for $L=0.1$ ($\theta \sim 0.8$ ML)



(e) LEED diffraction pattern of BlueP/Au(111) at $E=60.6$ eV ($\theta \sim 1$ ML)



(f) SXR D in-plane reciprocal space map of BlueP/Au(111) for $L=0.1$ ($\theta \sim 1$ ML)

Figure 5.1: LEED and SXR D diffraction patterns before and after P deposition.

5.2 Black and Red P yield the same Blue

Figure 5.2 displays a direct comparison of SXRD data of BlueP/Au(111) grown from RedP and BlackP. The two sets of rods display the same sequence of peaks and valleys and they are fully compatible unless for a scaling factor within the experimental error bars. Given the fact that SXRD is a technique sensitive to atomic displacement of the order of $<10^{-2}$ Å this result provides a further experimental evidence in favour of the previously proposed thesis ([97]) that the BlueP structure is the same whenever it was obtained evaporating Black or Red P. The physical reason behind the latter phenomena can be unveiled by looking closely at the transition mechanism towards the gas phase of the two allotropes: both sublime in the form of small P clusters, mainly P_2 and P_4 , which then condensate from the gas phase at the Au(111) surface. This result could be of real importance for technological and industrial applications as it was proved that in order to grow BlueP on the Au(111) surface termination it's not mandatory to utilise the BlackP allotrope as a precursor, which requires a specific time- and energy-consuming synthesis process. In fact, the already commercially available and considerably less expensive red allotrope (RedP) could be successfully exploited. This is a remarkable result in terms of the future scalability of the growth process, a crucial step in enabling this system to be exploited in technological applications in a large-scale industrial environment.

5.3 Structure determination of BlueP/Au(111)

The main aim of this experiment was to shed light onto the geometric structure of the BlueP film on Au(111) and, in particular, to discriminate between two structural models, depicted in Fig.5.3. The main difference between the two lies in the incorporation of substrate Au adatoms bridging the pyramidal islands of BlueP. In particular, the $P_9 \times 2 + Au_9$ model, most recently proposed by Zhao *et al.* [44], consists of two pyramidal islands of 9 P atoms each, which are linked together by 3 Au adatoms on each side. The second model, $P_9 \times 2$, retains the two pyramidal BlueP islands but without the bridging Au adatoms. The following section presents the primary experimental outcomes and a thorough comparison with theoretical results. It is noteworthy that the author did not actively participate in the STM and ARPES analysis and theoretical research. Nevertheless, the latter findings were obtained in the framework of a scientific collaboration and are

presented here in order to give a complete picture of the subject under investigation.

5.3.1 STM

Figure 5.4 contains a direct comparison between experimental, atomically resolved, STM topography and simulated images for both models. The surface consists of a rhombic unit cell containing two triangular, mirrored protrusions of three atoms each, separated by an intermediate atomic level. Hexagonal-shaped depressions, with precise orientation, emerge at the corners of the unit cell, sometimes filled with additional P clusters [41, 42]. Simulated images reveal comparable features with the experimental counterpart, including triangular, mirrored protrusions and hexagonal depressions, yet also show some subtle discrepancies. The intermediate level situated between the mirrored protrusions are composed of a triple intensity modulation along the mirror axis in both models, however, the shape varies slightly between the two. Furthermore, the orientation of the hexagonal (black) depression in the models varies by 30° , aligned with the experimental counterpart for the $P_{\phi} \times 2 + Au_{\phi}$. Consequently, this model, with an additional 9 Au atoms, appears to be in better agreement with the experimental STM data. Nevertheless, it is worth noting that certain features can only be distinguished in experimental data obtained with a perfect, rounded scanning tip. In fact, even the careful examination of our experimental STM image reveals that it was produced by a very sharp but slightly asymmetric tip. Such artefacts are common and can lead to erroneous experiment-theory comparisons, as was observed with the atomic models initially proposed in the literature. Therefore, based solely on STM data, even supported by high-quality atomically-resolved images, comparison between theory and experiment cannot be definitive, retaining the possibility to provide relatively strong qualitative indications about the correct model.

5.3.2 ARPES

The SPELEEM microscope collects ARPES data as a stack of angle-resolved maps of the photoemitted electrons obtained by changing the probed electron kinetic energy, i.e. the binding energy (BE), for a selected impinging photon energy. Thus, the measurement delivers a 3D volume of data displayed along three axes, namely k_x , k_y (i.e. the electron momentum components parallel to

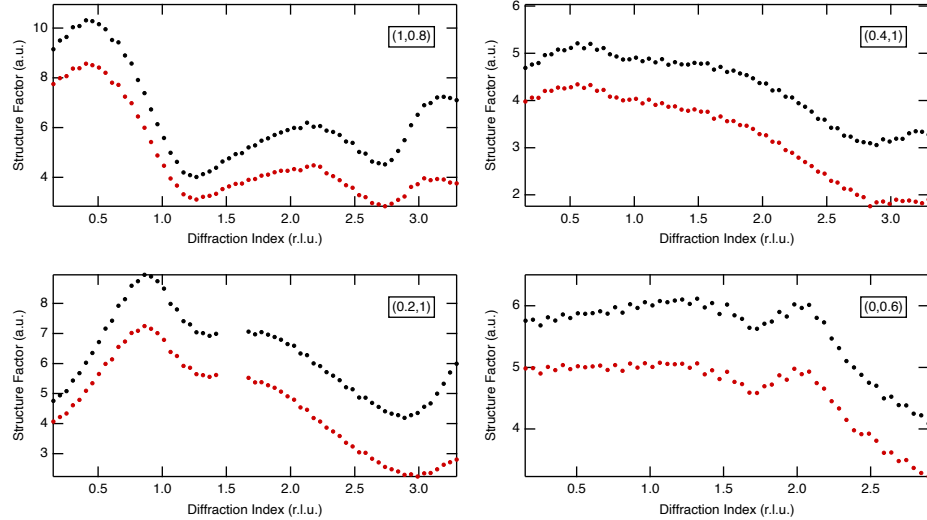


Figure 5.2: Selection of SSRs from the BlueP/Au(111) system obtained evaporating RedP (in red) or BlackP (in black). The scaling offset between the two groups of curves is likely due to slightly different experimental conditions such as the P coverage on sample.

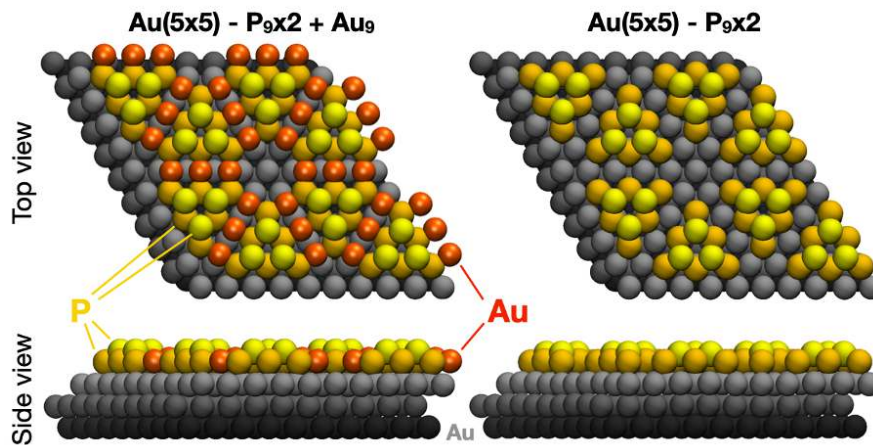


Figure 5.3: top and side view of ball rendering models of four (5 x 5) unit cells of BlueP/Au(111). The Au(111) slab is displayed in grey, the Au adatoms in red and the P atoms constituting the BlueP triangular islands in dark (lower) and light (higher) yellow.

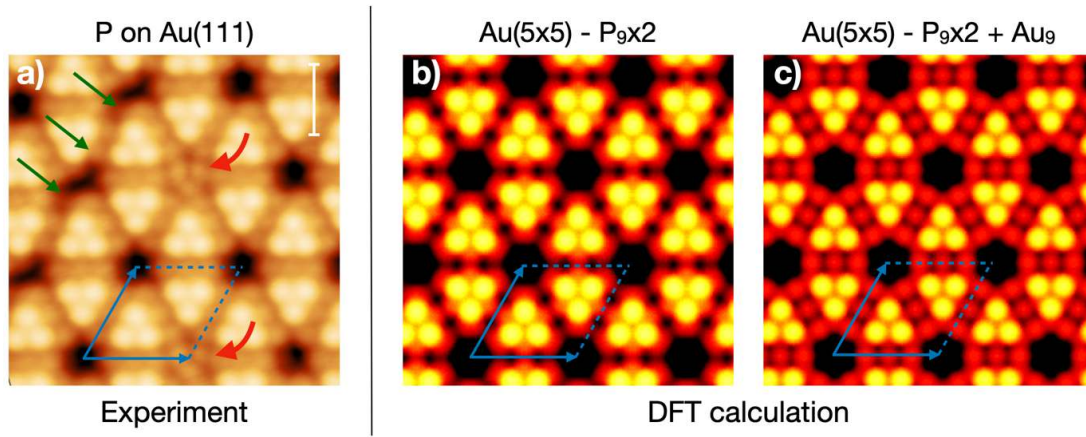


Figure 5.4: a) experimental STM image of the BlueP-Au/Au(111) surface. The rhombic unit cell, depicted in blue, consists of two triangular protrusions and an intermediate level delimited by four hexagonal-shaped depressions at the cell corners. Occasionally, the depressions can be filled by P clusters [41, 42] (red bended arrows). Green arrows delimit a domain boundary between two adjacent glided domains (Measuring parameters: $V_{\text{bias}} = -0.3$ V, $I = 1$ nA, scalebar = 1 nm.). b) and c) show the simulated appearance of the two model under STM inspection at the same lateral scale (Simulated parameters: $V_{\text{bias}} = -0.4$ V, isosurface at 3.0 Å above the highest P layer).

the surface) and BE. By slicing along specific planes, one can obtain either the electronic dispersion in reciprocal space (k_x, k_y) at a selected BE or the band structure along highly symmetrical crystallographic directions (\vec{k} , BE). Both quantities can be accurately simulated and displayed for a qualitative comparison between theory and experiment. The calculated band structure is extracted by integrating over the entire simulation cell, i.e. by summing the contributions of all atoms in the slab calculation. On the other hand, due to the finite inelastic mean free path of the emitted photoelectrons, just the topmost atomic layers contribute to the ARPES spectra. Therefore, a more reliable theory-experiment comparison can be obtained by firstly adding the contribution of the atoms lying on a single plane and then performing an overall layer-by-layer weighed sum, carefully unfolding the calculated band structure. Figure 5.5 depicts the momentum distribution curves, obtained from experimental data, extracted along the high-symmetry directions in the reciprocal space (K- Γ -K and M- Γ -M). These results are compared with the calculated band structure of the two structural models under consideration. We present columns featuring simulated data obtained from the complete simulation cell (Surface+Bulk, second column), fol-

lowed by the most important homogeneous atom groups, including the Au first layer (third column), P adatoms (fourth column) and, for the $P_9 \times 2 + Au_9$ model, Au adatoms (right-most column). The experimental results demonstrate that the BlueP-Au overlayer contributes between 1 and 2 eV BE [97], while the Au(111) substrate exhibits sp-bands across the Fermi energy along with a strong d-band structure contribution below 2 eV BE. In contrast, the calculated band structures, obtained by averaging over the entire slab, are mostly dominated by the sp-bands of Au(111) between the Fermi energy and 2 eV. However, by disentangling the contribution of each atomic layer, one can clearly see the effect of BlueP-Au on the band structure. While the band structure of the top Au(111) layer results very similar to the bulk one, the P atoms yield a strong density of states at low BE. The P band structure differs greatly between the two proposed models: the $P_9 \times 2 + Au_9$ model closely reproduces the experimental evidence, with a contribution to the density of states located between 1 and 2 eV BE and the proper position in the FBZ on both Γ -K and Γ -M profiles. Moreover, the Au9 adatoms deploy intense density of states around 4 eV BE. Conversely, the $P_9 \times 2$ model predicts in the band structure intense density of states across the Fermi level, a feature that is not observed experimentally.

Similar indications are obtained by comparing ARPES maps at selected BEs with the corresponding calculated momentum distribution of electrons in the (k_x, k_y) planes. Figure 5.6 summarises our experimental findings and the results of the DFT calculations for the two different models, right at the Fermi level (BE = 0) and at 1 eV. Experimental ARPES maps of the clean Au(111) termination and of the BlueP/Au(111) system are presented to highlight the differences induced by the overlayer. At the Fermi energy, BlueP fades out the Au(111) surface state close to Γ and contributes in a higher density of states around M. At 1 eV BE the band structure of the BlueP/Au(111) system assumes the shape of two rings with radii of 0.80 \AA^{-1} and of 0.11 \AA^{-1} centred in proximity of the Γ -M direction and close to the Γ point, respectively. These and other main features are well reproduced by the $P_9 \times 2 + Au_9$, while the $P_9 \times 2$ model yields strong density of states around Γ at the Fermi energy and just one ring of intermediate radius (0.65 \AA^{-1}) around Γ at 1 eV BE. The simulated ARPES maps of the clean Au(111) surface at both BEs are also reported in order to highlight the differences with the ones produced by the overlayers.

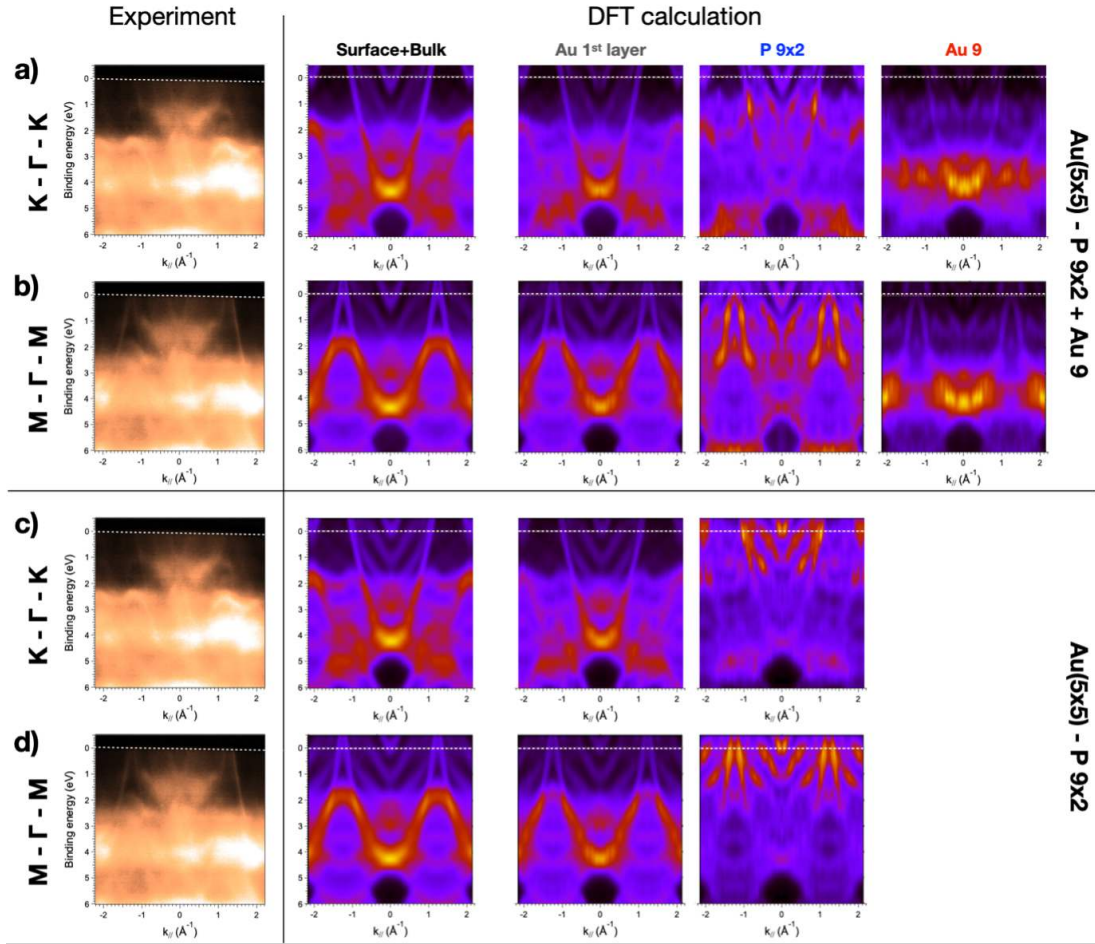


Figure 5.5: Experimental and theoretical band structure along K- Γ -K and M- Γ -M for $P_{9 \times 2} + Au_9$ model (a-b) and $P_{9 \times 2}$ model (c-d). The color scales are black-yellow-white for experimental data and black-purple-red-yellow for theoretical representation. Theoretical results have been unfolded from (5 x 5) FBZ to (1 x 1) FBZ and are displayed after integration over the entire simulation cell (Surface+Bulk) and after projection on separate parts (Au 1st layer, P surface atoms and Au surface atoms). The Fermi level is highlighted with a dashed white line. Experimental data taken with photon energy 65 eV.

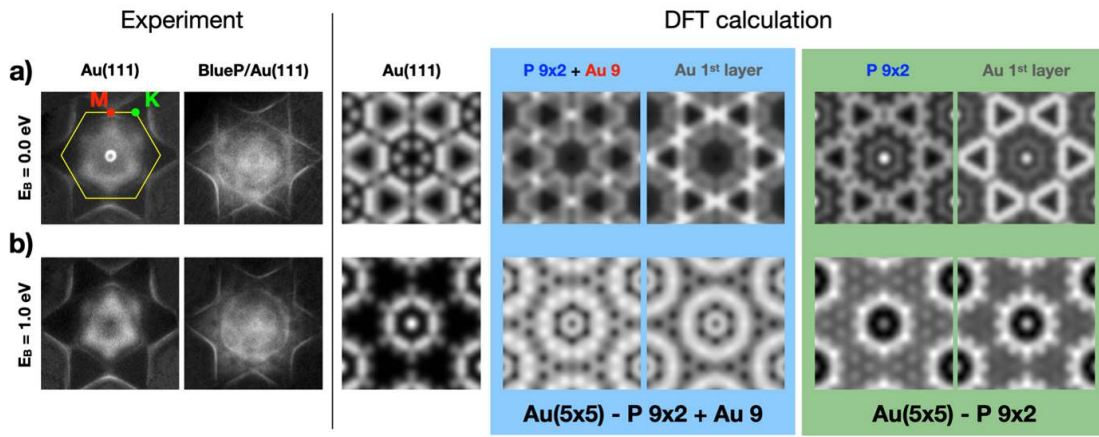


Figure 5.6: Experimental and theoretical distribution of photoemitted electrons in (k_x, k_y) (a) at Fermi energy (i.e. Fermi surface mapping, 0 BE) and (b) at 1 eV BE. The FBZ hexagonal border (yellow) and the position of high-symmetry M (red) and K (green) points are highlighted. Experimental data taken with photon energy 65 eV. DFT calculations include the mapping of clean Au(111) and the contribution of P and Au surface atoms for both $P_9 \times 2 + Au_9$ (light blue) and $P_9 \times 2$ (green) models. All pictures have the same lateral scale.

5.3.3 SXRD

The two models depicted in Fig.5.3, simulated by DFT *ab initio* calculations with a 4-layers Au slab, were the starting point for our experimental SXRD analysis. The SXRD dataset consists of 4 CTRs and 15 SSRs with a total of 1090 experimental datapoints. Each rod has been simultaneously and iteratively fitted. Starting from the structural models proposed by the DFT analysis, the atomic positions were slightly further optimised in order to maximise the agreement between the experimental and the simulated structure factors. In particular, several degrees of freedom were progressively released relying on the symmetry of the superstructure unit cell, identified with the $pm\bar{3}1$ spatial group, outlined in Fig. 5.7.

Parametrisation of the system

In fact, the symmetry of the system already imposes some constraints to the possible in-plane movements of the atoms in the superstructure but, in addition, further selected constrains were introduced in order to reduce the number of degrees of freedom and consequently the number of fitting parameters. Relying on the symmetry of the superstructure and the atomic positions in the proposed

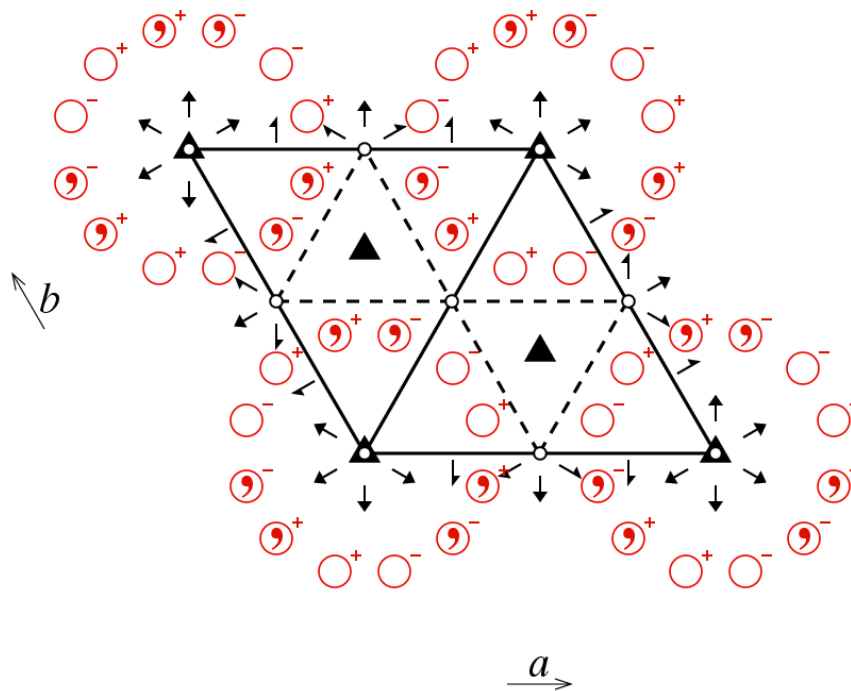


Figure 5.7: Representation of the space group $pm\bar{3}$ for a trigonal structure. The same red symbols identify symmetry equivalent points in the in the plane, whereas black symbols indicate the symmetry operators: the triangles stand for threefold rotation axes perpendicular to the plane of the screen, the circles for centres of inversion, the (half) arrows to (screw) twofold axes, the continuous and dashed lines for mirror and glide planes respectively. *Image from [98].*

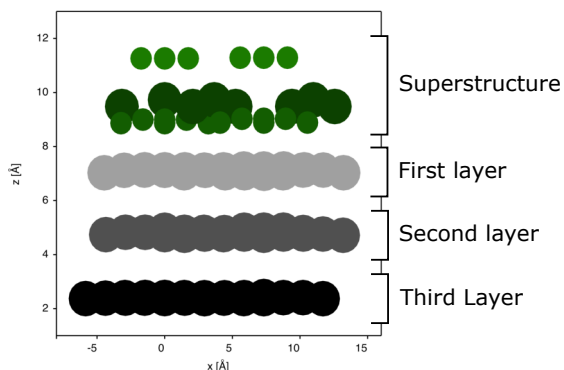
models it is possible to separate the surface atoms (the superstructure and the 3 topmost Au layers) into groups of equivalent atoms. This division allows to introduce some reasonable constraints also regarding the atomic motion along the z direction, i.e. out-of-plane, otherwise ignored by the symmetry in-plane constraints.

Therefore, the surface atoms have been separated in 4 different groups according to the pertaining layer, namely the superstructure layer and the 3 topmost Au layers. In addition, the atoms in the superstructure and in the first Au layer have been separated in 4 and 4 + 1 subgroups, respectively. Fig. 5.8 depicts both the separation in groups and the *Degrees of Freedom* (df) of the atoms in the supercell. The size of the spheres indicates the atomic element (smaller for P, larger for Au), while the colour is associated with a specific group of equivalent atoms. Lastly, the arrows depict the allowed directions for the atomic displacements. During the optimisation procedure, the atoms that belong to the same group were allowed to move by the same amount along the directions indicated by the arrows, in order to preserve the symmetry of the supercell.

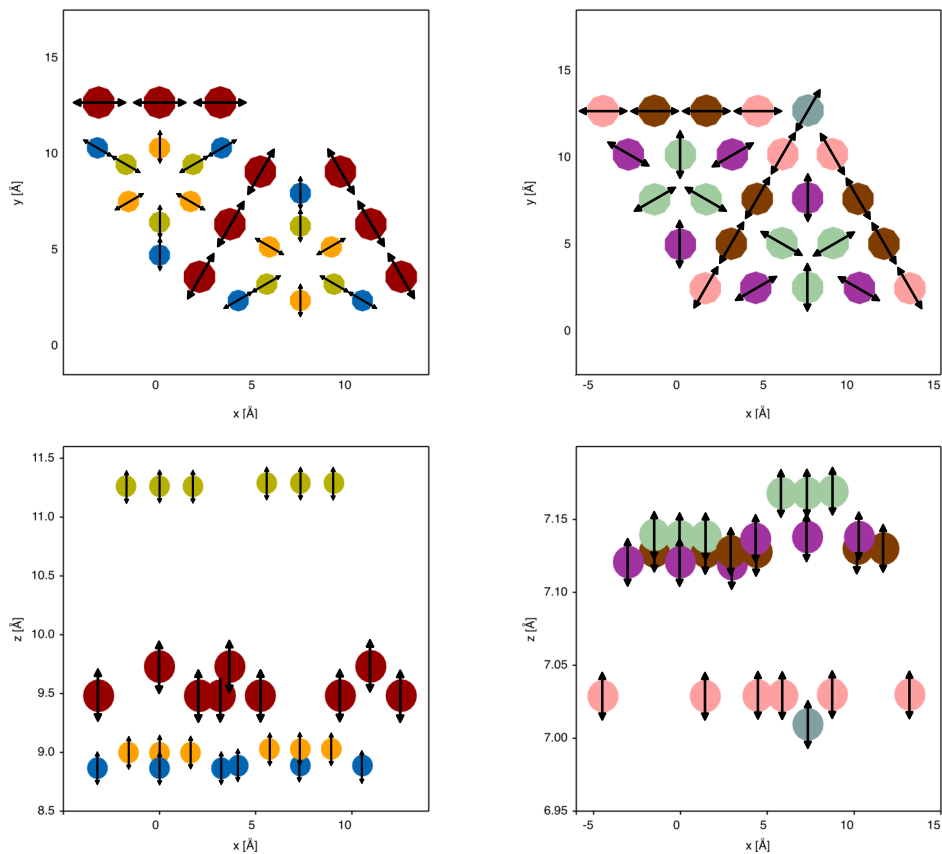
To summarise, a total number of 22 df were introduced in order to properly describe the necessary atomic displacements towards a satisfactory atomic model, namely:

- 4 df for the displacement of the atoms in the 4 layers (the superstructure and the 3 topmost Au layers) as a whole and independently of the others, along the z direction (see Fig. 5.8a).
- 4 df for the intra-layer displacement of the atoms belonging to the 4 subgroups in the superstructure along the $x-y$ directions (see Fig. 5.8b).
- 4 df for the displacement of the atoms belonging to the 4 subgroups in the superstructure along the z direction (see Fig. 5.8b).
- 4+1 df for the displacement of the atoms belonging to the 4 subgroups plus the single Au atom marked in grey colour in the first layer along the $x-y$ directions (see Fig. 5.8c).
- 4+1 df for the displacement of the atoms belonging to the 4 subgroups and the single Au atom in the first layer, along the z direction (see Fig. 5.8c).

In addition, three other parameters have been optimised on the experimental dataset:



(a) Side view of the supercell, illustrating the 4 main groups of atoms. In this picture, each layer can move along z , regardless of the others.



(b) Top and side view of the first Au

(c) Top and side view of the superstructure.

Figure 5.8: Illustration of the groups of equivalent atoms individuated in the superstructure and in the underlying layers. The z scaling is enhanced in b) and c), with respect to a), to highlight the subgroups. Equivalent atoms (depicted in the same colour) are forced to move of the same distance in the directions indicated by the arrows.

- The β -factor, which accounts for the surface roughness.
- The surface fraction parameter f_s , which accounts for the possibility of a non complete surface coverage.
- The occupancy θ of the Au adatoms in the superstructure, introduced due to the high mobility of Au adatoms at surfaces .

In the section above, the parametrisation related to the $P_9 \times 2 + Au_9$ model was described. To obtain the parametrisation related to the $P_9 \times 2$ one it is sufficient to remove the df associated to the Au adatoms in the superstructure.

The configuration of parameters depicted above has been developed in an iterative way, progressively adding df in order to refine the structure model and improve the agreement with the experimental data. Clearly more sophisticated solutions could be adopted allowing the search through a larger configuration space. However, that would increase the possibility of trapping in local minima of the χ^2 , increase the computational cost and yield even overfitting.

In conclusion, the depicted parametrisation of the system proved, as will be shown in the following, to be adequate in order to fulfill the main purpose of this work, which was to sort out the presence of the Au adatoms.

Fitting procedure

In this section, the details of the fitting procedure will be presented. The structural optimisation has been carried out running multiple fitting loops in which the fitting parameters are released step-by-step. This specific procedure was chosen for two main reasons. Firstly, this allowed us to minimise the computational effort, which rapidly increases with the number of fitting parameters, but most importantly it allows us to monitor the *R-factor* trend during the process. In fact, ANA-ROD exploits the steepest descent gradient algorithm in order to find the atomic configuration which minimises the value of the χ^2 , which does not correspond in general to the one which minimises the *R-factor*. Thus, the agreement between the simulated structure factors and the experimental data was tested by both methods for best solidity.

Nevertheless, even the optimised $P_9 \times 2 + Au_9$ model could not fully reproduce the experimental data. This is due to both physical-technical features not in-

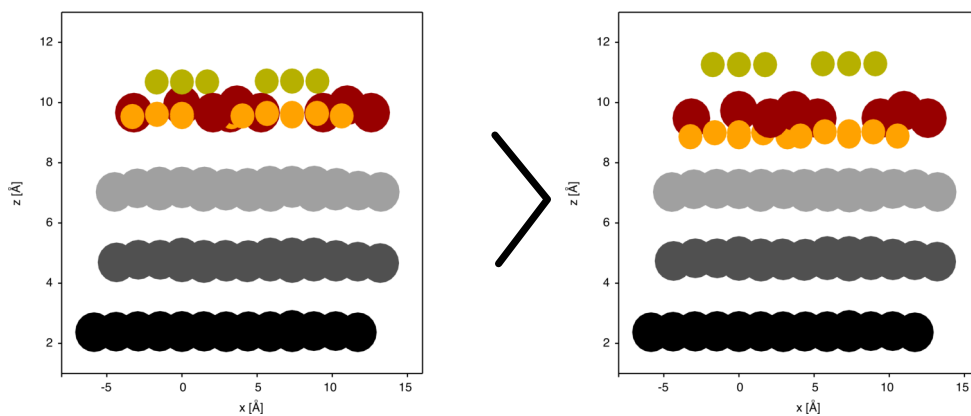
cluded in the theoretical model (the presence of more than a single ordered domain on the surface, the finite energy bandwidth of the x-ray source, the polarisation of the beam, ...) and to limitations of the fitting model. In fact, the best fit solution depends crucially both on the specific initial configuration and on the parametrisation of the system. Working with complex atomic structures, composed of a large number of atoms (the surface unit cell for the $P_9 \times 2 + Au_9$ model has 102 atoms), implies a large number of parameters in order to describe the system. Therefore, the best fit solution is most likely to depend crucially on the specific initial fitting configuration and even a slight modification of the latter could lead to traps in local minima of the parameters space, thus retrieving an improper solution. In order to overcome these problems one may, in addition to exploit different *figures of merit*, rely on more sophisticated methods (e.g. iterative phase retrieval algorithms, quantum monte carlo approaches, adaptive simulated annealing method, ...) in order to provide a more accurate data analysis. Nevertheless, the described fitting procedure and parametrisation of the system have been considered sufficiently precise to evince the main features of the BlueP/Au(111) structure and provide a solid evidence of the presence of the Au bridging adatoms.

Before presenting the results of the model optimisation, it is worth considering the fact that the CTRs are characterised by a significantly higher signal intensity with respect to the SSRs. This implies that one single CTR contributes considerably more to the χ^2 value than a SSRs. In addition, the atoms of the superstructure, which are the main focus of this work, contribute just marginally to the CTRs signal due to the different in-plane symmetry with respect to bulk atoms. Therefore, one could ask whether excluding the CTRs from the analysis, a subset of the diffraction data consisting only of SSRs could be reproduced by the fitting model in a more efficient way, but still converging to a meaningful solution. Therefore, the structure optimisation procedure has been tested fitting also a sub-dataset consisting of just the SSRs. The refined structures obtained including or not the CTRs in the dataset, coincide if the number of fitting parameters is limited, but start to diverge if further degrees of freedom are included. This is due to the fact that, increasing the size and the complexity of the parameter space, the number of local minima rapidly boosts. Thus, fitting just the SSRs subset of the experimental data is likely to converge to a different configuration with respect to the one that best fits the whole dataset. In the light of the results of this fitting test, the complete experimental dataset has been used to carry out this analysis.

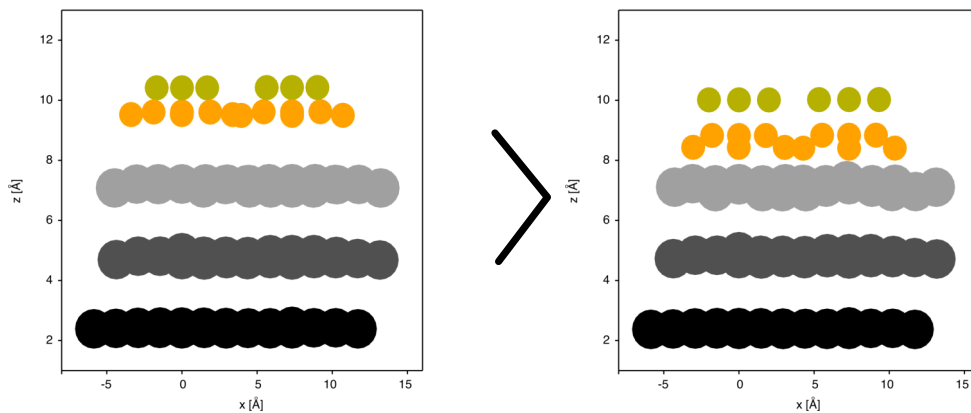
Refined models

In this section, the results of the structural refinement will be presented. The optimised models $P_9 \times 2 + Au_9$ and $P_9 \times 2$, together with their corresponding DFT optimum, used as a starting point for structural refinement, are depicted in Fig. 5.9. The atomic displacements and fitting parameters which were found to minimise the χ^2 for the various models are reported in Appendix C. What stands out comparing the starting models and the refined atomic structures in Fig. 5.9 is the difference of magnitude between the displacements of P and Au atoms. In particular, the Au atoms and the in-plane P atoms displacements vary from 0.01 to 0.4 Å, and are hardly appreciable in the scale range of the figure, while the out-of-plane displacements of P atoms vary from 0.8 to 1.6 Å and are clearly visible. The main reason for this difference has to be searched in the P atoms scattering cross section being considerably smaller with respect to the Au atoms one. Because of that, the iterative fitting process is not sufficiently efficient to accurately discriminate the effective positions of P atoms due to their marginal contribution to the simulated structure factor of the model.

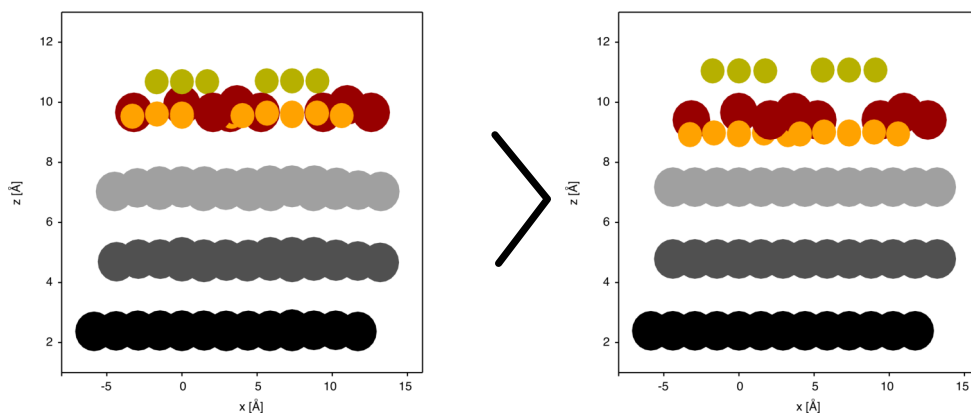
Figure 5.10 shows the experimental intensity modulation of the diffraction rods with respect to the diffraction index L together with the simulated structure factor starting from the DFT refined models. The same fitting procedure has been adopted for both models with just the 2 df associated with the Au adatoms in the superstructure removed from the list of parameters for the $P_9 \times 2$ model. What stands out comparing the two simulated structure factors in Fig. 5.10, is that the $P_9 \times 2 + Au_9$ model (red curves) is far more accurate in reproducing the experimental data with respect to the $P_9 \times 2$ model (green curves). A quantitative evidence in favour of this conclusion has been achieved by testing the agreement with the experimental data of the optimised models with both χ^2 and R -factor. The obtained values are listed in Table 5.1 from which it is possible to notice that the values related to the $P_9 \times 2$ model are 379% and 170% larger than the $P_9 \times 2 + Au_9$ model ones, for χ^2 and R -factor, respectively. This result provides a clear experimental evidence that the $P_9 \times 2 + Au_9$ model is the one that most accurately reproduces the effective surface structure of the BlueP/Au(111) system, eventually ruling out the possibility that Au linking adatoms aren't part of the superstructure.



(a) Model P_9x2+Au_9



(b) Model P_9x2



(c) Model P_9x2+Au_9 not including the out-of-plane surface relaxation of the first Au layers

Figure 5.9: Lateral views of the optimised structural models, on the right, together with their corresponding DFT optimum, which were used as a starting point.

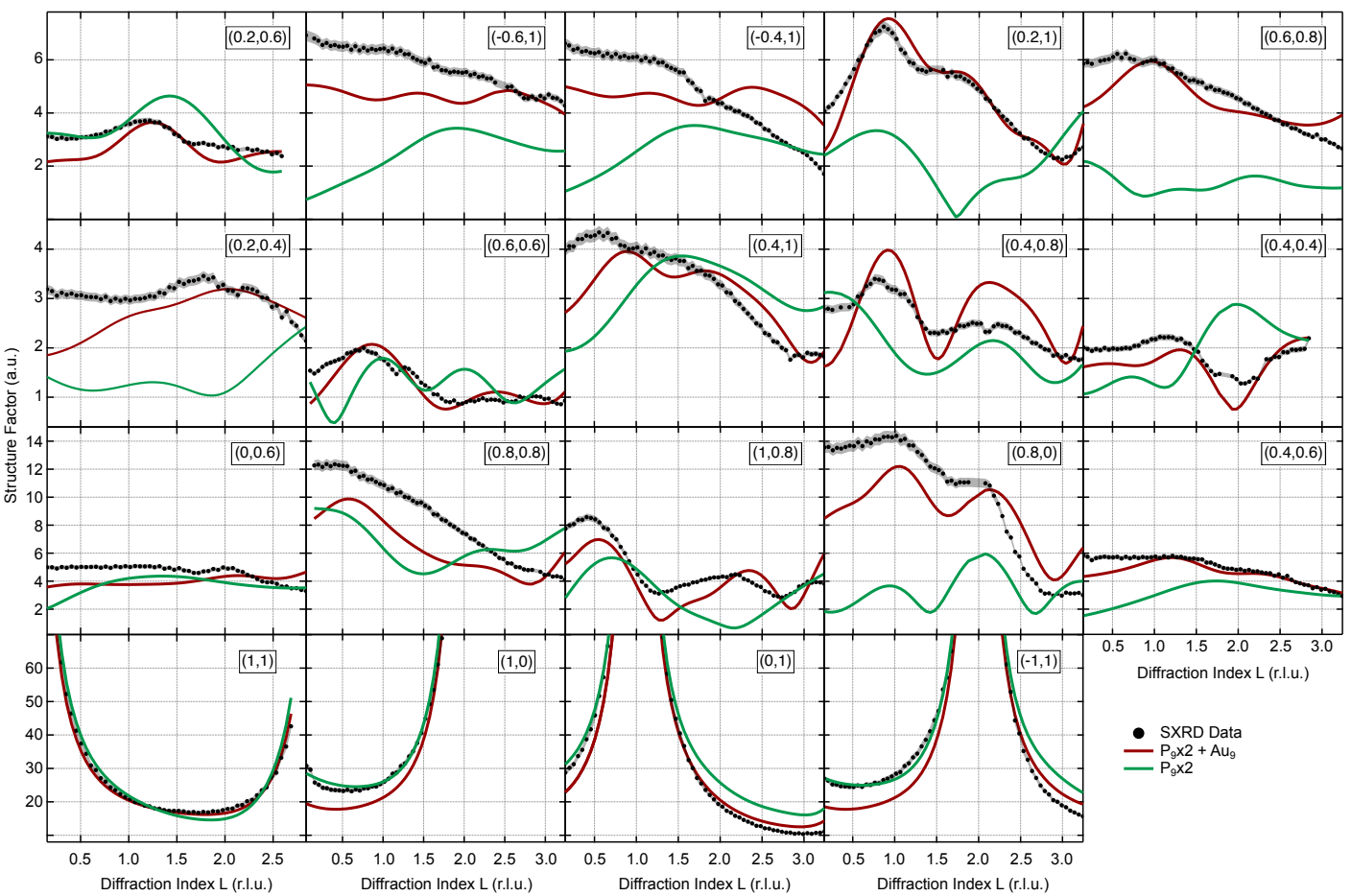


Figure 5.10: Measured CTRs (integer values of H and K) and SSRS (fractional values of H or K) of BlueP-Au(111) and the calculated structure factors for $P_9 \times 2 + Au_9$ and $P_9 \times 2$ optimised structural models.

	Normalised χ^2	<i>R-factor</i>
P_9x2+Au_9	59	0.146
P_9x2	224	0.249
P_9x2+Au_9 No Relaxation	58	0.154

Table 5.1: Normalized χ^2 and *R-factor* values computed for the optimised models

Surface Relaxation

Having successfully sorted out the presence of the bridging adatoms in the atomic structure, we investigated the role played by the relaxation of the first Au layers atomic positions. Starting from the P_9x2+Au_9 refined model we fixed the atomic coordinates of the Au atoms, belonging to the three topmost layers, to the positions of the corresponding bulk atoms and we excluded from the fitting procedure the *df* associated with the associated displacements. We will refer to the model obtained in this way as the *no relaxation* model in the following. Figure 5.11 shows the experimental intensity modulation of the diffraction rods with respect to the diffraction index *L* together with the simulated structure factor from the refined P_9x2+Au_9 model and from the *no relaxation* model. What stands out from the figure is that, excluding from the atomic structure the surface relaxation of the topmost Au layers, the general trend of the diffraction rods is still well reproduced, while the fine structure characterising the experimental data is completely missing. This behaviour is somewhat opposite to the one observed excluding the bridging Au adatoms from the atomic structure. In fact, as it can be appreciated in Fig. 5.10, the absence in the model of the Au adatoms prevents the simulated structure factors from reproducing the overall trend of the experimental diffraction rods. Nevertheless, the simulated structure factors associated with the P_9x2 model clearly show a fine structure besides not being in full agreement with the experimental data.

When examining the Normalized χ^2 and *R-factor* values calculated for the different optimised models, presented in Table 5.1, it is noticeable that while the χ^2 values calculated for the P_9x2+Au_9 and the *no relaxation* model are very close and do not allow to discriminate between them, the *R-factor* value clearly indicates the better agreement of the P_9x2+Au_9 with the experimental data. The latter observation confirms the crucial importance of exploiting different *figures of merit* in order to test the proposed atomic models.

In conclusion, both the presence of the surface adatoms and of the surface relaxation of the uppermost Au layers proved to be crucial for an adequate fit of the experimental data, in particular in order to appropriately reproduce the fine structure and the general trend of the measured diffraction rods, respectively.

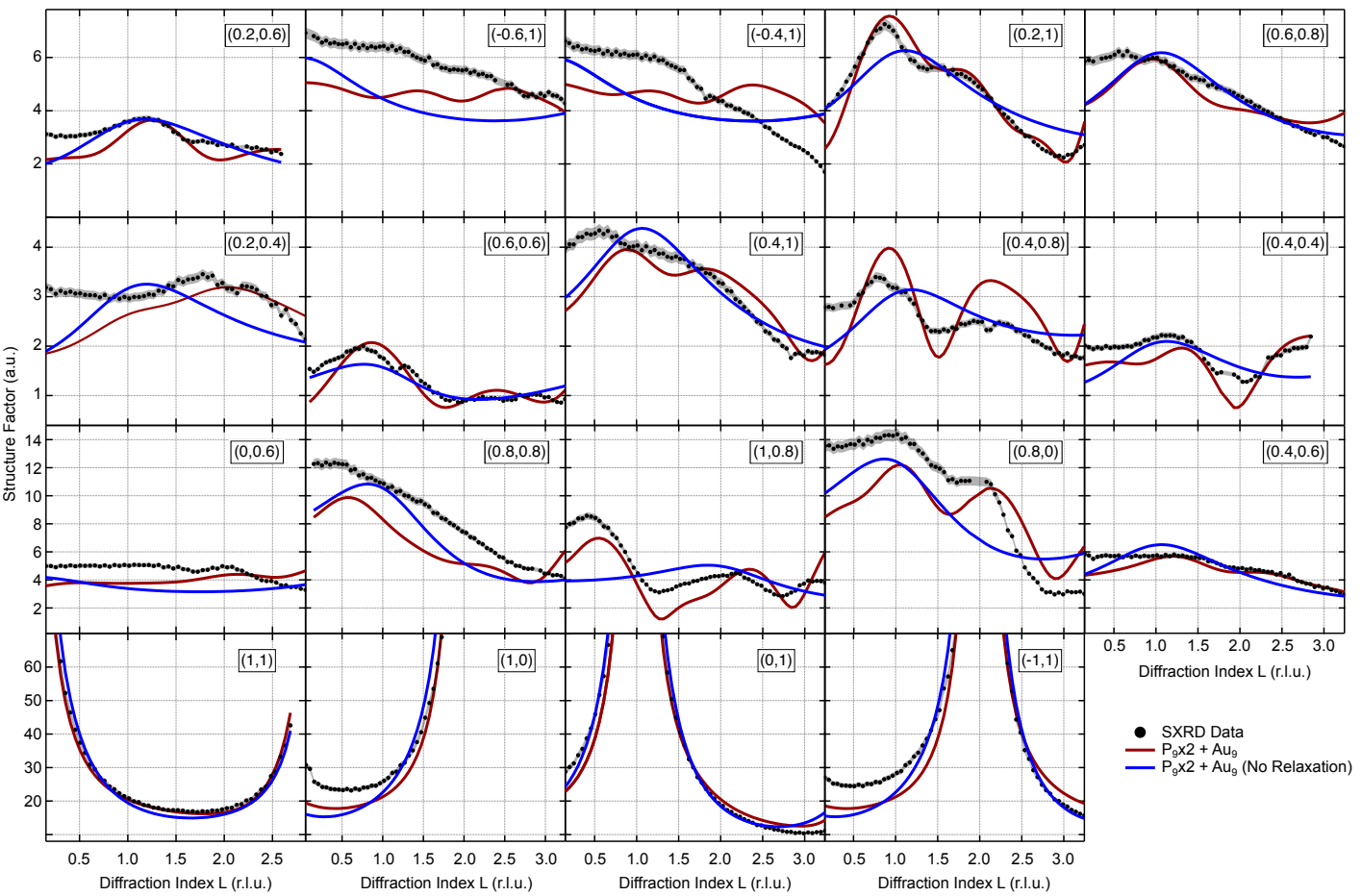


Figure 5.1.1: Measured CTRs (integer values of H and K) and SSRs (fractional values of H or K) of BlueP-Au/Au(111) and the calculated structure factors for $P_0 \times 2 + Au_9$ model with and without introducing the relaxation of the first Au layers.

Chapter 6

Conclusions

This thesis work focuses on the growth and experimental characterisation of B and P monolayers supported by metal surfaces. To fulfil these purposes, we have employed a combination of complementary surface science techniques (XPS, STM, IR-Vis SFG, SXRD, NEXAFS, LEED, AES), corroborated by *ab initio* DFT techniques within the framework of an external collaboration, providing a comprehensive picture of the investigated subjects.

In the first part of this thesis, we investigated the growth process of boron-based structures on the Al(111) surface termination. Boron evaporation on the latter substrate resulted in a complex phase diagram, generated by the boron's multi-centric bonding character and its relative electron and chemical affinities with respect to aluminium. Despite the available literature reporting about the stabilisation of an AlB₂ honeycomb phase, we revealed the effective co-presence of a variety of different B-Al ordered structures. Despite their relative abundance can be tuned by controlling the growth parameters, a single ordered phase cannot be obtained. Specifically, besides mono- and multi-layered AlB₂ structures, we reported the presence of two intermediate phases in the formation process of an AlB₂ layer. These structures are characterised by strain-release constraints that significantly affect their geometric and electronic features with respect to the complete AlB₂ layers.

We then exploited the (111) surface termination of the Ni₃Al alloy as a substrate for boron evaporation in order to dilute the Al concentration with the aim of weakening the Al-B interaction. We unveiled novel geometric and electronic configurations by investigated the growth process parameters

space, revealing the crucial role played by segregation and diffusion mechanisms and the atomic species relative chemical affinities in the formation of ordered phases. In particular, high substrate temperatures and B-loadings lead to boron diffusion into the bulk, while lowering the temperature, surface segregation occurs. By investigating the system with microscopic imaging we revealed the presence of substitutional B atoms embedded in the substrate lattice, which promote the formation of triangular-shaped clusters. Combining spectroscopic and microscopic insights, we proposed an interpretative model for the structure of the boron clusters, which resulted to be composed of boron trimers bridged by an aluminium adatom. While this interpretation seems to be adequate to support a plausible model, which is compatible with full set of experimental observations, further validation through DFT calculations or further experimental insight into the geometry of the surface structure, e.g. LEEM or LEED I(V) measurements, could be necessary in order to corroborate our findings.

In the following, we investigated the reactivity of the aforementioned B-based structures to ubiquitous gases, such as hydrogen and oxygen. Exposure of the $\text{AlB}_2/\text{Al}(111)$ system to atomic hydrogen resulted in the formation of a stable, long-range ordered honeycomb structure that is visible in the electron diffraction patterns and showing bridge-coordinated H atoms. The hydrogenation process turned out to be fully reversible by annealing the system above 400 K. On the other hand, exposure of the system to molecular oxygen resulted in an opposite and much more intricate situation. In fact, the honeycomb boron film is only hardly affected by oxidation, which involves instead mainly Al, yielding aluminium oxide at the $\text{AlB}_2/\text{Al}(111)$ interface, segregation of Al ad-atoms across the borophene layers, and formation of Al-O terminal structures via a mechanism that is similar to the one observed for the growth of thin alumina films. In a similar way, exposure of the $\text{B}/\text{Ni}_3\text{Al}(111)$ system to molecular oxygen turned out to induce segregation of boron atoms from the bulk to the surface and the formation of terminal and interfacial aluminium and boron oxides.

In the last part of this thesis, the structural determination of the $\text{BlueP}/\text{Au}(111)$ system is presented. In particular, we discriminated between two proposed structural models, which mainly differ for the presence, in the BlueP overlayer, of Au adatoms bridging triangular P islands. The 40% higher R-factor, obtained test-

ing any model without the linking Au adatoms, with respect to diffraction data, is statistically significant in order to corroborate the presence of the adatoms in the effective structure of the system. In addition, the surface relaxation of the uppermost Au layers proved to be crucial for an adequate fit of the experimental data. The model was supported by STM imaging and spectroscopy as long as by intensive DFT-based studies.

Appendix A

XPS Parameters

XPS best fit parameters are listed in the following tables referring to the Doniach-Šunjić function convoluted with a Gaussian:

$$I_{DS}(E_{Kin}) = I_0 \frac{\Gamma_E(1-\alpha)}{((E_{Kin} - BE)^2 + \Gamma^2/4)^{(1-\alpha)/2}} \zeta(E_{Kin}) \quad (\text{A.1})$$

where Γ_E is the Euler Gamma function, Γ the Lorentzian linewidth, α the asymmetry parameter, G the Gaussian linewidth, I_0 the intensity, and BE the binding energy position and $\zeta(E)$ is defined as:

$$\zeta(E) = \cos \left[\frac{\pi\alpha}{2} + (1-\alpha) \tan^{-1} \left(\frac{E_0 - E}{\Gamma/2} \right) \right] \quad (\text{A.2})$$

The errors are three times the standard deviations.

A.1 B/Al(111) + H_{ct}

B 1s

	B/Al(111)	B/Al(111) + H _{ct}
I_B	123539 ± 173	119058 ± 173
S_B	-3646 ± 50	-2941 ± 50
$\Gamma[eV]$	0.257 ± 0.002	0.257 ± 0.002
α	0.066 ± 0.001	0.066 ± 0.001
$G[eV]$	0.286 ± 0.003	0.286 ± 0.003
$A_1[eV]$	749917 ± 9790	752710 ± 8298
$BE_1[eV]$	-187.78 ± 0.05	-187.75 ± 0.05
$A_2[eV]$	142557 ± 11213	9934 ± 19049
$BE_2[eV]$	-0.29 ± 0.0178	-0.29 ± 0.02
$A_3[eV]$	103862 ± 5584	79756 ± 5399
$BE_3[eV]$	-0.656 ± 0.007	-0.656 ± 0.007
$A_{BH}[eV]$	18831 ± 20923	210816 ± 12059
$BE_{BH}[eV]$	-0.43 ± 0.01	-0.43 ± 0.01
$A_{BO}[eV]$	43952 ± 1373	37786 ± 1351
$BE_{BO}[eV]$	0.703 ± 0.003	0.703 ± 0.003

Table A.1: Fit parameters of B 1s core-level spectra.

Al 2p

	B/Al(111)	B/Al(111) + H _{at}
I_B	-1281	1087
S_B	126	15
$s.o.s.[e.v]$	0.41	0.41
$\Gamma[eV]$	0.072	0.077
α	0.161	0.099
$G[eV]$	0.081	0.076
$A_1[eV]$	288174	254473
$BE_1[eV]$	-72.69	-72.71
$A_2[eV]$	57325	54137
$BE_2[eV]$	0.60	0.58
$A_3[eV]$	7926	12557
$BE_3[eV]$	1.216	1.238
α_{molt}	-	1.43
G_{molt}	-	3.04

Table A.2: Fit parameters of Al 2p core-level spectra. The BE refers to the position of the $2p_{3/2}$ and the $s.o.s$ indicates the spin-orbit splitting between the $2p_{3/2}$ and $2p_{1/2}$ levels. The parameters α_{molt} and G_{molt} are multiplicative factors introduced upon hydrogenation, with respect to α and G , respectively.

A.2 B/Ni₃Al(111)**Ni 2p_{3/2}**

	Ni ₃ Al	B/Ni ₃ Al (T _D = 495 K) (ΘB = 0.7 ML)	B/Ni ₃ Al (T _D = 495 K) (ΘB = 0.7 ML)	B/Ni ₃ Al (T _D = 490 K) (ΘB = 1.6 ML)
I_B	1.18	1.14	1.12	1.12
S_B	-0.05	-0.04	-0.05	-0.04
$\Gamma_1[eV]$	0.41	0.41*	0.41*	0.41*
α_1	0.19	0.19*	0.19*	0.19*
$G_1[eV]$	0.66	0.66*	0.66*	0.66*
$A_1[eV]$	9.75 ± 0.01	8.2 ± 0.2	3.9 ± 0.3	1.9 ± 0.3
$BE_1[eV]$	-852.24 ± 0.03	-852.24 ± 0.04	-852.24 ± 0.04	-852.24 ± 0.06
$\Gamma_2[eV]$	-	0.41*	0.41*	0.41*
α_2	-	0.17	0.17*	0.17*
$G_2[eV]$	-	0.66*	0.66*	0.66*
$A_2[eV]$	-	2.6 ± 0.2	7.1 ± 0.3	9.8 ± 0.3
$BE_2[eV]$	-	0.446 ± 0.008	0.45 ± 0.02	0.45 ± 0.03
$\Gamma_p[eV]$	1.38	1.38*	1.38*	1.38*
α_p	0*	0*	0*	0*
$G_p[eV]$	2.63	2.63*	2.63*	2.63*
$A_p[eV]$	-1.058 ± 0.002	-0.846 ± 0.004	-0.786 ± 0.002	-0.675 ± 0.008
$BE_p[eV]$	6.14 ± 0.01	6.606 ± 0.005	6.85 ± 0.01	7.44 ± 0.03

Table A.3: Fit parameters of Ni 2p_{3/2} core-level spectra. The asterisk (*) indicates parameters that have been kept fixed during the fit operation.

Al 2p

	Ni ₃ Al	B/Ni ₃ Al (T _D = 495 K) (ΘB = 0.7 ML)	B/Ni ₃ Al (T _D = 495 K) (ΘB = 0.7 ML)	B/Ni ₃ Al (T _D = 490 K) (ΘB = 1.6 ML)
I_B	0.97	0.99	1.01	1.00
S_B	-0.02	-0.01	-0.02	-0.02
Γ_1 [eV]	0.03	0.03*	0.03*	0.03*
α_1	0.10	0.10*	0.10*	0.10*
G_1 [eV]	0.18	0.18*	0.18*	0.18*
$A_1^{(3/2)}$ [eV]	39.8 ± 0.1	21.3 ± 0.4	14.3 ± 0.1	4.33 ± 0.05
$BE_1^{(3/2)}$ [eV]	-72.14 ± 0.02	-72.11 ± 0.02	-72.11 ± 0.02	-72.15 ± 0.02
$BE_1^{(1/2)}$ [eV]	0.405 ± 0.005	0.405*	0.405*	0.405*
Γ_2 [eV]	-	0.03*	0.03*	0.03*
α_2	-	0.10*	0.10*	0.10*
G_2 [eV]	-	0.43	0.49	0.47
$A_2^{(3/2)}$ [eV]	-	21.7 ± 0.4	26.49 ± 0.07	26.95 ± 0.09
$BE_2^{(3/2)}$ [eV]	-	0.235 ± 0.005	0.235 ± 0.005	0.235 ± 0.002
$BE_2^{(1/2)}$ [eV]	-	0.64*	0.64*	0.64*
Γ_p [eV]	-	-	-	0.03*
α_p	-	-	-	0.10*
G_p [eV]	-	-	-	1.75
$A_3^{(3/2)}$ [eV]	-	-	-	7.09 ± 0.07
$BE_3^{(3/2)}$ [eV]	-	-	-	1.39 ± 0.01
$BE_3^{(1/2)}$ [eV]	-	-	-	1.79*

Table A.4: Fit parameters of Al 2p core-level spectra. The asterisk (*) indicates parameters that have been kept fixed during the fit operation.

B 1s

	B/Ni ₃ Al (T _D = 495 K) (ΘB = 0.7 ML)	B/Ni ₃ Al (T _D = 495 K) (ΘB = 0.7 ML)	B/Ni ₃ Al (T _D = 490 K) (ΘB = 1.6 ML)
I_B	1.04	1.04	1.04
S_B	-0.01	-0.01	-0.02
$\Gamma[eV]$	0.14	0.14*	0.14*
α	0.10	0.10*	0.10*
$G[eV]$	0.22	0.22*	0.22*
$A_2[eV]$	0.85 ± 0.07	0.7 ± 0.1	1.47 ± 0.08
$BE_2[eV]$	-187.70 ± 0.03	-187.66 ± 0.04	-187.68 ± 0.03
$A_1[eV]$	0.480 ± 0.005	0.63 ± 0.07	0.41 ± 0.08
$BE_1[eV]$	-0.35 ± 0.01	-0.35*	-0.35*
$A_3[eV]$	0.22 ± 0.03	0.40 ± 0.05	1.32 ± 0.03
$BE_3[eV]$	0.25 ± 0.07	0.25*	0.25*
$A_4[eV]$	0.18 ± 0.07	0.3 ± 0.1	-1.32 ± 0.04
$BE_4[eV]$	0.47 ± 0.03	0.47*	0.47*
$A_5[eV]$	0.05 ± 0.01	0.092 ± 0.006	0.12 ± 0.01
$BE_5[eV]$	1.43 ± 0.02	1.43*	1.43*

Table A.5: Fit parameters of B 1s core-level spectra. The asterisk (*) indicates parameters that have been kept fixed during the fit operation.

A.3 B/Ni₃Al(111) + O₂

Ni 2p_{3/2}

	B/Ni ₃ Al (T _D = 490 K) (ΘB = 1.6 ML)	B/Ni ₃ Al (Post-oxidation)	B/Ni ₃ Al (Peri-oxidation)
I_B	1.12	1.12	1.12
S_B	-0.04	-0.04	-0.03
$\Gamma_1[eV]$	0.41	0.41*	0.41*
α_1	0.19	0.19*	0.19*
$G_1[eV]$	0.66	0.66*	0.66*
$A_1[eV]$	1.9 ± 0.3	5.31 ± 0.08	1.4 ± 0.1
$BE_1[eV]$	-852.24 ± 0.06	-852.24 ± 0.034	-852.243 ± 0.05
$\Gamma_2[eV]$	0.41*	0.41*	0.41*
α_2	0.17	0.17	0.17*
$G_2[eV]$	0.66*	0.66*	0.66*
$A_2[eV]$	9.8 ± 0.3	3.33 ± 0.09	6.9 ± 0.1
$BE_2[eV]$	0.45 ± 0.03	0.45*	0.45*
$\Gamma_p[eV]$	1.38	1.38*	1.38*
α_p	0*	0*	0*
$G_p[eV]$	2.63	2.63*	2.63*
$A_p[eV]$	-0.675 ± 0.008	-0.592 ± 0.007	-0.458 ± 0.003
$BE_p[eV]$	7.44 ± 0.03	6.47 ± 0.02	7.142 ± 0.02

Table A.6: Fit parameters of Ni 2p_{3/2} core-level spectra. The asterisk (*) indicates parameters that have been kept fixed during the fit operation.

Al 2p

	B/Ni ₃ Al (T _D = 490 K) (ΘB = 1.6 ML)	B/Ni ₃ Al (Post-oxidation)	B/Ni ₃ Al (Peri-oxidation)
I_B	1.00	0.99	0.98
S_B	-0.02	0.01	0.01
Γ [eV]	0.03	0.03*	0.03*
α	0.10	0.10*	0.10*
G_1 [eV]	0.18 0.18*	0.18*	0.18*
$A_1^{(3/2)}$ [eV]	4.33 ± 0.05	-3.7 ± 0.2	2.6 ± 0.1
$BE_1^{(3/2)}$ [eV]	-72.15 ± 0.02	-72.15 ± 0.02	-72.15 ± 0.02
$BE_1^{(1/2)}$ [eV]	0.41*	0.41*	0.41*
G_2 [eV]	0.47	0.40	0.50
$A_2^{(3/2)}$ [eV]	26.95 ± 0.09	11.2 ± 0.2	10.5 ± 0.1
$BE_2^{(3/2)}$ [eV]	0.235 ± 0.002	0.219 ± 0.006	0.261 ± 0.005
$BE_2^{(1/2)}$ [eV]	0.64*	0.62*	0.67*
G_3 [eV]	1.75	1.28	0.81
$A_3^{(3/2)}$ [eV]	7.09 ± 0.07	9.0 ± 1.9	8.3 ± 0.1
$BE_3^{(3/2)}$ [eV]	1.39 ± 0.01	1.66 ± 0.03	1.66*
$BE_3^{(1/2)}$ [eV]	1.79*	2.07*	2.07*
G_4 [eV]	-	1.27	1.20
$A_4^{(3/2)}$ [eV]	-	20.7 ± 1.9	18.9 ± 0.1
$BE_4^{(3/2)}$ [eV]	-	2.59 ± 0.05	2.81 ± 0.01
$BE_4^{(1/2)}$ [eV]	-	3.00*	3.22*

Table A.7: Fit parameters of Al 2p core-level spectra. The asterisk (*) indicates parameters that have been kept fixed during the fit operation.

B 1s

	B/Ni ₃ Al (T _D = 490 K) (Θ _B = 1.6 ML)	B/Ni ₃ Al (Post-oxidation)	B/Ni ₃ Al (Peri-oxidation)
I_B	1.04	0.81	1.04
S_B	-0.21	0.00	-0.01
Γ [eV]	0.14	0.14*	0.14*
α	0.10	0.10*	0.10*
G [eV]	0.22	0.22*	0.22*
A_2 [eV]	1.47 ± 0.08	-0.27 ± 0.02	-0.99 ± 0.06
BE_2 [eV]	-187.68 ± 0.03	-187.690 ± 0.04	-187.743 ± 0.03
A_1 [eV]	0.41 ± 0.08	0.23 ± 0.03	0.18 ± 0.03
BE_1 [eV]	-0.35*	-0.35*	-0.35*
A_3 [eV]	1.32 ± 0.03	0.40 ± 0.07	1.32 ± 0.05
BE_3 [eV]	0.25*	0.25*	0.25*
A_4 [eV]	-1.32 ± 0.04	0.38 ± 0.03	-0.30 ± 0.04
BE_4 [eV]	0.48*	0.48*	0.48*
A_5 [eV]	0.12 ± 0.01	0.50 ± 0.01	1.12 ± 0.011
BE_5 [eV]	1.43*	1.36 ± 0.02*	1.36*
G_6 [eV]	-	0.96	0.96*
A_6 [eV]	-	0.29 ± 0.03	-0.48 ± 0.01
BE_6 [eV]	-	2.78 ± 0.04	2.78*
α_7	-	0.07	0*
G_7 [eV]	-	1.68	1.92
A_7 [eV]	-	8.44 ± 0.03	11.48 ± 0.02
BE_7 [eV]	-	4.89 ± 0.01	4.89 ± 0.01

Table A.8: Fit parameters of B 1s core-level spectra. The asterisk (*) indicates parameters that have been kept fixed during the fit operation.

O 1s

	B/Ni ₃ Al (T _D = 490 K) (ΘB = 1.6 ML)	B/Ni ₃ Al (Post-oxidation)	B/Ni ₃ Al (Peri-oxidation)
I_B	1.04	1.04	1.04
S_B	-0.01	-0.01	-0.02
$\Gamma_1[eV]$	0.40	0.40*	0.40*
α_1	0.13	0.13*	0.13*
$G_1[eV]$	1.34	1.81	0.98
$A_1[eV]$	1.769 ± 0.01	6.28 ± 0.02	3.95 ± 0.1
$BE_1[eV]$	-531.00 ± 0.02	-531.11 ± 0.02	-531.14 ± 0.01
$\Gamma_2[eV]$	-	0.40*	0.40*
α_2	-	0*	0*
$G_2[eV]$	-	1.77	1.77*
$A_2[eV]$	-	17.22 ± 0.02	21.50 ± 0.05
$BE_2[eV]$	-	1.099 ± 0.005	1.313 ± 0.005

Table A.9: Fit parameters of O 1s core-level spectra. The asterisk (*) indicates parameters that have been kept fixed during the fit operation.

Appendix B

SFG Parameters

SFG best fit parameters are listed in the following tables referring to the SFG signal intensity expression:

$$I_{SFG}(\omega_{IR}) \propto \left[A_{NR} + \sum_n \frac{A_n e^{i\Delta\phi_n}}{\omega_{IR} - \omega_n + i\Gamma} \right]^2 I_{VIS} I_{IR}(\omega_{IR}) \quad (\text{B.1})$$

where A_{NR} is the non-resonant amplitude, A_n the resonance amplitudes, $\Delta\phi$ the phase differences, ω_n resonance frequencies, and Γ resonance broadenings. The errors are three times the standard deviations.

B.1 B/Al(111) + H₂O

	293 K	381 K	399 K	428	455 K	473 K
A_{NR}	28.0 ± 0.1	28.3 ± 0.1	25.0 ± 0.1	23.0 ± 0.1	21.8 ± 0.1	23 ± 0.1
A_{RES}	68.3 ± 0.1	55.7 ± 0.1	41.0 ± 0.1	32.8 ± 0.1	33.3 ± 0.1	38.6 ± 0.1
G	1.9 ± 0.1	3.7 ± 0.1	1.5 ± 0.1	7.3 ± 0.1	9.2 ± 0.1	12.7 ± 0.1
$\Delta\phi$	25 ± 13	25	25	25	25	25
ω	1934 ± 2.5	1934	1934	1934	1934	1934
Γ	10 ± 3	10	10	10	10	10

Table B.1: Best Fit parameters of B-H stretching mode resonance at increasing temperatures.

B.2 B/Al(111) + O₂

	BO ₁	BO ₃	BO ₂
A_{NR}	22.3 ± 0.2	22.3 ± 0.2	22.3 ± 0.2
A_{RES}	4 ± 1	3 ± 1	4 ± 1
$\Delta\phi$	78 ± 41	142 ± 38	329 ± 39
ω	1200 ± 2	1231 ± 2	1213 ± 2
Γ	2.9	2.9	2.9

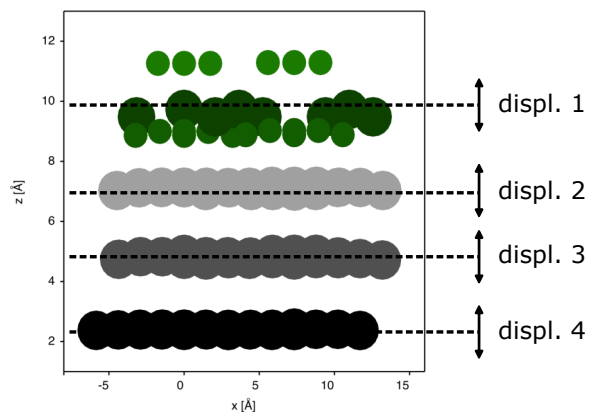
Table B.2: Best Fit parameters of B-O vibrational modes.

Appendix C

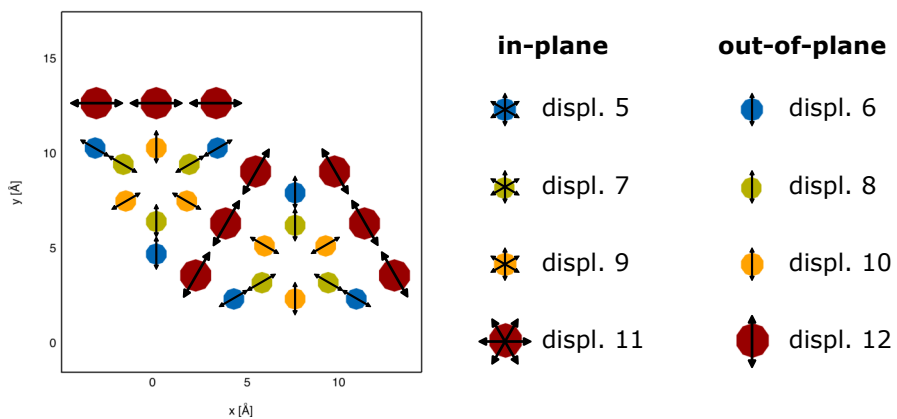
SXRD Models and Parameters

This appendix reports the representation and the fitting coefficients obtained for the $P_9 \times 2 + Au_9$ model, the $P_9 \times 2$ model and the $P_9 \times 2 + Au_9$ without the relaxation of the Au layers. The associated diffraction data, with the corresponding best fits, are shown in Figs. 5.10 and 5.11, section 5.3.3. The parameters related to the atoms displacements are expressed as fractions of the (5×5) unit cell (whose side size is estimated to be $\sim 14.648 \text{ \AA}$ by DFT calculations) and are labelled as summarised in the figure in the next page.

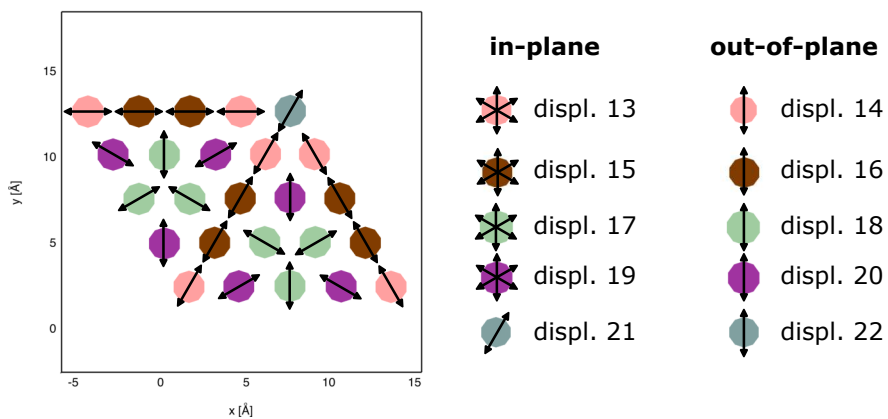
Interlayer



Superstructure

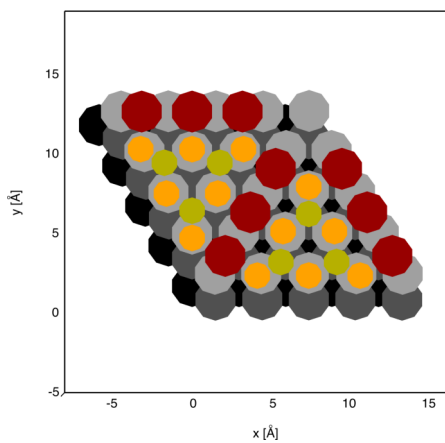


Firts Au layer

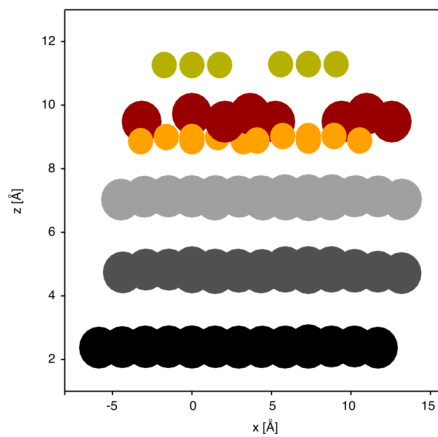


	$P_9 \times 2 + Au_9$	$P_9 \times 2$	$P_9 \times 2 + Au_9$ (no relax)
<i>scale</i>	0.0259	0.0283	0.0321
β	0.11	0	0.2876
f_s	1	1	0.9931
<i>displ.1</i>	-0.0307	-0.0733	-0.0539
<i>displ.2</i>	-0.0024	-0.0071	-
<i>displ.3</i>	0.0066	0.0045	-
<i>displ.4</i>	-0.0001	-0.0026	-
<i>displ.5</i>	-0.0056	-0.0265	-0.0032
<i>displ.6</i>	-0.0627	-0.0788	-0.0313
<i>displ.7</i>	-0.0041	-0.0077	-0.0001
<i>displ.8</i>	-0.0545	-0.0354	-0.0339
<i>displ.9</i>	0.0047	0.0247	0.0056
<i>displ.10</i>	0.111	0.0174	0.1041
<i>displ.11</i>	-0.0023	0	-0.0023
<i>displ.12</i>	0.0051	0	0.0185
<i>displ.13</i>	-0.0011	-0.014	-
<i>displ.14</i>	0.002	0.0109	-
<i>displ.15</i>	-0.0007	-0.001	-
<i>displ.16</i>	0.01	-0.026	-
<i>displ.17</i>	-0.0009	0.0005	-
<i>displ.18</i>	-0.0078	0.0024	-
<i>displ.19</i>	0.0019	0.0053	-
<i>displ.20</i>	-0.0018	0.009	-
<i>displ.21</i>	0.0029	-0.0199	-
<i>displ.22</i>	-0.019	0.041	-
θ	0.8169	-	0.7896

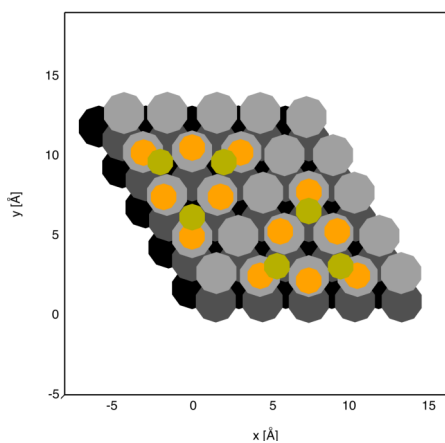
Table C.1: Best Fit parameters of diffraction data.



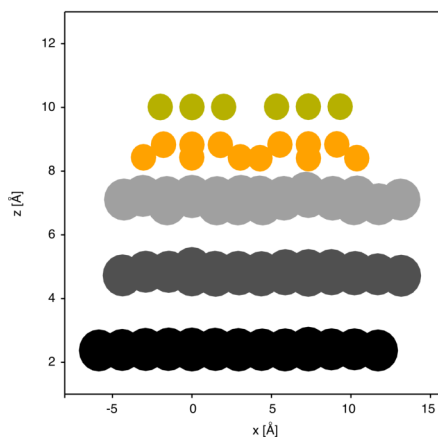
(a) Top view of the P_9x2+Au_9 model.



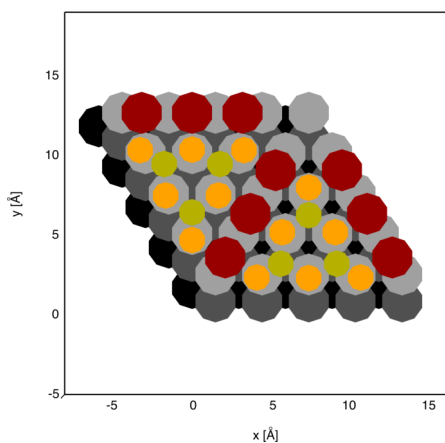
(b) Side view of the P_9x2+Au_9 model.



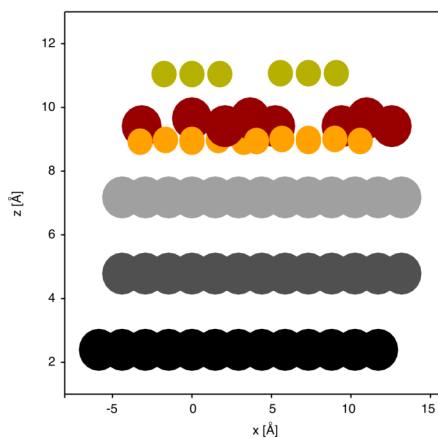
(c) Top view of the P_9x2 model.



(d) Side view of the P_9x2 model.



(e) Top view of the P_9x2+Au_9 model (no relaxation).



(f) Side view of the P_9x2+Au_9 model (no relaxation).

Bibliography

- [1] H. Schäfer. "J. Donohue: The Structures of the Elements". In: *Berichte der Bunsengesellschaft für physikalische Chemie* 79.1 (Jan. 1975), 110–110. ISSN: 0005-9021. DOI: 10.1002/BBPC.19750790123.
- [2] Koun Shirai. "Phase diagram of boron crystals". In: *Japanese Journal of Applied Physics* 56.5 (May 2017), 05FA06. ISSN: 13474065. DOI: 10.7567/JJAP.56.05FA06.
- [3] Michiel J. Van Setter et al. "Thermodynamic stability of boron: The role of defects and zero point motion". In: *Journal of the American Chemical Society* 129.9 (Mar. 2007), 2458–2465. ISSN: 00027863. DOI: 10.1021/ja0631246.
- [4] Iwao Matsuda and Kehui Wu. *2D Boron: Boraphene, Borophene, Boronene*. Springer International Publishing, 2021, 160. ISBN: 978-3-030-49999-0. DOI: 10.1007/978-3-030-49999-0.
- [5] Zachary A. Piazza et al. "Planar hexagonal B36 as a potential basis for extended single-atom layer boron sheets". In: *Nature Communications* 2014 5:1 5.1 (Jan. 2014), 1–6. ISSN: 2041-1723. DOI: 10.1038/ncomms4113.
- [6] Hui Tang and Sohrab Ismail-Beigi. "Novel precursors for boron nanotubes: The competition of two-center and three-center bonding in boron sheets". In: *Physical Review Letters* 99.11 (Sept. 2007), 115501. ISSN: 00319007. DOI: 10.1103/PhysRevLett.99.115501. arXiv: 0710.0593.
- [7] Evgeni S. Penev et al. "Polymorphism of two-dimensional boron". In: *Nano Letters* 12.5 (May 2012), 2441–2445. ISSN: 15306984. DOI: 10.1021/nl3004754.
- [8] Sharmila N. Shirodkar, Evgeni S. Penev, and Boris I. Yakobson. "Honeycomb boron: alchemy on aluminum pan?" In: *Science Bulletin* 63.5 (Mar. 2018), 270–271. ISSN: 2095-9273. DOI: 10.1016/J.SCIB.2018.02.019.
- [9] Xiaojun Wu et al. "Two-dimensional boron monolayer sheets". In: *ACS Nano* 6.8 (Aug. 2012), 7443–7453. ISSN: 19360851. DOI: 10.1021/nl302696v.

- [10] Yuanyue Liu, Evgeni S. Penev, and Boris I. Yakobson. "Probing the Synthesis of Two-Dimensional Boron by First-Principles Computations". In: *Angewandte Chemie* 125.11 (Mar. 2013), 3238–3241. ISSN: 1521-3757. DOI: 10.1002/ANGE.201207972.
- [11] Andrew J. Mannix et al. "Synthesis of borophenes: Anisotropic, two-dimensional boron polymorphs". In: *Science* 350.6267 (Dec. 2015), 1513–1516. ISSN: 10959203. DOI: DOI:10.1126/science.aad1080.
- [12] Baojie Feng et al. "Experimental realization of two-dimensional boron sheets". In: *Nature Chemistry* 8.6 (2016), 563–568. ISSN: 17554349. DOI: 10.1038/nchem.2491.
- [13] Gavin P. Campbell et al. "Resolving the Chemically Discrete Structure of Synthetic Borophene Polymorphs". In: *Nano Letters* 18.5 (2018), 2816–2821. ISSN: 15306992. DOI: 10.1021/acs.nanolett.7b05178.
- [14] Brian Kiraly et al. "Borophene Synthesis on Au(111)". In: *ACS Nano* 13.4 (Apr. 2019), 3816–3822. ISSN: 1936086X. DOI: 10.1021/acsnano.8b09339.
- [15] Wenbin Li et al. "Experimental realization of honeycomb borophene". In: *Science Bulletin* 63.5 (Mar. 2018), 282–286. ISSN: 20959273. DOI: 10.1016/j.scib.2018.02.006.
- [16] Daiyu Geng et al. "Experimental evidence of monolayer AlB_2 with symmetry-protected Dirac cones". In: *Physical Review B* 101.16 (Apr. 2020), 161407. ISSN: 2469-9950. DOI: 10.1103/PhysRevB.101.161407.
- [17] Alexei B. Preobrajenski et al. "Honeycomb Boron on Al(111): From the Concept of Borophene to the Two-Dimensional Boride". In: *ACS Nano* 15.9 (Sept. 2021), 15153–15165. ISSN: 1936-0851. DOI: 10.1021/acsnano.1c05603.
- [18] Chengyong Zhong et al. "Two-dimensional honeycomb borophene oxide: strong anisotropy and nodal loop transformation". In: *Nanoscale* 11.5 (Jan. 2019), 2468–2475. ISSN: 2040-3372. DOI: 10.1039/C8NR08729F.
- [19] Luo Yan et al. "Theoretical dissection of superconductivity in two-dimensional honeycomb borophene oxide B_2O crystal with a high stability". In: *npj Computational Materials* 2020 6:1 6.1 (July 2020), 1–7. ISSN: 2057-3960. DOI: 10.1038/s41524-020-00365-9.

- [20] Xinzhou Ma and Sebastian Günther. "Imaging the confined surface oxidation of Ni₃Al(111) by in situ high temperature scanning tunneling microscopy". In: *Physical Chemistry Chemical Physics* 20.34 (Aug. 2018), 21844–21855. ISSN: 1463-9084. DOI: 10.1039/C8CP03197E.
- [21] Erik Vesselli et al. "Large interlayer relaxation at a metal-oxide interface: The case of a supported ultrathin alumina film". In: *Physical Review Letters* 105.4 (July 2010), 046102. ISSN: 00319007. DOI: 10.1103/PhysRevLett.105.046102.
- [22] Douglas J. Klein et al. "Hückeloid model for planar boranes". In: *Theoretical Chemistry Accounts* 140.5 (May 2021), 1–10. ISSN: 14322234. DOI: 10.1007/s00214-021-02752-x.
- [23] M. Nakhaee, S. A. Ketabi, and F. M. Peeters. "Tight-binding model for borophene and borophane". In: *Physical Review B* 97.12 (Mar. 2018), 125424. ISSN: 24699969. DOI: /10.1103/PhysRevB.97.125424.
- [24] Qiucheng Li et al. "Synthesis of borophane polymorphs through hydrogenation of borophene". In: *Science* 371.6534 (Mar. 2021), 1143–1148. ISSN: 0036-8075. DOI: 10.1126/science.abg1874.
- [25] Ying Xu et al. "Borophane Polymorphs". In: *Journal of Physical Chemistry Letters* 13.4 (Feb. 2022), 1107–1113. ISSN: 19487185. DOI: 10.1021/acs.jpcllett.1c03827.
- [26] Yuchong Kang et al. "Substrate-Mediated Borophane Polymorphs through Hydrogenation of Two-Dimensional Boron Sheets". In: *Journal of Physical Chemistry Letters* 13.43 (Nov. 2022), 10222–10229. ISSN: 19487185. DOI: 10.1021/acs.jpcllett.2c02417.
- [27] N.N. Greenwood and A. Earnshaw. *Chemistry of the Elements*. Elsevier Science, 2012. ISBN: 9780080501093.
- [28] Ralph Hultgren, N. S. Gingrich, and B. E. Warren. "The Atomic Distribution in Red and Black Phosphorus and the Crystal Structure of Black Phosphorus". In: *The Journal of Chemical Physics* 3.6 (June 1935), 351–355. ISSN: 0021-9606. DOI: 10.1063/1.1749671.
- [29] Alexandra Carvalho et al. "Phosphorene: from theory to applications". In: *Nature Reviews Materials* 2016 1:11 1.11 (Aug. 2016), 1–16. ISSN: 2058-8437. DOI: 10.1038/natrevmats.2016.61.

- [30] Michael Ruck et al. "Fibrous Red Phosphorus". In: *Angewandte Chemie International Edition* 44.46 (Nov. 2005), 7616–7619. ISSN: 1521-3773. DOI: 10.1002/ANIE.200503017.
- [31] P. W. Bridgman. "Two new modifications of phosphorus". In: *Journal of the American Chemical Society* 36.7 (July 1914), 1344–1363. ISSN: 15205126. DOI: 10.1021/ja02184a002.
- [32] Yongqing Cai et al. "Giant Phononic Anisotropy and Unusual Anharmonicity of Phosphorene: Interlayer Coupling and Strain Engineering". In: *Advanced Functional Materials* 25.15 (Apr. 2015), 2230–2236. ISSN: 1616-3028. DOI: 10.1002/ADFM.201404294.
- [33] Andres Castellanos-Gomez et al. "Isolation and characterization of few-layer black phosphorus". In: *2D Materials* 1.2 (June 2014), 025001. ISSN: 2053-1583. DOI: 10.1088/2053-1583/1/2/025001.
- [34] Yukihiro Takao and Akira Morita. "Electronic structure of black phosphorus: Tight binding approach". In: *Physica B+C* 105.1-3 (May 1981), 93–98. ISSN: 0378-4363. DOI: 10.1016/0378-4363(81)90222-9.
- [35] Menghao Wu et al. "Nine new phosphorene polymorphs with non-honeycomb structures: A much extended family". In: *Nano Letters* 15.5 (May 2015), 3557–3562. ISSN: 15306992. DOI: 10.1021/acs.nanolett.5b01041.
- [36] Zhen Zhu and David Tománek. "Semiconducting layered blue phosphorus: A computational study". In: *Physical Review Letters* 112.17 (May 2014), 176802. ISSN: 10797114. DOI: 10.1103/PhysRevLett.112.176802. arXiv: 1403.1300.
- [37] Enrique Montes and Udo Schwingenschlögl. "High-Performance Field-Effect Transistors Based on α P and β P". In: *Advanced Materials* 31.18 (May 2019), 1807810. ISSN: 1521-4095. DOI: 10.1002/ADMA.201807810.
- [38] Barun Ghosh et al. "Electric field induced gap modification in ultrathin blue phosphorus". In: *Physical Review B - Condensed Matter and Materials Physics* 91.11 (Mar. 2015), 115433. ISSN: 1550235X. DOI: 10.1103/PhysRevB.91.115433. arXiv: 1412.0858.
- [39] Ankit Jain and Alan J.H. McGaughey. "Strongly anisotropic in-plane thermal transport in single-layer black phosphorene". In: *Scientific Reports* 2015 5:1 5.1 (Feb. 2015), 1–5. ISSN: 2045-2322. DOI: 10.1038/srep08501.

- [40] Evangelos Golias et al. "Band Renormalization of Blue Phosphorus on Au(111)". In: *Nano Letters* 18.11 (Nov. 2018), 6672–6678. ISSN: 15306992. DOI: 10.1021/acs.nanolett.8b01305. arXiv: 1803.08862.
- [41] Jia Lin Zhang et al. "Epitaxial Growth of Single Layer Blue Phosphorus: A New Phase of Two-Dimensional Phosphorus". In: *Nano Letters* 16.8 (Aug. 2016), 4903–4908. ISSN: 15306992. DOI: 10.1021/acs.nanolett.6b01459.
- [42] Jincheng Zhuang et al. "Band Gap Modulated by Electronic Superlattice in Blue Phosphorene". In: *ACS Nano* 12.5 (May 2018), 5059–5065. ISSN: 1936086X. DOI: 10.1021/acsnano.8b02953.
- [43] Wei Zhang et al. "Epitaxial Synthesis of Blue Phosphorene". In: *Small* 14.51 (Dec. 2018), 1804066. ISSN: 16136829. DOI: 10.1002/smll.201804066.
- [44] Songtao Zhao et al. "Structure of Blue Phosphorus Grown on Au(111) Surface Revisited". In: *Journal of Physical Chemistry C* 124.3 (Jan. 2020), 2024–2029. ISSN: 19327455. DOI: 10.1021/acs.jpcc.9b10511.
- [45] Jia Lin Zhang et al. "Reversible Oxidation of Blue Phosphorus Monolayer on Au(111)". In: *Nano Letters* 19.8 (Aug. 2019), 5340–5346. ISSN: 15306992. DOI: 10.1021/acs.nanolett.9b01796.
- [46] Hao Tian et al. "Two-Dimensional Metal-Phosphorus Network". In: *Matter* 2.1 (Jan. 2020), 111–118. ISSN: 2590-2385. DOI: 10.1016/J.MATT.2019.08.001.
- [47] M. P. Seah and W. A. Dench. "Quantitative electron spectroscopy of surfaces: A standard data base for electron inelastic mean free paths in solids". In: *Surface and Interface Analysis* 1.1 (Feb. 1979), 2–11. ISSN: 1096-9918. DOI: 10.1002/SIA.740010103.
- [48] Siegfried Hofmann. "Auger- and X-Ray Photoelectron Spectroscopy in Materials Science". In: *Springer Series in Surface Sciences* 49 (2013). DOI: 10.1007/978-3-642-27381-0.
- [49] Stefan Hüfner. "Introduction and Basic Principles". In: (2003), 1–60. DOI: 10.1007/978-3-662-09280-4_1.
- [50] Andrea Damascelli, Zahid Hussain, and Zhi Xun Shen. "Angle-resolved photoemission studies of the cuprate superconductors". In: *Reviews of Modern Physics* 75.2 (Apr. 2003), 473. ISSN: 00346861. DOI: 10.1103/RevModPhys.75.473.

- [51] Pardis Simon, Víctor G. Baldovino-Medrano, and Robert Wojcieszak. "X-Ray Photoelectron Spectroscopy (XPS): Principles and Application for the Analysis of Photoactive Materials". In: *Springer Handbooks* (2022), 249–271. ISSN: 25228706. DOI: 10.1007/978-3-030-63713-2_10.
- [52] Fred A. Stevie and Carrie L. Donley. "Introduction to x-ray photoelectron spectroscopy". In: *Journal of Vacuum Science & Technology A: Vacuum, Surfaces, and Films* 38.6 (Dec. 2020). ISSN: 0734-2101. DOI: 10.1116/6.0000412/1024200.
- [53] S. Doniach and M. Sunjic. "Many-electron singularity in X-ray photoemission and X-ray line spectra from metals". In: *Journal of Physics C: Solid State Physics* 3.2 (Feb. 1970), 285. ISSN: 0022-3719. DOI: 10.1088/0022-3719/3/2/010.
- [54] Joachim Stöhr. "NEXAFS Spectroscopy". In: *Springer Series in Surface Sciences* 25 (1992). DOI: 10.1007/978-3-662-02853-7.
- [55] David Attwood. "Soft X-Rays and Extreme Ultraviolet Radiation: Principles and Applications". In: *Soft X-Rays and Extreme Ultraviolet Radiation* (Aug. 1999). DOI: 10.1017/CB09781139164429.
- [56] Bertrand Busson and Abderrahmane Tadjeddine. "Non-uniqueness of parameters extracted from resonant second-order nonlinear optical spectroscopies". In: *Journal of Physical Chemistry C* 113.52 (2009), 21895–21902. ISSN: 19327447. DOI: doi.org/10.1021/jp908240d.
- [57] Alex G. Lambert, Paul B. Davies, and David J. Neivandt. "Implementing the Theory of Sum Frequency Generation Vibrational Spectroscopy: A Tutorial Review". In: *Applied Spectroscopy Reviews* 40.2 (2005), 103–145. ISSN: 1520569X. DOI: 10.1081/ASR-200038326.
- [58] Hong Fei Wang et al. "Quantitative Sum-Frequency Generation Vibrational Spectroscopy of Molecular Surfaces and Interfaces: Lineshape, Polarization, and Orientation". In: <https://doi.org/10.1146/annurev-physchem-040214-121322> 66 (Apr. 2015), 189–216. ISSN: 15451593. DOI: 10.1146/ANNUREV-PHYSCHEM-040214-121322.
- [59] Robert W. Boyd. "Nonlinear Optics, Third Edition". In: *Nonlinear Optics, Third Edition* (Jan. 2008), 1–613.

- [60] J. H. Hunt, P. Guyot-Sionnest, and Y. R. Shen. "Observation of C-H stretch vibrations of monolayers of molecules optical sum-frequency generation". In: *Chemical Physics Letters* 133.3 (Jan. 1987), 189–192. ISSN: 0009-2614. DOI: 10.1016/0009-2614(87)87049-5.
- [61] A. G. Lambert. "Resonantly enhanced sum frequency spectroscopy of adsorption on hydrophilic mica substrates". PhD thesis.
- [62] S. H. Lin and A. A. Villaeys. "Theoretical description of steady-state sum-frequency generation in molecular adsorbates". In: *Physical Review A* 50.6 (Dec. 1994), 5134. ISSN: 10502947. DOI: 10.1103/PhysRevA.50.5134.
- [63] Günther Rupprechter. "Sum Frequency Generation and Polarization-Modulation Infrared Reflection Absorption Spectroscopy of Functioning Model Catalysts from Ultrahigh Vacuum to Ambient Pressure". In: *Advances in Catalysis* 51 (Jan. 2007), 133–263. ISSN: 0360-0564. DOI: 10.1016/S0360-0564(06)51004-1.
- [64] Eskpla. *FG Spectrometer: Technical Description and User's Manual*. 2013.
- [65] Tetsuroh Shirasawa. "X-Ray Crystal Truncation Rod Scattering". In: *Compendium of Surface and Interface Analysis* (2018), 821–825. DOI: 10.1007/978-981-10-6156-1_130.
- [66] Claude Lecomte. "Understanding Single-Crystal X-ray Crystallography". By Dennis W. Bennett. Weinheim: Wiley-VCH, 2010. Pp. xx + 811. Price (hardcover) GBP 115.00, EUR 138.00. ISBN 978-3-527-32677-8. In: *Acta Crystallographica Section A Foundations of Crystallography* 69.2 (Mar. 2013), 208–209. ISSN: 0108-7673. DOI: 10.1107/S0108767313000639.
- [67] "Operando Research in Heterogeneous Catalysis". In: Springer Series in Chemical Physics 114 (2017). Ed. by Joost Frenken and Irene Groot. DOI: 10.1007/978-3-319-44439-0.
- [68] Sander Roobol et al. "BINoculars: data reduction and analysis software for two-dimensional detectors in surface X-ray diffraction". In: *urn:issn:1600-5767* 48.4 (June 2015), 1324–1329. ISSN: 1600-5767. DOI: 10.1107/S1600576715009607.
- [69] E. Vlieg and IUCr. "ROD: a program for surface X-ray crystallography". In: *urn:issn:0021-8898* 33.2 (Apr. 2000), 401–405. ISSN: 0021-8898. DOI: 10.1107/S0021889899013655.

- [70] A C Anderson et al. "Surface Studies by Scanning Tunneling Microscopy". In: *Physical Review Letters* 49.1 (July 1982), 57. ISSN: 00319007. DOI: 10.1103/PhysRevLett.49.57.
- [71] C. Julian Chen. "Introduction to scanning tunneling microscopy". In: *Introduction to Scanning Tunneling Microscopy* (Apr. 2021), 1–452. DOI: 10.1093/oso/9780198856559.001.0001.
- [72] J. Bardeen. "Tunnelling from a Many-Particle Point of View". In: *Physical Review Letters* 6.2 (Jan. 1961), 57. ISSN: 00319007. DOI: 10.1103/PhysRevLett.6.57.
- [73] J. Tersoff and D. R. Hamann. "Theory of the scanning tunneling microscope". In: *Physical Review B* 31.2 (Jan. 1985), 805. ISSN: 01631829. DOI: 10.1103/PhysRevB.31.805.
- [74] Flemming Besenbacher. "Scanning tunnelling microscopy studies of metal surfaces". In: *Reports on Progress in Physics* 59.12 (Dec. 1996), 1737. ISSN: 0034-4885. DOI: 10.1088/0034-4885/59/12/004.
- [75] Liyan Zhu et al. "How is Honeycomb Borophene Stabilized on Al(111)?" In: *Journal of Physical Chemistry C* 123.23 (June 2019), 14858–14864. ISSN: 19327455. DOI: 10.1021/acs.jpcc.9b03447.
- [76] L. Bartels, G. Meyer, and K. H. Rieder. "Controlled vertical manipulation of single CO molecules with the scanning tunneling microscope: A route to chemical contrast". In: *Applied Physics Letters* 71.2 (July 1997), 213–215. ISSN: 0003-6951. DOI: 10.1063/1.119503.
- [77] M. Schmid et al. "Nanotemplate with holes: Ultrathin alumina on Ni₃Al(111)". In: *Physical Review Letters* 99.19 (Nov. 2007), 196104. ISSN: 00319007. DOI: 10.1103/PhysRevLett.99.196104.
- [78] L. Jurczyszyn et al. "Atomic structure and electronic properties of Ni₃Al(111) and (011) surfaces". In: *Physical Review B - Condensed Matter and Materials Physics* 76.4 (July 2007), 045101. ISSN: 10980121. DOI: 10.1103/PhysRevB.76.045101.
- [79] Toma Susi et al. "Core level binding energies of functionalized and defective graphene". In: *Beilstein Journal of Nanotechnology* 5:12 5.1 (Feb. 2014), 121–132. ISSN: 2190-4286. DOI: 10.3762/BJNANO.5.12.

- [80] U. Bischler and E. Bertel. "Simple source of atomic hydrogen for ultrahigh vacuum applications". In: *Journal of Vacuum Science & Technology A* 11.2 (Mar. 1993), 458–460. ISSN: 0734-2101. DOI: 10.1116/1.578754.
- [81] Li Shao et al. "A theoretical study of several fully hydrogenated borophenes". In: *Physical Chemistry Chemical Physics* 21.14 (2019), 7630–7634. ISSN: 14639076. DOI: 10.1039/c9cp00468h.
- [82] Paolo Giannozzi et al. "QUANTUM ESPRESSO: a modular and open-source software project for quantum simulations of materials". In: *Journal of Physics: Condensed Matter* 21.39 (Sept. 2009), 395502. ISSN: 0953-8984. DOI: 10.1088/0953-8984/21/39/395502. arXiv: 0906.2569.
- [83] Yajun Wang, Jingfu Fan, and Michael Trenary. "Surface Chemistry of Boron Oxidation. 1. Reactions of Oxygen and Water with Boron Films Grown on Ta(110)". In: *Chemistry of Materials* 5.2 (1993), 192–198. ISSN: 15205002. DOI: 10.1021/cm00026a007.
- [84] C. W. Ong et al. "X-ray photoemission spectroscopy of nonmetallic materials: Electronic structures of boron and B_xO_y". In: *Journal of Applied Physics* 95.7 (Apr. 2004), 3527–3534. ISSN: 0021-8979. DOI: 10.1063/1.1651321.
- [85] C. Ocal, B. Basurco, and S. Ferrer. "An ISS-XPS study on the oxidation of Al(111); identification of stoichiometric and reduced oxide surfaces". In: *Surface Science* 157.1 (July 1985), 233–243. ISSN: 0039-6028. DOI: 10.1016/0039-6028(85)90645-4.
- [86] K. A. Simonov et al. "Controllable oxidation of h-BN monolayer on Ir(111) studied by core-level spectroscopies". In: *Surface Science* 606.3-4 (Feb. 2012), 564–570. ISSN: 0039-6028. DOI: 10.1016/J.SUSC.2011.11.031.
- [87] Shaodong Cheng et al. "Quantification of the boron speciation in alkali borosilicate glasses by electron energy loss spectroscopy". In: *Scientific Reports* 2015 5:1 5.1 (Dec. 2015), 1–7. ISSN: 2045-2322. DOI: 10.1038/srep17526.
- [88] A. B. Preobrajenski et al. "Strong participator channels in the non-radiative resonant decay of B 1s excitation in B₂O₃". In: *Physica Scripta T* 115.T115 (Jan. 2005), 1071–1073. ISSN: 02811847. DOI: 10.1238/Physica.Topical.115a01071.

- [89] G. Simon et al. "Hyper-Raman scattering analysis of the vibrations in vitreous boron oxide". In: *Physical Review B - Condensed Matter and Materials Physics* 76.5 (Aug. 2007), 054210. ISSN: 10980121. DOI: 10.1103/PhysRevB.76.054210.
- [90] H. Brune et al. "Interaction of oxygen with Al(111) studied by scanning tunneling microscopy". In: *Journal of Chemical Physics* 99.3 (Aug. 1993), 2128–2148. ISSN: 00219606. DOI: 10.1063/1.465278.
- [91] Linfei Li et al. "Chemically identifying single adatoms with single-bond sensitivity during oxidation reactions of borophene". In: *Nature Communications* 2022 13:1 13.1 (Apr. 2022), 1–9. ISSN: 2041-1723. DOI: 10.1038/s41467-022-29445-8.
- [92] Mandana Safari et al. "Growing borophene on metal substrates: A theoretical study of the role of oxygen on Al(111)". In: *Physical Review Materials* 6 (2022), 115801. DOI: 10.1103/PhysRevMaterials.6.115801.
- [93] Xiaolong Liu et al. "Probing borophene oxidation at the atomic scale". In: *Nanotechnology* 33.23 (Mar. 2022), 235702. ISSN: 0957-4484. DOI: 10.1088/1361-6528/AC56BD.
- [94] A. Stierle et al. "X-ray Diffraction Study of the Ultrathin Al₂O₃ Layer on NiAl(110)". In: *Science* 303.5664 (Mar. 2004), 1652–1656. ISSN: 00368075. DOI: 10.1126/science.1094060.
- [95] Georg Kresse et al. "Materials Science: Structure of the ultrathin aluminum oxide film on NiAl(110)". In: *Science* 308.5727 (June 2005), 1440–1442. ISSN: 00368075. DOI: 10.1126/science.1107783.
- [96] Yajun Wang and Michael Trenary. "Surface Chemistry of Boron Oxidation. 2. The Reactions of B₂O₂ and B₂O₃ with Boron Films Grown on Ta(110)". In: *Chemistry of Materials* 5.2 (1993), 199–205. ISSN: 15205002. DOI: 10.1021/cm00026a008.
- [97] Alessandro Sala et al. "Black or red phosphorus yields the same blue phosphorus film". In: *Nanoscale* 14.43 (Nov. 2022), 16256–16261. ISSN: 20403372. DOI: 10.1039/D2NR02657K.
- [98] Jeremy Karl Cockcroft. *A Hypertext Book of Crystallographic Space Group Diagrams and Tables*.

Acronyms

AES	Auger Electron Spectroscopy
ARPES	Angle-Resolved PhotoEmission Spectroscopy
BlackP	Black Phosphorus
BlueP	Blue Phosphorene
BP	Black Phosphorene
CTR	Crystal Truncation Rod
DOS	Density of States
df	Degrees of Freedom
DFT	Density Functional Theory
FL	Fermi Level
FWHM	Full Width Half Maximum
hB	Honeycomb borophene
HH	Hexagonal Holes
LEED	Low Energy Electron Diffraction
ML	MonoLayer
NEXAFS	Near Edge X-ray Absorption Fine Structure
NAP	Near Ambient Pressure
pDOS	partial Density of States
PVD	Physical Vapour Deposition
RedP	Red Phosphorus
SFG	Sum Frequency Generation
SSR	Surface Rod
STM	Scanning Tunneling Microscopy

ACRONYMS

STS Scanning Tunneling Spectroscopy

SXRD Surface X-Ray Diffraction

UHV Ultra High Vacuum

VL Vacuum Level

XPS X-ray Photoelectron Spectroscopy